Transport Kinetics of Hydrogen Permeable Lanthanum Tungstate

Von der Fakultät für Mathematik, Informatik und Naturwissenschaften der RWTH Aachen University zur Erlangung des akademischen Grades eines Doktors der Naturwissenschaften genehmigte Dissertation

vorgelegt von
Diplom-Chemiker Andreas Falkenstein
aus Aachen

Berichter:
Universitätsprofessor Dr. rer. nat. Manfred Martin
Universitätsprofessor Dr. rer. nat. Wolfgang Stahl

Tag der mündlichen Prüfung: 24.01.2017

Diese Dissertation ist auf den Internetseiten der Universitätsbibliothek online verfügbar.

Acknowledgement

First of all, I would like to thank my supervisor, Univ.-Prof. Dr. rer. nat. Manfred Martin, for the opportunity to perform my doctoral studies in his group and for fruitful scientific discussions in the past years.
I would also like to thank Univ.-Prof. Dr. rer. nat. Wolfgang Stahl for being the second referee of this thesis.

There are a lot of people that have added to this thesis and I would like to gratefully thank: Bernd Huppertz and Christoph Heeren from the electronic workshop. I have quite often been a customer and they were never annoyed by my requests but have instead constructed and explained with highest motivation and diligence. Thank you! Our technical staff, Resi Zaunbrecher for the SEM images, and Dieter Kerschgens for providing infinite gas streams in the high temperature laboratory. The mechanical workshop and glassblower, represented by Guido Kirf and Thorsten Marioneck, for their help with my experimental setups. Janka Seeger and Willi Meulenberg from FZ Juelich for the lanthanum tungstate bar samples. My Bachelor student and student coworker Jonas Schumacher for his contribution to the ECR results and my research student and student coworker Tobias Romstadt for the results of the infrared experiments as well as Alexandra von der Heiden and Philipp Hein for their help with the thin film preparation.
Roger De Souza, Steffen Grieshammer, Fabian Draber, Manuel Krott and Birgit Gerhards for a lot of scientific discussions and proof reading of this thesis. Michael Schroeder, David Müller, Thomas Kirschgen, Andreas Houben and all PhD students and Postdocs of our group for scientific and experimental discussions. You all have added to this thesis, to my talks, articles and posters.
The entire martin group, former and current members, scientific and non-scientific: the time with you — at work and at various occasions after work — has been a pleasure. Especially the offices 'Sibirien' and 2400|126.
Finally, I would like to thank my mother, Karin, for her steady support during my entire time at RWTH Aachen University.

This work has been conducted between 10/01/2012 and 10/31/2016 at the Institute of Physical Chemistry I at RWTH Aachen University under supervision of Univ.-Prof. Dr. rer. nat. Manfred Martin.

Parts of this work have been previously published:

- Andreas Falkenstein, David N. Mueller*, Roger A. De Souza, Manfred Martin, Chemical relaxation experiments on mixed conducting oxides with large stoichiometry deviations, *Solid State Ionics* **2015**, *280*, 66-73.
- Jonas Schumacher, Transportkinetik von $La_{5.4}WO_{11.1}$ mittels Leitfähigkeitsrelaxation unter Potentialgradienten multipler ionischer Spezies, *Bachelor thesis* **2014**, RWTH Aachen University, Aachen, Germany.
- Tobias Romstadt B.Sc., Ionenleitfähigkeit von $La_{28-x}W_{4+x}O_{54+1.5x}$ mittels FTIR-Spektroskopie, *Research report* **2017**, RWTH Aachen University, Aachen, Germany.

Contents

1

Introduction

»*I am applying a voltage to stones.*« — This is what I usually reply to family and friends asking about my research. A stone is commonly the epitome of a dead material, but it is not, considering numerous applications using solid state materials nowadays. Not only the (physical) magnetic and electronic properties but also physico-chemical properties like diffusion or phase change are of interest. This work is focusing on diffusion in solids. In the last 150 years, a large field of research has been established describing diffusion in solids in terms of quantity and quality and there is still a lot to discover. The phenomenon of diffusion is used in the tiniest parts of information technology, e.g. in phase change materials for resistive random access memory, in length scales of a few nanometers. This effect can also be utilized in large scale fossil power plants or chemical reactors in the form of gas separation membranes, e.g. oxygen transport membranes (OTMs) or hydrogen transport membranes (HTMs). With the introduction of renewable energy sources like wind power and photovoltaics, the need for energy storage systems arose in recent years. In electrolyzer cells for chemical energy storage and in batteries, diffusion is the key effect beside the electrochemical potential, enabling these storage technologies.

Finding materials with high diffusivities of the desired species — which are preferably chemically and mechanically stable to satisfy the engineers — is crucial for the development of these technologies. The most important characteristic is the diffusion coefficient. If it is necessary to interact with the gas phase (e.g. in gas separation membranes), also the surface reaction rate is of interest. Experimental and computational methods have been developed to quantify these coefficients. For the experimental methods, isotope exchange depth profiles (IEDPs) analyzed by time-of-flight secondary ion mass spectrometry (ToF-SIMS) and relaxation experiments are the most common techniques (the first yielding tracer coefficients while the latter yields ambipolar coefficients; details

follow in the theory section of this work).

In order to optimize, for example, a membrane, knowledge of the kinetic transport parameters, namely the diffusion coefficient and the surface reaction rate, is required. For example, if the bottleneck of a membrane is the bulk diffusion, an optimization by applying catalytic surfaces to increase the surface reaction coefficient is of no effect, or, in the opposite case, if the membrane is surface reaction limited, a decrease of the membrane's thickness to improve the diffusion length is irrelevant. The bottleneck can be identified, e.g. by modeling plants using these parameters in finite element method (FEM) calculations.

In this work, the fluorite type oxide lanthanum tungstate — $La_{5.4}WO_{11.1-0.2\delta}$ (LaWO54) — has been investigated using the electrical conductivity relaxation (ECR) technique. LaWO54 is a mixed ionic–electronic conductor (MIEC) with high protonic conductivity. It combines good permeation behavior with chemical and mechanical stability and is therefore a candidate for future applications. In the low temperature regime it can be utilized as an electrolyte material with proton conductivity and in high temperature applications it can be used as an electrode material or as a membrane material in gas separation membranes as well as in chemical reactors.

With the ECR technique, the transport parameters for protons and oxygen ions in LaWO54 have been determined. Another focus of this work lies on methodological questions regarding ECR — or relaxation techniques in general — when analyzing hydration behavior instead of the commonly investigated behavior upon oxidation.

2

Lanthanum Tungstate — Structure and Defect Chemistry

Lanthanum tungstate is an MIEC with high protonic and electronic conductivity[1], both between 10^{-3} and 10^{-2} S cm^{-1} in a temperature range from 700 °C to 900 °C[2, 3]. Its mechanical and chemical stability against relevant process gases such as hydrocarbons, carbon dioxide and water, make LaWO54 an interesting material for high temperature applications.[2, 4] At temperatures below 750 °C and in humid atmospheres, LaWO54 is predominantly a protonic conductor with low electronic contribution to the conductivity.[5] Thus, it is an interesting electrolyte material for proton conducting solid oxide fuel cells (PC-SOFCs), competitive to $BaZrO_3$ when deposited as a thin film.[6] At high temperatures LaWO54 is also an electronic conductor and a suitable material for gas separation membranes (HTM)[7] or for cathodes in solid oxide fuel cells (SOFCs)[8].
The defect chemistry shows not typical behavior and a detailed examination of its structure is required. In this section, the crystal structure will be described first and the resulting effects on lanthanum tungstate's defect chemistry required for understanding the effects discussed in Chapters 3 and 4 will be described afterwards. Finally, an overview of the electrochemical properties, which have been published in literature, will be provided.

2.1 Structure

Lanthanum tungstate is a solid solution of lanthanum(III) oxide, La_2O_3, and tungsten(VI) oxide, WO_3, with a lanthanum/tungsten ratio of approximately 5.4. The phase diagram of this system has been described by Yoshimura and Rouanet[9] forty years ago. Works on the crystal structure and stable region of LaWO54 have been initiated after identifying this material as a high temperature protonic conductor.[1, 2] The stoichiometric composition follows the formula $La_{28-x}W_{4+x}O_{54+1.5x}v_{2-1.5x}$ and contains two structural vacancies (v) in the anion sublattice.[3] The undoped composition (x = 0, with a lanthanum/tungsten ratio of 7) is not stable but by increasing the tungsten content ($x \approx 1$ with La/W ≈ 5.4), this structure can be stabilized.[3, 10] It crystallizes in the fluorite structure.

2.1.1 Single Phase Solid Solution

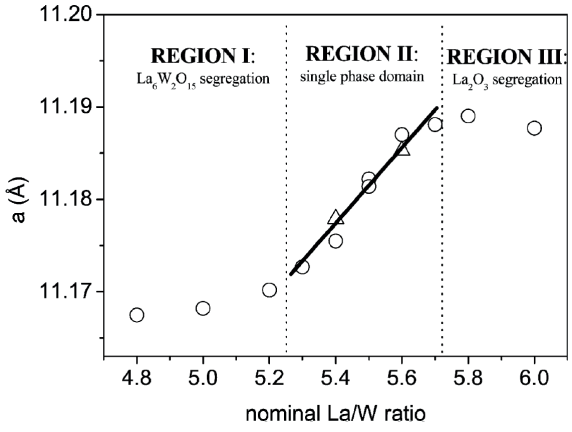

Figure 2.1: LaWO phases dependent on the lanthanum/tungsten ratio: in region II a single phase of lanthanum tungstate is stable. In regions I and III second phases appear. Triangles are the results of a second synthesis. They sintered the powders at 1500 °C in air. Reproduced from Ref. [3] with permission from The Royal Society of Chemistry.

In the crystal structure of LaWO54 two different Wyckoff-positions for La^{3+} exist (see Tab. 2.1), La1 and La2. Increasing the tungsten content by x = 1, i.e. replacing one lanthanum on a La2-48h site by tungsten, leads to a composition of $La_{5.4}WO_{11.1}$, normalized to tungsten. By X-ray diffraction (XRD) measurements of lanthanum tungstates with different La/W ratios the stable region of the solid solution has been identified[3] (see Fig. 2.1): the lattice parameter, a, is dependent on the La/W ratio in the single phase region. If the ratio is higher, a lanthanum(III) oxide phase appears and the lattice parameter of lanthanum tungstate is unchanged with increasing lanthanum content; if it is lower, a tungsten rich phase ($La_6W_2O_{15}$) appears. The lattice parameter of lanthanum tungstate is constant with increasing tungsten content. This experiment has been repeated with different firing temperatures and hereby it has been shown that the solubility of tungsten on a La2 position is temperature-dependent.[10] It was shown by Yoshimura and Rouanet that the solid solutions depicted with a blue background in Fig. 2.2 are in fact a single phase of the solid solution. A new phase diagram has been created by Magrasó *et al.*[10] based on the XRD measurements from Ref. [3], shown in Fig. 2.3. Depending on the firing temperature, the single phase region of the solid solution has La/W ratios between 5 and 6.[10]

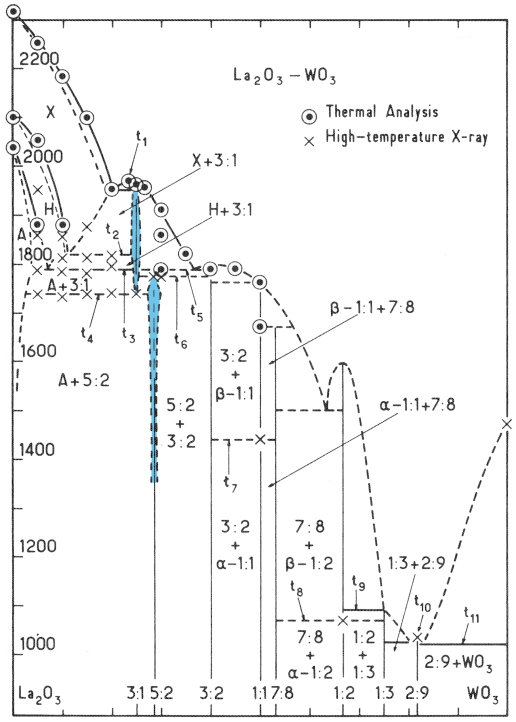

Figure 2.2: Phase diagram of the system $La_2O_3 - WO_3$ in air reprinted from Reference [9], with permission from Elsevier. A blue background is added to the stable single phase region. Temperatures in °C.

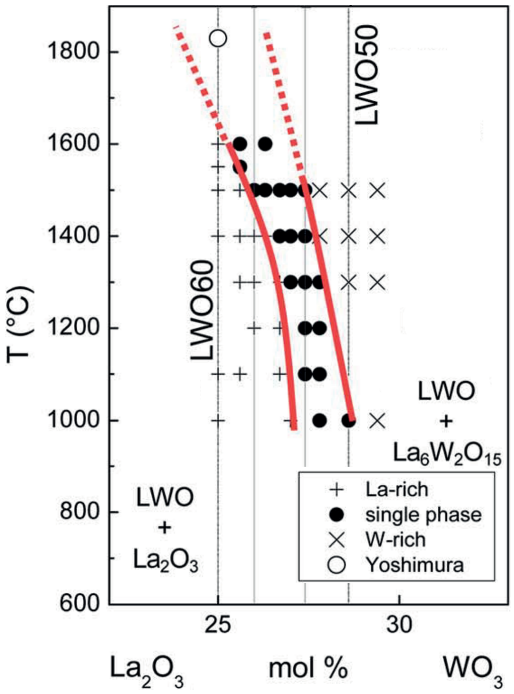

Figure 2.3: Revised phase diagram in air by Magrasó *et al.* taken from Reference [10] (adapted; published by The Royal Society of Chemistry). The four vertical lines represent a La/W ratio of 6.0, 5.7, 5.3 and 5.0.

2.1.2 Crystal Structure

LaWO54 crystallizes in the fluorite structure with a lattice parameter, *a*, between 11.17 Å and 11.19 Å. In a first study of the structure, XRD patterns were described by space group (s.g.) $F\bar{4}3m$ (216)[3] but later publications of the same group[10, 11] suggested that the crystal structure can be described by s.g. $F\bar{4}3m$ (216) or $Fm\bar{3}m$ (225). At the same time Scherb[12] described low temperature synchrotron XRD profiles with s.g. $Fm\bar{3}m$ but neutron scattering data showed bad agreement with this s.g. Thus, the cation ordering can be described by s.g. $Fm\bar{3}m$ but the oxygen ions, which have been uncovered in neutron diffraction data, cannot be described sufficiently in this s.g. A new model with s.g. $F\bar{4}3m$ (216) has been proposed showing good agreement with neutron and synchrotron data. In a later publication, Scherb *et al.*[13] improved the crystal structure to a fluorite supercell with s.g. $Pa\bar{3}$ (205). In parallel, Kalland *et al.*[14] suggested that the crystal structure cannot be described by an average symmetric structure.

Rietveld refinement of XRD data of powders and samples used in this work, however, show a better agreement of the cation sublattice (XRD is not sensitive to oxygen because of the low atomic form factor) to the first model of Scherb[12] (see Section 6.1.3) using s.g. $Fm\bar{3}m$. As the s.gs. mentioned

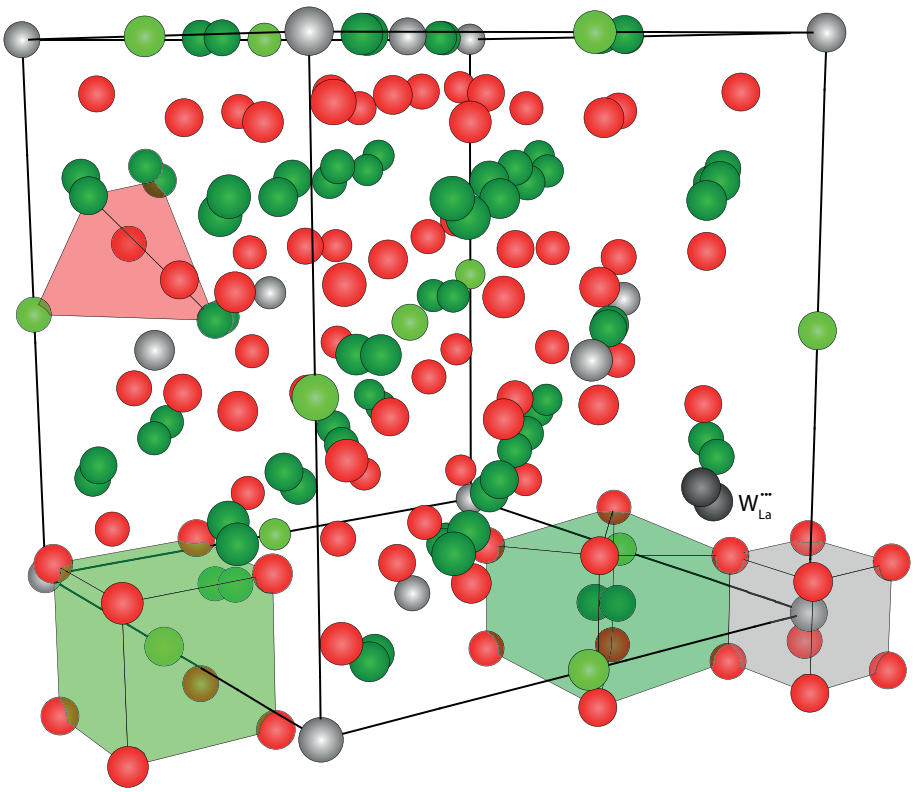

Figure 2.4: Structure of LaWO54. Light green: lanthanum (La1), dark green: lanthanum (La2 split sites), red: oxygen, light gray: tungsten, dark gray: tungsten on a lanthanum split site (W2, $W_{La}^{\bullet\bullet\bullet}$).

are very similar to each other, the structure will be presented in the more general s.g. $Fm\bar{3}m$ here. The lower symmetry of the other s.gs. can alternatively be described in s.g. 225 by lower site occupancy factors (sofs). The s.g. 225 has a higher multiplicity of oxygen sites and thus only a part of them are occupied. Seeger[1] *et al.*[15] suggest the first model of Scherb. The structural information is summarized in Tab. 2.1 with the lattice parameter gained from Rietveld refinement and other structural information such as assignment of Wyckoff positions, sofs and isotropic temperature factors, B_{iso}, taken from Reference [12]. The structure is depicted in Fig. 2.4. Tungsten (W1) is coordinated cubic by oxygen (O1) and occupies the corners and the face centers of the unit cell (0 0 0, light gray atoms and coordination polyhedron in Fig. 2.4). The coordination number is 6, resulting from a sof of oxygen on O1 site of ≈ 0.75.[12] According to Diot *et al.*[16], tungsten (W1) is coordinated cubic with two vacancies on diagonal sites, $[WO_6\square_2]$. The structure is therefore called an 'ordered defective fluorite structure'[2, 16, 17] with 56 remaining anion sites (64 regular sites per unit cell minus 4 × 2 oxygen vacancies next to the W1 site). As mentioned before, two different lanthanum sites exist, La1 in the center and on the edges of the cubic cell, coordinated cubic by oxygen (O1) (light green atoms and coordination polyhedron). The second lanthanum site (approx. 0 1/4 1/4, shown

[1] J. Seeger prepared the bar samples used for ECR measurements in this work.

in dark green) is distortedly coordinated rhombic prismatic by oxygen (O1 and O2). The position of lanthanum is slightly off-site ($x = y \approx 0.235$ instead of 0.25), causing split sites due to symmetry. The site is thus fully occupied with a sof of 0.5.[12] The split position is caused by oxygen vacancies at the W1 polyhedron and depending on the local oxygen environment of La2 (or W2, see later), either one or the other split position is occupied.[12] Oxygen is coordinated tetrahedrally either by lanthanum (O2) or tungsten and lanthanum (O1). All 32 O2 sites are fully occupied whereas 8 of the 32 O1 sites are vacant ($\mathrm{sof(O1)} = 0.75$, see above). Furthermore, two of the remaining 56 anion sites are vacant due to stoichiometry, described by $v_{2-1.5x}$ in $La_{28-x}W_{4+x}O_{54+1.5x}v_{2-1.5x}$ in the undoped material, i.e. $x = 0$. According to Erdal *et al.*, density functional theory calculations indicated that oxygen vacancies neighboring tungsten are slightly higher in energy. However, for temperatures used in this work — which are typical for applications of ion conductors ($T > 500\,°C$) — it can be assumed that the 56 sites of the perfect lattice are degenerate and statistically occupied by 54 oxygen anions and 2 structural vacancies.[18] The two vacancies in the vicinity of W1 can be treated as structural vacancies — though the only constraint is that they are located diagonally to each other — and do not contribute to the order/disorder equilibrium.

In LaWO54, one lanthanum on a La2 site per unit cell is replaced by tungsten (W2, $x = 1$). Like lanthanum, tungsten is also distortedly coordinated rhombic prismatic by oxygen. By replacing one lanthanum by tungsten, additional 1.5 of the two structural vacancy sites are occupied by oxygen to maintain charge neutrality. The ionic radius of tungsten on this site is much smaller: the Shannon radius of lanthanum is between $r(^{VI}La^{3+}) = 1.032\,Å$ and $r(^{VIII}La^{3+}) = 1.160\,Å$, and the radius of tungsten is $r(^{VI}W^{6+}) = 0.60\,Å$.[19] Magrasó *et al.*, however, allocated the solubility of tungsten on the La2 site to its highly distorted oxygen environment.[20] Scherb proposed a sevenfold coordination polyhedron for both cations, La2 and W2, considering the occupation numbers of oxygen and the experimentally derived coordination number of La2 and W2 of ≈ 7.[12] The W2 – O distances are equal to the regular W1 – O distances[20] and the lattice positions of La2 and W2 are almost equal, shown by computational simulations[20] and diffraction methods[12].

2.2 Defect Chemistry

Defects in the crystal structure of materials are crucial for the transport of species in solid state materials. This work focuses on bulk properties of solid state materials and thus only zero-dimensional defects (point defects) are described in the following, although one- and multi-dimensional defects also enable transport phenomena.[21, 22] Point defects are typically written in the Kröger–Vink notation[23], using charges relative to the perfect crystal: '•' for a relative positive charge, '′' for a relative negative charge and '×' as relative neutral. 'v' denotes a vacancy and 'i' an interstitial position. In this work, '*v*' is used to distinguish a structural vacancy from a vacancy of a regular oxygen site, v. The notation uses the element or species that is creating the defect, S, with the relative charge, q, as superscript and the lattice position in the perfect crystal, p, as subscript: S_p^q. Example: yttrium

Table 2.1: Phase information for the Rietveld refinement (see Section 6.1.3) of lanthanum tungstate taken from Reference [12].

Site	Wyckoff	Coordinates			$B_{iso}/0.01\,Å^2$	sof	Occupancy
		x	y	z			
W1	4*a*	0	0	0	0.457	1.000	0.02083
La1	4*b*	0.5	0.5	0.5	1.125	0.979	0.02040
W2	48*h*	0	0.23520	0.23520	0.776	0.018	0.00450
La2	48*h*	0	0.23520	0.23520	0.776	0.482	0.12050
O1	32*f*	0.0971	0.0971	0.0971	8.26	0.729	0.12150
O2	32*f*	0.3663	0.3663	0.3663	1.39	0.967	0.16117
Space group		$Fm\bar{3}m$ (225)					
Lattice parameter		a = 11.1716 Å					

(Y^{3+}) doped into zirconia, ZrO_2, by replacing one zirconium(IV) cation with an yttrium(III) cation has the notation Y'_{Zr}. It is also possible to describe electronic defects by free electrons in the conduction band, e', and electron holes in the valence band, $h^\bullet$.

The defect fraction, [def], is the fraction of the defect relative to the stoichiometric composition. E.g. an acceptor doped (Acc'_M) oxide with the stoichiometric composition MO has a defect fraction, $[Acc'_M]$, of $N_{Acc'_M}/N_{MO}$ with the amounts N_i of species i (or equivalent, the concentration of defects in mole per mole oxide). The volume concentration of the defect, c_{def}, can be set into relation to the defect fraction, [def], by

$$c_{def} = \frac{[def] \cdot Z}{N_A \cdot V_{UC}}, \tag{2.1}$$

with the number of formula units per unit cell, Z, the Avogadro number, N_A, and the volume of the unit cell, V_{UC}.

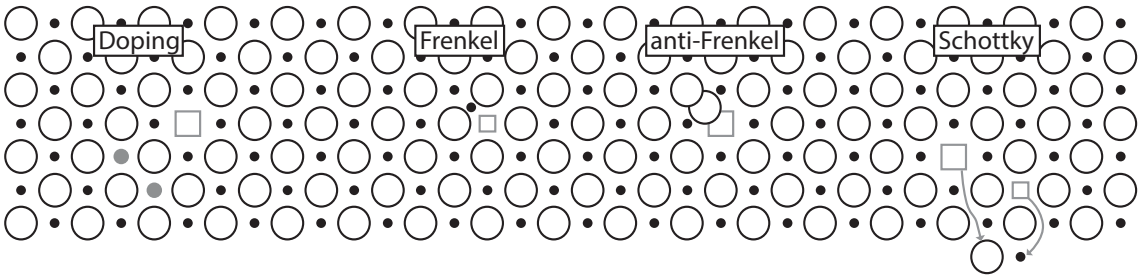

Figure 2.5: Point defects in an exemplary crystal lattice. •: cation; ◯: anion; •: lesser valent dopant; □: vacancy. Please compare to Reference [24].

2.2.1 Point Defects in Lanthanum Tungstate

2.2.1.1 Donor Doping with Tungsten

The single-phase solid solution is — as discussed above — stabilized by doping with an additional tungsten on a La2 site per unit cell. Consequently, it contains four regular tungsten species on tungsten sites, $W_W^\times$, and one tungsten (W^{6+}) on a lanthanum (La^{3+}) site, $W_{La}^{\bullet\bullet\bullet}$. In the temperature range where transport kinetics are examined in this thesis, i.e. $T \leq 950\,°C$, the mobility of tungsten and lanthanum can be assumed zero (compare to cation diffusion in other fluorites[25, 26]). The concentration of tungsten and lanthanum in the samples is, hence, constant throughout space and time. XPS analysis by Erdal *et al.* has shown that lanthanum and tungsten have their maximum positive charge, La^{3+} and W^{6+}.[18] Therefore, doping with tungsten leads to three relative positive charges compensated by 1.5 additional oxygen:

$$La_{28}W_4O_{54} + WO_3 \rightarrow La_{27}W_5O_{55.5} + \frac{1}{2}La_2O_3 \tag{2.2}$$

2.2.1.2 Oxygen

In the stoichiometric composition two types of intrinsic oxygen defects can be created to increase configurational entropy, Schottky disorder[27] and anti-Frenkel disorder[28]. Schottky disorder consists of defects involving multiple oppositely charged ions creating vacancies by adding ions to the surface according to

$$M_M^\times + O_O^\times \rightleftharpoons v_M'' + v_O^{\bullet\bullet} + M_{surf}^\times + O_{surf}^\times \qquad \text{with} \qquad K_S = [v_M''][v_O^{\bullet\bullet}] \tag{2.3}$$

for an exemplary divalent metal oxide with the Schottky equilibrium constant K_S. Anti-Frenkel disorder in oxides is formed by an oxygen vacancy and an oxygen interstitial, O_i'', with the equilibrium constant K_{aF} and the reaction

$$O_O^\times + v_i^\times \rightleftharpoons v_O^{\bullet\bullet} + O_i'' \qquad \text{with} \qquad K_{aF} = [O_i''][v_O^{\bullet\bullet}] \tag{2.4}$$

Additionally, an equilibrium with oxygen of the surrounding gas atmosphere, dependent on the partial pressure of oxygen, pO_2, is present. Oxygen from the surrounding gas atmosphere can be incorporated into or be released from the solid oxide according to the following surface equilibrium:

$$\frac{1}{2}O_2(g) + v_O^{\bullet\bullet} \rightleftharpoons O_O^\times + 2h^\bullet \qquad \text{with} \qquad K_{O_2} = \frac{[O_O^\times][h^\bullet]^2}{\sqrt{pO_2}[v_O^{\bullet\bullet}]} \tag{2.5}$$

Oxygen from an oxygen molecule in the gas phase is incorporated onto a surface near oxygen vacancy, creating two electron holes (see Section 2.2.1.4 for further considerations about electronic defects). The formation of (thermal) oxygen vacancies leads to an oxygen non-stoichiometry in the material, described by the value δ in the material's chemical formula, $MO_{1-\delta}$.

In the case of lanthanum tungstate, two different types of oxygen vacancies are present: $2 - 1.5x$ structural vacancies on the anion sublattice per unit cell due to stoichiometry, $v_v^{\times}$, depending on excess tungsten concentration x; and δ thermal oxygen vacancies per unit cell, $v_O^{\bullet\bullet}$, depending on temperature and partial pressure of oxygen (and, to anticipate Chapter 3, on partial pressure of water). Both types of vacancies can also be occupied, subsequently forming the defect either oxygen on a structural vacancy site, O_v'', or a regular oxygen on oxygen site, $O_O^{\times}$. As mentioned in the previous sections, the remaining 56 anion lattice sites are degenerate at high temperatures[18], and as a consequence, one cannot distinguish between oxygen on an oxygen site or on a structural vacancy site and also not between a vacancy on an oxygen site and on a structural vacancy site.
In this work, the oxygen sublattice is thus split according to the composition of LaWO54, $La_{28-x}W_{4+x}O_{54+1.5x}v_{2-1.5x}$, into two virtual sublattices with a ratio of 54 : 2. The defect fractions of the components occupying the 56 anion sublattice sites, $O_O^{\times}$, $v_O^{\bullet\bullet}$, O_v'', and $v_v^{\times}$, are in the following relation:

$$[O_v''] + [v_v^{\times}] = 2 \tag{2.6}$$

$$[O_O^{\times}] + [v_O^{\bullet\bullet}] = 54 \tag{2.7}$$

It is important to keep in mind that no anti-Frenkel equilibrium is present between both virtual sublattices because the sites are degenerate at high temperatures. It can be seen as an order-disorder-transition with the following quasi-chemical reaction:

$$O_O^{\times} + v_v^{\times} \rightleftharpoons v_O^{\bullet\bullet} + O_v'' \qquad \text{with} \qquad K_{o/do} = \frac{[v_O^{\bullet\bullet}][O_v'']}{[O_O^{\times}][v_v^{\times}]} \tag{2.8}$$

It is comparable to the reversible order-disorder-transition in spinels where the 'normal' spinel structure (e.g. Ni_2GeO_4) or 'inverse' spinel structure exist at low and medium temperatures. At high temperatures the cations are distributed to the A-site and B-site depending on the equilibrium temperature.[29] For lanthanum tungstate, the Gibbs energy of the quasi-chemical reaction, $\Delta_R G^{\ominus}$ of Eq. (2.8), is assumed to be small compared to RT at high temperatures: $\exp\{-\Delta_R G^{\ominus}/RT\} \approx 1$. The equilibrium constant of the order-disorder-transition of the oxygen sublattice is approximately unity and the combined sites of both sublattices are statistically occupied by oxygen. The total defect fractions of oxygen, $([O_v''] + [O_O^{\times}])$, and vacancies, $([v_v^{\times}] + [v_O^{\bullet\bullet}])$, by combining the two virtual sublattices can thus directly be inserted into the laws of mass action for the incorporation equations that will be presented in Chapter 3. Additionally, oxygen on structural vacancy sites and oxygen on regular oxygen sites and structural vacancies and oxygen vacancies are in the following relationship due to the splitting into the virtual sublattices and the order-disorder-transition, derived from Eq. (2.8):

$$[O_v''] = \frac{2}{54}[O_O^{\times}] \qquad \text{and} \qquad [v_v^{\times}] = \frac{2}{54}[v_O^{\bullet\bullet}] \tag{2.9}$$

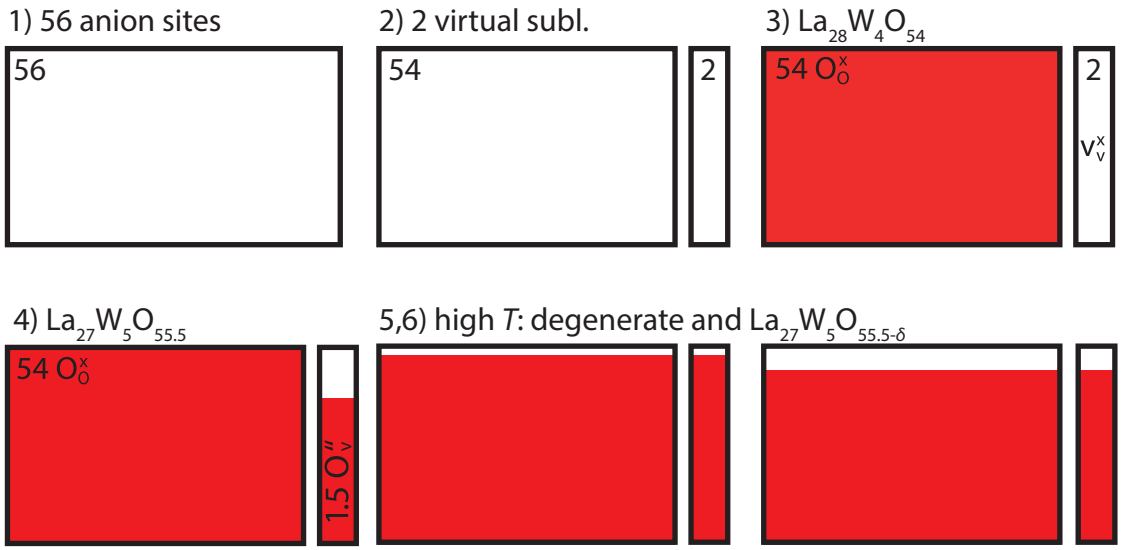

Figure 2.6: Oxygen sublattice of LaWO54 (vacancies in 3)–6) white, oxygen red): 1) 56 anion sites can be occupied by oxygen. 2) This sublattice is split into two virtual sublattices. 3) In the stoichiometric composition at 0 K two structural vacancies exist while the first sublattice is occupied by 54 regular oxygen. 4) Doping with one tungsten fills 1.5 structural vacancies with oxygen. 5) At high temperatures all oxygen sites are degenerate. 6) Above zero temperature oxygen vacancies (oxygen non-stoichiometry δ) are created to increase configurational entropy.

Norby suggested a new approach to the Kröger–Vink nomenclature of such crystal structures by using fractional charges (statistical charge of the lattice site) and fractional lattice sites as a result of combining the two virtual sublattices of the defective structure described above.[30] This takes also into account that there is no anti-Frenkel equilibrium between oxygen vacancies and structural vacancies. It is beneficial in Norby's nomenclature that less defect reactions must be formulated (see Section 3.1).

Erdal *et al.*[18] have presented the defect chemistry of LaWO54 based on the model of Norby[30]: the combined oxygen sublattice can be described by the occupied defect $O_{\frac{54}{56}O}^{\frac{4}{56}\prime}$ and the vacancy $v_{\frac{54}{56}O}^{\frac{108}{56}\bullet}$ with a charge relative to the statistical ideal charge of −108/56.

2.2.1.3 Protonic defects

Many solid state oxide materials are able to dissolve protons. Studies on proton conductivity on perovskite type materials by Kreuer[31, 32] revealed that protons are bound to oxygen. Depending on the distance between oxygen ions, d, three types of bonds can be categorized:

- Large O – O distances ($d > 280$ pm): protons are strongly bound to oxygen ions with a bond distance lower than 100 pm. Thus, the proton is embedded in the electron shell of oxygen (Shannon crystal radius of oxygen: 121 pm to 128 pm[19]).
- Medium distances (250 pm $< d <$ 280 pm): hydrogen shows a strong (mainly covalent) bond to one of the oxygen ions and a weak hydrogen bond to the other.
- Short distances ($d \leq 250$ pm): the proton is bound to both oxygen ions by covalent bonds.

Kinetic Monte Carlo simulations by Björketun *et al.*[33] have shown that the minimum O–H distance is 98 pm in barium zirconate and that the bond is oriented along the angle bisector between the oxygen ion and the two neighboring barium ions that are not diagonal to each other. By reorientation of the cation polyhedra the distance between two oxygen ions can be shorter at a specific time ('instant configuration') and temporary hydrogen bonds to nearest-neighbor oxygen ions are possible.[32] Using s.g. $Fm\bar{3}m$ (225) with lattice parameter a = 11.1716 Å and no further distortion of the coordination polyhedra, the oxygen–oxygen distances in LaWO54 are $d(\mathrm{O1-O1}) = 217$ pm, $d(\mathrm{O2-O2}) = 298$ pm and $d(\mathrm{O1-O2}) = 306$ pm. In instant configurations, other oxygen–oxygen distances occur than in the average configuration. It can be assumed that protons in the vicinity of tungsten have a covalent bond to two oxygen O1 ions. In instant configurations, hydrogen bonds to oxygen O2 ions might be possible. In the average configuration, the hydrogen bond breaks and the proton is bound to a single oxygen ion, if oriented towards an O2 oxygen ion. There are two different notations for the same protonic defect: one describes the proton in the electron shell of oxygen forming a hydroxy anion on an oxygen lattice site, $\mathrm{OH}_{\mathrm{O}}^{\bullet}$. The other notation defines the proton as an interstitial, $\mathrm{H}_{\mathrm{i}}^{\bullet}$ (which must be in the vicinity of an oxygen ion, $\mathrm{O}_{\mathrm{O}}^{\times}$).
For lanthanum tungstate the notation of hydroxy anions is either $\mathrm{OH}_{\mathrm{O}}^{\bullet}$ for the first virtual sublattice and OH_{v}' for the second virtual sublattice or in Norby's notation for inherently defective sublattices $\mathrm{OH}_{\frac{54}{56}\mathrm{O}}^{\frac{52}{56}\bullet}$.[18, 30] However, describing the proton as an interstitial, $\mathrm{H}_{\mathrm{i}}^{\bullet}$, is always valid.
The migration of protons — reorientation and transfer processes — will be discussed in Section 3.2.1.1.

2.2.1.4 Electronic Defects

In solid state materials the energy levels of molecule orbitals are so close together that one can define them as a band.[34] The highest occupied band at zero temperature is called the valence band and the lowest unoccupied band is called the conduction band. Semiconductors like LaWO54 possess a (not too large) band gap between both bands, and the Fermi energy, ϵ_F, is located within the band gap. Above zero temperature, electrons follow the Fermi–Dirac distribution, causing valence electrons to be excited into the conduction band. Thus, free electrons are located in the conduction band, e', leaving an electron hole, $h^\bullet$, behind. Recombination of free electrons and electron holes is also possible. The electronic equilibrium is defined by

$$\text{nil} \rightleftharpoons e' + h^\bullet \qquad \text{with} \qquad K_e = [e'][h^\bullet] \tag{2.10}$$

At the stoichiometric point, the concentrations of electronic defects are equal, $[e'] = [h^\bullet]$. At partial pressures of oxygen higher than the stoichiometric point (p-type regime), electron holes, $h^\bullet$, are electronic majority defects due to the oxygen incorporation equation. At partial pressures below the stoichiometric point (n-type regime), free electrons, e', are electronic majority defects.[24] For the first case, the oxygen incorporation equation (2.5) can be formulated while for the second case, it can be reformulated by combining with Eq. (2.10) to

$$\frac{1}{2}O_2(g) + v_O^{\bullet\bullet} + 2e' \rightleftharpoons O_O^\times \qquad \text{with} \qquad K_{O_2} = \frac{[O_O^\times]}{\sqrt{pO_2}[v_O^{\bullet\bullet}][e']^2} \tag{2.11}$$

2.2.2 Electroneutrality Condition

The concentrations of all charged point defects are set into relation to each other in the electroneutrality condition. All positive charges must be compensated by negative charges — regardless if declared as absolute or relative charges. First, the complete electroneutrality condition will be presented, including intrinsic defects such as Frenkel, anti-Frenkel and Schottky disorder. The electroneutrality condition can be simplified by neglecting defects with very small concentrations, depending on the conditions that will be examined and on the material.
The complete list of defects for lanthanum tungstate is:

- Tungsten dopant, $W_{La}^{\bullet\bullet\bullet}$
- Electronic defects, e' and $h^\bullet$
- Thermal oxygen vacancies, $v_O^{\bullet\bullet}$
- Oxygen ions on structural vacancy sites, O_v''
- Proton interstitials, $H_i^\bullet$
- Frenkel defects, $v_{La}''' + La_i^{\bullet\bullet\bullet}$ and $v_W^{6\prime} + W_i^{6\bullet}$, and anti-Frenkel defects, $v_O^{\bullet\bullet} + O_i''$

- Schottky defects, $v_{La}''' + 1.5v_O^{\bullet\bullet}$ and $v_W^{6\prime} + 3v_O^{\bullet\bullet}$.

The full electroneutrality condition is accordingly

$$3[W_{La}^{\bullet\bullet\bullet}] + [h^{\bullet}] + 2[v_O^{\bullet\bullet}] + [H_i^{\bullet}] + 3[La_i^{\bullet\bullet\bullet}] + 6[W_i^{6\bullet}] = 2[O_v''] + 2[O_i''] + 3[v_{La}'''] + 6[v_W^{6\prime}] + [e'] \tag{2.12}$$

The following simplifications for lanthanum tungstate and the experimental conditions analyzed in this work are valid: the oxygen sublattice of fluorites and perovskites is not close packed and defects in this sublattice are dominating over defects in the cation sublattice. Hence, Schottky and anti-/Frenkel type defects are minority defects and can be neglected in the electroneutrality condition.[24] At the temperatures and pO_2s examined in this work the simplifications of oxidizing conditions can be applied (see below). Consequently, electronic majority defects in the *p*-type regime are electron holes. Free electrons, e', can be neglected. As the temperature range is higher than the commonly used range up to approx. 700 °C, electronic defects that are neglected in the work of Erdal *et al.*[18] cannot be neglected here (see a later publication of the same group, Magrasó *et al.*[10]). N.B.: The 'high' temperature range (above 1500 °C) enables cation diffusion. Such high temperatures are only used for sintering in this work.
With these simplifications a new electroneutrality condition for intermediate temperatures can be formulated:

$$3[W_{La}^{\bullet\bullet\bullet}] + [h^{\bullet}] + 2[v_O^{\bullet\bullet}] + [H_i^{\bullet}] = 2[O_v''] \tag{2.13}$$

This equation can also be written in Norby's notation for inherently defective sublattices[30] (compare to Erdal *et al.*[18]):

$$3[W_{La}^{\bullet\bullet\bullet}] + [h^{\bullet}] + \frac{108}{56}\left[v_{\frac{54}{56}O}^{\frac{108}{56}\bullet}\right] + [H_i^{\bullet}] = \frac{4}{56}\left[O_{\frac{54}{56}O}^{\frac{4}{56}\prime}\right] \tag{2.14}$$

Lanthanum tungstate is donor doped with tungsten but the oxygen ions occupying structural vacancies, compensating the positive charges of tungsten and, at high pO_2 and intermediate temperatures, of electron holes, render lanthanum tungstate an effectively acceptor doped material[10]: with $[W_{La}^{\bullet\bullet\bullet}] = 1$ and $[O_v''] \approx 2 \cdot 55.5/56 \approx 2$ equivalent to an effective acceptor with concentration $[Acc_{eff}'] \approx 1$ and relative charge of $-55.5/56 \approx -1$.

2.2.3 Defect Concentrations and Brouwer Diagram

The amount of tungsten dopant is constant in the entire pO_2 and temperature range. The total oxygen sublattice is occupied by approximately 55.5 oxygen ions and can be assumed constant ($La_{27}W_5O_{55.5-\delta}$ with $\delta \ll 55.5$). The concentration of the other defects is mainly dependent on the partial pressure of oxygen and can be divided into three regions:

1. Reducing conditions (low pO_2):
   The following concentrations are negligible at extremely reducing conditions: electron holes, tungsten dopant and oxygen on structural vacancy sites, while the latter can also be expressed as an effective acceptor dopant as already discussed before, which is also negligible compared to oxygen vacancies. Thus, the electroneutrality condition, Eq. (2.13), including free electrons for this regime, e', can be simplified to

   $$2[v_O^{\bullet\bullet}] = [e'] \tag{2.15}$$

   The equilibrium constant for the oxygen incorporation equation in the *n*-type regime, Eq. (2.11), can be written as

   $$K_{O_2} = \frac{([O_O^{\times}] + [O_v'])}{\sqrt{pO_2}([v_O^{\bullet\bullet}] + [v_v^{\times}])[e']^2} = \frac{54}{56} \cdot \frac{2 \cdot 55.5}{\sqrt{pO_2}[e']^3} \tag{2.16}$$

   Please compare this to the general equation (2.11) and the *p*-type equation for lanthanum tungstate in Chapter 3, Eq. (3.4) combined with Eq. (2.9). The slope of the concentrations of free electrons and oxygen vacancies in the extremely reducing regime is –1/6 and the electron hole concentration in the (double logarithmic) Brouwer diagram has a slope of +1/6.

2. Stoichiometric region (medium pO_2):
   Electronic defects, e' and $h^{\bullet}$, can be neglected when close to the stoichiometric point. The concentration of oxygen vacancies is compensated by oxygen on structural vacancy sites which also compensate the tungsten dopant. When regarding the system as effectively acceptor doped, oxygen vacancies are compensated by effective acceptor dopands. The electroneutrality condition, Eq. (2.13), reduces to

   $$2[v_O^{\bullet\bullet}] = \left(2[O_v'] - 3[W_{La}^{\bullet\bullet\bullet}]\right) = [Acc'_{eff}] \tag{2.17}$$

   The equilibrium constant can be expressed by

   $$K_{O_2} = \frac{([O_O^{\times}] + [O_v'])}{\sqrt{pO_2}([v_O^{\bullet\bullet}] + [v_v^{\times}])[e']^2} = \frac{54}{56} \cdot \frac{2 \cdot 55.5}{\sqrt{pO_2}[Acc'_{eff}][e']^2} \tag{2.18}$$

   The slope of the concentrations of electronic defects is thus –1/4 and +1/4 for free electrons and electron holes, respectively. As the concentration of oxygen vacancies is dependent on the acceptor concentration, it is constant in this region.

3. Oxidizing conditions (high pO_2):
   In the oxidizing region the concentrations of oxygen vacancies and free electrons can be neglected in the electroneutrality condition, resulting in

$$[h^{\bullet}] = \left(2[O_v''] - 3[W_{La}^{\bullet\bullet\bullet}]\right) = [Acc_{eff}'] \tag{2.19}$$

   Tungsten dopant and oxygen on structural vacancies can be treated as effective acceptor dopants as discussed before. Electron holes are thus compensated by these acceptors and their concentration is constant in this region. The concentration of oxygen vacancies can be calculated by the law of mass action:

$$K_{O_2} = \frac{54}{56} \cdot \frac{55.5 \cdot [h^{\bullet}]^2}{\sqrt{pO_2}[v_O^{\bullet\bullet}]} = \frac{54}{56} \cdot \frac{55.5 \cdot [Acc_{eff}']^2}{\sqrt{pO_2}[v_O^{\bullet\bullet}]} \tag{2.20}$$

   The concentrations of electronic defects are constant as well as the concentration of the effective acceptor. The slope of the concentration of oxygen vacancies is –1/2 in this region.

From these considerations a sketch of the Brouwer diagram is generated in Fig. 2.7. Partial pressure of water or hydrogen and thus proton concentration is zero in this treatment. By increasing the temperature, the region for medium pO_2 (around the stoichiometric point) is shrinked and shifted towards higher pO_2 (compare Fig. 2.11). This shows that oxidation is favored over reduction in lanthanum tungstate (enthalpies of quasi-chemical oxygen incorporation reactions $\Delta_{n-\text{type}}H > \Delta_{p-\text{type}}H$).[35]

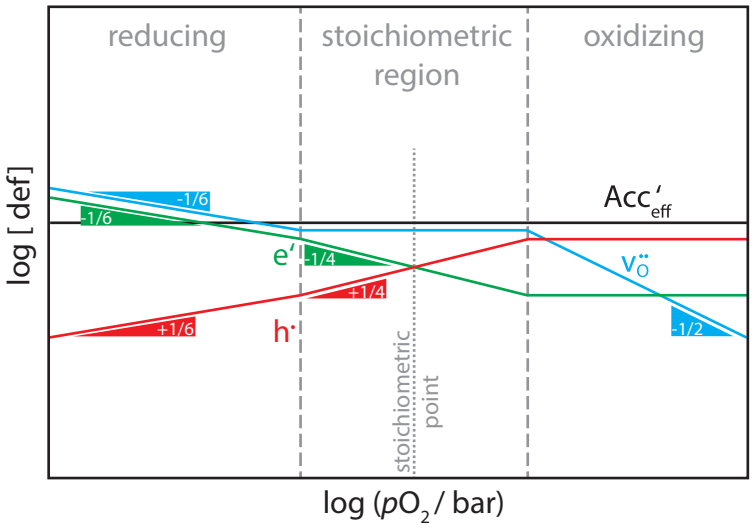

Figure 2.7: Sketch of the Brouwer diagram (double logarithmic [def], pO_2–diagram) of lanthanum tungstate for $pH_2O = 0$.

For the oxidizing region it is possible to calculate the defect fractions with the equilibrium constants K_{O_2} and K_{H_2O} (see Eqs. (3.4) and (3.16)), including the proton concentration and the partial

pressure of water into the treatment.[36] The concentration of oxygen over the total anion sublattice is 55.5 and it is regarded as approximately constant in the entire pO_2 and pH_2O regime. The concentrations of protons, oxygen vacancies and electron holes are consequently:

$$[H_i^{\bullet}] = -\frac{28 \cdot K_{H_2O}}{4 \cdot 27 \cdot 55.5} \cdot pH_2O \cdot \left(1 + \frac{K_{O_2} \cdot \sqrt{pO_2}}{K_{H_2O} \cdot pH_2O}\right)^{\frac{1}{2}} + \left\{\left[\frac{28 \cdot K_{H_2O}}{4 \cdot 27 \cdot 55.5} \cdot pH_2O \cdot \left(1 + \frac{K_{O_2} \cdot \sqrt{pO_2}}{K_{H_2O} \cdot pH_2O}\right)^{\frac{1}{2}}\right]^2 + \frac{28 \cdot K_{H_2O}}{27 \cdot 55.5} \cdot pH_2O \cdot [O_v''] - \frac{3 \cdot 28 \cdot K_{H_2O}}{2 \cdot 27 \cdot 55.5} \cdot pH_2O \cdot [W_{La}^{\bullet\bullet\bullet}]\right\}^{\frac{1}{2}} \tag{2.21}$$

$$[v_O^{\bullet\bullet}] = \frac{55.5}{K_{H_2O}} \cdot \frac{54}{56} \cdot \frac{[H_i^{\bullet}]^2}{pH_2O} \tag{2.22}$$

$$[h^{\bullet}] = \left(\frac{K_{O_2}}{55.5} \cdot \frac{56}{54} \cdot \sqrt{pO_2} \cdot [v_O^{\bullet\bullet}]\right)^{\frac{1}{2}} \tag{2.23}$$

pO_2- (Fig. 2.8) and pH_2O- (Fig. 2.9) dependent concentration diagrams can be simulated with arbitrary equilibrium constants and a tungsten dopant concentration of one. N.B.: The defect fraction is referred to the complete unit cell of lanthanum tungstate consisting of 32 cation sites and 56 anion sites that can be occupied.

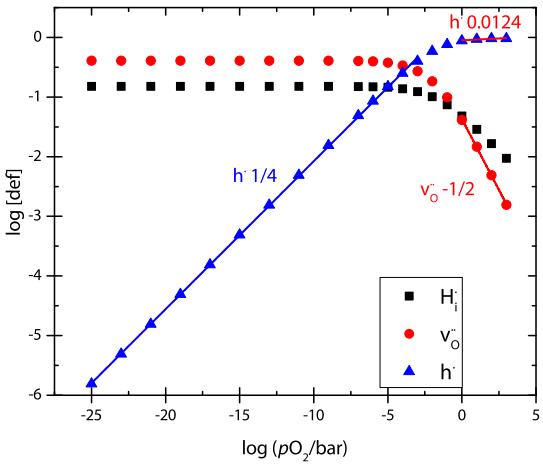

Figure 2.8: Defect fractions for the arbitrary equilibrium constants K_{O_2} = 1000 and K_{H_2O} = 87 under oxidizing conditions with one tungsten on a La2 site per unit cell. pH_2O = 30 mbar.

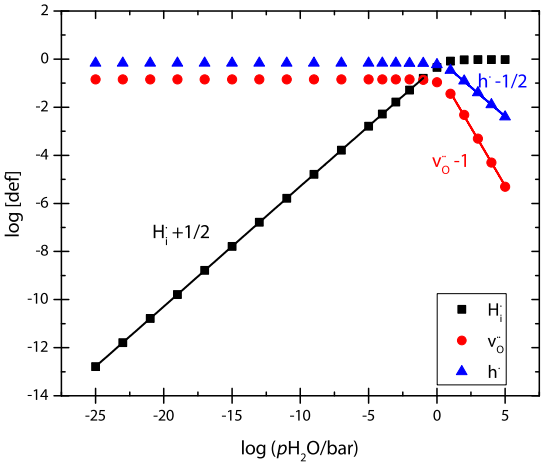

Figure 2.9: Defect fractions for the arbitrary equilibrium constants K_{O_2} = 1000 and K_{H_2O} = 87 under oxidizing conditions with one tungsten on a La2 site per unit cell. pO_2 = 30 mbar.

2.3 Material Properties

In this section an overview of recent publications about the electrochemical properties of lanthanum tungstate will be given. The focus lies on publications regarding lanthanum tungstate as a material for gas separation membranes and as an electrode or electrolyte material in SOFCs/solid oxide electrolyzer cells (SOECs).

2.3.1 Conductivity

The electrical conductivity and permeation rates of lanthanum tungstate as a protonic conductor were first investigated by Shimura *et al.*[1]: temperature-dependent conductivity measurements in humid gases — air, H_2 and D_2 — suggested that LaWO54 is a protonic conductor because the electrical conductivity in a humid deuterium atmosphere is lower than in a humid hydrogen atmosphere. A more detailed analysis by Haugsrud and Kjølseth shown in Fig. 2.10, which is taken from Reference [5], indicates that protonic charge carriers are dominating under approx. 800 °C, while above, the electronic contribution to the total conductivity dominates. The electrical conductivity between 600 °C and 1000 °C is reported to be $1 \times 10^{-3}\,\mathrm{S\,cm^{-1}}$ to $2 \times 10^{-2}\,\mathrm{S\,cm^{-1}}$. $p\mathrm{O_2}$-dependent measurements of the total conductivity in a range from $\log(p\mathrm{O_2}/\mathrm{atm}) = -20$ to 0 have shown that lanthanum tungstate has a broad stoichiometric region with dominating ionic conductivity. The *n*-type and *p*-type regions concatenated to the stoichiometric region at reducing and oxidizing conditions, respectively, show slopes of less than 1/4 or 1/6. Partial pressures of oxygen for the fully *p*-type oxidizing or *n*-type reducing regions could not be reached. This substantiated the assumption that the electronic contribution to the total conductivity is low for low temperatures.[1] However, conductivity measurements at higher temperatures over a large $p\mathrm{O_2}$ range by Haugsrud and Kjølseth revealed that the electronic contribution to the total conductivity is increased at temperatures at or above 800 °C, shown in Fig. 2.11 taken from Reference [5].
Doping with other cations, e.g. molybdenum, results in a significant increase of the electronic conductivity in the *n*-type regime as shown by Amsif *et al.*[37] This is especially interesting for the application in gas separation membranes which operate at extremely reducing conditions: electronic conductivity is required to enable hydrogen flux without second phases that are electronic conductors or electrodes. The ionic conductivity is almost unchanged by doping with molybdenum. In the oxidizing regime that is analyzed in this work, however, the total conductivity is decreased by doping.[37] Doping lanthanum tungstate with calcium leads to steeper slopes in a $\log\sigma, \log p\mathrm{O_2}$–diagram at reducing and oxidizing conditions but the total conductivity decreases significantly.[2]

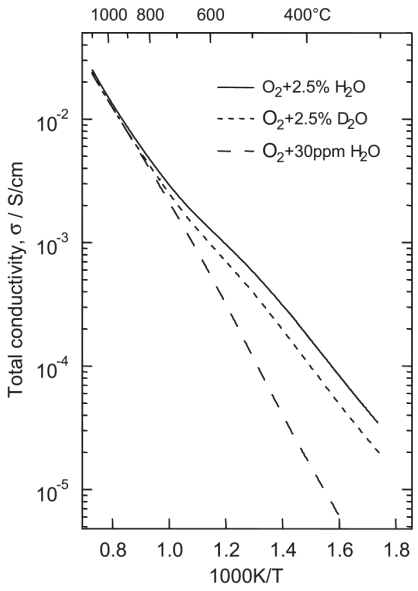

Figure 2.10: Total conductivity measurements of lanthanum tungstate in different atmospheres reprinted from Reference [5], with permission from Elsevier. The large difference between the humid (solid and short dashed lines) and the less humid (long dashed line) atmosphere at low temperatures proves that lanthanum tungstate is a protonic conductor. However, at elevated temperatures, the electronic contribution gains significance and all three lines combine.

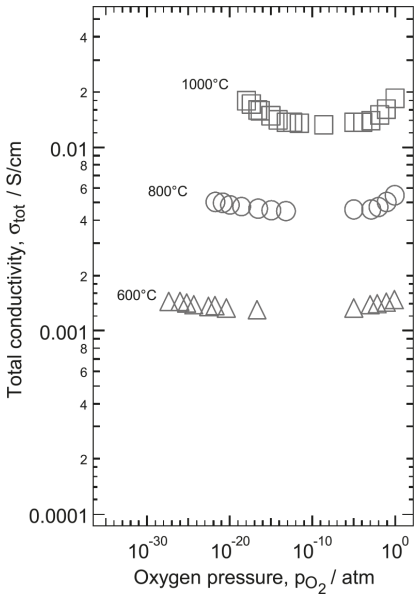

Figure 2.11: Temperature and pO_2-dependent measurements of the total conductivity of lanthanum tungstate reprinted from Reference [5], with permission from Elsevier. At elevated temperatures the slope of the conductivity in the oxidizing regime of the double-logarithmic diagram and thus the electronic contribution increases.

2.3.2 Transport Kinetics and Permeation

The transport kinetics of lanthanum tungstate have already been analyzed by IEDP followed by ToF-SIMS[39], mass relaxation studies by thermogravimetry[40, 41] and ECR[38]. The latter two studies yielded chemical transport parameters which are also investigated in this work.

ECR experiments by Solís *et al.*[38] were performed in a temperature range between 680 °C and 750 °C in the oxidizing regime. The kinetics of oxidative and reductive steps as well as hydrating and dehydrating steps were evaluated. They have observed single fold relaxation behavior in all cases. They have not observed the expected two-fold relaxation behavior, which will be discussed in detail in Section 4.6. Thy attributed it to the fact that the electronic contribution to the conductivity is low in lanthanum tungstate. In Fig. 2.12, chemical diffusion coefficients and chemical surface reaction constants are shown, taken from Reference [38]. Hydration and dehydration kinetics are significantly slower than oxidation and reduction kinetics. Chemical diffusion coefficients

for hydration are between 4×10^{-6} cm^2 s^{-1} and 1×10^{-5} cm^2 s^{-1} and chemical surface reaction rates are approximately 1×10^{-4} cm s^{-1}. The corresponding activation energies were determined to be 0.57(10) eV and 0.58(20) eV, respectively. Oxidative and reductive steps as well as hydration and dehydration steps yielded almost the same parameters, which may be attributed to the fact that the step size is rather small and/or the relaxation is not hindered by limited mass transport (compare to Refs. [42] and [43]). The difference between dry and wet oxidative steps seems also small (see Fig. 2.12) and, therefore, it has been stated that the hydration does not interfere with the oxygen diffusion.[38]

Chemical and tracer diffusion coefficients and surface reaction rates upon hydration or H/D isotope exchange, respectively, of lanthanum tungstate have been studied by mass relaxation by Hancke *et al.*[40] Isotope exchange experiments were performed in a temperature range between 300 °C and 550 °C. Tracer diffusion coefficients between 4×10^{-8} cm^2 s^{-1} and 1×10^{-6} cm^2 s^{-1} with an activation energy of 0.79(4) eV and tracer surface reaction rates between 9×10^{-6} cm s^{-1} and 7×10^{-5} cm s^{-1} with an activation energy of 0.33(1) eV were obtained. Hydration experiments in a temperature range between 550 °C and 800 °C yielded chemical diffusion coefficients between 1×10^{-7} cm^2 s^{-1} and 1×10^{-5} cm^2 s^{-1} with an activation energy of 1.24(4) eV and chemical surface reaction rates between 2×10^{-4} cm s^{-1} and 1×10^{-3} cm s^{-1} with an activation energy of 0.50(1) eV for oxidizing conditions and 0.25(3) eV for reducing conditions.[40] In a later study they have analyzed hydration enthalpy and entropy by thermogravimetry and differential scanning calorimetry yielding $\Delta H^{\ominus}_{H_2O} = 90(10)$ kJ mol^{-1} and $\Delta S^{\ominus}_{H_2O} = -110(10)$ J mol^{-1} K^{-1}. For the analyzed temperature range between 400 °C and 700 °C equilibrium constants between $-1 < \log K_{H_2O} < 1.5$ were obtained.[41] Simultaneously, the same group has performed IEDP experiments analyzed by ToF-SIMS with ^{18}O and deuterium as tracer. The obtained tracer diffusion coefficients and tracer surface reaction rates were in agreement with the values obtained by thermogravimetric relaxation measurements.[39, 40]

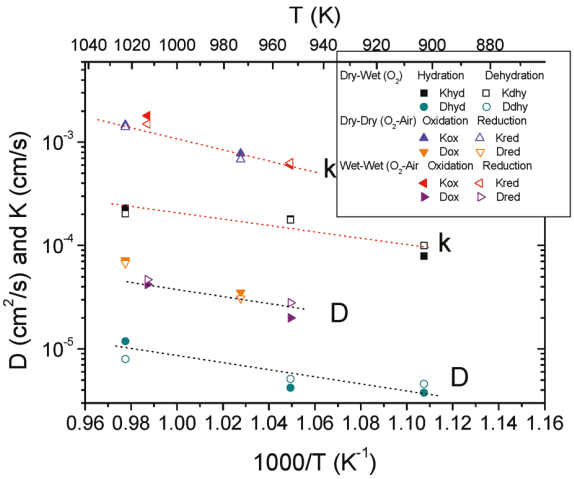

Figure 2.12: Chemical surface reaction rates and chemical diffusion coefficients of lanthanum tungstate obtained by ECR measurements. Reprinted with permission from Reference [38]. Copyright 2011 American Chemical Society.

The permeation flux of hydrogen in a gas separation membrane setup was analyzed by Escolástico *et al.*[44] A layer of lanthanum tungstate (900 µm) was coated with platinum ink to improve the surface reaction. Highest hydrogen flux was achieved at a temperature of 1000 °C under humid air (pH_2O = 0.025 atm on feed and sweep side) with values above 0.04 mL cm^{-2} min^{-1}.[44] A later

study of the same group improved the hydrogen flux to values up to 0.12 mL cm^{-2} min^{-1} for the composition ($Nd_{5/6}Ln_{1/6}WO_{11.25-\delta}$) with Ln = La, Ce, Eu, Pr, Tb. They explained that the improvement of the ambipolar conductivity by cation substitution is the reason for the drastic increase of the hydrogen flux.[7]

Preparation of thin layer dense lanthanum tungstate (30 µm) on a porous support by Gil *et al.*[45] led to comparable hydrogen fluxes of approximately 0.15 mL cm^{-2} min^{-1}. The flux is in the same order of magnitude as for acceptor doped strontium cerate perovskite membranes, which show currently one of the highest hydrogen fluxes.[45, 46]

At low temperatures the electronic contribution to the total conductivity is low enough to use lanthanum tungstate as an electrolyte material in SOFCs/SOECs setups. Resistances and microstructural analyses with various cathode and anode materials have been published by Balaguer *et al.*[8] and Zayas-Rey *et al.*[6] The latter publication also included power density curves with a maximum power density of 140 mW cm^{-2} at 900 °C and a comparison to perovskite type materials: while the power density is comparable to the power density for $BaZr_{0.9}Y_{0.1}O_{3-\delta}$, the power density achieved by $BaZr_{0.1}Ce_{0.7}Y_{0.1}Yb_{0.1}O_{3-\delta}$ is unrivaled.[6, 47, 48]

3

Hydrogen Incorporation and Permeation

Many fluorite- and perovskite-type oxide materials show a pO_2-dependent concentration of oxygen vacancies. Some of them also show a solubility of protons originating from hydrogen or water in the surrounding gas phase. Proton permeability is usually higher than oxygen permeability (e.g. barium zirconate or lanthanum tungstate), thus PC-SOFCs are favored over regular SOFCs transporting oxygen (or their vacancies). Though all proton conducting solid oxides also show good oxygen permeation behavior. Highest oxygen permeability does not necessarily correlate with highest proton permeability.

In this chapter, the incorporation of protons originating from hydrogen and water from the gas phase as well as the permeation of protons within the bulk phase will be discussed. The treatment of oxygen incorporation and permeation is, however, inevitable for understanding the relaxation behavior this work is focusing on and will be discussed in this chapter first. Finally, the composition of the gas phase will be calculated as the chemical potentials of the species involved are responsible for the equilibrium content of protons and oxygen in the bulk.

There are multiple possible driving forces for chemical transport in solids. In this work, only gradients in the activity of a species, i.e. a gradient in concentration or partial pressure, will be treated. Other driving forces may be gradients in temperature, electric or magnetic fields, mechanical stress etc.

3.1 Surface Reactions

A first glimpse at the surface reactions taking place at solid oxide surfaces has already been discussed in Chapter 2, e.g. Eq. (2.5). Quasi-chemical reactions can be defined using the Kröger–Vink notation. The kinetics of such incorporation equations are usually of first order, meaning that the reaction rate is linear proportional to the concentration of the ionic species. The exact mechanism of the incorporation reaction, however, is not known. Some works introduce suggestions of mechanisms based on experimental evidence.[49, 50] In principle, the incorporation of gas molecules into a solid oxide consist of the following steps:

- Convection and diffusion in the gas phase.
- Film diffusion in the surface-near gas phase (no slip condition).
- Adsorption of the gas molecule. The exact orientation of the molecule and number of bonds to the surface is usually unknown.
- Dissociation and, in the case of hydrogen and oxygen, electron transfer. The exact order of the steps and the exact nature (bonds and charges) of the species is unknown.
- Incorporation into a surface near vacancy or, in the case of protons, to a surface near oxygen ion.
- Bulk diffusion.

For the incorporation of a water molecule, the steps are schematically shown in Fig. 3.1 and are discussed in Section 3.1.3. The steps 3, 4 and 5, i.e. the surface reaction, are summarized in the incorporation equation. The incorporation equations will first be described for a general acceptor doped (*p*-type) system followed by the case of lanthanum tungstate for each compound, i.e. oxygen, hydrogen and water. With the recombination of electrons and electron holes, $e' + h^{\bullet} \rightleftharpoons \text{nil}$, *n*-type and *p*-type incorporations can be transformed into each other. The kinetics of the surface reactions are similar to each other and will be discussed afterwards in Section 3.1.4.

3.1.1 Oxygen

The oxygen incorporation equation has already been mentioned in Chapter 2. Half of an oxygen molecule is incorporated onto a surface-near vacancy forming oxygen on a regular oxygen site and two electron holes. The oxidation number of oxygen is thus reduced from 0 to −2. Therefore, two electrons have to be transferred to the adsorbed oxygen species before it can be incorporated into the crystal lattice. The second oxygen atom from the oxygen molecule should also be adsorbed and can be incorporated in the same way. The general incorporation equation and the corresponding

law of mass action is:

$$\frac{1}{2}O_2(g) + v_O^{\bullet\bullet} \rightleftharpoons O_O^{\times} + 2h^{\bullet} \qquad \text{with} \qquad K_{O_2} = \frac{[O_O^{\times}][h^{\bullet}]^2}{\sqrt{pO_2}[v_O^{\bullet\bullet}]} \tag{3.1}$$

In the case of lanthanum tungstate oxygen can be incorporated onto a thermal or a structural oxygen vacancy leading to two different incorporation equations. The equation for lanthanum tungstate, however, can also be formulated by the above equation combined with the order-disorder-transition, Eq. (2.8). The incorporation equations for the statistically occupied two virtual sublattices are as follows:

$$\frac{1}{2}O_2(g) + v_O^{\bullet\bullet} \rightleftharpoons O_O^{\times} + 2h^{\bullet} \qquad \text{with} \qquad K_{O_2,\,1} = \frac{[O_O^{\times}][h^{\bullet}]^2}{\sqrt{pO_2}[v_O^{\bullet\bullet}]} \tag{3.2}$$

$$\frac{1}{2}O_2(g) + v_v^{\times} \rightleftharpoons O_v'' + 2h^{\bullet} \qquad \text{with} \qquad K_{O_2,\,2} = \frac{[O_v''][h^{\bullet}]^2}{\sqrt{pO_2}[v_v^{\times}]} \tag{3.3}$$

Dividing both laws of mass action from Eqs. (3.2) and (3.3) yields the law of mass action of the order-disorder-transition, Eq. (2.8). As $K_{o/do} \approx 1$, the equilibrium constants of both incorporation equations mentioned above are equal, $K_{O_2,\,1} \approx K_{O_2,\,2}$. Combining both virtual sublattices and with Eq. (2.9) the law of mass action of the oxygen incorporation equations can be condensed to

$$K_{O_2} = \frac{([O_O^{\times}] + [O_v''])[h^{\bullet}]^2}{\sqrt{pO_2}([v_O^{\bullet\bullet}] + [v_v^{\times}])} \tag{3.4}$$

For the sake of completeness the incorporation equation for lanthanum tungstate can also be established with fractional charges and fractional oxygen lattice sites supposed by Erdal *et al.*[18]:

$$\frac{1}{2}O_2(g) + v_{\frac{54}{56}O}^{\frac{108}{56}\bullet} \rightleftharpoons O_{\frac{54}{56}O}^{\frac{4}{56}\prime} + 2h^{\bullet} \qquad \text{with} \qquad K_{O_2} = \frac{\left[O_{\frac{54}{56}O}^{\frac{4}{56}\prime}\right][h^{\bullet}]^2}{\sqrt{pO_2}\left[v_{\frac{54}{56}O}^{\frac{108}{56}\bullet}\right]} \tag{3.5}$$

3.1.2 Hydrogen

Lanthanum tungstate can, among other oxides, incorporate hydrogen in form of proton interstitials or, equivalently, as hydroxy-anions (see Section 2.2.1.3). A hydrogen molecule can be adsorbed at the surface. After breaking the bond and transferring an electron to the bulk (or removing an electron hole from the bulk), a proton can form a hydroxy-anion with a surface-near oxygen ion. The incorporation equation can be formulated as

$$\frac{1}{2}H_2(g) + O_O^{\times} + h^{\bullet} \rightleftharpoons OH_O^{\bullet} \equiv O_O^{\times} + H_i^{\bullet} \qquad \text{with} \qquad K_{H_2} = \frac{[H_i^{\bullet}]}{\sqrt{pH_2}[h^{\bullet}]} \tag{3.6}$$

The proton is usually located within the electron shell of oxygen with a distance of approximately 100 pm (see Section 2.2.1.3). In the case of lanthanum tungstate, the proton can be assigned to

an oxygen ion on an oxygen site, $O_O^\times$, or to an oxygen ion occupying a structural vacancy, O_v''. The relative charge is reduced by one and the hydroxy-anion has thus a charge of +1 for a regular site, $OH_O^\bullet$, and a charge of −1 for a hydroxy-anion on a structural vacancy, OH_v'. The permuted incorporation equations for both virtual sublattices are thus:

$$\frac{1}{2}H_2(g) + O_O^\times + h^\bullet \rightleftharpoons OH_O^\bullet \equiv O_O^\times + H_i^\bullet \tag{3.7}$$

$$\frac{1}{2}H_2(g) + O_v'' + h^\bullet \rightleftharpoons OH_v' \equiv O_v'' + H_i^\bullet \tag{3.8}$$

If the proton, however, is defined as an interstitial proton, $H_i^\bullet$, oxygen is canceled in the law of mass action so that the oxygen species to which the proton is assigned to is irrelevant, leaving the law of mass action unchanged.

With the use of fractional charges and fractional oxygen lattice sites both equations can be reduced to

$$\frac{1}{2}H_2(g) + O_{\frac{54}{56}O}^{\frac{4}{56}\prime} + h^\bullet \rightleftharpoons OH_{\frac{54}{56}O}^{\frac{52}{56}\bullet} \equiv O_{\frac{54}{56}O}^{\frac{4}{56}\prime} + H_i^\bullet \tag{3.9}$$

If the oxygen partial pressure is not negligible, the water equilibrium in the gas phase that will be discussed in Section 3.3 has to be considered. In the presence of oxygen, hydrogen is almost entirely oxidized to water.

3.1.3 Water

Hydration and dehydration kinetics are the main topic of this work. The incorporation of water into the bulk is the essential incorporation equation. The solubility, reaction and first kinetic studies go back to Wagner in the late 1960s.[51] The incorporation requires a vacancy and an oxygen ion forming two hydroxy-anions according to

$$H_2O(g) + O_O^\times + v_O^{\bullet\bullet} \rightleftharpoons 2OH_O^\bullet \equiv 2O_O^\times + 2H_i^\bullet \qquad \text{with} \qquad K_{H_2O} = \frac{[O_O^\times][H_i^\bullet]^2}{pH_2O[v_O^{\bullet\bullet}]} \tag{3.10}$$

Although there is no direct change in electron hole concentration, the oxygen equilibrium has to be taken into account upon hydration with constant pO_2: the concentration of oxygen vacancies decreases and thereby, from Eq. (3.1), the concentration of electron holes decreases as well. The ratio of proton interstitials and electron holes can be described, using both equilibrium constants, K_{O_2} and K_{H_2O}, by

$$\frac{[H_i^\bullet]}{[h^\bullet]} = \sqrt{\frac{K_{H_2O}}{K_{O_2}} \cdot \frac{pH_2O}{\sqrt{pO_2}}} \tag{3.11}$$

This equation has already been used to describe the defect fraction of proton interstitials in Eq. (2.21). Please compare this also to Reference [36].

The incorporation of water can be split into two elementary reactions. In the next section, the necessity of splitting this reaction will become evident when kinetics are treated. The incorporation reaction, Eq. (3.10), is the sum of Eq. (3.1) and two times Eq. (3.6):

$$\begin{aligned} 2\times \quad & \tfrac{1}{2}\mathrm{H_2(g)} + \mathrm{O_O^\times} + \mathrm{h^\bullet} \rightleftharpoons \mathrm{OH_O^\bullet} \\ 1\times \quad & \tfrac{1}{2}\mathrm{O_2(g)} + \mathrm{v_O^{\bullet\bullet}} \rightleftharpoons \mathrm{O_O^\times} + 2\mathrm{h^\bullet} \\ \hline & \mathrm{H_2O(g)} + \mathrm{O_O^\times} + \mathrm{v_O^{\bullet\bullet}} \rightleftharpoons 2\mathrm{OH_O^\bullet} \end{aligned}$$

In the case of lanthanum tungstate, four permutations of Eq. (3.10) are possible when the anion sublattice is divided, but they can also be achieved by inserting the equation for the order-disorder-transition, Eq. (2.8), into the water incorporation reaction, Eq. (3.10).

$$\mathrm{H_2O(g)} + \mathrm{O_O^\times} + \mathrm{v_O^{\bullet\bullet}} \rightleftharpoons 2\mathrm{OH_O^\bullet} \tag{3.12}$$

$$\mathrm{H_2O(g)} + \mathrm{O_\upsilon''} + \upsilon_\upsilon^\times \rightleftharpoons 2\mathrm{OH_\upsilon'} \tag{3.13}$$

$$\mathrm{H_2O(g)} + \mathrm{O_O^\times} + \upsilon_\upsilon^\times \rightleftharpoons \mathrm{OH_O^\bullet} + \mathrm{OH_\upsilon'} \tag{3.14}$$

$$\mathrm{H_2O(g)} + \mathrm{O_\upsilon''} + \mathrm{v_O^{\bullet\bullet}} \rightleftharpoons \mathrm{OH_O^\bullet} + \mathrm{OH_\upsilon'} \tag{3.15}$$

Analogously to the law of mass action for the incorporation of oxygen, Eq. (3.4), and hydrogen, Eq. (3.6), the law of mass action for the incorporation of water can be established:

$$K_{\mathrm{H_2O}} = \frac{([\mathrm{O_O^\times}] + [\mathrm{O_\upsilon''}])[\mathrm{H_i^\bullet}]^2}{p\mathrm{H_2O}([\mathrm{v_O^{\bullet\bullet}}] + [\upsilon_\upsilon^\times])} \tag{3.16}$$

The use of fractional charges and fractional oxygen lattice sites reduces Eq.s (3.12-3.15) to

$$\mathrm{H_2O(g)} + \mathrm{O}_{\frac{54}{56}\mathrm{O}}^{\frac{4}{56}\prime} + \mathrm{v}_{\frac{54}{56}\mathrm{O}}^{\frac{108}{56}\bullet} \rightleftharpoons 2\mathrm{OH}_{\frac{54}{56}\mathrm{O}}^{\frac{52}{56}\bullet} \equiv 2\mathrm{O}_{\frac{54}{56}\mathrm{O}}^{\frac{4}{56}\prime} + 2\mathrm{H_i^\bullet} \text{ with } K_{\mathrm{H_2O}} = \frac{\left[\mathrm{O}_{\frac{54}{56}\mathrm{O}}^{\frac{4}{56}\prime}\right][\mathrm{H_i^\bullet}]^2}{p\mathrm{H_2O}\left[\mathrm{v}_{\frac{54}{56}\mathrm{O}}^{\frac{108}{56}\bullet}\right]} \tag{3.17}$$

3.1.4 Kinetics of Surface Reactions

A brief overview of the steps involved when a molecule is incorporated into a bulk sample is already given in Section 3.1. The surface reaction is usually assumed to be a first order reaction. If multiple species are present, multiple first order reactions are assumed. The flux j_i of species i (e.g. of oxygen) at the surface can be described by[49]

$$j_i = \tilde{k}_i(c_i^\infty - c_i^{\mathrm{surf}}), \tag{3.18}$$

with the ambipolar surface reaction rate $\tilde{k}_i$ as proportionality constant and the concentrations of species i, c_i^∞ and c_i^{surf}. c_i^∞ is the concentration that would be present if the bulk phase is in equilibrium with the gas phase. c_i^{surf} is the concentration of species i of the bulk at the surface.

The time-dependent concentration assuming infinitely fast diffusion can be described by a simple exponential function. For example, the equation for a finite medium, here a plane sheet with thickness $2a$, can be derived by integration of Eq. (3.18) from $-a$ to a.

$$\frac{\bar{c}_i(t) - c_i^0}{c_i^\infty - c_i^0} = 1 - e^{-\frac{\tilde{k}_i}{a}t}, \tag{3.19}$$

with the initial concentration of species i, c_i^0. In Eqs. (3.18) and (3.19), $\tilde{k}_i$ or sometimes written k_{chem} or k^δ is the chemical surface reaction rate with the dimension of length per time. The chemical surface reaction rate can be equal to the tracer surface reaction rate, $k_i^\star$, or orders of magnitude higher. A relationship between both rates has been extensively discussed by Maier.[52]

The rate determining step within the surface reaction is unknown. However, the rate determining step is assumed to be a first order reaction and all other steps are in pre-equilibrium and thus irrelevant for the kinetics of the surface reaction. This is at least valid for oxidation or reduction kinetics. On the other hand, as will be discussed in the results of this work, a surface reaction with two different first order kinetics for the incorporation of water upon hydration or dehydration are present. It can be assumed that protons can easily be incorporated into the lattice. Oxygen or hydroxy-anions, on the other hand, show a slow and similar incorporation reaction (compare to the vehicle mechanism described in Section 3.2.1.1). A further discussion will be presented in the results of the ECR experiments.

Previous works in our group by Pietrowski and by Kessel have shown that the origin of the oxygen species is important for the surface reaction rate. For yttria stabilized zirconia, $Y_xZr_{1-x}O_2$ (YSZ), oxygen can easier be incorporated from a water molecule than from an oxygen molecule.[53, 54] This topic will be treated in the results section as well. In the case of lanthanum tungstate, an incorporation of oxygen onto a thermal or structural vacancy should be indistinguishable as both sites are degenerate in the temperature range used here.

The surface reaction upon hydration is schematically shown in Fig. 3.1. It should be noted that this is only one possible pathway and the fact that the incorporation into the lattice is the rate determining step is only an assumption.

Possible pathways of the incorporation of oxygen into iron-doped strontium titanate single crystals have been analyzed by Merkle and Maier, including kinetic studies in order to identify possible rate determining steps by experimental evidence.[49]

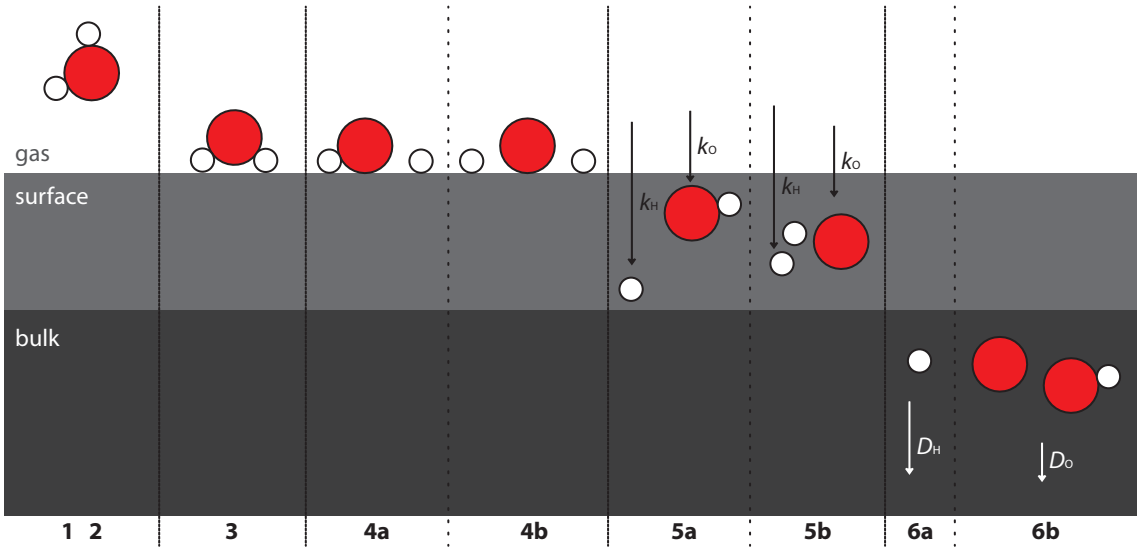

Figure 3.1: Surface reaction of water incorporation: **1**: convection in the gas phase; **2**: film diffusion to the surface; **3**: adsorption of a water molecule; **4**: dissociation: **a)** into a proton and a hydroxy anion or **b)** into two protons and an oxygen ion; **5**: surface reaction of proton(s) and **a)** a hydroxy anion or **b)** an oxygen anion into the lattice; **6**: diffusion with **a)** the Grotthuss mechanism by hydrogen bonds or **b)** the vehicle mechanism of mobile hydroxy anions and simple oxygen migration.

3.2 Diffusion in Solids

Diffusion processes are based on the Brownian motion of atoms and molecules and have been investigated in the early 19th century for gases and liquids and in the late 19th century for solids by Roberts-Austen after first diffusion phenomena in solids had been observed by Boyle.[55] In crystals, diffusion is enabled by the motion of point defects.[24] The mobility of point defects is very low compared to the fast motion of atoms or molecules in the gas phase and the rather slow motion within liquids. The mobility is increased with increasing temperature (see Section 3.2.2, Eq. (3.30)). Diffusion of oxygen in perovskite or fluorite type oxides, which is needed for application, requires elevated temperatures (e.g. for SOFCs above 450 °C, usually about 750 °C) and cation diffusion requires very high temperatures in these oxides. Tammann's rule of thumb states that solids should be sintered at 2/3 of the melting point, which is ≈ 1600 °C for many oxides with fluorite or perovskite structure. Cation mobility is essential for the sintering process.

Depending on the environment of the diffusing species, various types of diffusion can be defined: in homogeneous materials, self-diffusion leads to an exchange of atoms or ions within the crystal. The material remains homogeneous, meaning that no concentration gradients are developed. Self-diffusion can be observed by marking a defect with an isotope. The so-called tracer-diffusion can be analyzed e.g. by ToF-SIMS after an exchange anneal where the surrounding gas atmosphere is replaced by an isotope enriched gas and all thermodynamic properties are unchanged.[56–58]

If the material shows a concentration gradient in a chemical component, chemical diffusion leads to

an equalization of the concentration of that component. If two concentration gradients in opposite direction are present, the chemical diffusion can be specified as 'interdiffusion'. The Kirkendall-effect describes the diffusion process when two species are present with two different diffusion coefficients on the same sublattice.[59]

External driving forces can affect diffusion processes, e.g. if a constant external oxygen potential gradient exists — typical for gas separation membranes — diffusion does not lead to an equalization of the concentrations but it leads instead to a steady-state, where the electrochemical potential is in equilibrium for the entire system but concentration gradients still exist. Other driving forces may be electrical or magnetic fields or temperature gradients, etc. If an external field is applied as the external driving force, the diffusion is extended by a so called drift.

3.2.1 Diffusion Mechanisms

Opposite to the gas phase and liquids, the diffusion in a crystal is limited to discrete diffusion paths following specific diffusion mechanisms as the defects cannot move freely. Depending on the crystal structure and ionic radii, one of the mechanisms is favorable in migration energy, E_{mig}, — not necessarily the same mechanism for each material. Typical mechanisms for the diffusion of oxygen are depicted in Fig. 3.2 and include the vacancy mechanism where an oxygen ion passes cations and jumps onto an adjacent oxygen vacancy (left mechanism), the interstitial mechanism where an interstitial oxygen ion moves to an adjacent unoccupied interstitial position (top center), and the interstitialcy mechanism, where an interstitial oxygen ion pushes a regular oxygen ion to the next interstitial position and the interstitial oxygen occupies the regular site (bottom center). Additional mechanisms may be divacancy, collective, etc.[60]

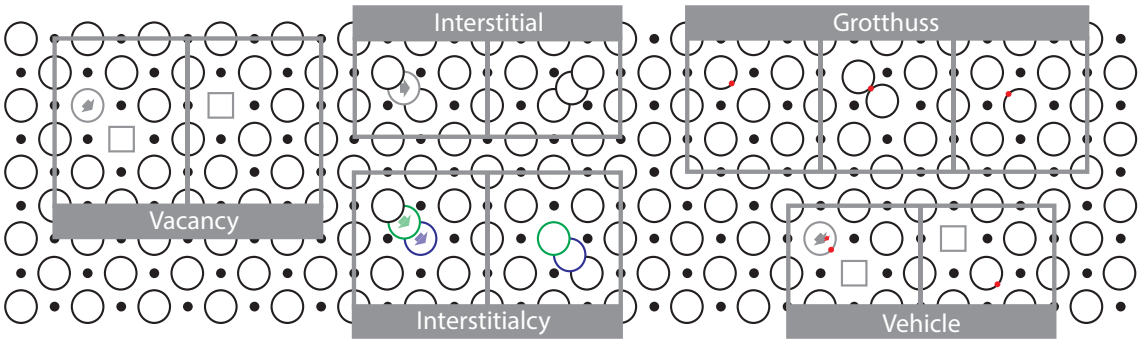

Figure 3.2: Sketch of bulk diffusion mechanisms for oxygen (left/center) and for hydrogen (top right) or hydroxy-anions (bottom right). •: cation; ◯: anion; □: vacancy; ◯, ◯: tracer ion; •: proton.

3.2.1.1 Proton Conductivity

The diffusion of protons is based on three different mechanisms. The first is the rotational diffusion of a proton around an oxygen ion. Protons are relaxing to one of four positions around an oxygen ion in perovskite type oxides calculated by computational methods (compare to Section 2.2.1.3). Rotational diffusion — the reorientation of the proton to one of the other adjacent sites around the same oxygen ion — is a prerequisite for macroscopic diffusion via the second mechanism, the Grotthuss mechanism, which will be discussed in more detail in the following paragraph. The third mechanism is the vehicle mechanism, which is equivalent to one of the oxygen mechanisms but instead of an oxygen ion a hydroxy-ion moves. This will be discussed in the paragraph thereafter.

Grotthuss Mechanism

For a macroscopic diffusion, at least one rotational diffusion step must be inserted between two Grotthuss mechanism steps so that the proton does not move back and forth. By reorientation ('rotational diffusion'[32]) the proton can be realigned to one of the other three possible angle bisectors. The activation energy for the reorientation process is generally very low[32], e.g. E_A = 0.18 eV for indium doped barium zirconate[33] or 0.065 eV for barium cerate[61].

By the Grotthuss[62] mechanism, the proton can be transferred to an adjacent oxygen ion. The Grotthuss mechanism is based on hydrogen bonds, where the proton has a covalent bond to the oxygen ion, referred to as 'free OH' (Fig. 3.3(a)). If the oxygen ions have a smaller distance to each other in an instant configuration, e.g. by thermal motion or due to the electrostatic attraction to the proton, a strong hydrogen bond to an adjacent oxygen ion is established (Fig. 3.3(b)). With a very low energy barrier, the hydrogen bond and the covalent bond can be interchanged (Fig. 3.3(c)). When the oxygen ions are separated again, either the hydrogen bond or the covalent bond breaks and the proton is again covalent bound to one oxygen ion (free OH, Fig. 3.3(d)). For protonated water ($H_3O^+_{(aq)}$), Agmon proposed that the cleavage of the hydrogen bond is the rate determining step in the Grotthuss mechanism.[63] It is possible that the proton remains at the first oxygen ion but also a proton transfer to the adjacent oxygen ion is possible.[32] In MIECs, the transfer of protons is compensated by a transfer of electronic defects.

Vehicle Mechanism

A proton that is migrating as a passenger on a *vehicle*, i.e. attached to another species, e.g. an oxygen ion, also leads to proton permeability, but the mobility is governed by the mobility of the vehicle. A hydroxy-anion, $OH^{\bullet}_{O}$, is migrating to an adjacent vacancy, leaving a vacancy behind. The vehicle mechanism is schematically shown in Fig. 3.2 (bottom right mechanism).

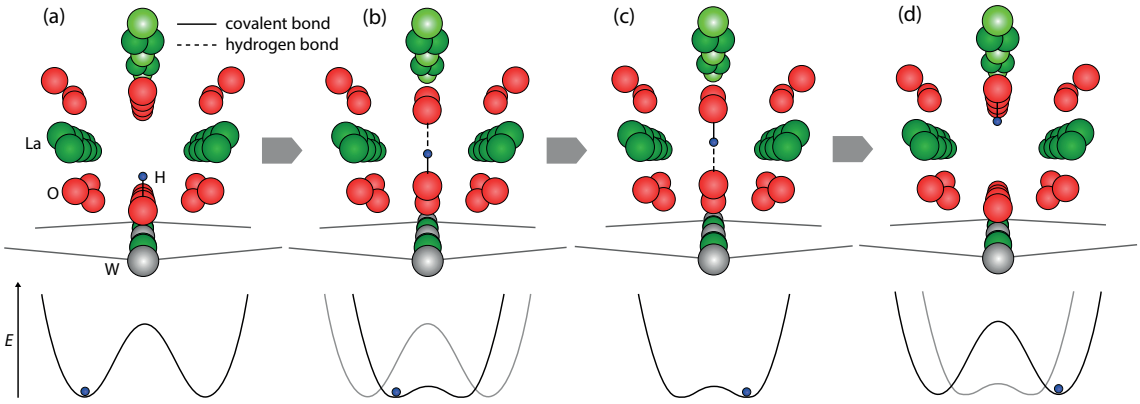

Figure 3.3: Sketch of the Grotthuss mechanism. (a) The hydrogen is bound covalent to an oxygen ion, forming a free hydroxy group, OH. (b) In an instant configuration, two neighboring oxygen ions are closer together and a hydrogen bond to the other oxygen ion is established. (c) Covalent and hydrogen bond are interchanged with a low barrier. (d) The oxygen ions are separated again and the hydrogen bond to the oxygen ion, to which the proton was originally bound to, breaks.

3.2.2 Fickian Diffusion

As mentioned above, diffusion is a statistical effect based on the Brownian motion of molecules and atoms. The mathematical description of diffusion processes is based on the works of Fick in the 19th century. The mathematics of diffusion is very similar to the mathematics of heat transport (compare to Section 4.2). In most cases, the diffusion is not based on the direction of the motion, i.e. the medium, in which the diffusion occurs, is isotropic[60], and the flux of species can be described by Fick's first law (for simplicity reasons here in a one-dimensional system):

$$j = -D\frac{\partial c}{\partial x} \tag{3.20}$$

For transient processes, the diffusion equation can be obtained by the help of the equation of continuity: for a small given volume, the influx minus the out-flux is equal to the rate of accumulation of the diffusing species within the volume, written

$$-\frac{\partial j}{\partial x} = \frac{\partial c}{\partial t} \tag{3.21}$$

Combining Fick's first law, Eq. (3.20), and the equation of continuity, Eq. (3.21), the diffusion equation is yielded, Fick's second law, assuming a constant diffusion coefficient:

$$\frac{\partial c}{\partial t} = D\frac{\partial^2 c}{\partial x^2} \tag{3.22}$$

The diffusion coefficient in Fick's laws is the proportionality constant to link e.g. the flux, j, with the driving force, $\partial c/\partial x$. In most solids, the diffusion coefficient shows an Arrhenius-type temperature dependence[64] and is a function of the activation enthalpy of diffusion, $\Delta_D H$, and a

pre-exponential factor, $D^{\ominus}$:[64]

$$D(T) = D^{\ominus} \exp\left\{-\frac{\Delta_D H}{RT}\right\} \tag{3.23}$$

From irreversible thermodynamics[65] Fick's first law, Eq. (3.20), can be expressed by a gradient in chemical potential instead of a gradient in concentration by

$$j_i = -\frac{D_i c_i}{RT} \cdot \frac{\partial \mu_i}{\partial x} \tag{3.24}$$

With $\partial\mu_i/\partial x = \partial\mu_i/\partial c_i \cdot \partial c_i/\partial x$ and $\partial\mu_i = RT\partial \ln a_i$ Eq. (3.24) can be written as

$$j_i = -\frac{D_i c_i}{RT} \cdot \frac{\partial \mu_i}{\partial c_i} \cdot \frac{\partial c_i}{\partial x} = -D_i \cdot \frac{\partial \ln a_i}{\partial \ln c_i} \cdot \frac{\partial c_i}{\partial x} \tag{3.25}$$

The expression $\partial \ln a_i/\partial \ln c_i$ is called the thermodynamic factor, γ_i. The thermodynamic factor of oxygen is defined as

$$\gamma_{\mathrm{O}} = \frac{1}{2}\frac{\partial \ln a\mathrm{O}_2}{\partial \ln c_{\mathrm{O}}} \tag{3.26}$$

The driving force for the diffusion of charged species is, likewise to the surface reaction, not the gradient in chemical potential, μ, but the gradient in electrochemical potential, η or $\tilde{\mu}$.[66] The fluxes of two mobile charge carriers can be described in an isothermal system by[24, 64, 67]

$$j_i = -\frac{D_i c_i}{RT} \cdot \frac{\partial \tilde{\mu}_i}{\partial x} = -\frac{D_i c_i}{RT}\left(\frac{\partial \mu_i}{\partial x} + z_i F \frac{\partial \phi}{\partial x}\right), \tag{3.27}$$

with the electric potential ϕ. The negative gradient in electric potential is called the Nernst field. In a typical oxide with mobile oxygen vacancies and, e.g., highly mobile electron holes, the oxygen vacancies are accelerated by the Nernst field and the electron holes are slowed down.
The Nernst field for a MIEC with mobile oxygen ions can be calculated by the fluxes of $\mathrm{h}^{\bullet}$ and $\mathrm{v}_{\mathrm{O}}^{\bullet\bullet}$ and the relation $j_{\mathrm{h}^{\bullet}} + 2j_{\mathrm{v}_{\mathrm{O}}^{\bullet\bullet}} = 0$, which is required for maintaining local charge neutrality.

$$-F\frac{\partial \phi}{\partial x} = \frac{2D_{\mathrm{v}_{\mathrm{O}}^{\bullet\bullet}} c_{\mathrm{v}_{\mathrm{O}}^{\bullet\bullet}} \frac{\partial \mu_{\mathrm{v}_{\mathrm{O}}^{\bullet\bullet}}}{\partial x} + D_{\mathrm{h}^{\bullet}} c_{\mathrm{h}^{\bullet}} \frac{\partial \mu_{\mathrm{h}^{\bullet}}}{\partial x}}{D_{\mathrm{h}^{\bullet}} c_{\mathrm{h}^{\bullet}} z_{\mathrm{h}^{\bullet}} + 2D_{\mathrm{v}_{\mathrm{O}}^{\bullet\bullet}} c_{\mathrm{v}_{\mathrm{O}}^{\bullet\bullet}} z_{\mathrm{v}_{\mathrm{O}}^{\bullet\bullet}}} \tag{3.28}$$

With the fluxes $j_{\mathrm{v}_{\mathrm{O}}^{\bullet\bullet}}$ and $j_{\mathrm{h}^{\bullet}}$ and the relations $j_{\mathrm{h}^{\bullet}} = -2j_{\mathrm{v}_{\mathrm{O}}^{\bullet\bullet}}$, $j_{\mathrm{O}} = -j_{\mathrm{v}_{\mathrm{O}}^{\bullet\bullet}}$, $\nabla\mu_{\mathrm{O}} = 2\nabla\mu_{\mathrm{h}^{\bullet}} - \nabla\mu_{\mathrm{v}_{\mathrm{O}}^{\bullet\bullet}}$ and $\partial\mu_{\mathrm{O}} = (RT/2)\partial \ln a\mathrm{O}_2$, the ambipolar chemical diffusion coefficient of oxygen, $\tilde{D}_{\mathrm{O}}$, can be written as[64]

$$\tilde{D}_{\mathrm{O}} = \frac{D_{\mathrm{v}_{\mathrm{O}}^{\bullet\bullet}} c_{\mathrm{v}_{\mathrm{O}}^{\bullet\bullet}} D_{\mathrm{h}^{\bullet}} c_{\mathrm{h}^{\bullet}}}{4D_{\mathrm{v}_{\mathrm{O}}^{\bullet\bullet}} c_{\mathrm{v}_{\mathrm{O}}^{\bullet\bullet}} + D_{\mathrm{h}^{\bullet}} c_{\mathrm{h}^{\bullet}}} \cdot \left(\frac{1}{2}\frac{\partial \ln a\mathrm{O}_2}{\partial c_{\mathrm{O}}}\right) \tag{3.29}$$

All derivatives with respect to depth x in this section can also be written with the nabla operator, ∇, for a three-dimensional treatment. The second derivative with respect to depth x can accordingly be described by the squared nabla operator, ∇^2, or the LaPlace operator, Δ.

The diffusion coefficient of species i can be set into relation with the electrochemical mobility, u_i, using the Nernst–Einstein equation:

$$D_i = B_i k_B T = \frac{u_i k_B T}{z_i e}, \tag{3.30}$$

with the mechanical mobility B_i of the charge carrier i, which is defined by the electrochemical mobility u_i and charge $z_i e$ of the charge carrier by $B_i = u_i/(z_i e)$. The mechanical mobility is sometimes denoted as μ and the electrochemical mobility as μ_q.

3.2.3 Three Mobile Charge Carriers

The above mathematics of diffusion are valid for two mobile charge carriers, i.e. an electronic defect and an ionic species. In a MIEC with additional protonic conductivity three independent mobile charge carriers are present (see also Section 2.2.2): oxygen vacancies, protons and electron holes. Each species is not coupled with one but with two species for charge compensation in the electroneutrality condition. First conductivity relaxation experiments on systems with three mobile charge carriers — in this case oxygen vacancies, titanium vacancies, and electron holes — were performed by Yoo and Lee[68], extracting chemical diffusion coefficients for titanium and oxygen. In a later study, Yoo *et al.*[69] examined hydration and oxidation kinetics of a proton conducting MIEC.

The flux equations for proton interstitials and oxygen vacancies can be established using the chemical potentials upon hydration and oxidation.[70, 71]

$$j_{V_O^{\bullet\bullet}} = \frac{\sigma_{V_O^{\bullet\bullet}} t_{h^\bullet}}{4F^2} \nabla \mu_O + \frac{\sigma_{V_O^{\bullet\bullet}} t_{H_i^\bullet}}{4F^2} \nabla \mu_{H_2O} \tag{3.31}$$

$$j_{H_i^\bullet} = \frac{\sigma_{H_i^\bullet} t_{h^\bullet}}{2F^2} \nabla \mu_O - \frac{\sigma_{H_i^\bullet} (1 - t_{H_i^\bullet})}{2F^2} \nabla \mu_{H_2O} \tag{3.32}$$

However, the flux equations become more complex if a gradient in defect concentration is considered instead of a gradient in chemical potential. In the following equations, the fluxes are described by gradients in oxygen vacancy concentration and in proton interstitial concentration. They may also be expressed by other concentration gradients, but the equations can be transformed into each other.[71]

$$j_{V_O^{\bullet\bullet}} = -D_{VV} \nabla c_{V_O^{\bullet\bullet}} - D_{VH} \nabla c_{H_i^\bullet} \tag{3.33}$$

$$j_{H_i^\bullet} = -D_{HV} \nabla c_{V_O^{\bullet\bullet}} - D_{HH} \nabla c_{H_i^\bullet} \tag{3.34}$$

The four chemical diffusion coefficients with the diffusing species and the gradient that is consid-

ered as subscript[71] are defined as follows:

$$D_{VV} = (1 - t_{v_O^{\bullet\bullet}}) D_{v_O^{\bullet\bullet}} + t_{v_O^{\bullet\bullet}} D_{h^\bullet} \tag{3.35}$$

$$D_{VH} = \frac{1}{2} t_{v_O^{\bullet\bullet}} (D_{h^\bullet} - D_{H_i^\bullet}) \tag{3.36}$$

$$D_{HV} = 2 t_{H_i^\bullet} (D_{h^\bullet} - D_{v_O^{\bullet\bullet}}) \tag{3.37}$$

$$D_{HH} = (1 - t_{H_i^\bullet}) D_{H_i^\bullet} + t_{H_i^\bullet} D_{h^\bullet} \tag{3.38}$$

In principle, the concentrations of $v_O^{\bullet\bullet}$, $H_i^\bullet$ and $h^\bullet$ show two-fold depth profiles. This behavior is different for extreme cases, e.g. if all diffusivities are equal or if one of the charge carriers is immobile, resulting in single fold concentration profiles of the other species. The two-fold profiles can, however, be described by two effective diffusion coefficients if the electron hole concentration is high, $\tilde{D}_H^{\text{eff}}$ and $\tilde{D}_O^{\text{eff}}$.[71]

3.3 Composition of Gas Atmosphere

In Chapter 2 the defect chemistry of the bulk phase has been discussed. As the sample's oxygen and hydrogen content is in equilibrium with the gas phase — see Eqs. (3.1), (3.6) and (3.10) —, the knowledge of the composition of the gas phase is primal.

In the experiments, the samples were surrounded by gas streams of nitrogen and oxygen, saturated with water. The total pressure is assumed constant at 1 bar, which is the ambient pressure of the open ended experimental setup. Nitrogen can be assumed to be inert, and water is in an equilibrium with hydrogen and oxygen, where the additional oxygen is shifting the equilibrium towards water. In the following section the partial pressure of hydrogen, pH_2, will be calculated for high temperature experiments.

If the equilibrium is significantly shifted to the left side, pO_2 and pH_2O are affected. As the pO_2 will be set so that the voltage of the potentiometric O_2 sensor is constant and $\Delta pO_2 = 0$, the former can be neglected as will be discussed later. A change in pH_2O is not wanted because the pH_2O is one of the variables for which the kinetic transport parameters are provided. Furthermore, if pH_2 has a significant fraction, it would be necessary to discuss if the reactive protonic species is hydrogen or water and/or if different kinetics are effective. The Gibbs energy can be calculated by the heat capacities of the components at constant pressure and the reaction enthalpy.

3.3.1 Gibbs Energy, Equilibrium Constant and Resulting Partial Pressure of Hydrogen

The formation enthalpy of water vapor at room temperature and the corresponding equilibrium reaction are defined as

$$H_2(g) + \frac{1}{2}O_2(g) \rightleftharpoons H_2O(g) \qquad \Delta_f H(298.15\,K) = -241.82\,kJ\,mol^{-1} \tag{3.39}$$

For the calculation of the equilibrium constant, the Gibbs energy of the reaction in dependency of the temperature is required

$$\Delta_R G^{\ominus}(T) = \Delta_R H^{\ominus}(T) - T\Delta_R S^{\ominus}(T), \tag{3.40}$$

using the temperature-dependent change of the molar heat capacity of the reaction at constant pressure,

$$\Delta_R C_p(T) = \sum_i \nu_i c_{p,i}(T), \tag{3.41}$$

with the stoichiometric coefficient of species i, ν_i, which is negative for reactants. The temperature-dependent molar heat capacities, $c_p(T)$, of H_2, O_2 and H_2O were taken from Reference [72] and are depicted in Fig. 3.4 together with the heat capacity of the Reaction (3.39) and the corresponding Gibbs energy, calculated by numeric integration of the reaction enthalpy and entropy.
The equilibrium constant, K, can be calculated by the Gibbs energy of the reaction,

$$\ln K = -\frac{\Delta_R G(T)}{RT} \tag{3.42}$$

The law of mass action for this reaction using partial pressures can be expressed as

$$K_p = \prod_i p_i^{\nu_i} = \frac{pH_2O}{pH_2 \cdot \sqrt{pO_2}} \tag{3.43}$$

The equilibrium constant, which is plotted in Fig. 3.5, is linked with the equilibrium constant of the partial pressures by

$$K = \left(p^{\ominus}\right)^{-\sum \nu_i} \cdot \prod_i [\varphi_i]^{\nu_i} \cdot K_p \tag{3.44}$$

As the total pressure is $p = 1\,bar$, the fugacity coefficients, φ_i, can be assumed to be 1, approximating for this reaction:

$$K \approx K_p \cdot bar^{0.5} \tag{3.45}$$

The calculation of the resulting partial pressure of hydrogen is exemplary performed for an initial water vapor pressure of $pH_2O^0 = 0.03\,bar$ and an initial oxygen pressure of $pO_{2,MFC} = 0.03\,bar$. By increasing the pO_2, the equilibrium is shifted to the product side so that the partial pressure of hydrogen is decreased significantly compared to oxygen-free atmospheres. Nitrogen is inert

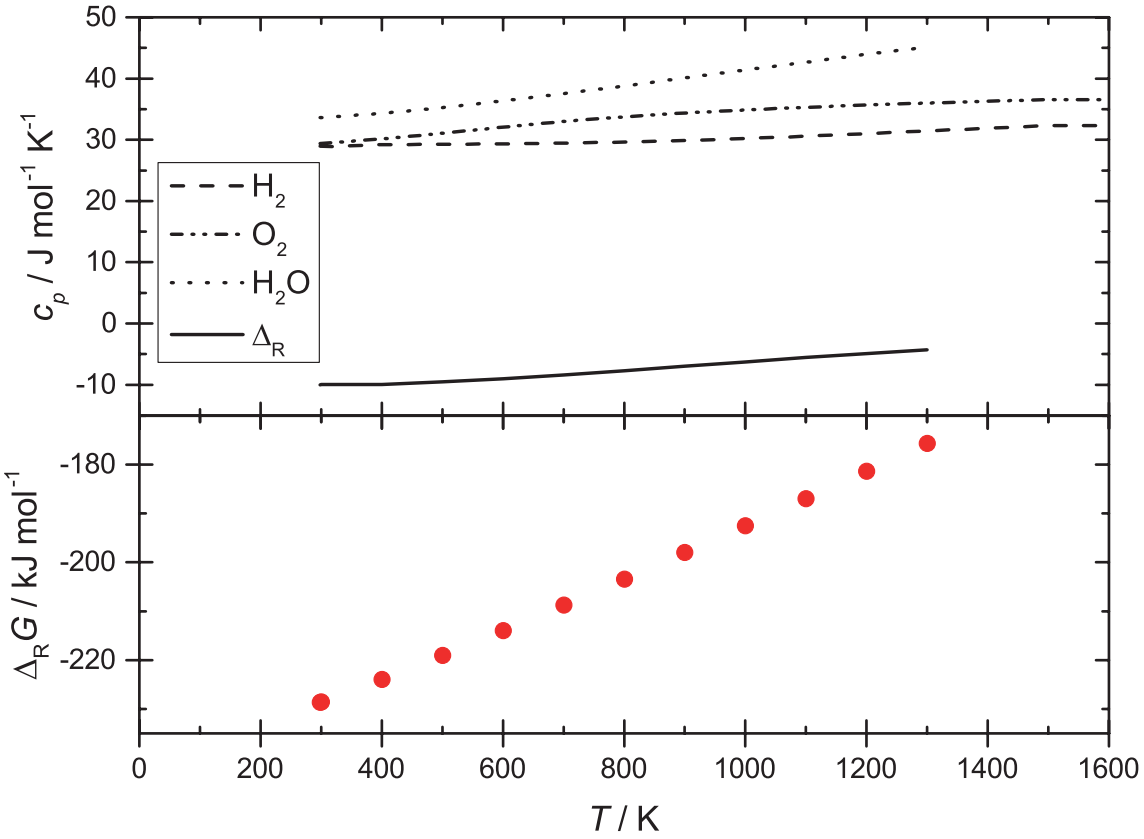

Figure 3.4: Temperature-dependent molar heat capacities at constant pressure and the resulting heat capacity of Eq. (3.39) (top). Corresponding temperature-dependent Gibbs energy (bottom).

and can be canceled in the law of mass action. The resulting partial pressure of oxygen is $pO_2 = pO_{2,K_p} + pO_{2,\mathrm{MFC}}$, meaning the sum of the initial partial pressure of oxygen provided by the mass flow controller, increased by the oxygen partial pressure formed by the equilibrium reaction. The partial pressure of hydrogen is two times the partial pressure of oxygen formed by the equilibrium reaction, $pH_2 = 2pO_{2,K_p}$.

The total pressure, neglecting inert nitrogen, is

$$p = pH_2O^0 + pO_{2,\mathrm{MFC}} + 0.5pH_2 = pH_2O + 1.5pH_2 + pO_{2,\mathrm{MFC}} \tag{3.46}$$

with an increase of $0.5pH_2$ due to the change in stoichiometric coefficients, $\Delta\nu_g = -0.5$. The equilibrium can be written as

$$K_p = \frac{pH_2O}{pH_2 \cdot \sqrt{pO_2}} = \frac{p - 1.5pH_2 - pO_{2,\mathrm{MFC}}}{pH_2\left(pO_{2,K_p} + pO_{2,\mathrm{MFC}}\right)^{0.5}} = \frac{pH_2O^0 - pH_2}{pH_2\left(0.5pH_2 + pO_{2,\mathrm{MFC}}\right)^{0.5}} \tag{3.47}$$

The partial pressure of hydrogen can be obtained by a numerical solution of this equation, depicted in Fig. 3.6.

All experiments are performed in a temperature range between 650 °C and 950 °C. The partial pressure of hydrogen in this regime is approximately between 10^{-12} bar and 10^{-8} bar. Compared

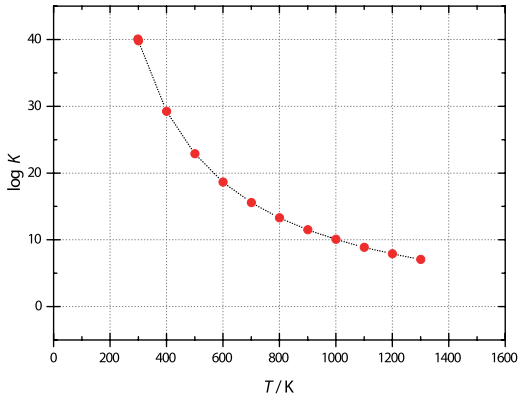

Figure 3.5: Equilibrium constant, K, of the reaction (3.39).

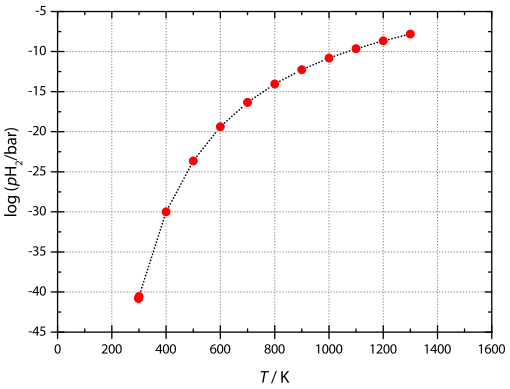

Figure 3.6: Partial pressure of hydrogen with 30 mbar water and oxygen partial pressures.

to the pO_2 provided by the gas stream, the oxygen formed in the equilibrium reaction, pO_{2,K_p}, is negligible. In the experiment, the overall pO_2 is monitored and controlled *in operando* so that the required $\Delta pO_2 = 0$ (see Chapter 4) is easy to achieve. However, if the equilibrium would be shifted significantly to the left side, the resulting pH_2O had to be monitored experimentally.

4

The Electrical Conductivity Relaxation Technique

Relaxation techniques are a widely used method to obtain the chemical diffusion coefficient $\tilde{D}$ and/or the surface reaction constant $\tilde{k}$ of a species in a solid state sample. First relaxation studies on solid state materials were performed almost a century ago by Dünwald and Wagner.[73] They are based on monitoring a sample's property as a function of time after disturbing the equilibrium (i.e. a step-like change in the activity of oxygen in the gas phase surrounding the sample). The property monitored is not necessarily the electrical conductivity[74–76] but can also be the color[77–79] or weight[80] of a sample — or any property proportional to the concentration of the monitored species in the sample. By fitting the diffusion model (see Section 4.3) that reflects the experimental setup and physics to the resulting experimental relaxation curve, one can obtain the rate limiting kinetic transport parameters of the species for the corresponding material. The determinability of the transport parameters will be discussed in Section 4.4.

The relaxation technique upon hydration and dehydration is based on the theory of oxidative and reductive steps and their equilibration. The principle will be discussed first for the latter, followed by the considerations that have to be made for (de-)hydration kinetics.

4.1 Electrical Conductivity as an Observable

The electrical conductivity is an easily accessible sample property. Measurement devices (typically digital multimeters in combination with constant current sources) are comparatively low priced and provide data with high precision. The electrical conductivity, σ, is a function of the charges, z_i, electrochemical mobilities, u_i, and concentrations, c_i, of all charge carriers i:

$$\sigma = \sum_i \sigma_i = F \sum_i \left(|z_i| u_i c_i\right) \tag{4.1}$$

If the step in oxygen activity is small, the charge and electrochemical mobility can be assumed constant during the entire experiment thus rendering the conductivity a direct observable of the concentration of all charge carriers, $\sigma(t) \propto \sum_i c_i(t)$. The concentration within the bulk phase, however, is not only a function of time but also a function of space, $c(x,t)$. If one divides the cross-sectional area of a bulk phase into infinitesimal lengths for a one-dimensional treatment the conductivity can be obtained by integration over length x.[81] Thus, the conductivity is more precisely proportional to the *average* concentration of all charge carriers, $\sigma(t) \propto \sum_i \bar{c}_i(t)$. With the electroneutrality condition the concentrations of the charge carriers can be set into relation. For typical acceptor doped oxides with oxygen non-stoichiometry and p-type conductivity, the electroneutrality condition can be expressed as:

$$2[\mathrm{v}_\mathrm{O}^{\bullet\bullet}] + [\mathrm{h}^\bullet] = [\mathrm{Acc}'] \tag{4.2}$$

The concentration of acceptors is constant throughout the experiment while the concentration of electron holes, $\mathrm{h}^\bullet$, and oxygen vacancies, $\mathrm{v}_\mathrm{O}^{\bullet\bullet}$, change over time according to the corresponding oxygen incorporation equation

$$\frac{1}{2}\mathrm{O}_2(\mathrm{g}) + \mathrm{v}_\mathrm{O}^{\bullet\bullet} \rightleftharpoons \mathrm{O}_\mathrm{O}^\times + 2\mathrm{h}^\bullet \tag{4.3}$$

Eq. (4.1) becomes

$$\sigma(t) = F \sum_i \left(|z_i| u_i c_i^0\right) + F|z_{\mathrm{v}_\mathrm{O}^{\bullet\bullet}}| u_{\mathrm{v}_\mathrm{O}^{\bullet\bullet}} \Delta\bar{c}_{\mathrm{v}_\mathrm{O}^{\bullet\bullet}}(t) + F|z_{\mathrm{h}^\bullet}| u_{\mathrm{h}^\bullet} \Delta\bar{c}_{\mathrm{h}^\bullet}(t), \tag{4.4}$$

and with Eqs. (2.1), (4.2) and (4.3) the concentration changes of oxygen vacancies and electron holes can be set into relation, $\Delta\bar{c}_{\mathrm{v}_\mathrm{O}^{\bullet\bullet}}(t) = -2\Delta\bar{c}_{\mathrm{h}^\bullet}(t)$, simplifying Eq. (4.4) to

$$\sigma(t) = \sigma^0 + F\left(|z_{\mathrm{v}_\mathrm{O}^{\bullet\bullet}}| u_{\mathrm{v}_\mathrm{O}^{\bullet\bullet}} - 2|z_{\mathrm{h}^\bullet}| u_{\mathrm{h}^\bullet}\right) \Delta\bar{c}_{\mathrm{v}_\mathrm{O}^{\bullet\bullet}}(t) \tag{4.5}$$

The time-dependent electrical conductivity, $\sigma(t)$, is thus a function of the time-dependent average oxygen vacancy concentration with the initial conductivity, σ^0, as offset and Faraday's constant, charges and electrochemical mobilities as proportionality constant. By a normalization function the observable can be directly connected to the average concentration:

$$\sigma_\mathrm{norm} = \frac{\sigma(t) - \sigma^0}{\sigma^\infty - \sigma^0} = \frac{\bar{c}_{\mathrm{v}_\mathrm{O}^{\bullet\bullet}}(t) - c^0_{\mathrm{v}_\mathrm{O}^{\bullet\bullet}}}{c^\infty_{\mathrm{v}_\mathrm{O}^{\bullet\bullet}} - c^0_{\mathrm{v}_\mathrm{O}^{\bullet\bullet}}}, \tag{4.6}$$

with the initial conductivity σ^0 for $t = 0$ and the conductivity in equilibrium σ^∞ for $t \to \infty$. In the following formulae in this work, a superset '0' and '∞' denote the initial or equilibrium value, respectively. These values are usually constant over x and the usage of average values is superfluous. A more detailed discussion including considerations for the n-type regime can be found elsewhere[82]. In the case of lanthanum tungstate, both the fact that two mobile ionic species are present and its electroneutrality condition (Eq. (2.13)) is different to Eq. (4.2) add to a more complex behavior that will be discussed in Section 7.2.2.

4.2 Principle of Electrical Conductivity Relaxation Measurements

The electrical conductivity, σ, of a sample that is in equilibrium with the surrounding gas atmosphere is monitored as a function of time. At time zero, $t = 0$, an instantaneous change of the activity of the surrounding gas, e.g. a step-like change in $p\mathrm{O}_2$, initializes the relaxation process. As a consequence, the sample takes up or releases oxygen according to Eq. (4.3) until the sample is in equilibrium with the new $p\mathrm{O}_2$. For ceramic samples usually a four point DC conductivity measurement is used (the van der Pauw method[83, 84] is favorable for ECR on thin films). The resulting curve is then fitted to a diffusion model corresponding to the geometry of the sample (e.g. plane sheet, cylinder). Analytic solutions to diffusion models with various geometries and boundary conditions are summarized in the book of J. Crank[85] based on the book of Carslaw and Jaeger[86] for the transport of heat in solids. A typical normalized conductivity relaxation curve and the ideal step-like change in oxygen partial pressure is shown in Fig. 4.1.

4.2.1 Prerequisites

In order to determine transport parameters with the ECR technique, a few prerequisites must be fulfilled.

i. The material must be a MIEC when investigating the relaxation behavior upon oxidation. Electronic conductivity is required for charge compensation within the bulk phase. As a consequence, the ECR technique cannot be used to determine oxygen conductivity in electrolyte materials. In this case, other techniques, e.g. IEDP followed by ToF-SIMS, are used to determine the tracer diffusion coefficient in order to describe the transport efficiency. However, in the presence of protons, charge compensation is also possible by ionic species only. In this case, the charge carriers cannot move independently and a single diffusion coefficient of water, $\tilde{D}_{\mathrm{H_2O}}$, will be determined in a relaxation experiment. Thus, relaxation upon (de-)hydration — if the material shows a solubility for protons — can always be measured with the ECR technique.

ii. It is necessary that the total electrical conductivity changes with a change in oxygen activity. This is usually given near the n-type and p-type regime, though the change in total conduc-

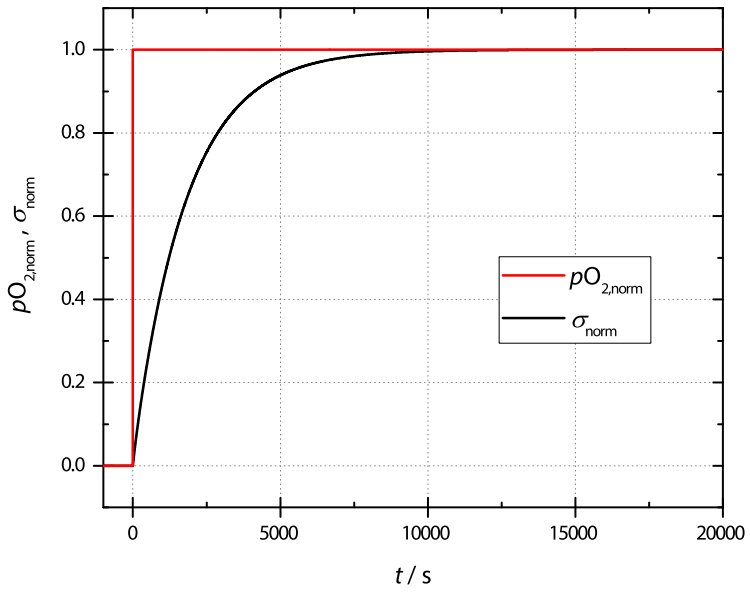

Figure 4.1: Typical relaxation curves: normalized pO_2, $pO_{2,\mathrm{norm}} = (pO_2(t) - pO_2^0)/(pO_2^\infty - pO_2^0)$, and normalized conductivity, both as a function of time. In this example the kinetic transport parameters for the simulated curve (Eq. (4.18)) are $\tilde{k} = 1.5 \times 10^{-4}\,\mathrm{cm\,s^{-1}}$, $\tilde{D} = 3.0 \times 10^{-5}\,\mathrm{cm^2\,s^{-1}}$ and $a = 0.2\,\mathrm{cm}$. Normalized curves start at zero and end at one as time approaches infinity, independent if the step is oxidative or reductive and if the absolute electrical conductivity is consequently increased or decreased. The change in partial pressure of oxygen is defined to be instantaneous.

tivity near the *n*-type regime is negative for increasing pO_2 while it is positive near the *p*-type regime. Near the stoichiometric point (see Figs. 2.7 and 2.11), the change in total conductivity is zero.

iii. The disturbance of the equilibrium, i.e. the step-size of the change in partial pressure of oxygen, must be small. From an experimental point of view it must be large enough to yield a significant change in sample property to improve the signal-to-noise ratio. The charge, z_i,[87] and electrochemical mobility, u_i, (from Nernst–Einstein equation, Eq. (3.30)) may be pO_2-dependent, thus the electrical conductivity is only an observable of the vacancy concentration for small step-sizes.

For small steps in pO_2, the diffusion process and the surface reaction are within the linear regime in a $j, \Delta c$-diagram, i.e. Fickian diffusion as well as a first order surface reaction are present. If the step-size is too large, diffusion and surface reaction may leave the linear regime. The limits of the linear regime can be different for both parameters and have been analyzed for $\tilde{k}$[88] and $\tilde{D}$[89] of strontium titanate.

Additionally, $\tilde{k}$ and $\tilde{D}$ are usually dependent on pO_2 and the diffusion model assumes constant transport parameters. A detailed analysis of the suggested step-sizes of an ECR experiment has been discussed by Wang *et al.*[90] Usually, step-sizes of half an order of magnitude

in pO_2 are chosen. N.B.: The transport parameters determined in an ECR experiment are the transport parameters in the new equilibrium for $t \rightarrow \infty$.

iv. The diffusion model used for fitting the experimental relaxation curve to obtain $\tilde{k}$ and $\tilde{D}$ requires a step-like change in oxygen activity. A change in oxygen activity is usually achieved by changing the partial pressure of oxygen whilst the flow rate is maintained constant, i.e. the composition of the gas stream is changed. However, in an experimental setup, an instantaneous change in oxygen activity is hard to achieve but the change follows a simple exponential function, $f(t) = 1 - \exp\{-t/\tau_{\Delta \text{ or } \sigma}\}$, with the time constant, τ_Δ, as the flush time of the reactor. If the flush time is much shorter than the relaxation time, τ_σ, the diffusion model described hereafter can directly be used to fit the relaxation data. If the flush time is an order of magnitude shorter than the relaxation time, $10\tau_\Delta < \tau_\sigma$, it is possible to correct the flush time by a convolution theorem introduced by den Otter *et al.* If the flush time approaches the relaxation time constant, $\tau_\Delta \approx \tau_\sigma$, the sample acts like an oxygen sensor and ECR measurements are not possible.[91]

v. If the change in non-stoichiometry, $\Delta\delta$, upon a step-like change in pO_2, is large along with large transport parameters, $\tilde{k}_O$ and $\tilde{D}_O$, the relaxation can be affected by a limited gas phase mass transport. In an oxidative step, the provided oxygen can severely be reduced in the vicinity of the sample by an uptake of oxygen or, in a reductive step, the sample releases huge amounts of oxygen that are not transported away from the sample's surface in order to maintain a constant outer oxygen activity. This effect has first been identified by Preis *et al.*[92] and a finite element study has later been performed by Lohne *et al.*[42].

In a recent article we have discussed how this effect can be identified to be relevant and possibilities to alleviate this effect for a material with large transport parameters and oxygen non-stoichiometry, e.g. $Ba_{0.5}Sr_{0.5}Co_{0.8}Fe_{0.2}O_{3-\delta}$.[43] The constraint can be formulated by

$$\dot{n}_{\text{sample}} \ll \dot{n}_{\text{cell}} \tag{4.7}$$

The amount of oxygen that is released or taken up by the sample per time unit must be much smaller than the amount of oxygen provided by the carrier gas stream per time unit. With knowledge of the thermodynamic factor, γ_O, the change in oxygen non-stoichiometry, $\Delta\delta$, upon a reductive or oxidative step can be calculated. By a multiplication of the differentiated normalized conductivity relaxation curve with the total amount of oxygen released or taken up by the sample, Δn_{sample}, the amount of oxygen leaving the sample per time unit can be

calculated:

$$\dot{n}_{\text{cell}} = \frac{\dot{V}}{V_{\text{m}}} \cdot \frac{p\text{O}_2}{p^{\ominus}} \tag{4.8}$$

$$-\Delta\delta = \int_{\ln p\text{O}_2^0}^{\ln p\text{O}_2^{\infty}} \frac{1}{2\gamma_{\text{O}}} \text{d} \ln p\text{O}_2 \tag{4.9}$$

$$\Delta n_{\text{sample}} = -\frac{1}{2} \cdot \frac{V_{\text{sample}} \cdot \Delta\delta \cdot Z}{V_{\text{UC}} \cdot N_{\text{A}}} \tag{4.10}$$

$$\dot{n}_{\text{sample}} = \Delta n_{\text{sample}} \cdot \frac{\text{d}}{\text{d}t} \left(\frac{\sigma(t) - \sigma^0}{\sigma^{\infty} - \sigma^0} \right) \tag{4.11}$$

With the flow rate $\dot{V}$ of the carrier gas stream, the gases molar volume, V_{m}, the thermodynamic factor, γ_{O}, the sample's volume, V_{sample}, the volume of the unit cell, V_{UC}, and the number of formula units per unit cell, Z.

For $Ba_{0.5}Sr_{0.5}Co_{0.8}Fe_{0.2}O_{3-\delta}$, it was shown that the amount of oxygen released by the sample per time unit is, especially in the first seconds of a relaxation, sometimes higher than the amount released by the sample in a reductive step, and that even for extremely high flow rates, the amount of oxygen released by the sample per time unit is in the same order of magnitude as $\dot{n}_{\text{cell}}$.

To alleviate this effect, one can either decrease the left side of Eq. (4.7) or increase the right side. The left side can be decreased by smaller samples or smaller step-sizes in $p\text{O}_2$ and the right side can be increased by higher flow rates or larger reactors whilst maintaining the same flux of oxygen.[43]

While the first two are mandatory, the others may introduce systematic errors to the determination of the transport parameters if they deviate significantly from the ideal situation that corresponds to the diffusion model.

4.3 Diffusion Model

The diffusion model defines the conditions and parameters which are necessary to fit an analytical function to experimental data in order to obtain transport parameters. In this section, the geometry — here a one-dimensional plane sheet — and the boundary conditions that are met in the ECR experiment, will be discussed. An analytical solution by J. Crank[85] based on a model of Carslaw and Jaeger[86] for surface radiation and transport of heat in solids considering all boundary conditions will be described. The diffusion model provides an equation of the concentration as a function of time and space, $c(x, t)$.

4.3.1 Geometry

The geometry used in this work is a one-dimensional plane sheet extended to three dimensions, i.e. a cuboid ingot. The diffusion model will first be discussed for the one dimensional case and the extension of the analytical function to three dimensions will be discussed at the end. A cuboid ingot (bar shaped sample), a pellet or a thin film can be represented by a plane sheet.
A plane sheet has an infinite extent in y- and z-direction and two plane surfaces parallel to each other at $x = -a$ and $x = a$ resulting in a thickness of $2a$. Fig. 4.2 shows a section of the plane sheet with the surface area A (dark blue), spanning the volume V (light blue cuboid). The sheet is symmetric at the plane $x = 0$ so that there is a second surface area and volume for $x > 0$. Between $-a$ and a is a solid phase and at $x < -a$ and $x > a$ there is a gas phase. The model is therefore described as a model for *'finite media'* and describes the diffusion within the solid state.

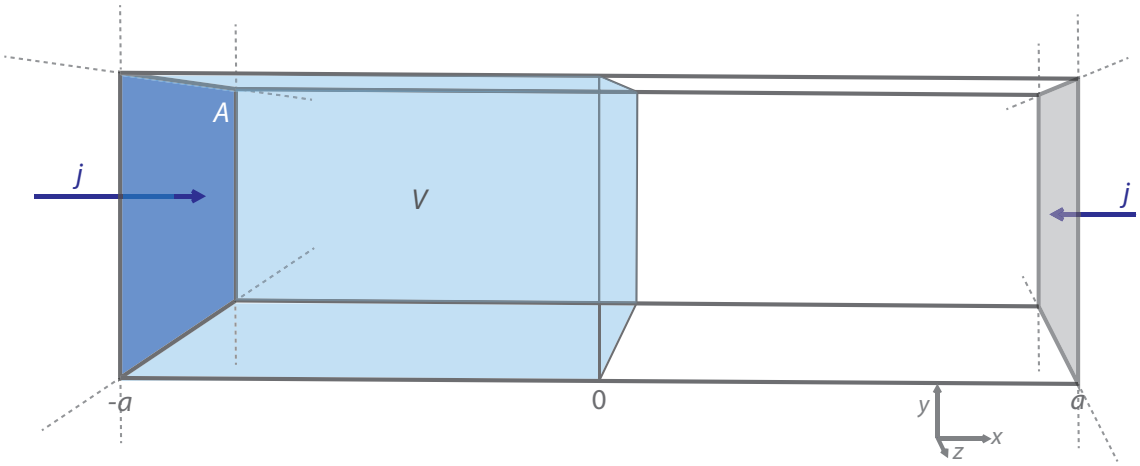

Figure 4.2: Plane sheet with two plane surfaces at $x = a$ and $x = -a$. The flux, j, is related to a surface area, A (dark blue plane), causing the filling of volume, V (light blue cuboid box), limited by symmetry by the center of the sample, $x = 0$, upon oxidation. The volume on the right side is formally filled by flux through the right surface area (gray plane).

The book of Crank treats further geometries which will not be discussed here. These geometries include a semi-infinite media suitable for fitting IEDPs with profiles smaller than the sample thickness, an infinite media, a cylinder and a sphere.

4.3.2 Fickian Diffusion

Within the bulk phase, Fick's second law, Eq. (3.22) in Section 3.2.2, must be fulfilled:

$$\frac{\partial c}{\partial t} = \tilde{D}\frac{\partial^2 c}{\partial x^2} \tag{4.12}$$

The first derivation with respect to time of the diffusion model's solution must be equal to the second derivation with respect to space, multiplied with $\tilde{D}$.

4.3.3 Initial Distribution

At the start of the relaxation process, the concentration of all species must be uniform for the entire bulk phase,

$$c(x, t = 0) = c^0 \tag{4.13}$$

This boundary condition is achieved by equilibration of the sample to the prior pO_2 and an instantaneous change in pO_2 at $t = 0$. In the resulting equation, which will be presented in Section 4.3.7, the above is achieved by a summarization over an infinite number of cosine functions. However, in practice, only a limited number of summarizations, N, can be performed (this will be discussed in Section 4.3.7), so that this boundary condition is only approximated by a sufficiently high number of summarized functions. The dependency of the normalized initial distribution on N is shown in Fig. 4.3. The experimental data in this work has been fitted with 100 summarizations.

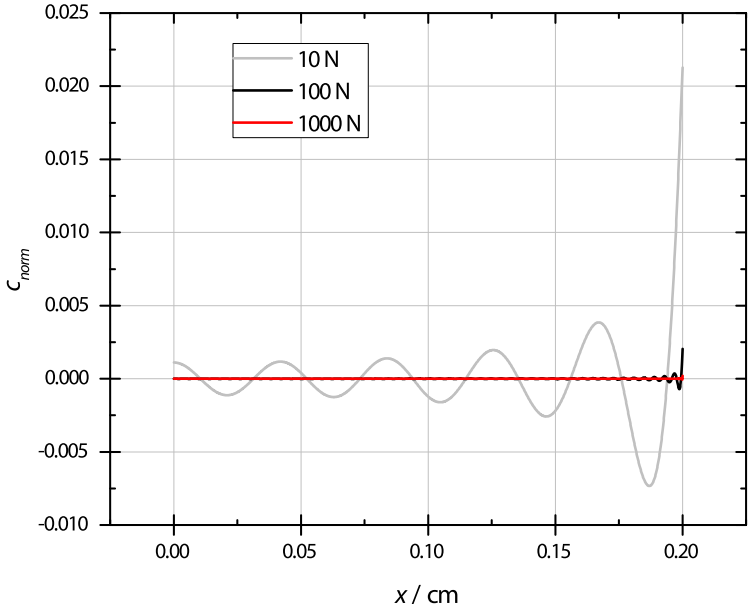

Figure 4.3: Solution for the sample's half-thickness $0 < x < a = 0.2\,\text{cm}$ at $t = 0$ with 10, 100 and 1000 roots for $L_a = \beta \tan \beta$. The concentration is normalized, $c_{\text{norm}} = 1 - \sum_{n=1}^{N}(\ldots)$, according to Eq. (4.17).

4.3.4 Constant Outer Concentration

The concentration of oxygen in the gas phase is constant during the entire relaxation process. The bulk concentration that is in equilibrium with the concentration of oxygen in the gas phase is represented by c^{∞} in the flux's equation of the surface reaction, Eq. (3.18). The boundary condition of an instantaneous change in oxygen activity is, as discussed above, experimentally hard to achieve. The flush time of the reactor[91] and the gas phase mass transport limitation[42, 43, 92] render the actual concentration of oxygen at the surface of the sample a function of time and location. The flush time correction regarding the reactor as a continuously ideal stirred tank reactor simplifies the gas phase concentration to a function of time only. However, the mass transport limitation cannot be corrected in the same way as it is strongly dependent on the location of the sample.

4.3.5 Flux in Center Zero

The flux in the center of the sheet, at $x = 0$, is zero,

$$-\tilde{D}\frac{\mathrm{d}c}{\mathrm{d}x}\bigg|_{x=0} = 0 \tag{4.14}$$

Statistically, the amount of ions flowing through the center of the sample in a positive direction is equal to the amount of ions moving in a negative direction. The resulting flux in the center is zero. The concentration profile shows a minimum or a maximum at the center during the relaxation process. The driving forces for diffusion, i.e. the concentration gradients, have a symmetry plane at $x = 0$, and compensate at this plane.

4.3.6 Surface Evaporation (First Order Surface Reaction)

The reaction of oxygen at the surface has already been discussed in Section 3.1.4 and the corresponding flux through the surface is described in Eq. (3.18). The flux at the sample's surface has to be connected to the diffusion within the bulk phase. At the surface planes, $x = -a$ and $x = a$, the flux into the sample is equal to the amount of species diffusing at this plane, i.e. fluxes defined in Eq. (3.18) and in Fick's first law, Eq. (3.20), are equal. For the left surface, $x = -a$ (dark blue plane in Fig. 4.2), the boundary condition is

$$-\tilde{D}\,\frac{\mathrm{d}c}{\mathrm{d}x}\bigg|_{x=-a} = \tilde{k}\left(c^{\infty} - c^{t,x=-a}\right), \tag{4.15}$$

and for the right surface, $x = a$ (gray plane in Fig. 4.2), the surface reaction is a negative flux from right to left upon incorporation, yielding

$$-\tilde{D}\,\frac{\mathrm{d}c}{\mathrm{d}x}\bigg|_{x=a} = -\tilde{k}\left(c^{\infty} - c^{t,x=a}\right) \tag{4.16}$$

The concentrations $c^{t,x=-a}$ and $c^{t,x=a}$ are the concentrations at the surface, c^{surf}, in Eq. (3.18).

4.3.7 Analytical Solution

An analytical function for the diffusion model was described by Crank[85] with the keywords *'diffusion in a plane sheet, uniform initial distribution, surface concentrations equal, surface evaporation'*. The corresponding model for the transport of heat in solids by Carslaw and Jaeger treats *'linear flow of heat in a solid bounded by parallel planes'* with a *'radiation boundary condition at* $-l < x < l$*'*.[86]

4.3.7.1 Function of Time and Space

For the time- and space-dependent concentration, $c(x, t)$, an equation giving respect to the geometry and all above mentioned boundary conditions, is

$$c_{\text{norm}} = \frac{c(x,t) - c^0}{c^\infty - c^0} = 1 - \sum_{n=1}^{\infty} \frac{2L_a \cos(\beta_n x/a) \exp\{-\beta_n^2 \tilde{D} t/a^2\}}{\cos\beta_n(\beta_n^2 + L_a^2 + L_a)} \tag{4.17}$$

with the dimensionless parameter $L_a = a \cdot \tilde{k}/\tilde{D}$ and β_n the positive roots of the function $L_a = \beta \tan\beta$ (see Fig. 4.6 and a more detailed discussion in Section 4.3.7.3). The concentration profiles are exemplarily calculated for a plane with a half-thickness of 0.2 cm and transport parameters of $\tilde{k} = 1.5 \times 10^{-4}$ cm s^{-1} and $\tilde{D} = 3.0 \times 10^{-5}$ cm^2 s^{-1} for different times and displayed in Fig. 4.4. At the center of the sample, $x = 0$, there is a minimum resulting in a zero flux. At $x = a$, the endpoint of the curve is the surface concentration, $c^{t,x=a}$. $c_{\text{norm}}(t = \infty)$ is unity, and the difference between 1 and the time-dependent surface concentration is the driving force for the surface reaction.

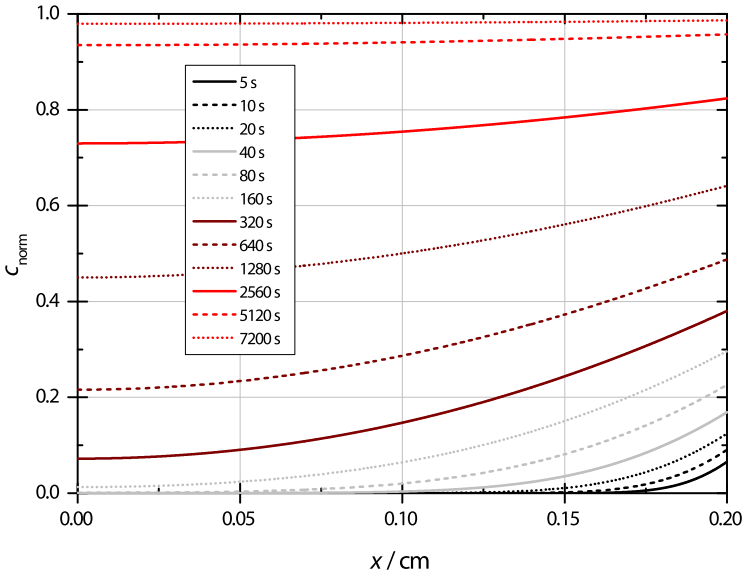

Figure 4.4: Concentration profiles for a plane sheet with $a = 0.2$ cm, $\tilde{k} = 1.5 \times 10^{-4}$ cm s^{-1} and $\tilde{D} = 3.0 \times 10^{-5}$ cm^2 s^{-1}.

4.3.7.2 Relaxation Function

The electrical conductivity of a sample is measured as a function of time in a relaxation experiment, losing any lateral information that is regarded in Eq. (4.17). It is therefore necessary to integrate over space x, which is proportional to the average concentration, $\bar{c}(t)$ (see Section 4.1). By integration, the relaxation function is yielded, describing the amount of particles, which have been released or incorporated into the sample at time t, $M(t)$, set into relation to the amount of particles that are exchanged in the entire relaxation process, M^{∞}. N.B.: M is not a molecular weight but a chemical amount or simply an amount in accordance with the notation in Reference [85]. The ratio $M(t)/M^{\infty}$ is also equal to the normalized average concentration or conductivity, Eq. (4.6).

Integration of Eq. (4.17) yields:

$$\frac{1}{2a} \cdot \int_{-a}^{a} \frac{c(x,t) - c^0}{c^{\infty} - c^0} \, \mathrm{d}x = \frac{M(t)}{M^{\infty}} = 1 - \sum_{n=1}^{\infty} \frac{2L_a^2 \exp\{-\beta_n^2 \tilde{D} t / a^2\}}{\beta_n^2 (\beta_n^2 + L_a^2 + L_a)} \tag{4.18}$$

This is the one-dimensional function that is used for fitting normalized ECR curves. In Fig. 4.5, the concentration profiles depicted in Fig. 4.4 are integrated and shown as a function of time. The resulting curve is a typical ECR curve that can be fitted to Eq. (4.18). In the case of a cuboid, a three-dimensional version of this function is required, which was described by Yasuda and Hishinuma[76] or, as a two-dimensional model, by Wang *et al.*[93], neglecting the extent in the third dimension. See Section 4.5 for a further discussion about neglecting the third dimension.

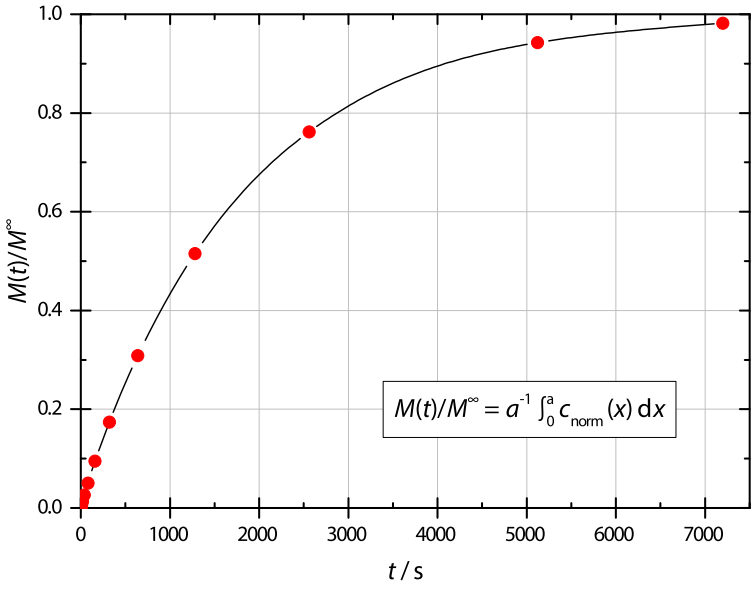

Figure 4.5: Integration of the curves depicted in Fig. 4.4 from $x = 0$ to a as a function of time.

Three-dimensional ECR equation:

$$\frac{M(t)}{M^{\infty}} = 1 - \sum_{n=1}^{\infty}\sum_{m=1}^{\infty}\sum_{i=1}^{\infty} \frac{2L_a^2 \cdot e^{-\frac{\beta_n^2 \tilde{D} t}{a^2}}}{\beta_n^2(\beta_n^2 + L_a^2 + L_a)} \cdot \frac{2L_b^2 \cdot e^{-\frac{\gamma_m^2 \tilde{D} t}{b^2}}}{\gamma_m^2(\gamma_m^2 + L_b^2 + L_b)} \cdot \frac{2L_c^2 \cdot e^{-\frac{\delta_i^2 \tilde{D} t}{c^2}}}{\delta_i^2(\delta_i^2 + L_c^2 + L_c)} \tag{4.19}$$

Two-dimensional ECR equation:

$$\frac{M(t)}{M^{\infty}} = 1 - \sum_{n=1}^{\infty}\sum_{m=1}^{\infty} \frac{2L_a^2 \cdot e^{-\frac{\beta_n^2 \tilde{D} t}{a^2}}}{\beta_n^2(\beta_n^2 + L_a^2 + L_a)} \cdot \frac{2L_b^2 \cdot e^{-\frac{\gamma_m^2 \tilde{D} t}{b^2}}}{\gamma_m^2(\gamma_m^2 + L_b^2 + L_b)} \tag{4.20}$$

4.3.7.3 The Parameters β_n and L_a

Many diffusion equations require the dimensionless parameter L_a, which sets the surface reaction rate and the diffusion coefficient into relation. A more common parameter is the 'characteristic length' (sometimes also denoted as 'critical length'), $L_C = \tilde{D}/\tilde{k}$. As a rule of thumb, if the sample's half-thickness is thicker than L_C, the diffusion limits the relaxation, if it is thinner, the surface reaction limits the relaxation process. If the sample's half-thickness is equal to the characteristic length, both parameters are rate determining. The parameter L_a combines the sample's half-thickness with the characteristic length in a single dimensionless parameter. It is defined as follows:

$$L_a = a \cdot \frac{\tilde{k}}{\tilde{D}} = \beta \tan \beta \tag{4.21}$$

$$L_b = b \cdot \frac{\tilde{k}}{\tilde{D}} = \gamma \tan \gamma \tag{4.22}$$

$$L_c = c \cdot \frac{\tilde{k}}{\tilde{D}} = \delta \tan \delta \tag{4.23}$$

In the second and third dimension, γ_m and δ_i are used corresponding to β_n, and L_b and L_c are used corresponding to L_a. The simultaneous determinability of both transport parameters has been addressed in some articles and will be discussed in detail in the following section. N.B.: The variable γ mentioned here or, in the diffusion model's equations, γ_m, has no relation to the thermodynamic factor, γ_O, and the variable δ or δ_i have no relation to the oxygen non-stoichiometry, δ.
The parameter β_n can be determined by numerically obtained roots of the equation

$$\beta \tan \beta - L_a = 0, \tag{4.24}$$

with the order n of the root. There is an infinite number of roots and β_n is the root in the interval $(n-1)\pi < \beta_n < (n-0.5)\pi$. The β_ns are visualized in Fig. 4.6. As mentioned above, only the positive roots are used for the determination of β_n. Cox-Galhotra *et al.* have analyzed the required number of roots for fitting relaxation profiles. They have found that their fit does not improve when more than 10 roots are determined. However, in the analyzed regime, $\tilde{k}$ still varied significantly in the fitting procedure although the root mean squared residuals did not decrease significantly. The

determined parameters converged to a certain value with increasing roots. Thus, they suggested to determine $\tilde{k}$ and $\tilde{D}$ in two separate relaxation experiments with different thicknesses.[94] This issue, however, might also be attributed to the simultaneous determinability of both parameters (see Section 4.4) and the error of the fit can be estimated (see Section 7.1.5) providing a confidence interval of the fit. As computational power for the fitting procedure is not expensive, a large number of roots has been chosen in this work for fitting relaxation curves (N = 100).

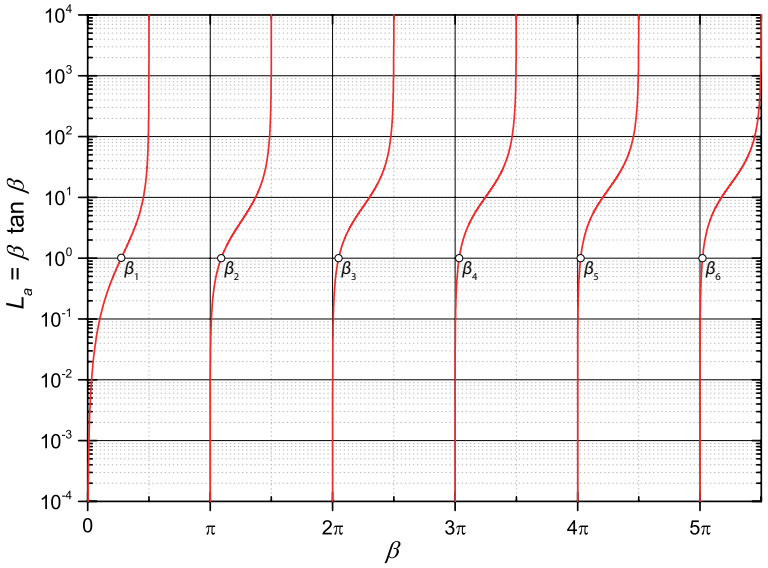

Figure 4.6: The function $f(\beta) = \beta \tan \beta$ and the roots for $L_a = 1$ for $\beta > 0$. From $L_a = a \cdot \tilde{k}/\tilde{D} > 0$ only the positive branch of the curves is shown.

The fitting procedure will be discussed in Section 7.1.2 and the MathWorks MATLAB® script used for fitting the data will be described in detail in Appendix A.

4.4 Simultaneous Determinability

In Section 4.3.7.3, the rule of thumb using the characteristic length as an indicator for the significance of the impact of the surface reaction or the bulk diffusion on the relaxation curve has been presented. In a recent article and in the preceding diploma thesis, the simultaneous determinability of both parameters in a single relaxation experiment has been discussed.[43, 95]
In a first step, $M(t)/M^{\infty}$ of a relaxation experiment has been calculated for a diffusion model ignoring the surface reaction and inserting the time constant of diffusion, $\tau_{\tilde{D}}$, into the time, t. The normalized time-dependent amount of a relaxation without surface reaction limitation, in other respects identical to the diffusion model presented in Section 4.3, can be expressed by the equation[85]

$$\frac{M(t)}{M^{\infty}} = 1 - \sum_{n=0}^{\infty} \left(\frac{8}{(2n+1)^2 \pi^2} \cdot \exp\left\{ -\frac{(2n+1)^2 \pi^2 \tilde{D} t}{4a^2} \right\} \right) \tag{4.25}$$

Inserting the time constant $\tau_{\tilde{D}} = a^2/(2\tilde{D})$ into time t of Eq. (4.25) yields

$$\frac{M(\tau_{\tilde{D}})}{M^{\infty}} = 1 - \sum_{n=0}^{\infty}\left(\frac{8}{(2n+1)^2\pi^2}\cdot\exp\left\{-\frac{(2n+1)^2\pi^2}{8}\right\}\right) \approx 0.9941705 \tag{4.26}$$

The time constant $\tau_{\tilde{k}}$ can be obtained by the conversion rate for the time constant $\tau_{\tilde{D}}$ and the simple exponential function of a first order surface reaction if the relaxation is limited by the surface reaction kinetics only:

$$\frac{M(\tau_{\tilde{D}})}{M^{\infty}} = 1 - \exp\left\{-\frac{\tilde{k}}{a}\tau_{\tilde{k}}\right\} \approx 0.9941705 \Rightarrow \tau_{\tilde{k}} \approx 5.145\frac{a}{\tilde{k}} \tag{4.27}$$

For the second step, multiple relaxation curves have been simulated with Eq. (4.18) for a fixed $\tilde{D}$ of $3.0 \times 10^{-5}\,\mathrm{cm^2\,s^{-1}}$ and a variation of $\tilde{k}$ with a sample thickness of $2a = 0.4\,\mathrm{cm}$. The time after which 99.41705% of the relaxation are completed, $t(\tau_{\tilde{D}})$, is plotted against the dimensionless parameter L_a in a double-logarithmic plot in Fig. 4.7. For $\log_{10} L_a < -1$, the time $t(\tau_{\tilde{D}})$ follows the linear behavior of the time constant $\tau_{\tilde{k}}$. The relaxation is controlled by the slow surface reaction. For $\log_{10} L_a > 2$, the time $t(\tau_{\tilde{D}})$ follows the time constant $\tau_{\tilde{D}}$ and the relaxation is governed by the slow bulk diffusivity. In the intermediate region, $-1 < \log_{10} L_a < 2$, both, the bulk diffusivity and the surface reaction, influence the relaxation process and both parameters can be determined simultaneously in a single relaxation experiment.[43] The simultaneous determinability is a property of the diffusion model and thus valid for all experiments, where this equation is used to determine transport parameters. In literature, there are other works treating the simultaneous determinability of both transport parameters in relaxation or tracer diffusion experiments, either by experimental [96] or by analytical[91, 97–99] approaches. The simultaneous determinability of hydrogen and oxygen transport coefficients in a relaxation experiment upon de-/hydration will be discussed in Section 7.1.3.

4.5 Simplifications

In an experimental environment, the required conditions for the diffusion model are hard to achieve, thus a few simplifications must be introduced. Some of them were already mentioned and are summarized here.

The equation for a two-dimensional diffusion model has been introduced in Section 4.3.7. It is necessary to use this equation instead of the three-dimensional case, which would be appropriate for a bar-shaped sample because of the method of the conductivity measurement: the conductivity is obtained by a four-point DC measurement. For details see Section 6.2.2. This measurement is based on a constant current directed along the third dimension of the sample by applying a time-dependent voltage in this direction, $U_{\mathrm{src}}(t)$. By this voltage, a time-dependent electric field acts as an additional external driving force, pumping ions towards the oppositely charged electrode, a so called *drift* of ions. This effect is not described in the analytical solution and, as the applied voltage is

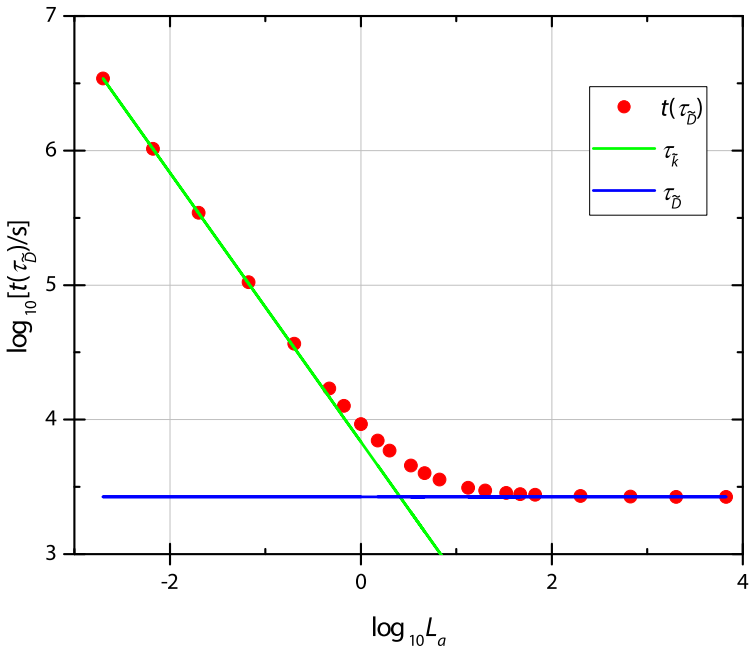

Figure 4.7: $t(\tau_{\tilde{D}})$ as a function of L_a (red dots) for a fixed diffusion coefficient of $\tilde{D} = 3.0 \times 10^{-5}$ cm^2 s^{-1} and a sheet thickness of $2a = 0.4$ cm. The time constants $\tau_{\tilde{k}}$ (green) and $\tau_{\tilde{D}}$ (blue) are linear in a double-logarithmic plot. Reprinted from Reference [43], with permission from Elsevier.

time-dependent, it can hardly be included in the equation. However, for sufficiently long samples, it is generally assumed that the diffusion in the third dimension can be neglected.[92, 93, 100] In our article, we have calculated the error introduced in the determination of the transport parameters by simulating a relaxation curve with the three-dimensional model, Eq. (4.19), and fitting the curve with the equation for a two-dimensional model, Eq. (4.20). The constant input parameters were $\tilde{k} = 1.5 \times 10^{-4}$ cm s^{-1}, $\tilde{D} = 3.0 \times 10^{-5}$ cm^2 s^{-1}, and $2a = 2b = 0.4$ cm. The characteristic length is equal to the sample's half-thickness. The three-dimensional curves have been simulated with various lengths, $2c$. In Fig. 4.8, the fitted transport parameters are plotted against the relation of the third dimension to the other two dimensions, $c/a = c/b$. The bar-shaped samples used in this work cause a systematic error of approximately 6% due to the simplification of assuming an infinite extent in z-direction.[43]

The step-size is small — half an order of magnitude in $p\mathrm{O}_2$ or $p\mathrm{H}_2\mathrm{O}$ — assuming a linear behavior of the driving forces and a constant charge and electrochemical mobility.

The reactor flush-time is fast compared to the relaxation. Additionally, there is no influence of limited gas phase mass transport. The flushing behavior of the reactor has been measured with an oxygen sensor and the flushing with water can be assumed equally fast. The reactor flushes within seconds[43] while relaxation times in this work are between 300 s and 30 000 s. Additionally, the amount of oxygen, $\Delta\delta$, and hydrogen that is exchanged, is generally low at fluorite type materials. Existence of gas phase mass transport limitation upon de-/hydration has been analyzed in Section

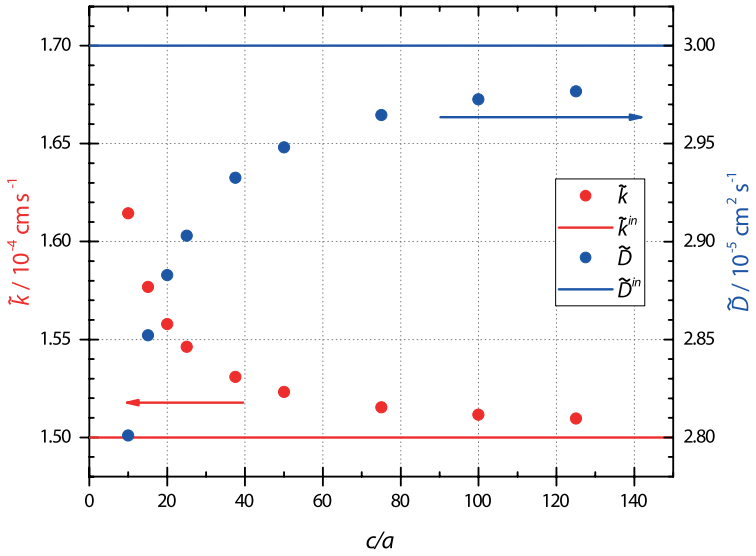

Figure 4.8: Input parameters for a three-dimensional model, $\tilde{k}^{in}$ and $\tilde{D}^{in}$, with a variation of the sample's length. The simulated curves were fitted with the analytical solution for a two-dimensional plane, Eq. (4.20), yielding the parameters $\tilde{k}$ (red symbols) and $\tilde{D}$ (blue symbols). The thickness of the sample is $2a = 2b = 0.4$ cm. Reprinted from Reference [43], with permission from Elsevier.

7.1.7.

The number of roots for fitting Eq. (4.18) is not infinite but has been chosen very high to avoid systematic errors.

In a recent article by He *et al.*[101], an analytical solution for a predefined diffusion model is not necessary, only the physics (Fickian diffusion, first order surface reaction) and the experimental setup (in the article the sample's arbitrary geometry) are necessary. This requires a fully functional FEM model and it requires also extensive computation times to fit the experimental data to the FEM model. The exact experimental setup can be included so that all limitations discussed above will be regarded in this method.

4.6 Two Mobile Ionic Species

In recent years, the conductivity relaxation technique has been used to determine transport parameters of mixed conductors with multiple mobile ionic species, e.g. titanium and oxygen or protons and oxygen. Relaxation patterns have been summarized in 2009 in an article by Yoo and Lee[70] referring to the individual observations in previous articles [68, 69, 102]. With a given high electronic conductivity, the relaxation behavior of two different mobile ionic species can be described by a superposition of two independent (single fold) relaxation curves resulting in a two-fold relaxation curve. Depending on the charge of the ionic species, monotonic and non-monotonic relaxation behavior has been observed. Titanium and oxygen in barium titanate, for example, show a two-fold

monotonic behavior[68] while hydration kinetics (oxygen and protons) in ytterbium doped strontium cerate are two-fold non-monotonic[69]. For the superposition, kinetic equations for both mobile species are multiplied with an amplitude or power factor. In the normalized case, the sum of the two amplitude factors is unity. If one describes the time-dependent total conductivity with a two-fold curve, the initial conductivity is added and both power factors, P_i, are *'constants each involving the mobilities and initial and final concentrations of the defects involved'*[70]. Yoo and Lee have analyzed samples that do not show a surface limitation. A later study by Lim *et al.* has replaced the diffusion limited kinetic function by the surface reaction and diffusion limited function, $f(\tilde{k}_i, \tilde{D}_i, t)$.[103] The resulting ECR curve can be described by[70, 103]

$$\sigma(t) = P^0 + P_i(c_i^0, c_i^\infty, u_i) \cdot f(\tilde{k}_i, \tilde{D}_i, t) + P_j(c_j^0, c_j^\infty, u_j) \cdot f(\tilde{k}_j, \tilde{D}_j, t), \tag{4.28}$$

with equal functions f for i and j, here described for i:

$$f(\tilde{k}_i, \tilde{D}_i, t) = 1 - \sum_{n=1}^{\infty} \frac{2L_{a,i}^2 \exp\{-\beta_{n,i}^2 \tilde{D}_i t/a^2\}}{\beta_{n,i}^2(\beta_{n,i}^2 + L_{a,i}^2 + L_{a,i})} \tag{4.29}$$

The two-fold relaxation behavior and the explanation will be discussed in more detail in the results of the relaxation experiments, Section 7.1.

5

Infrared Spectroscopy

The interaction of infrared light with molecules can lead to vibrations within the molecules. For two-atomic molecules, only one mode of vibration is possible, i.e. a stretching vibration. Molecules with more than two atoms can show deformation (change of bond angles) and stretching (change of bond lengths) vibrations. They can be classified into symmetric and asymmetric vibrations. For the excitation of a molecule, a dipole must be created or an existing dipole must be changed by vibration.

In proton conducting oxides, the proton is usually bound to oxygen by a covalent bond forming a hydroxy-anion (see Section 2.2.1.3). By infrared (IR) radiation, this bond can be excited, causing an absorption band in a transmission Fourier-transform infrared (FTIR) spectrometer.

The vibration of a molecule can be described by a harmonic oscillator for small vibrations and by an anharmonic oscillator for large vibrations. The potential curves of both oscillators are shown in Fig. 5.1. The vibration can only have discrete energy levels with the quantum number v, which are equidistant for the harmonic oscillator with selection rule $\Delta v = \pm 1$ and decrease in energy difference with the increasing quantum number for the anharmonic oscillator with selection rule $\Delta v = \pm n$. The quantum number v is a natural number including zero. The absorbed radiation must have the same energy as the difference in two energy levels. The energy of the vibration for a harmonic oscillator, and thus the frequency of radiation that excites this vibration, is

$$\nu = \frac{1}{2\pi}\sqrt{\frac{k}{\mu}} \qquad \text{with} \qquad \mu = \frac{m_1 m_2}{m_1 + m_2} \tag{5.1}$$

The use of the reduced mass, μ, is necessary because the center of the vibration is the mass balance point. k is the force constant, analogous to the spring constant for a mechanic spring, of the bond.

The definition of the reduced mass is valid for a two-atomic molecule.

For the excitation of vibrations using the model of an anharmonic oscillator, overtones with $\Delta v > \pm 1$ are possible. These overtones are used in the near infrared (NIR) spectroscopy.

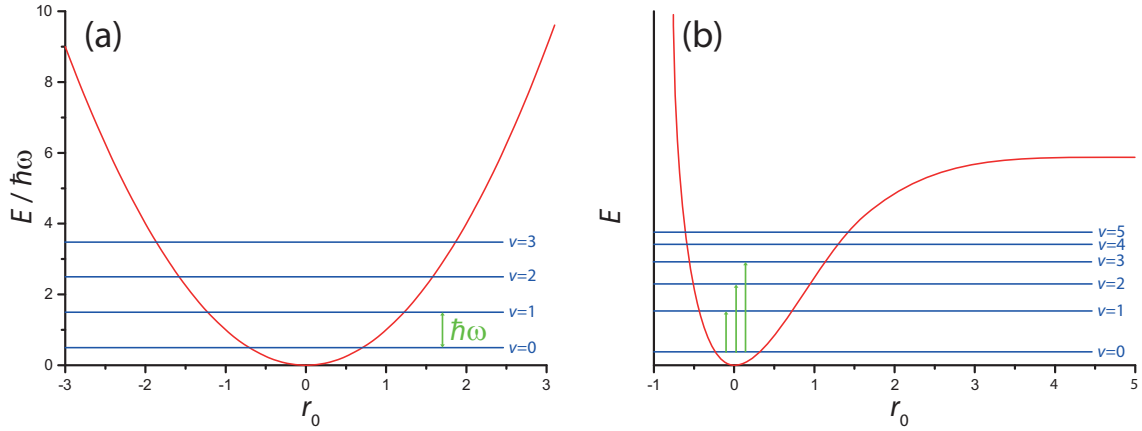

Figure 5.1: (a) Energy curve of a harmonic oscillator. The energy levels are equidistant with $\Delta E = \hbar\omega$. $\Delta v = \pm 1$. (b) Sketch of the Morse potential of an anharmonic oscillator with energy levels. $\Delta v = \pm n$

5.1 Fourier Transformation

Classic dispersive IR spectrophotometers measure the spectrum in dependence of the wavelength. FTIR machines have the benefit that the signal is quickly measured in dependence of a moving mirror's position (Michelson interferometer). Another advantage is the fact that the intensity of the detected beam is orders of magnitude larger as nearly the whole spectrum is analyzed instead of a discrete wavenumber. The Michelson interferometer consists, in principle, of a beam splitter, a fixed and a moving mirror. In order to determine the position of the moving mirror, monochromatic light by a red HeNe laser is directed through the interferometer and sample compartment. At the centerburst of the interferogram the optical path lengths of the two splitted beams is identical and the whole spectrum shows maximum constructive interference. If the optical path length is different, the spectrum — and thus the integrated intensity — is changed because of a wavenumber dependent phase shift. By Fourier transformation, the interferogram is converted into a spectrum. The resolution is dependent on the maximum optical path length difference, i.e. the moving mirror's maximum displacement. The maximum wavenumber is dependent on the resolution of the interferogram.[104]

The boundaries of the interferogram are cut off because the moving mirror has a limited displacement. Fourier transformation uses an integration up to infinity. Therefore, an apodization function, usually Happ–Genzel, which is a cosine function, is multiplied with the interferogram, yielding a high central peak and a cut-off of the ripples that result due to oscillations at the boundaries of the

interferogram. By apodization, the resolution is slightly decreased but irregularities in the resulting spectrum due to the cut-off integration are minimized.[104]

5.2 Near Infrared Spectroscopy

In the near infrared spectroscopy ($3800\,\mathrm{cm^{-1}} < \tilde{\nu} < 12\,500\,\mathrm{cm^{-1}}$), overtones of the normal vibrations are detected. The intensity of absorption bands is one to two orders of magnitude lower. Hence, thicker samples can be used in NIR spectroscopy due to higher penetration depths. The absorption bands are, however, much broader than in the mid infrared (MIR) spectroscopy. They have an extent of $30\,\mathrm{cm^{-1}}$ to $60\,\mathrm{cm^{-1}}$ and hence, an overlay of different absorption bands is likely. While the chemical environment has little influence on normal vibrations, overtones are highly influenced.[105] Ishiyama *et al.*[1] have analyzed infrared spectra on yttria doped barium zirconate and have found three different hydroxy-anion absorption bands for Y-OH-Y, Zr-OH-Y and Zr-OH-Zr environments, which overlap. By fitting Gauss curves, they have determined the site in dependency on the temperature, where protons are located.

5.3 Quantitative Analysis using Lambert–Beer's Law

The spectrum that is yielded by the Fourier transformation is an emission spectrum. However, in common qualitative and quantitative IR-spectroscopic applications, transmission or absorbance spectra are often used. For these spectra, a reference emission spectrum, I_0, is measured followed by the measurement of an emission spectrum with the sample, I. By the reference spectrum, the wavelength-dependent intensity of the IR source is taken into account as well as the absorption caused by the cuvette or the solvent in case of liquids.
The transmission, which is a function of wavelength, is defined as

$$T = \frac{I}{I_0} \tag{5.2}$$

and the absorbance spectrum follows the equation

$$A = -\log_{10} T \tag{5.3}$$

The absorbance A — the negative logarithmic transmission — is dependent on the thickness of the cuvette, d, the concentration, c, and an extinction coefficient that is dependent on the wavelength and the material, ϵ_λ. The corresponding equation is Lambert–Beer's law:

$$A = -\log_{10} \frac{I}{I_0} = \epsilon_\lambda \cdot c \cdot d \tag{5.4}$$

[1] Poster K1.05 at *20th International Conference on Solid State Ionics* **2015**, Keystone, USA.

However, to determine the concentration of the species that has to be analyzed, knowledge of the extinction coefficient is vital. It may be found in tables for common materials but for other materials, a reference solution with known concentration has to be analyzed first against the background measurement, I_0, to determine the extinction coefficient.

6

Experimental

6.1 Sample Preparation

6.1.1 Powder

Lanthanum tungstate, LaWO54, was prepared by the citrate complexation route, which is a modified Pechini[106] method. This method was applied by Yoshimura *et al.*[107] to synthesize yttrium tungstate. For lanthanum tungstate, the precursor yttrium nitrate hexahydrate has been replaced by lanthanum nitrate hexahydrate. Please compare Seeger *et al.*[15] and Escolástico *et al.*[108] for the citrate-complexation route of LaWO54.

Synthesis
The precursors ammonium tungstate (2.043 g, 0.6676 mmol) and lanthanum nitrate hexahydrate (18.709 g, 43.206 mmol) were weighed with a lanthanum/tungsten ratio of 5.4 (5.393), and two times of the precursor's chemical amount of citric acid monohydrate (18.219 g, 86.70 mmol) was added. In a 2 L beaker the precursors were partially solved in 200 mL of demineralized water and four times of the precursor's chemical amount of ethylene glycol (9.7 mL) was added. The mixture was stirred and heated to 150 °C for 3 h. After esterification of citric acid and ethylene glycol — forming the complexation agent — all precursors were solved and first a transparent gel, finally a colorless resin was formed by evaporating water and expelling nitrous fumes while heating to 300 °C. Organic compounds were removed in a furnace at 350 °C overnight. The now brownish black residue was pestled and the powder was calcinated in an alumina crucible at 900 °C. The now colorless powder was ball milled with 30 mL ethanol and zirconia balls with ∅5 mm. After drying, a pale yellow pow-

der of LaWO54 was yielded (8.192 g, 1.474 mmol, 92%). Phase purity was confirmed with XRD (see Fig. 6.1). Broad peaks in the XRD indicated small grain sizes, which were then roughly estimated by a powder scanning electron microscopy (SEM) micrograph. Grain sizes between 200 nm and 1 µm were observed. The chemicals used in this process are listed in Tab. 6.1. Details on the methods of diffractometry and electron microscopy will be presented in Section 6.1.3.

Table 6.1: Chemicals used for the synthesis of LaWO54 powder.

Name / Formula	Purity	CAS	Vendor
Ammonium tungstate $(NH_4)_{10}H_2(W_2O_7)_6$	99.99%	11140-77-5	Sigma Aldrich, USA
Lanthanum nitrate hexahydrate $La(NO_3)_3 \cdot 6H_2O$	99.99%	10277-43-7	ChemPur GmbH, DE
Citric acid monohydrate $HOC(COOH)(CH_2COOH)_2 \cdot H_2O$	99.7%	5949-29-1	VWR Int. BVBA, BE
Ethylene glycol $HOCH_2CH_2OH$	99.5%	107-21-1	Merck KGaA, DE

6.1.2 Pellets

Disc shaped pellets of LaWO54 were prepared as targets for pulsed laser deposition (PLD) film preparation, for electrical measurements that will not be reported in this thesis, and for FTIR measurements. All pellets were prepared with the powder yielded from the citrate-complexation route. All pellets were first pressed uniaxial with 30 kN and finally pressed isostatically with a pressure of 283 MPa. The greenlings were placed on a sintering bed in an alumina crucible and sintered using the temperature program depicted in Fig. 6.2 with a maximum temperature of 1550 °C. The pellets were polished subsequently using SiC abrasive papers with grit P180, P320, P800, P1200, P2500 and finished with diamond pastes of 1 micron and 1/4 micron on micro-cloth support. Surface roughness was measured with interference microscopy (details on the method see Section 6.1.3) with a root-mean-squared roughness of 246 nm over an area of 1.1 mm^2, grain sizes and density with SEM, and phase purity with XRD. A list of pellets used in this work is summarized in Tab. 6.2. From the SEM micrograph of pellet F004 shown in Fig. 6.3, a grain size of 8 µm to 40 µm can be observed after sintering but before polishing the sample. The grains show different gray scales which might be a hint to different phases. Hence, a back scattering image (see Fig. 6.4) was taken to identify differences in the composition. In the back scattering micrograph, all grains show the same gray scale, thus a homogeneous phase can be assumed. The samples show a density above 99% — no pores are visible in the SEM micrograph in Fig. 6.3.

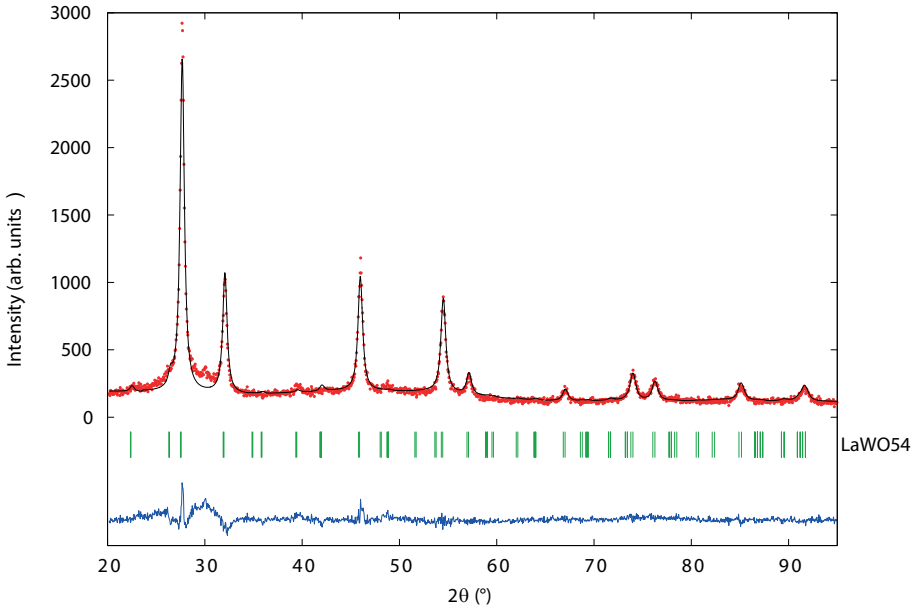

Figure 6.1: Rietveld refinement of X-ray diffraction data of powder synthesized via the citrate complexation route. Refined parameters: Scale $S = 0.877 \times 10^{-5}$; zero correction: -0.16; lattice parameter $a = 11.166$ Å; full width half maximum parameters $U = 0.1579$ and $W = 0.2568$ The mixing parameter was set to 1 (Lorentzian function only). The atomic positions of the second lanthanum and tungsten site and of the oxygen sites differ slightly from the parameters shown in Tab. 2.1: La2/W2: 0 0.2330 0.2330; O1: 0.05243 0.05243 0.05243; O2: 0.37812 0.37812 0.37812. The Bragg R-factor is $R_B = 15\%$.

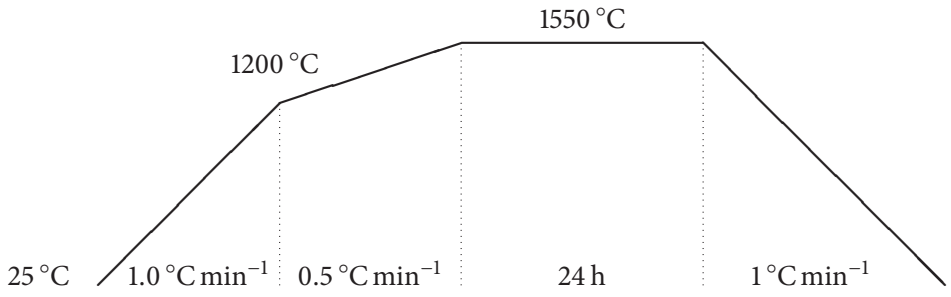

Figure 6.2: Temperature profile of the sintering program used for the pellets listed in Tab. 6.2.

6.1.3 Bar Samples

The bar samples used for ECR measurements in this work were prepared by J. Seeger and W.A. Meulenberg from IEK-1, FZ Jülich GmbH with a geometry of approximately $(4 \times 4 \times 33)$ mm^3. In contrast to the other samples, the LaWO54 powder used for these samples was prepared by solid state synthesis from the oxides.[15] The bar shaped samples were sintered at 1500 °C at IEK-1. The samples F001, F002 and JS001[109] were taken from the same batch and can be assumed identical

Table 6.2: A list of pellets used in this work with diameter and thickness.

ID	Diameter	Thickness	Purpose
F003	8 mm	—	first FTIR measurements (broken)
F004	8 mm	0.601 mm	first FTIR measurements
F006	15 mm	0.873 mm	PLD target
F010	15 mm	1.237 mm	PLD target

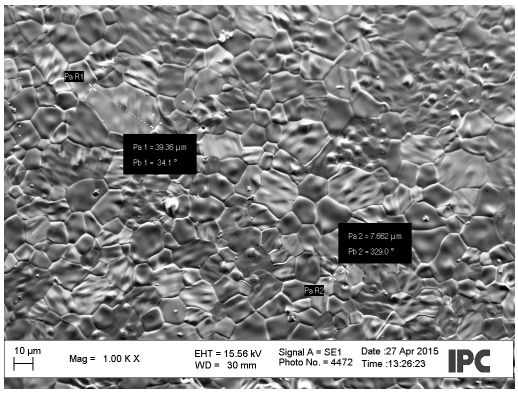

Figure 6.3: SEM micrograph of sample F004 with secondary electron detector. Lengths of a small and a large grain were determined to estimate grain sizes.

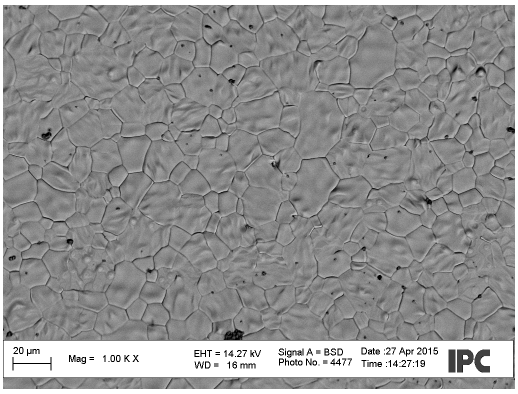

Figure 6.4: SEM micrograph of sample F004 with quadrupole backscattering detector: all grains show the same composition.

in composition, phase purity, and density. Before use, the samples were polished by SiC abrasive papers with grit P180, P320, P800, P1200, P2500 and finished with diamond pastes of 1 micron and 1/4 micron on micro-cloth support. The root-mean-squared surface roughness of sample F002 was determined by interference microscopy to be 60 nm over an area of 1.1 mm^2, phase purity with XRD, and density and homogeneity with SEM.

Samples and Dimensions

The dimensions of the samples were determined after polishing. To be consistent with the diffusion model (symmetrical flux at center), the thicknesses of the sample are 2*a* and 2*b* and the length is 2*c*. The samples have shown a few depositions of silica on the surface, originating from the quartz glass reactor tube at elevated temperatures. Hence, the samples were removed from the reactor tube after approximately three months and polished again (in the same way as fresh samples except for grit P180 and P320) before they were used for the next measurements. Samples F001, F005, F011 and F012 are an identical sample as well as F001 and F001b, i.e. a new identifier was assigned after polishing a used sample. The bar sample F009 has been prepared by powder yielded from the citrate-complexation route described above and has been sintered like the disc-shaped samples.

After sintering, a twist in z-direction occurred and the sample was rather thin. Therefore, instead of using own samples, it was chosen to fall back to the samples prepared by Seeger and Meulenberg from IEK-1, which show high density, mechanical stability, and a well defined cuboid geometry. A list of all bar samples is shown in Tab. 6.3. The methods used to determine phase purity, surface roughness, and creating SEM micrographs are described in the following paragraphs, exemplary for either sample F001 or sample F002.

Table 6.3: Bar samples used in this work with dimensions $2a$, $2b$ and $2c$. The distance between the inner contacts for the four-point DC conductivity measurement (see Section 6.2.2) is denoted as d. *Deviation might occur due to a slightly bend sample and its placement on the micrometer test stand or due to adhesion of contact pastes at the ends of the sample. The sample is, of course, not thicker than sample F011.

ID	Sample dimensions			Contact distance
	$2a$	$2b$	$2c$	d
F001	3.784 mm	4.142 mm	33.1 mm	17.7 mm
F001b	3.767 mm	4.128 mm	33.1 mm	13.1 mm
F002	3.688 mm	4.130 mm	33.2 mm	13.0 mm
F005	3.701 mm	4.082 mm	33.1 mm	13.0 mm
F009	1.452 mm	4.298 mm	36 mm	—
F011	3.661 mm	4.019 mm	33.1 mm	14.0 mm
F012	*3.695 mm	3.995 mm	33.1 mm	12.9 mm

X-Ray Diffraction

Phase purity was determined by X-ray diffractometry. The diffractometer is a STOE Theta-Theta, STOE & Cie GmbH, Darmstadt, Germany, controlled by software 'WinXPOW 2.1.2'. It is used in a reflexion geometry ω:2θ. The X-ray source is a copper anode with $\lambda(\mathrm{Cu-K}\alpha_1) = 1.540\,590$ Å and $\lambda(\mathrm{Cu-K}\alpha_2) = 1.544\,310$ Å radiation. $\mathrm{Cu-K}\beta$ radiation was removed by a secondary monochromator. The detector is a scintillation counter. Details on X-ray diffractometry can be found elsewhere.[110] The software 'FullProf Suite' was used for determining lattice parameters and structural information by Rietveld refinement. The Rietveld method is used for pattern matching of XRD diffractograms requiring phase information as input parameters. The fitted parameters are listed in the tables corresponding to the diffractograms. Details on the Rietveld method are described in the book of Young[111]. The structural information used for fitting the experimental data is taken from the thesis of Scherb[12] and has already been presented in Tab. 2.1. In this reference, the sof has been mentioned. From the multiplicity of the Wyckoff site, the resulting occupancy can be

calculated with the sof according to

$$\text{occupancy} = \frac{\text{multiplicity}}{\max(\text{multiplicity})} \cdot \text{sof} \tag{6.1}$$

As a peak-shape function, which is required for Rietveld refinement, a 'Pseudo-Voigt' function has been chosen. It is a convolution of Gaussian and Lorentzian distribution functions. The fit has been performed with the 'Maximum Likelihood' weighting model, which is beneficent for the determination of lattice parameters.[112] The following parameters have been fitted to the experimental diffractogram with a subtracted background by subsequently enabling variation in FullProf[113]:

- Scale factor:
  The intensity of a diffractogram is in arbitrary units, thus the entire profile must be scaled so that the calculated and observed intensities match. The scale factor S is independent of the angle and is introduced to the entire diffractogram, $I_{calc} = S \cdot I_{obs}$.

- Zero-point correction (Instrumental):
  The sample, the detector and the X-ray source usually show a small misalignment in the instrumental setup. From the distances of the reflexes, the zero-point, $\theta = 0°$, can be extrapolated and thus corrected.

- Lattice parameter a:
  The lattice parameter, a, of a cubic phase, is equal to the parameters b and c and thus only one lattice parameter is fitted with the constraint $a = b = c$. The angles have not been fitted and assumed as $\alpha = \beta = \gamma = 90°$.

- Peak-shape-function full width half maximum parameters W and U:
  The squared full width at half maximum, H^2, is defined by the parameters U, V and W for a constant wavelength

  $$H^2 = U \tan^2\theta + V \tan\theta + W \tag{6.2}$$

  The full width half maximum parameter V has not been fitted ($V = 0.002$). The limits are $0 \leq U \leq 1$, $0 \leq V \leq 1$ and $0 \leq W \leq 1$. These parameters, however, only influence the full width half maximum of the Gaussian functions. For the Lorentzian function, the parameter X must be fitted. However, fitting X was not possible here because one of the Gaussian FWHM parameters became negative.

- The mixing parameter η_0:
  This parameter describes the fraction of Gaussian and Lorentzian functions, which are used for the peak-shape-function. The limits of η_0 are $0 < \eta_0 < 1$. If the mixing parameter is near zero, the peak shapes are of Gaussian type and the use of Pseudo Voigt is not necessary. However, the refined profiles show a large contribution of Lorentzian functions to the peak shape.

- Atomic positions x, y, z:
  For each atom on a Wyckoff site, the coordinate can be refined. The resulting coordinates differ slightly from the structural parameters from Tab. 2.1.

The quality of fit is expressed by the Bragg R-factor, R_B, defined as

$$R_B = \frac{\sum_i |I_{obs} - I_{calc}|}{\sum_i |I_{obs}|} \tag{6.3}$$

For a good fit, R-factors lower than 20% or even lower than 10% are possible. After fitting, a diagram with the experimental data (red dots), the fitted profile (black line), the Bragg positions for the corresponding phase (green lines) and the residual (blue line) is obtained (see Figs. 6.1 and 6.5).

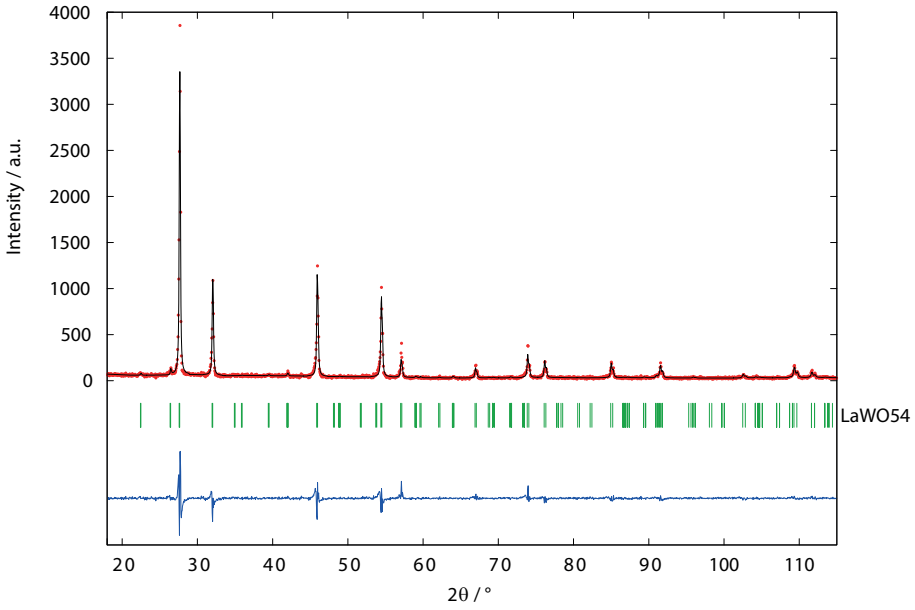

Figure 6.5: Rietveld refinement of X-ray diffraction data of the bar sample F002. Refined parameters: Scale $S = 0.387 \times 10^{-5}$; zero correction: -0.067; lattice parameter $a = 11.170$ Å; full width half maximum parameters $U = 0.0265$ and $W = 0.0228$; mixing parameter $\eta_0 = 0.823$. The atomic positions of the second lanthanum and tungsten site and of the oxygen sites differ slightly from the parameters shown in Tab. 2.1: La2/W2: 0 0.2347 0.2347; O1: 0.08677 0.08677 0.08677; O2: 0.37001 0.37001 0.37001. The Bragg R-factor is $R_B = 8.8\%$.

The lattice parameter obtained by Rietveld refinement of the bar sample F002 is $a = 11.170$ Å and corresponds to a lanthanum/tungsten ratio between 5.2 and 5.3 according to Fig. 2.1.[3] However, a second tungsten rich phase could not be observed so that the material is still in the single phase region.

Interference Microscopy

The surface roughness of bar samples and pellets after polishing has been analyzed with an interference microscope (WYKO NT1100, Veeco Instruments Inc.,USA with 10× lens and 0.5× ocular and software WYKO Vision 32). It was used in the 'PSI' mode, the *phase shift interference* mode, based on different path lengths of the light reflected at the sample's surface and at a reference mirror of the Mirau interferometer. After a measurement, the data was corrected for a curvature and tilt shift. The surface roughness is detected over an area of 1.1 mm^2. A typical two-dimensional heat-map of the surface roughness and a histogram are depicted in Figs. 6.6 and 6.7, respectively. The root-mean-squared roughness is calculated from the height Z_{jk} of each pixel of the rastered interference image with $(M \times N)$ pixels according to

$$R_q = \sqrt{\frac{1}{MN} \sum_{j=1}^{M} \sum_{k=1}^{N} Z_{jk}^2} \tag{6.4}$$

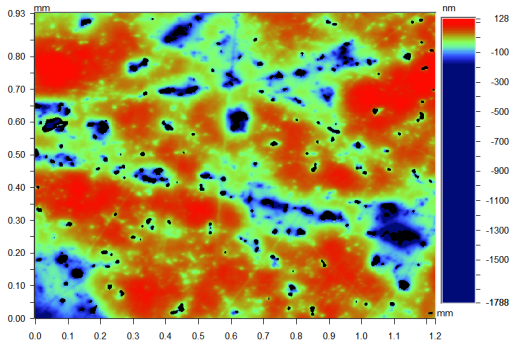

Figure 6.6: Interference microscopy in PSI mode: two-dimensional heat map of the surface roughness.

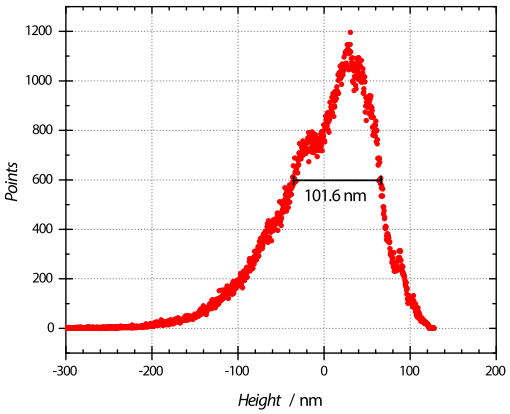

Figure 6.7: Histogram of the interference microscope image of sample F002. The full width half maximum is 101.6 nm and the root-mean-squared roughness is 59.67 nm.

Scanning Electron Microscopy

SEM was used to get an impression of density and grain sizes of the samples. It was also used to confirm the lanthanum/tungsten ratio. However, the exact composition cannot accurately be determined by electron microscopy for these samples. The SEM machine is a Leo 1450VP, LEO Electron Microscopy Inc., UK (now Carl Zeiss AG, Germany) with secondary electron and quaternary back-scattering detectors and software SmartSEM 05.03.04. The energy dispersive X-ray spectroscopy (EDX) system is an Oxford x-act 51-ADD0005 detector, Oxford Instruments plc, UK, with software INCA Suite 5.05 fitted into the Leo 1450 VP machine. SEM micrographs of the polished bar sample F001 are shown in Figs. 6.8 and 6.9. It can be seen that the porosity is a little bit

higher than that of the pellets but the samples are still very dense. An EDX analysis of this sample shows a La/W ratio of 5.2 but the error might be very large as the oxygen content is rather large. Thermal etching of the bar samples followed by secondary electron micrographs showed that the grain size is between 9 µm and 24 µm.

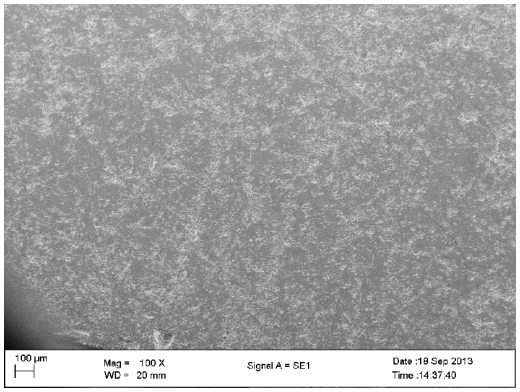

Figure 6.8: Secondary electron microcraph of bar sample F001 with magnification 100×.

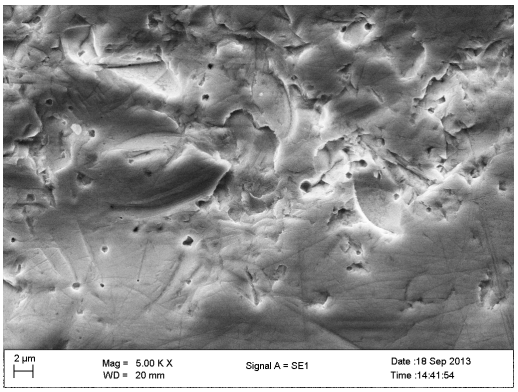

Figure 6.9: Secondary electron microcraph of bar sample F001 with magnification 5000×.

6.1.4 Thin Films

For FTIR measurements, thin films of LaWO54 were deposited on quartz glass substrates (HOQ310, ∅15 mm × 1 mm) using PLD (PLD workstation, SURFACE systems + technology GmbH & Co. KG, Germany). The recipe was taken from Reference [114] and the samples were prepared by A. von der Heiden. The substrate was heated to 600 °C. The distance between target and substrate was 45 mm. The energy of the KrF excimer laser was 250 mJ. The fifth PLD film was used for FTIR measurements and 150.000 shots were fired by the laser with 10 Hz. After evacuating a pO_2 of 50 mtorr was applied. The thickness of the film was determined by a Profilometer (Dektak 150, Veeco Instruments Inc., USA) to approx. 3 µm to 5 µm.

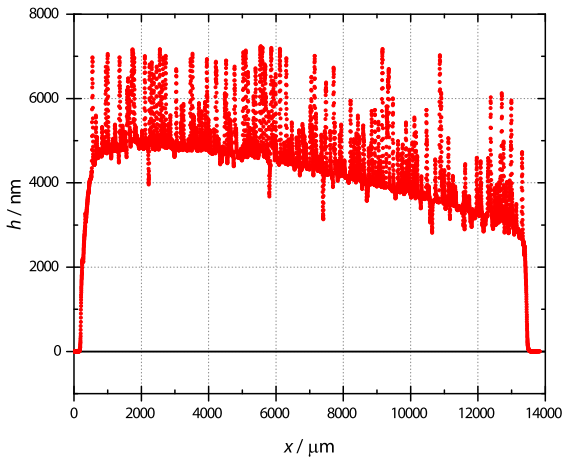

Figure 6.10: Height profile of thin film PLD5.

6.2 Experimental Setup ECR

The experimental setup was initially constructed and used by D. Müller and Y. Gensterblum for ECR experiments with oxygen. As a part of this work, the experimental setup has been extended to additionally provide two distinctive partial pressures of water vapor, and the software controlling all parts of the plant has been rewritten from scratch using C#. The setup is schematically shown in Fig. 6.11. At the inlet side of the reactor, two gas streams are mixed: first, a mixture of oxygen and nitrogen (both 5.0 purity, Westfalen AG, Germany) is prepared using different mass flow controllers (MFCs) (MKS Instruments, Germany). Each stream uses four MFCs with a maximum flow rate of 1000, 100, 10, and 1 mL min^{-1} (calibrated for nitrogen at 0 °C and 1.013 25 bar). The MFC with maximum 1000 mL min^{-1} is always connected to the nitrogen line and the MFC with 1 mL min^{-1} is always connected to the oxygen line. The two inner MFCs can be attached to either the oxygen or the nitrogen line via three way needle valves (Swagelok Company, USA with HL geometry). Possible maximum ratios of nitrogen/oxygen are: 1110/1, 1100/11, 1000/111. The analog MFCs are attached to a digital-analog converter and can be controlled in 256 steps from zero to maximum flux. Behind the MFC unit the plant is open and thus a total pressure of approximately 1 bar is present in the remaining setup. Each of the two streams of nitrogen and oxygen is now directed into a water vapor saturator (see Section 6.2.1). The gas stream is saturated with a higher pH_2O than intended and then directed into a second saturator, where the final pH_2O is adjusted. The pH_2O can directly be controlled by the temperature of the saturators whereas the flux of oxygen for the pO_2 must be calculated by

$$\dot{V}_{O_2} = \frac{pO_2}{1\,\text{bar} - pH_2O} \cdot \dot{V}_{N_2+O_2} \tag{6.5}$$

Here, $\dot{V}_{N_2+O_2}$ is the total flux controlled at the MFC unit. The resulting total flux of the gas stream behind the saturator assuming room temperature is

$$\dot{V}_{tot} = \dot{V}_{N_2+O_2}\left(1 + \frac{pH_2O}{p^{\ominus}}\right) \tag{6.6}$$

The two gas streams with a defined pO_2 and pH_2O are now directed into a four way valve (VICI A 90, Valco Instruments Co. Inc., USA with magnetic valve 5420, Bürkert Fluid Control Systems, Germany), which allows a very short switching time of less than one second. One of the gas streams is discarded while the other enters the quartz glass reactor tube, which is placed in a tube furnace. The gas lines are heated to avoid condensation of water before the gas enters the furnace. The furnace (constructed at RWTH IPC) is controlled by a direct current power source (PS8160-04T, Elektro Automatik GmbH & Co. KG) and a temperature control (CN7800, Omega Engineering Inc., USA). The quartz glass tube has a diameter of 3 mm at the inlet and within the furnace it has a diameter of 15 mm. The sample is placed behind the diminution of the quartz glass tube. Hereby, the gas stream is quickly reaching the sample's surrounding after a switch of the four way valve to

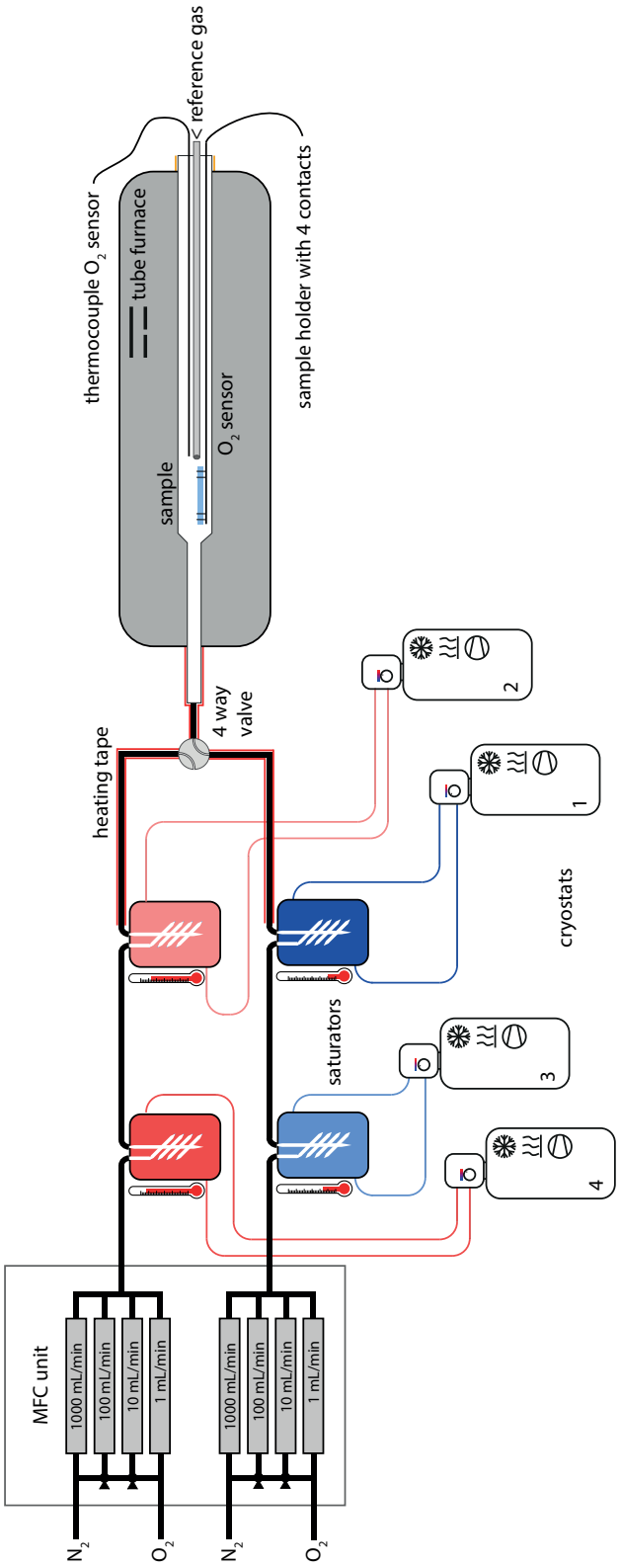

Figure 6.11: Construction scheme of the experimental setup of the entire ECR plant.

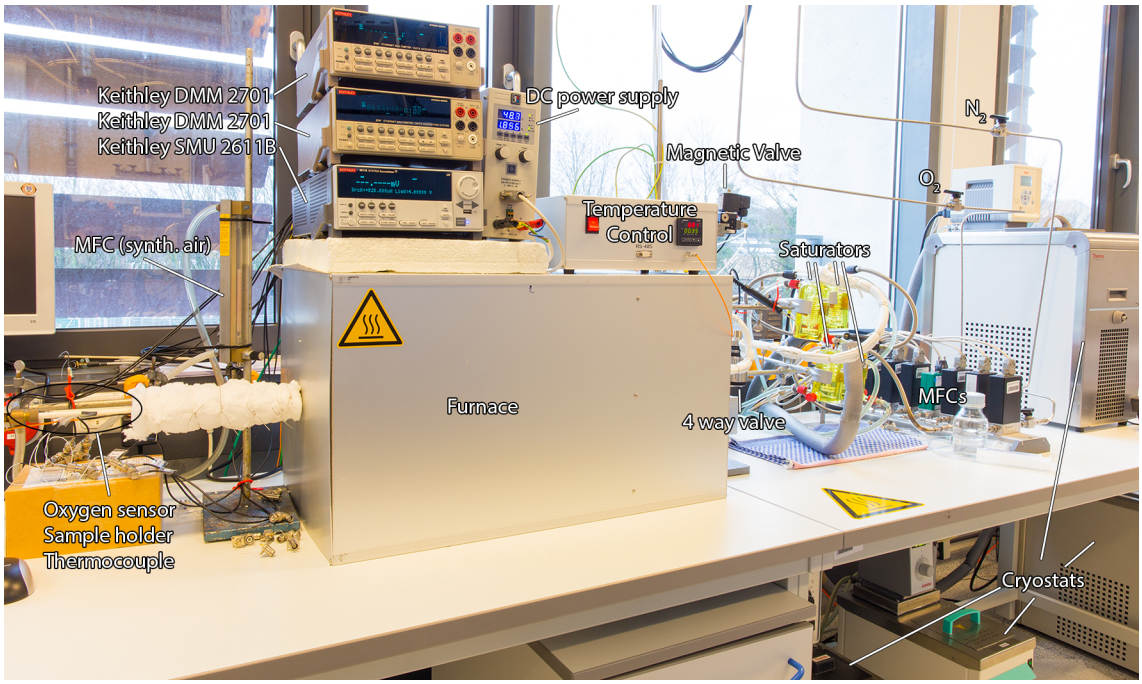

Figure 6.12: Photography of the experimental setup for ECR measurements at RWTH Aachen University, Institute of Physical Chemistry, High Temperature Laboratory 2400|131.

minimize axial dispersion. The sample is placed on an alumina sample holder with four electrodes for the four point DC conductivity measurement. The platinum (outer electrodes for the constant current source) and gold (inner electrodes for the measurement of the voltage) wires are contacted with gold paste (KQ500, Heraeus Holding GmbH, Germany). The use of gold wires and paste for the inner contacts is necessary to avoid catalytic behavior of platinum for the water splitting reaction. See Section 6.2.2 for details on the four point DC conductivity measurement. Right behind the sample, a potentiometric oxygen sensor is placed, measuring the pO_2 of the gas stream. A type S thermocouple probes the temperature at the oxygen sensor. Details on the potentiometric oxygen sensor see Section 6.2.3. The outlet of the reactor tube directs the exhaust gas into the laboratory. It is isolated with alumina wool to avoid condensation of water. Although the water content of the gas stream at this side is irrelevant for the sample, a condensation leads to a conductivity of the sample holder: a water film on alumina enables conduction, making the determination of the sample's conductivity impossible.

6.2.1 Water Vapor Saturator

The stream of nitrogen and oxygen is directed into the saturator (see Fig. 6.13, produced individually by Aachener Quarz-Glas Technologie Heinrich, Germany) and tempered at a spiral tube to the water vapor saturator's temperature, which is adjusted by cryostats (2× SC150/A28, Thermo Fisher Scientific Inc., USA, for the main saturators and F12, JULABO GmbH, Germany and C10/K10, Thermo Fisher Scientific Inc., USA, for pre-saturation). By a frit filter, the gas is led into a reservoir of demineralized water and by the large surface of the frit filter, the gas is assumed to be saturated to 100% humidity. The gas forms small bubbles within the water reservoir and can further be saturated if the humidity has not yet reached 100%. The gas stream is then leaving the saturator into a heated gas line to avoid condensation of water if the saturator's temperature is above room temperature. The water reservoir is approximately 40 mL. It has not been checked if the humidity is actually 100%. However, the most important property is a constant pH_2O throughout the course of the experiment, which can be derived from a constant conductivity of the sample in equilibrium. The oxygen sensor's constant signal shows that there is no big difference in pH_2O during the experiment as oxygen would be displaced by water time-dependent and this would be monitored at the oxygen sensor. The water content can be controlled by the temperature of the saturator's cooling fluid. For example, a pH_2O of 30 mbar is achieved by setting the saturator's temperature to 24.09 °C and a pH_2O of 10 mbar by a temperature of 6.98 °C.

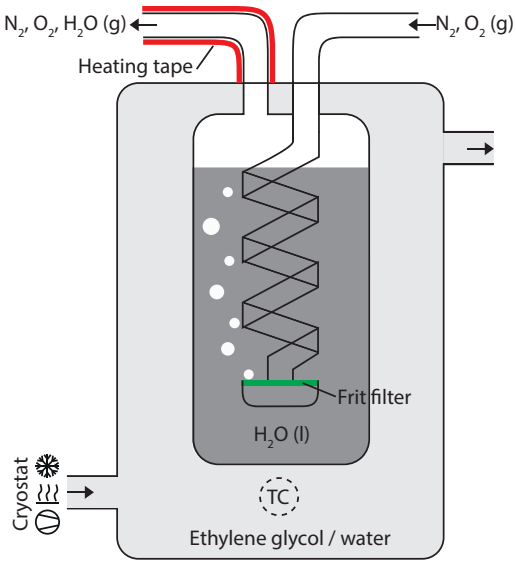

Figure 6.13: Sketch of the water vapor saturator. 'TC' is a thermocouple reading the temperature near the water reservoir. The coolant ethylene glycol/water is held at constant temperature by a cryostat.

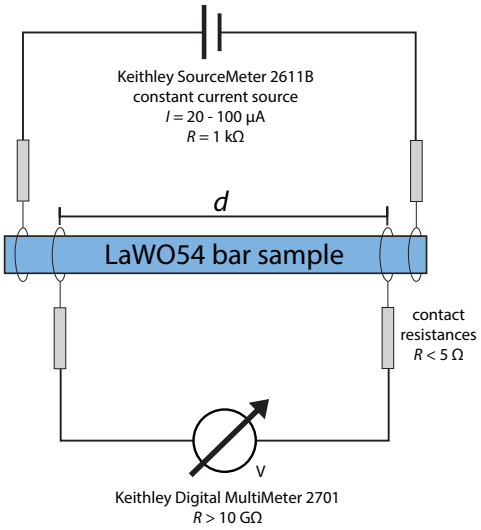

Figure 6.14: Four point DC conductivity measurement. The wires attached to the inner contacts are gold wires with 0.3 mm diameter and the wires for the outer contacts are platinum wires with the same diameter. Both are contacted with sintered gold paste.

6.2.2 Conductivity: Four Point DC Measurement

The four point DC conductivity measurement is one of the most common methods for accurately determining conductivities. In this method, four electrodes are attached to a sample in a row (see Fig. 6.14 for a schematical setup). The outer contacts are connected to a constant current source (SourceMeter 2611B, Keithley Instruments Inc., USA) with currents of I = 20 µA for low temperature measurements to I = 100 µA for high temperature measurements. The inner contacts are connected to a digital multimeter (DMM 2701, Keithley Instruments Inc., USA) measuring the voltage, which is applied between the inner contacts. The voltage is measured at zero current, thus the resistances of the contacts are neglected and only the resistance of the material is measured. This method can be used to determine the total conductivity (both, ionic and electronic) of homogeneous (bulk) materials. The distance d between the inner contacts is required as well as the cross-sectional area A over the entire length of the sample. With the constant current I and the measured voltage U between the inner contacts, d, and the area of the sample, $A = 2a \times 2b$, the conductivity of the sample can be calculated by

$$\sigma = \frac{Id}{UA} \tag{6.7}$$

6.2.3 Potentiometric Oxygen Sensor

The potentiometric oxygen sensor ($SIRO_2$ C700, Ceramic Oxide Fabricators Pty. Ltd., Australia) works like a lambda probe in automotives with catalytic converters: the voltage between a reference gas, here synthetic air (nitrogen with 20.5% oxygen, Westfalen AG, Germany), and the atmosphere, which has to be monitored, is measured. In between is an oxygen conductive electrolyte (e.g. YSZ), contacted by two platinum wires (see Fig. 6.15). It is an open cell voltage with a concentration cell for the redox pair $O_2(g) + 4e^- \rightleftharpoons 2O^{2-}$. The potential between the outer and inner electrode of the electrolyte is measured with a digital multimeter (Digital Multimeter 2701, Keithley Instruments Inc., USA) and the temperature is measured by a type S thermocouple next to the electrolyte. The pO_2 of the probe can be calculated from the voltage U by the Nernst equation for a concentration cell with four electrons

$$pO_{2,\,\mathrm{probe}} = pO_{2,\,\mathrm{ref}} \cdot e^{-\frac{4UF}{RT}} \tag{6.8}$$

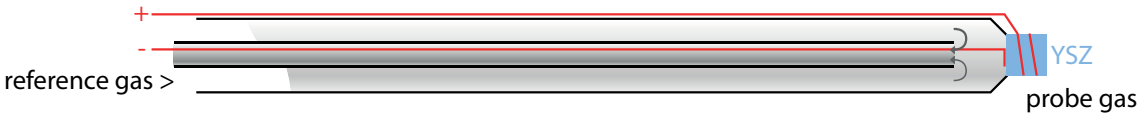

Figure 6.15: Potentiometric oxygen sensor: two electrodes (red) at an electrolyte material (e.g. YSZ, blue) measure the potential between the probe gas and the reference gas, directed through the inner part of the sensor.

6.2.4 Four Way Valve

The four way valve directs one of the two gas streams into the reactor tube while discarding the other stream. It can be switched by the magnetic valve and pressured air within less than a second so that the second stream is directed into the sample while the first is discarded. During the switching process, the flow rate drops shortly to zero and sometimes one or two data points of the voltage measurements of the oxygen sensor and/or the sample are outliers. The switching process takes less than one second and the empty reactor requires less than 5 seconds to flush. The flushing of this reactor has been analyzed in a previous publication.[43] A flush time correction[91] has not been introduced because of the fast flushing of the reactor. The flushing with water vapor should be approximately equal, although this has not been tested. The signal of the oxygen sensor upon hydrating steps will be shown in Section 7.1.1.

6.2.5 Furnace

The furnace was constructed by the electronic and mechanical workshops of RWTH IPC. An electric coil around an alumina tube is powered by a DC power supply unit (PS8160-04T, Elektro Automatik GmbH & Co. KG, Germany) with limits of 120 V and 4 A, controlled by a temperature control unit with a DC module (CN7800, Omega Engineering Inc., USA). The alumina tube and electric coil reside in a case with thermal isolation and an aluminium box. A type S thermocouple within the coil is connected to the temperature control unit.

For previous measurements with perovskite type MIECs like $Ba_{0.5}Sr_{0.5}Co_{0.8}Fe_{0.2}O_{3-\delta}$ or similar, which show high electric conductivities, the constant current was set to approximately 10 mA and the use of a common temperature control unit with a pulsed AC signal (230 V) was possible. However, first measurements with lanthanum tungstate, which shows a rather low electric conductivity, a constant current of 20 µA is used for temperatures of up to 800 °C. The measurements revealed periodic signals in the voltages of the oxygen sensor and of the sample between the inner contacts. These two signals are shown in Figs. 6.16 and 6.17: with an interval of 41.5 min a peak-shaped drop in the voltages of the sensor and the sample is observed. Also the temperature signal shows a small oscillation. The second periodic signal is a smaller oscillation on a shorter time scale (150 s). The second oscillation is only observed in the voltages of the sample and the oxygen sensor. The measured temperature is constant. The reason for these two periodic signals is unknown, however, the source could be identified: after replacing the temperature control unit by a temperature control unit with DC module and a DC power supply, the signals vanish, but the noise of the signals prevails. A possible explanation is that the pulsing of a strong current/voltage causes induction of a small current at the sample. This effect is not negligible for lanthanum tungstate samples as the constant current is very low compared to previous measurements (20 µA vs. 10 mA). The voltage is measured every two seconds (with an offset of tens of milliseconds between the measurement of the sample's and the oxygen sensor's voltages) and the interval between two pulses of the furnace is approximately one second. The interval of the shorter periodic signal is much larger, thus maybe it is an interference between the voltage measurement and the pulse. For a couple of seconds — during the periodic signal — the voltage is measured during the pulse while for the interval between two periodic signals the voltage is measured between two pulses of the furnace.

6.2.6 Measurement Software

The measurement software was created from scratch for the extended experimental setup. The software was written with MicroSoft Visual Studio 2010 (C#/WPF) using libraries of the suppliers Keithley and ADDI-DATA and the library OxyPlot for the diagram. It controls the main parts of the experimental setup, including the Digital Multimeter and the SourceMeter, the four way valve, the MFCs and the main cryostats 1 & 2. The furnace control and the readback of the thermocouples at the water reservoir of the water vapor saturators are not yet implemented. Details on the

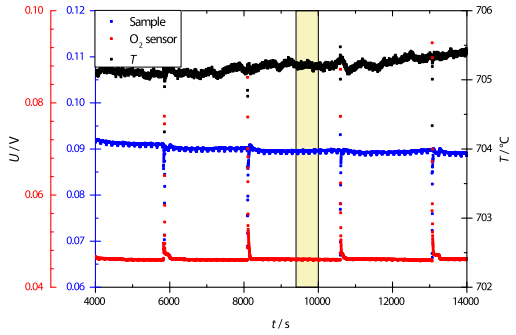

Figure 6.16: Two periodic signals at sample and oxygen sensor with pulsed AC furnace. The yellow part is zoomed in Fig. 6.17. Sample: F001; pO_2 = 30 mbar; pH_2O = 30 mbar; I = 20 µA.

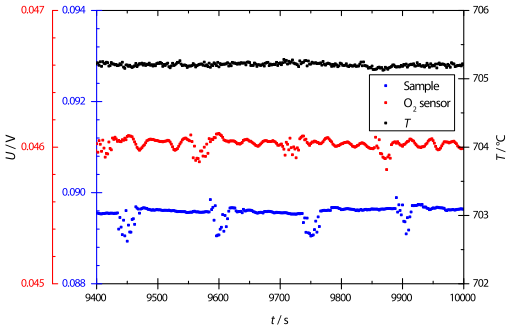

Figure 6.17: Magnification of the yellow area in Fig. 6.16.

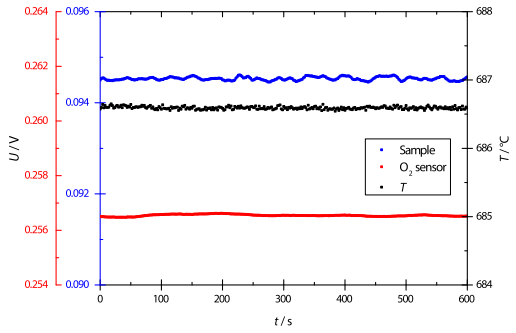

Figure 6.18: DC power supply with approximately equal conditions like in Fig. 6.17. The scale of all axes is equal to the AC case, except a factor of 5 for the sample's voltage as the constant current in this case is 100 µA.

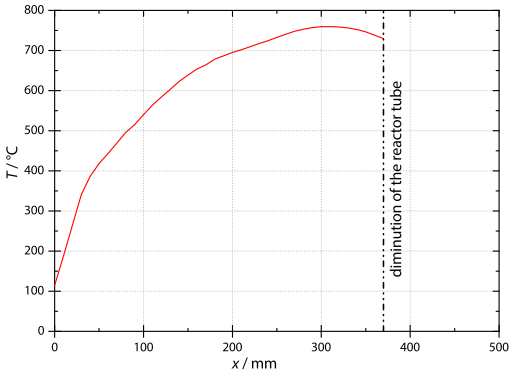

Figure 6.19: Temperature profile of the furnace at a set temperature of 750 °C. The length of the furnace is 500 mm and the diminution of the reactor tube is located at x = 370 mm. The sample is placed at x = 300 mm.

programming of the devices and screenshots of the software are presented in Appendix B.

The data-acquisition is performed mainly by the two digital multimeters. The first digital multimeter reads four channels consecutively: i) the voltage of the inner contacts of the sample ii) the voltage of the oxygen sensor iii) the temperature in °C iv) 'Channel 111' currently not in use (in previous experiments, two pairs of inner contacts existed). The switching of the channels is achieved by relays and it takes a couple of milliseconds to switch the channels, to perform the reading (typically 1 or 10 power line cycles at 50 Hz) and to send the data to the computer. An interval of 2000 ms is the lowest to read these channels. In order to perform faster readings, a second multimeter is connected with only one channel to the inner contacts of the sample and thus readings of approximately 200 ms are possible. However, if both multimeters are connected to the same electrode, the faster multimeter 'sees' the state of the relay at high or low. After screening the sample's conductivity relaxation curves, important measurements were performed with only the second multimeter and a disconnected first multimeter at the inner contacts.
The data files created by the software are explained in Appendix B.

6.3 FTIR Setup

The IR spectroscopy was performed with a standard FTIR machine (IRpresitge-21, Shimadzu Corporation, Japan). For relaxation experiments, the construction of a heatable reactor with variable gas atmospheres was necessary to fit into the sample chamber. One of the main issues is the isolation of the reactor, which must fit into the sample chamber and keep the outer temperature as low as possible because of plastic parts in the FTIR machine. The reactor and the case containing the reactor and isolation is depicted in Fig 6.21. It is a construction scheme of Guido Kirf, who created the reactor and isolation. It consists, in principle, of a steel block that is heated by six cartridge heaters (Maxiwatt 250 W, 40 mm × ∅4 mm, Resistencias Industriales Maxiwatt S.L., Spain). A hole for the IR and laser beam is isolated with NIR transparent quartz glass (HOQ310, Heraeus Holding GmbH, Germany; transmission of approx. 90% for $\tilde{\nu} > 2000\,\mathrm{cm}^{-1}$) and in the center of the block, a pellet or a thin film on a substrate with a diameter of 15 mm can be placed. A thermocouple measures the temperature next to the sample. A gas stream is directed from the four way valve (fourth gas line of the ECR setup) into this reactor and leaves it over an exhaust line. The reactor can be heated up to 550 °C while the temperature of the case does not exceed 60 °C. The experimental setup for IR relaxation experiments is shown in Fig. 6.20.
The FTIR machine can be operated in a standard MIR setup (typically $400\,\mathrm{cm}^{-1} < \tilde{\nu} < 4000\,\mathrm{cm}^{-1}$), using a ceramic lamp, a KBr beam splitter and a standard detector. An alternative setup enables measurements in the NIR regime (approx. $3800\,\mathrm{cm}^{-1} < \tilde{\nu} < 12\,500\,\mathrm{cm}^{-1}$). The IR source is a tungsten lamp, using a CaF_2 beam splitter, and an InGaAs detector (option1 in the software).

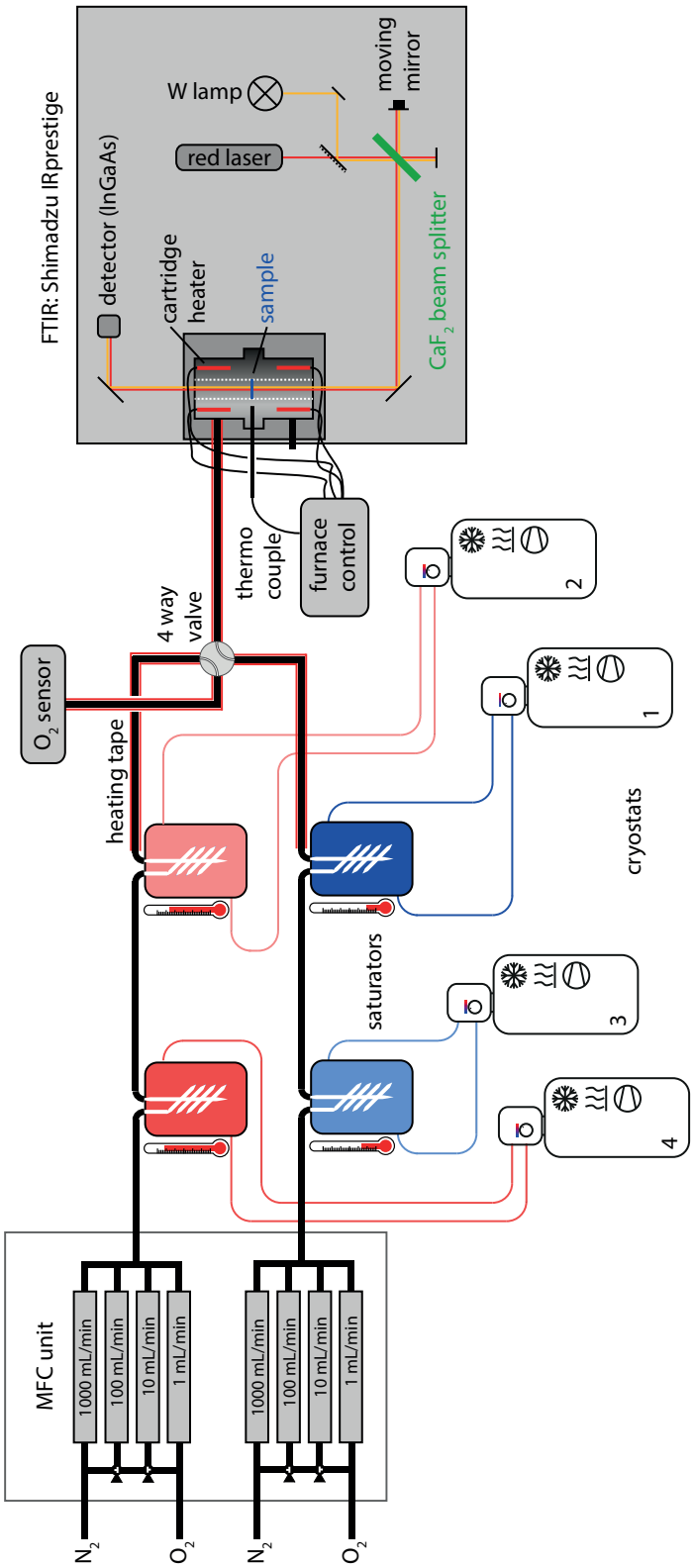

Figure 6.20: Construction scheme of the experimental setup of the FTIR plant. The part left of the four way valve is the same for both plants, the ECR and the FTIR plant, while the oxygen sensor is the oxygen sensor in the ECR reactor tube.

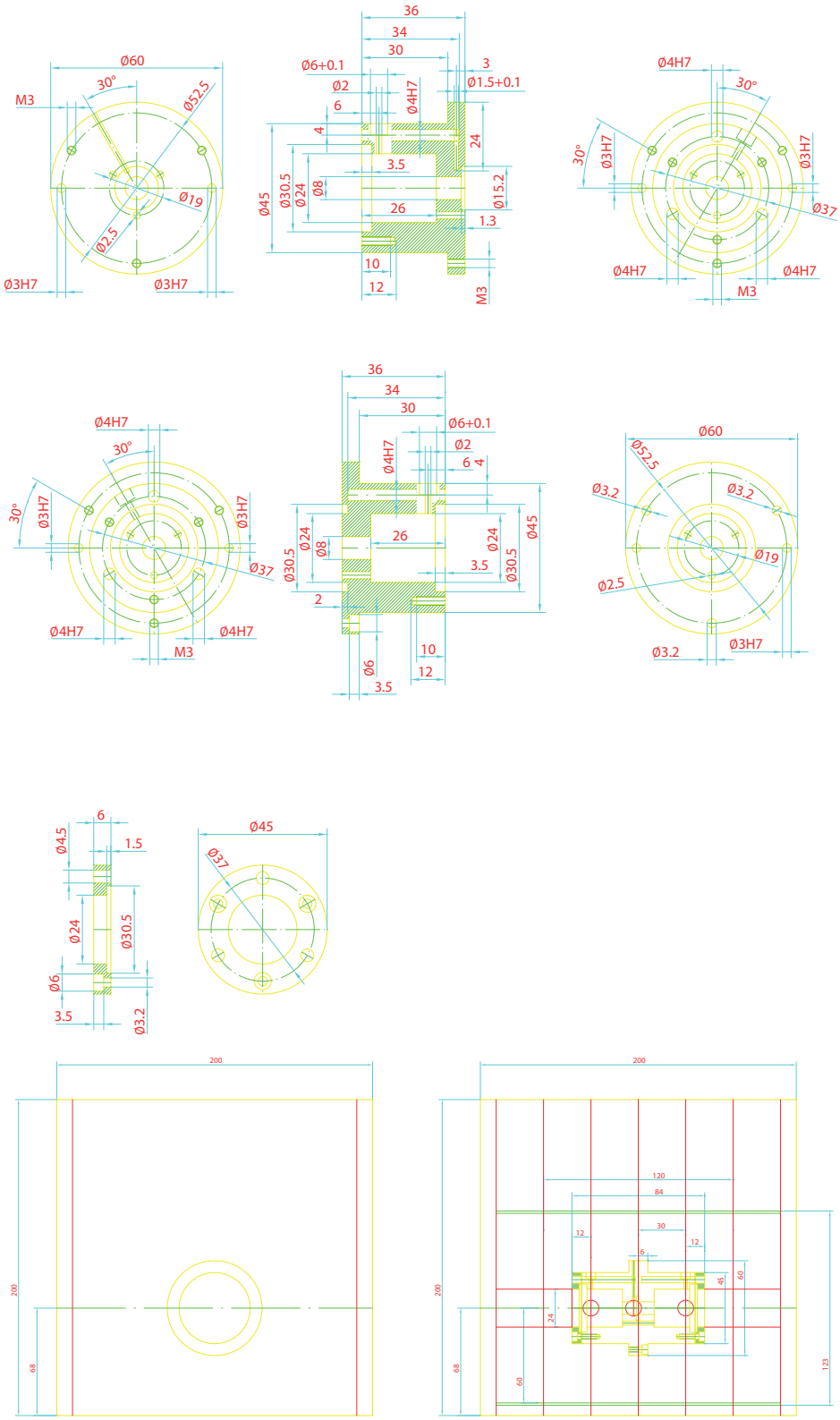

Figure 6.21: Construction scheme of the reactor for the FTIR furnace. Bottom panel: the isolation of the reactor. This graphic was created by G. Kirf (mechanical workshop).

6.4 Software

The following software was used for calculations, which are not related to specific instruments. All calculations were performed under MicroSoft Windows 8.1 x64 and MicroSoft Windows 10 x64 using Intel processors i7-4770K, i5-2400 and i5-3317U.

- OriginLab OriginPro 2015 and 2016, x64, for calculating conductivities and fitting activation energies.
- MathWorks MatLAB 2014a, 2014b, 2015a, 2015b and 2016a, each x64, for fitting experimental data to diffusion model and modeling concentration profiles, ECR curves.

7

Electrical Conductivity Relaxation Experiments

In this chapter, the results of the ECR experiments of lanthanum tungstate will be presented. In the first section, general considerations on relaxation experiments upon hydration are described, the fitting procedure and the limits of the method. In the second part, the transport parameters were determined in dependency of the temperature and the partial pressures of oxygen and water vapor for hydrating steps. An interesting effect requires the derivation of the power factors. The oxidation behavior of lanthanum tungstate in dependency of the partial pressure of water will be discussed finally.

7.1 General Relaxation Behavior upon Hydration

The principle of ECR measurements has been described in Section 4.2 for oxidative and reductive steps. A first glimpse at hydration relaxation kinetics and recent publications on this topic have been given in Section 4.6. For hydration kinetics, the partial pressure of water has to be switched step-like at $t = 0$ to a higher partial pressure while the partial pressure of oxygen must be constant before and during the relaxation process.

$$\Delta p\mathrm{O_2} = 0 \qquad \text{and} \qquad \Delta p\mathrm{H_2O} > 0 \tag{7.1}$$

For the change in $p\mathrm{H_2O}$, the same step-size has been chosen for most experiments as suggested for oxidation kinetics ($\Delta p\mathrm{O_2}$) by Wang *et al.*[90], i.e. half an order of magnitude. The $p\mathrm{H_2O}$ can be adjusted by the water vapor saturators described in Section 6.2.1. However, there are two methods to adjust the $p\mathrm{O_2}$ via the MFCs: the flux that has to be set at the MFCs can be calculated by Eq. (6.5) for both gas streams or it can be adjusted so that both streams show the same $p\mathrm{O_2}$ at the oxygen

sensor situated behind the sample. Both methods have systematic and/or experimental disadvantages. The first method has two issues: i) the MFCs' accuracy is not high enough to yield equal pO_2 in both streams just by setting the correct flow. The flow is precise with little noise but not very accurate if one assumes correct values yielded by the potentiometric oxygen sensor in dry N_2/O_2 mixtures. Even if one uses the same setting for both streams and the same technical parts to mix both streams, there is a step in pO_2 measured at the oxygen sensor. ii) As shown in Section 3.3, the final pO_2 depends on the pO_2 provided by the MFCs and the gas phase water equilibrium, Eq. (3.43). However, the second issue can be neglected in the temperature range where the ECR experiments are carried out, as shown in Fig. 3.6. The second method detects the actual gas composition near the sample as a probe for the pO_2. This method, however, has a different disadvantage: the gas stream is not only a mixture of inert nitrogen and oxygen that can be detected by the sensor, it also consists of water vapor, which might influence the potential at the probe side of the potentiometric oxygen sensor's electrolyte. This has been checked by directing nitrogen (5.0 purity) into the water vapor saturators with three different partial pressures of water (pH_2O = 10 mbar, 30 mbar and 100 mbar) monitoring the voltage of the oxygen sensor. The first observation is that with increasing pH_2O the noise of the oxygen sensor's signal increases. The pO_2 calculated from Eq. (6.8) decreases with increasing pH_2O. However, this change is negligible and might be caused by another effect: the water vapor added to the nitrogen displaces nitrogen as the total pressure is constant. The remaining oxygen ($\leq$ 0.001%) in the nitrogen stream is also displaced and the decrease in pO_2 might also be attributed to the displacement. The calculated pO_2 for the three pH_2Os are 1.85×10^{-5} bar, 1.71×10^{-5} bar and 1.70×10^{-5} bar. The difference is small compared to the huge difference in pH_2O between probe and reference ('dry') gas of the sensor.

Because of the low influence of pH_2O on the voltage of the potentiometric oxygen sensor, the second method has been chosen for ECR measurements. Before starting the automated switching processes of the four-way valve, both streams were set to the same pO_2 measured at the sensor.

7.1.1 A first Relaxation Experiment

The relaxation curve upon hydration of bar sample F002 is shown in Fig. 7.1. In this experiment, the following parameters were kept constant: the temperature was 950 °C, the pO_2 was 100 mbar, the current was 500 µA and the total flow rate was approximately 100 mL min^{-1} for both gas streams. At t = 0, the pH_2O was changed step-like from 10 mbar to 30 mbar (the water vapor saturators were cooled/heated to 6.98 °C and 24.09 °C, respectively).

The conductivity curve in Fig. 7.1 shows that the sample is in equilibrium with the gas phase before the switch ($t < 0$, pO_2 = 100 mbar, pH_2O = 10 mbar, T = 950 °C) as it is constant. After the switch ($t \geq 0$, pO_2 = 100 mbar, pH_2O = 30 mbar, T = 950 °C), the conductivity rapidly dropped to a minimum at 37 s and afterwards slowly increased to a constant value that is above the initial value. The temperature did not change during the switch and the oxygen sensor does not show any significant change in pO_2.

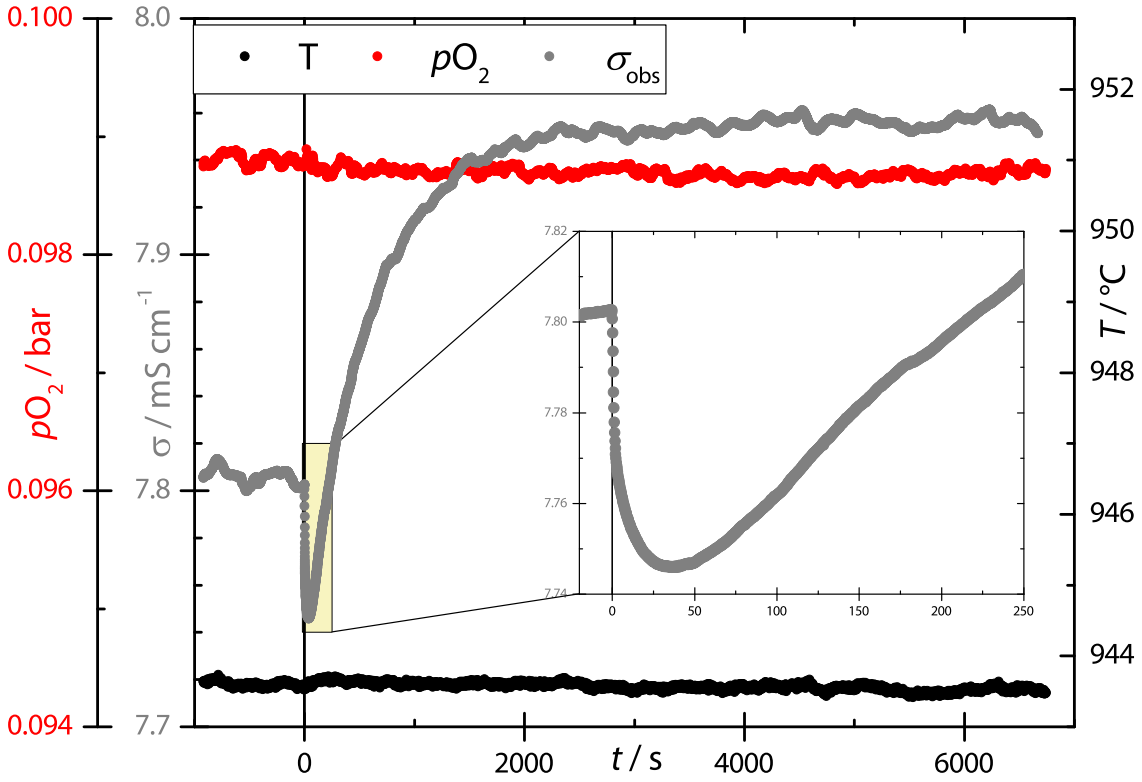

Figure 7.1: Relaxation curve of sample F002 after a hydrating step from pH_2O = 10 mbar to 30 mbar (gray symbols). $T \approx 950\,°C$; $pO_2 \approx 100$ mbar. The inset is a magnification of the start of the relaxation. pO_2 (red symbols) and temperature (black symbols) are almost constant before and after the switch.

The conductivity relaxation curve is similar to the curves described by Yoo and Lee[70, 102] for hydration kinetics. The shape of the curve can be described as *'two-fold non-monotonic'*. 'Two-fold' means that two different kinetics seem to be present — a fast kinetic responsible for the drop in conductivity and a slow kinetic for the increase — and that the resulting curve is a superposition of two single fold relaxation curves. 'Non-monotonic' means that the sign of the slope changes during the experiment — in this case from negative to positive.

The nominal reaction taking place is described in Eq. (3.10), recapitulating

$$H_2O(g) + O_O^{\times} + v_O^{\bullet\bullet} \rightleftharpoons 2OH_O^{\bullet} \qquad \text{with} \qquad K_{H_2O} = \frac{[O_O^{\times}][H_i^{\bullet}]^2}{pH_2O[v_O^{\bullet\bullet}]} \tag{7.2}$$

However, in order to understand the two-fold behavior, this reaction must be split into the two reactions, the hydrogen incorporation reaction, Eq. (3.6), and the oxygen incorporation reaction, Eq. (3.1). Both reactions show different kinetics, the first of which is assumed to be very fast and the second is slow. A first glimpse at the kinetics of the hydration reaction has been given in Section 3.1.4 and the occurrence of two different kinetics will further be discussed in Section 7.1.2.1. For now, the assumption that two reactions with two different kinetics take place must suffice.

The reaction governing the first part of the relaxation is the fast incorporation of hydrogen, Eq. (3.6), recapitulating

$$\frac{1}{2}H_2(g) + O_O^{\times} + h^{\bullet} \rightleftharpoons OH_O^{\bullet} \qquad \text{with} \qquad K_{H_2} = \frac{[H_i^{\bullet}]}{\sqrt{pH_2}[h^{\bullet}]} \tag{7.3}$$

Hydrogen is incorporated into the bulk phase forming a hydroxy-anion (or a proton interstitial) at the expense of an electron hole. The source of the hydrogen species is not known — either a H_2 or a H_2O molecule is adsorbed at the surface. The exact nature of the adsorbed species (charge, bonds) is also unknown. As the incorporation of the hydrogen species follows its own kinetic, Eq. (7.3) can formally be used to describe the equilibrium reaction. The mobility of protons is usually between the mobility of oxygen vacancies and of the electrons/-holes. As a consequence, the electrical conductivity decreases. When this reaction is almost complete (the driving force of this reaction gets lower when the equilibrium is almost reached and the slope of the single fold relaxation curve flattens) the second reaction — the incorporation of oxygen — mainly influences the resulting curve as it is much slower and still large driving forces exist. The oxygen incorporation equation, Eq. (3.1), is

$$\frac{1}{2}O_2(g) + v_O^{\bullet\bullet} \rightleftharpoons O_O^{\times} + 2h^{\bullet} \qquad \text{with} \qquad K_{O_2} = \frac{[O_O^{\times}][h^{\bullet}]^2}{\sqrt{pO_2}[v_O^{\bullet\bullet}]} \tag{7.4}$$

Oxygen is incorporated onto an oxygen vacancy and two highly mobile electron holes are created. As a consequence, the electrical conductivity increases. From the water incorporation equation, Eq. (7.2), the absolute change in electron hole concentration upon hydration should be zero as it is not mentioned in K_{H_2O}. However, the oxygen vacancy concentration decreases upon hydration and with Eq. (7.4), it is evident that the concentration of electron holes is also decreasing (pO_2 is constant and the change in $[O_O^{\times}]$ is negligible), $\Delta c_{h^{\bullet}} < 0$. This has also been discussed by Merkle *et al.* in a recent article simulating concentration profiles.[115] The decrease of the concentration of electron holes caused by the hydrogenation at the start of the relaxation is not entirely compensated by the increase of electron hole concentration upon oxidation in the second part of the relaxation. Hence, there must be another reason for the increase of the total conductivity in equilibrium, $\Delta\sigma > 0$. The mobility of protons in LaWO54 is rather high and their concentration is increasing during the entire relaxation process. The increase of the total conductivity instead of a decrease can only be explained by a large contribution of protonic conductivity to the total conductivity. The importance of protons for the electrical conductivity relaxation will be discussed soon.

For the conditions chosen in this experiment, two-fold non-monotonic relaxation behavior, which has up to now only been investigated for perovskite type oxides, could be observed for lanthanum tungstate. Solís *et al.* have not observed two-fold behavior for lanthanum tungstate — using lower temperatures and different atmospheres.[38]

7.1.2 Fitting the Relaxation Curve

Yoo and Lee[70] fitted a superposition of two relaxation curves to the total conductivity. They have used a diffusion model without surface reaction limitation (see Section 4.3 and Eq. (4.25)). Lim *et al.* replaced this equation with the diffusion model presented in Section 4.3 including a surface reaction limitation. The time-dependent conductivity can be expressed by Eq. (4.28), using the initial conductivity, P^0, as an offset and two different kinetics, $f_{\tilde{k}_i,\tilde{D}_i}(t)$, and their corresponding power factors, $P_i(c_i^0, c_i^\infty, u_i)$, for the single fold relaxation curve of each ionic species. Usually, single fold relaxation curves are fitted with a least square fit. However, in two-fold relaxation curves, the beginning of a relaxation process is very important for the determination of the fast kinetic's transport parameters. Therefore, the fit has been weighted so that especially the fit of the start of the relaxation shows good agreement with the experiment by minimizing

$$\text{Error} = \sum_r \frac{(\sigma_{\text{obs},r} - \sigma_{\text{calc},r})^2}{t_r + 1} \tag{7.5}$$

with the calculated and observed electrical conductivities, σ_{calc} and σ_{obs}. The last data point in the previous equilibrium is set to $t = 0$. The data points have equidistant time intervals. The data point r is measured at time t_r.

The script used for fitting the diffusion model to the data will be discussed in detail in Appendix A. It is based on MATLAB's minimization function fminsearch by minimizing the error by varying five parameters, the surface reaction rates $\tilde{k}_\text{H}$ and $\tilde{k}_\text{O}$, the diffusion coefficients $\tilde{D}_\text{H}$ and $\tilde{D}_\text{O}$ and one of the two power factors. In a first step, the other two power factors are calculated. The power factor P^0 (later in this work denoted as $\tilde{A}$) is equal to the initial conductivity, σ^0_{obs}. The second power factor, P_H (later $\tilde{B}$) is varied by fminsearch and is a constant for one iteration of the routine. The third power factor, P_O (later $\tilde{C}$) can be calculated by the final conductivity, $P_\text{O} = \sigma^\infty_{\text{obs}} - P_\text{H} - P^0$. The new notation of the power factors used in this work will be explained in Section 7.2.2. In the second step, the parameters $L_{a,\text{H}}$ and $L_{a,\text{O}}$ are calculated and $\beta_{i,\text{H}}$ and $\beta_{i,\text{O}}$ are obtained by finding the first N positive roots of Eq. (4.24). The corresponding parameters for the second dimension are calculated in the same way. In the third step, the diffusion model's analytical solution is solved for each time step, t_r, yielding the total conductivity at this time:

$$\begin{aligned}\sigma(t_r) = \tilde{A} + \tilde{B}\left(1 - \sum_{i=1}^{N}\sum_{n=1}^{N} \frac{2L_{a,\text{H}}^2 \cdot e^{-\frac{\beta_{i,\text{H}}^2 \tilde{D}_\text{H} t_r}{a^2}}}{\beta_{i,\text{H}}^2(\beta_{i,\text{H}}^2 + L_{a,\text{H}}^2 + L_{a,\text{H}})} \cdot \frac{2L_{b,\text{H}}^2 \cdot e^{-\frac{\gamma_{n,\text{H}}^2 \tilde{D}_\text{H} t_r}{b^2}}}{\gamma_{n,\text{H}}^2(\gamma_{n,\text{H}}^2 + L_{b,\text{H}}^2 + L_{b,\text{H}})}\right) \\ + \tilde{C}\left(1 - \sum_{i=1}^{N}\sum_{n=1}^{N} \frac{2L_{a,\text{O}}^2 \cdot e^{-\frac{\beta_{i,\text{O}}^2 \tilde{D}_\text{O} t_r}{a^2}}}{\beta_{i,\text{O}}^2(\beta_{i,\text{O}}^2 + L_{a,\text{O}}^2 + L_{a,\text{O}})} \cdot \frac{2L_{b,\text{O}}^2 \cdot e^{-\frac{\gamma_{n,\text{O}}^2 \tilde{D}_\text{O} t_r}{b^2}}}{\gamma_{n,\text{O}}^2(\gamma_{n,\text{O}}^2 + L_{b,\text{O}}^2 + L_{b,\text{O}})}\right)\end{aligned} \tag{7.6}$$

The relaxation curve shown in Fig. 7.1 was used to fit the diffusion model with the method described above. In Fig. 7.2, the fit, σ_{calc}, is shown as a pink line. The initial conductivity, σ^0 or $\tilde{A}$, is shown as

a green dotted line and the contributions of the fast hydrogen kinetic (red dotted line, $\tilde{B} \cdot f_{\tilde{k}_H,\tilde{D}_H}(t)$) and the slow oxygen kinetic (blue dotted line, $\tilde{C} \cdot f_{\tilde{k}_O,\tilde{D}_O}(t)$) are also shown. The residual of the fit, $\sigma_{obs} - \sigma_{calc}$, is shown in the lower diagram as a red line. The transport parameters and power factors obtained by the fit are summarized in Tab. 7.1. The surface reaction rate of hydrogen is approximately two orders of magnitude higher than the rate of oxygen and the diffusion coefficient is one order of magnitude higher. The fit shows good agreement with the experimental data indicated by low residuals with no systematic characteristics.

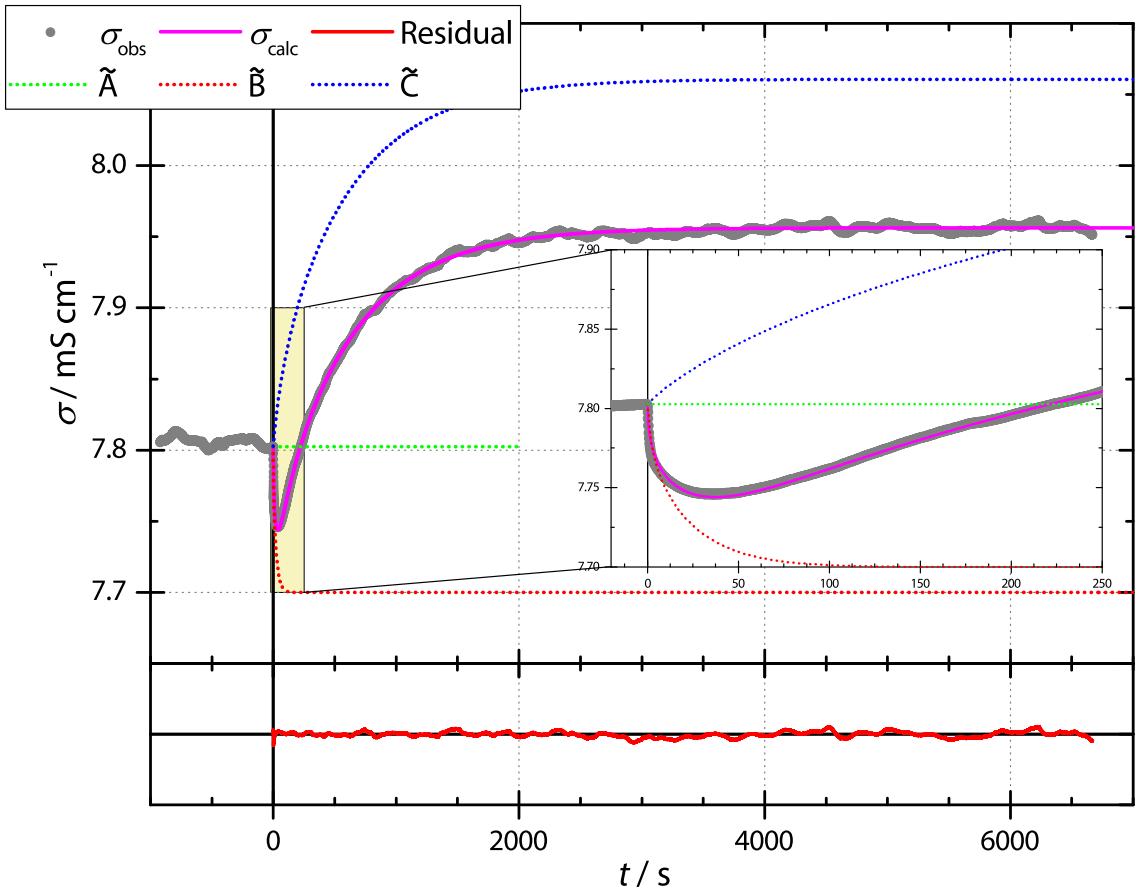

Figure 7.2: The conductivity relaxation curve shown in Fig. 7.1 (gray symbols) and the diffusion model fitted to the experimental data with Eq. (7.6) (pink line). The contributions of the power factors are shown as dotted lines: $\tilde{A}$ (green); with $\tilde{A}$ as an offset, $\tilde{B} \cdot f_{\tilde{k}_H,\tilde{D}_H}(t)$ (red) and $\tilde{C} \cdot f_{\tilde{k}_O,\tilde{D}_O}(t)$ (blue). The residual of the fit, $\sigma_{obs} - \sigma_{calc}$, is shown in red in the lower diagram with equal scale.

Table 7.1: Transport parameters obtained by fitting the diffusion model to the relaxation curve shown in Fig. 7.2. T = 950 °C; pO_2 = 100 mbar; ΔpH_2O = 20 mbar (10 mbar → 30 mbar).

Parameter	Fitted Value
Surface reaction rate of hydrogen $\tilde{k}_H$	7.21×10^{-2} cm s^{-1}
Diffusion coefficient of hydrogen $\tilde{D}_H$	3.26×10^{-4} cm^2 s^{-1}
Surface reaction rate of oxygen $\tilde{k}_O$	5.15×10^{-4} cm s^{-1}
Diffusion coefficient of oxygen $\tilde{D}_O$	1.71×10^{-5} cm^2 s^{-1}
Power factor $\tilde{A}$	7.801 mS cm^{-1}
Power factor of hydrogen $\tilde{B}$	−0.103 mS cm^{-1}
Power factor of oxygen $\tilde{C}$	0.259 mS cm^{-1}

7.1.2.1 Fitting with one Surface Reaction Rate or one Diffusion Coefficient

In the previous section, two completely different kinetics for the incorporation of hydrogen and oxygen were assumed, i.e. the surface reaction and the diffusion of both species are based on mechanisms with different kinetics. The parameters obtained for both species differ significantly. However, to show that at least two different kinetics for both, the surface reaction and the diffusion, are present, the fitting procedure was performed with one surface reaction rate and two diffusion coefficients and with two surface reaction rates and one diffusion coefficient. This was achieved by the constraints $\tilde{k}_H = \tilde{k}_O$ and $\tilde{D}_H = \tilde{D}_O$, respectively, using the same analytical function. The resulting residuals of the fits are shown in Fig. 7.3. The best fit to the experimental data is achieved by a variation of all four parameters. Especially the very start of the relaxation process — the first 25 s — is better represented by a variation of four parameters (gray) than by one surface reaction rate for both curves (red). Fitting with a single diffusion coefficient (blue) introduces large errors to the fit during the first 750 s. The fast diffusion of protons compared to the slow oxygen diffusion cannot be described by a single diffusion coefficient. However, fixing the surface reaction rate has a significant but not too large impact on the quality of fit. A possible explanation might be the large influence of hydrogen diffusion as a rate limiting step for the hydrogen relaxation and that the surface reaction of hydrogen is at the limit of the determinability. This will be explained in more detail in the next section.

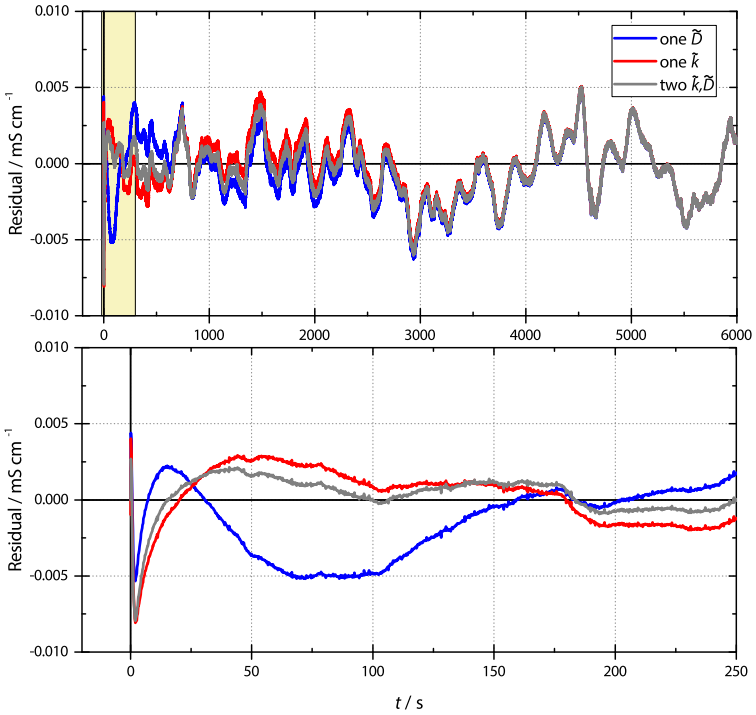

Figure 7.3: Residuals of fitting the diffusion model to the experimental data. Gray: all kinetic transport parameters are varied. Blue: a single diffusion coefficient for both species is assumed, $\tilde{D}_{\mathrm{H}} = \tilde{D}_{\mathrm{O}}$. Red: a single surface reaction rate is assumed, $\tilde{k}_{\mathrm{H}} = \tilde{k}_{\mathrm{O}}$. The lower diagram is a magnification of the yellow part of the upper diagram.

7.1.3 Simultaneous Determinability of the Surface Reaction Rates and Diffusion Coefficients

In Section 4.4, the simultaneous determinability of both parameters, the surface reaction rate and the diffusion coefficient, in a single experiment has been discussed. If the dimensionless parameter L_a is between 10^{-1} and 10^2, both parameters can be determined. For relaxation experiments upon hydration, two pairs of transport parameters are obtained by fitting the model to the experimental data and for both pairs the dimensionless parameter can be calculated, $L_{a,\mathrm{H}}$ and $L_{a,\mathrm{O}}$. For the parameters yielded for the experimental data shown above, $L_{a,\mathrm{H}}$ and $L_{a,\mathrm{O}}$ are within the curvature in Fig. 7.4 and can thus be determined. If one of the dimensionless parameters is not within the curvature but instead in the linear regime of τ_D or τ_k, it is possible to change L_a by adjusting the sample's thickness. The lines can be shifted left using thinner samples or right using thicker samples. However, the distance between both lines is constant and dependent on the transport parameters only. Changing the sample's thickness shifts both parameters by an equal amount in a logarithmic plot. If the distance between both lines is larger than the extent of the curvature in this plot, a maximum of three parameters can be determined simultaneously by shifting one of the two lines into the curved regime by adjusting the sample's thickness. N.B.: From the data yielded by the fitting routine, one cannot obtain a L_a, which is deep within the linear regime, because the fit becomes

independent of the corresponding parameter at the verge of the curved regime. The *true* parameter L_a of a sample, however, can be deep within the linear regime.

The dimensionless parameters $L_{a,\mathrm{H}}$ and $L_{a,\mathrm{O}}$ for the transport parameters listed in Tab. 7.1 for sample F002 with thickness $2a = 3.771\,\mathrm{mm}$ are depicted in Fig. 7.4 (see Fig. 4.7 and Reference [43]) as vertical lines at the corresponding values of L_a. The dimensionless parameter L_a for oxygen (blue line) lies within the center of the curved regime. The surface reaction and the diffusion have an almost equal contribution to the relaxation curve. The dimensionless parameter L_a for hydrogen, however, is in the curved regime but at the verge to the diffusion controlled regime. Both parameters are still determinable simultaneously but the relaxation of hydrogen is mainly limited by its diffusion whereas the surface reaction is very fast.

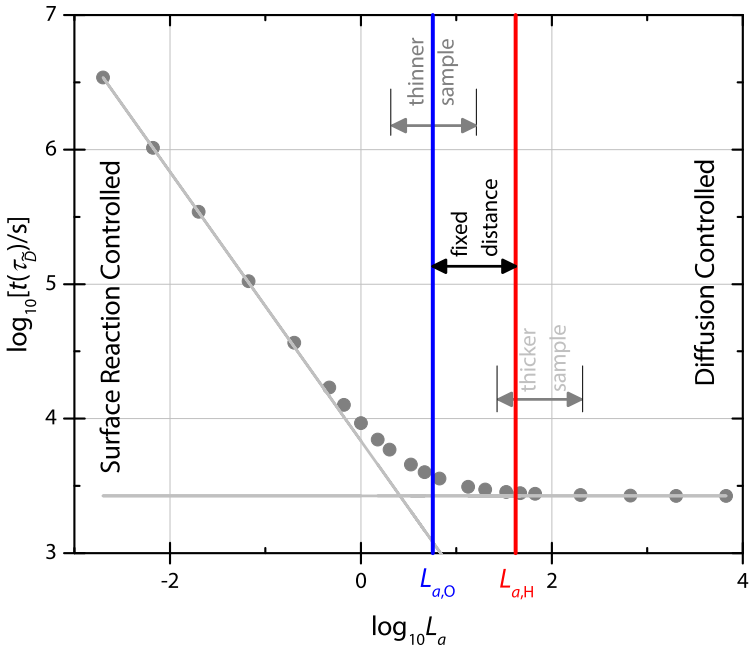

Figure 7.4: Simultaneous determinability of all four transport parameters. $L_{a,\mathrm{H}}$ and $L_{a,\mathrm{O}}$ are within the curved regime (see Section 4.4).

7.1.4 Relaxation upon Dehydration

In Section 7.1.1, the behavior upon hydration has been shown and the diffusion model was fitted to the experimental curve. Here, the behavior upon dehydration is presented, achieved by decreasing the $p\mathrm{H_2O}$ while maintaining a constant $p\mathrm{O_2}$. In principle, the transport parameters should be equal to the parameters obtained by fitting to the hydration curve. Transport parameters are usually specified to the final $p\mathrm{O_2}$ and $p\mathrm{H_2O}$, which is identical in the hydration and dehydration processes compared here. However, while the surface reaction is dependent on the final conditions only, the diffusion during the entire relaxation process is dependent on the diffusion coefficients between

initial and final conditions. Transport parameters with a large discrepancy between oxidative and reductive steps have been obtained for OTM materials in literature.[116, 117] However, simulations of Lohne *et al.*[42] and the effect described in our previous publication[43] can explain this behavior by a limited gas phase mass transport. The difference in non-stoichiometry for reductive and oxidative steps — if the same step-size, half an order of magnitude, is used — is not the same, $|\Delta\delta_{ox}| < |\Delta\delta_{red}|$. In Fig. 7.5, the relaxation curve for a dehydrating step at 950 °C and a pO_2 of 100 mbar is shown after a step in pH_2O from 100 mbar to 30 mbar. This is the same final pH_2O as in Fig. 7.1. The resulting transport parameters are summarized in Tab. 7.2.

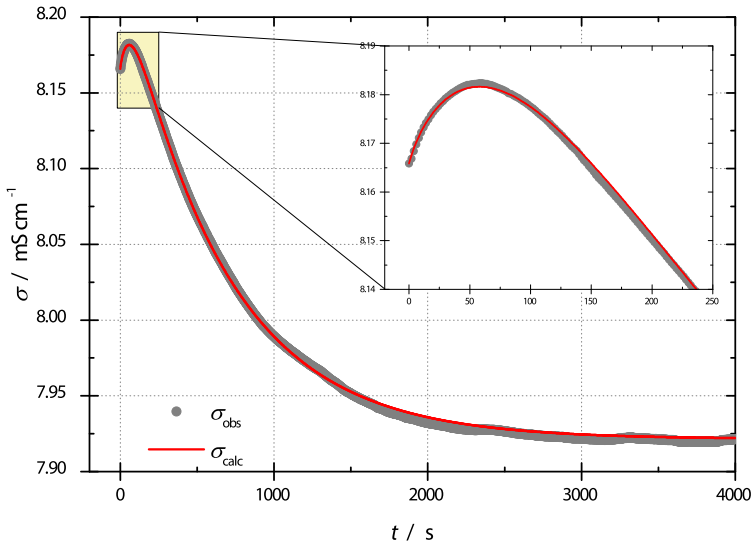

Figure 7.5: Relaxation curve of sample F002 after a dehydrating step from pH_2O = 100 mbar to 30 mbar (gray symbols). T = 950 °C; pO_2 = 100 mbar. The inset is a magnification of the start of the relaxation.

Table 7.2: Transport parameters obtained by fitting the diffusion model to the relaxation curve shown in Fig. 7.5. T = 950 °C; pO_2 = 100 mbar; ΔpH_2O = −70 mbar (100 mbar → 30 mbar).

Parameter	Fitted Value
Surface reaction rate of hydrogen $\tilde{k}_H$	1.98×10^{-3} cm s^{-1}
Diffusion coefficient of hydrogen $\tilde{D}_H$	3.22×10^{-4} cm^2 s^{-1}
Surface reaction rate of oxygen $\tilde{k}_O$	2.29×10^{-4} cm s^{-1}
Diffusion coefficient of oxygen $\tilde{D}_O$	3.19×10^{-5} cm^2 s^{-1}
Power factor $\tilde{A}$	8.166 mS cm^{-1}
Power factor of hydrogen $\tilde{B}$	0.089 mS cm^{-1}
Power factor of oxygen $\tilde{C}$	−0.333 mS cm^{-1}

An evaluation with regard to the power factors will be made later in this work. For now, it is only clear, that the final conductivity in both cases must be equal as the final conditions are equal and

the sample reaches equilibrium, $\sigma^{\infty}_{\mathrm{hyd}} = \sigma^{\infty}_{\mathrm{dehyd}}$. Comparing the final conductivities of the relaxation curves shown in Figs. 7.5 and 7.1, almost the same final conditions were met: $\sigma^{\infty}_{\mathrm{hyd}} = 7.956\,\mathrm{S\,cm^{-1}}$ and $\sigma^{\infty}_{\mathrm{dehyd}} = 7.922\,\mathrm{S\,cm^{-1}}$. Deviations might occur due to slightly different $p\mathrm{O_2}$ or $p\mathrm{H_2O}$ or because of degradation of the sample as the dehydration was performed weeks after the hydration experiments. Comparing the transport parameters upon dehydration to the values obtained by fitting to the relaxation curve upon hydration, Tab. 7.1, one can see that the transport parameters for oxygen do not differ significantly for hydration or dehydration behavior. The diffusion coefficient of hydrogen, $\tilde{D}_{\mathrm{H}}$, is almost equal. However, the surface reaction rate of hydrogen, $\tilde{k}_{\mathrm{H}}$, is almost one order of magnitude lower than for the hydrating step. One explanation might be the limit of the simultaneous determinability as discussed above. Another consideration for the surface reaction will be discussed with the power factors later in this work in Section 7.2.3.

7.1.5 Error Estimation

In a previous work, the error on the parameters yielded by an oxidative or reductive relaxation experiment has been estimated.[95] In this work, the sample's thickness was changed in the fitting procedure to reflect the error caused by the measurement of the sample's thickness. The deviation of the parameters for the thicker and thinner sample thickness from the unmodified sample thickness was added to the positive and negative error bars. A second error has been estimated by calculating the confidence interval of the fit. The surface reaction rate $\tilde{k}$ has been increased and decreased until the error of the fit exceeds a factor of 1.05 (5% deviation). In this fitting routine, the unweighted least-square error of the relaxation curve has been added up until time $t_{99.9\%}$, where the normalized calculated curve of the unmodified transport parameters reaches a value of 0.999. The introduction of time $t_{99.9\%}$ is necessary because the relative deviation of the least-square fit is smaller if many values are added up while the sample is in equilibrium. It was found that the error introduced by the measurement of the sample's thickness is small compared to the error estimated by the confidence interval. Hence, it has been neglected for further error estimations.

For the error estimation of two-fold relaxation curves additional considerations are necessary. The errors on the power factors $\tilde{B}$ and $\tilde{C}$ cannot be determined. In the following error estimation, the determined power factors are assumed to be exact. The weighting of the fit is necessary to reflect the start of the relaxation process. For the confidence interval, the fit cannot be weighted. Therefore, with the obtained parameters, two single fold relaxation curves — one for the fast hydrogen kinetic, one for the slow oxygen kinetic — were simulated and the time after which 99.9% of each conversion is complete, was saved ($t_{99.9\%,\mathrm{H}}$ and $t_{99.9\%,\mathrm{O}}$). In a second step, the non-weighted squared error was added up from $t = 0$ to $t_{99.9\%,\mathrm{H}}$ and from $t = 0$ to $t_{99.9\%,\mathrm{O}}$. In a third step, the confidence interval for the hydrogen kinetic was determined by a variation of $\tilde{k}_{\mathrm{H}}$ and $\tilde{D}_{\mathrm{H}}$, respectively, up to an error of $1.05 \cdot \sum_{t=0}^{t_{99.9\%,\mathrm{H}}} \left(\sigma_{\mathrm{obs},t} - \sigma_{\mathrm{calc},t}\right)^2$. The confidence interval of the slow oxygen kinetic was accordingly determined by a variation of $\tilde{k}_{\mathrm{O}}$ and $\tilde{D}_{\mathrm{O}}$ up to an error of $1.05 \cdot \sum_{t=0}^{t_{99.9\%,\mathrm{O}}} \left(\sigma_{\mathrm{obs},t} - \sigma_{\mathrm{calc},t}\right)^2$. While one parameter was varied, all other transport parameters were fixed.

In contrast to the determination of the confidence interval of a single fold relaxation curve, where the factor of the error by changing the parameters is always larger than unity (if it is lower, the fit has not found the minimum), the fact that the fit was performed with a weighting and the determination of the confidence interval was unweighted, the factor of the error can be lower than unity. This is especially the case for the fast hydrogen kinetic. It should also be mentioned that the determination of the confidence interval of the fast hydrogen relaxation neglects the slower oxygen relaxation curve for $t > t_{99.9\%,H}$. The confidence interval is shown as an error bar for the kinetic transport parameters in the diagrams of Section 7.2.

7.1.6 Ohmic Resistance

The measurement of a conductivity by the four point direct current method requires an ohmic resistance of the sample and of the contacts. The resulting conductivity relaxation curve should be independent of the constant current. However, the voltage was limited to 2 V to avoid electrolysis or a very high drift of charge carriers. In most cases the constant current was chosen to yield a voltage of a few hundred mV so that the signal-to-noise ratio was good and no other effects (e.g. the signal caused by the furnace, see Section 6.2.5) influenced the measurement. To show that the sample and the contacts describe ohmic behavior, an I–V curve (current–voltage curve, I, U-diagram) has been measured. In Fig. 7.6, the I–V curve shows a linear correlation between voltage and current with the ohmic resistance as slope. The electrical conductivity is calculated from Eq. (6.7) using the distance of the contacts and the cross-sectional area. Ohm's law is already inserted into this equation, assuming an ohmic resistance. For the diagram shown in Fig. 7.6, the voltage was increased stepwise up to a voltage of 2 V, then decreased to −2 V before increasing to 0 V while monitoring the current. The measurement was performed in a two point setup using the SourceMeter at contacts 1 and 4 of the sample.

7.1.7 Variation of the Flow Rate

The issues caused by a limited gas phase mass transport of oxygen have already been discussed in Section 4.2.1 and in References [42, 43, 92]. These problems occur for materials with high transport parameters and high differences in oxygen non-stoichiometry, $\Delta\delta$. Lanthanum tungstate has rather high protonic transport parameters and medium oxygen transport parameters upon hydration (the transport parameters of oxygen upon oxidation will be discussed later). Therefore, the first condition is met. To analyze, if the relaxation is influenced by a gas phase mass transport limitation, relaxation measurements in dependency on the flow rate were performed and the transport parameters for flow rates between 25 mL min^{-1} and 200 mL min^{-1} were determined. Higher flow rates can be applied by the MFCs but the water vapor saturators feed liquid water into the tube caused by strong bubbling at high flow rates and the $p\mathrm{H_2O}$ cannot be assumed constant. The results are shown in Fig. 7.7. All transport parameters are almost constant over the analyzed flow rate region and do not show any trend. Thus, it can be assumed that the difference in hydrogen

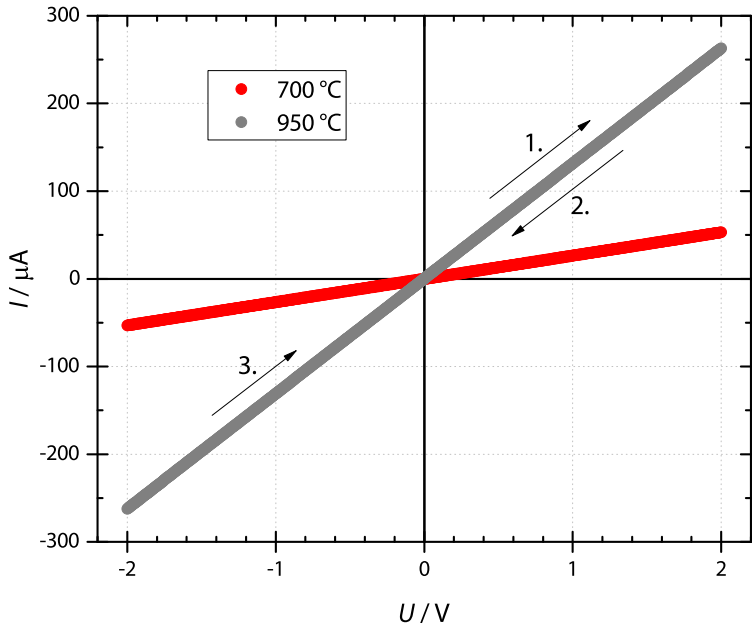

Figure 7.6: I–V characteristics of sample F012. T =700 °C and 950 °C; pO_2 = 100 mbar; pH_2O = 30 mbar.

and oxygen concentration is not large enough to influence the relaxation. Some perovskite type materials like BSCF and LSCF (barium / lanthanum strontium cobalt ferrates) show large oxygen non-stoichiometry differences[118, 119] — causing a gas phase mass transport limited relaxation. The fact that the determined parameters do not change with higher flow rates — which lead to a faster flushing and thus a smaller time constant of the reactor — also indicate that the flush time correction proposed by den Otter *et al.*[91] is not necessary here.

The obtained transport parameters for sample F011 are — except for the surface reaction rate of hydrogen — approximately equal to the parameters summarized in Tab. 7.1 for sample F002. The issue of determining the surface reaction rate of hydrogen is at the limit of the determinability and the deviation might originate from this effect, similar to the issues described in Section 7.1.2.1.

7.2 Electrical Conductivity Relaxation of LaWO54

In the previous section it has been shown that lanthanum tungstate shows two-fold relaxation behavior upon hydration while maintaining a constant pO_2. From fitting the diffusion model to the relaxation data, the following parameters are accessible: the ambipolar surface reaction rates for hydrogen and oxygen, $\tilde{k}_H$ and $\tilde{k}_O$, the ambipolar diffusion coefficients for hydrogen and oxygen, $\tilde{D}_H$ and $\tilde{D}_O$, the initial conductivities, σ^0 or $\tilde{A}$, the power factors for hydrogen, $\tilde{B}$, and for oxygen, $\tilde{C}$.

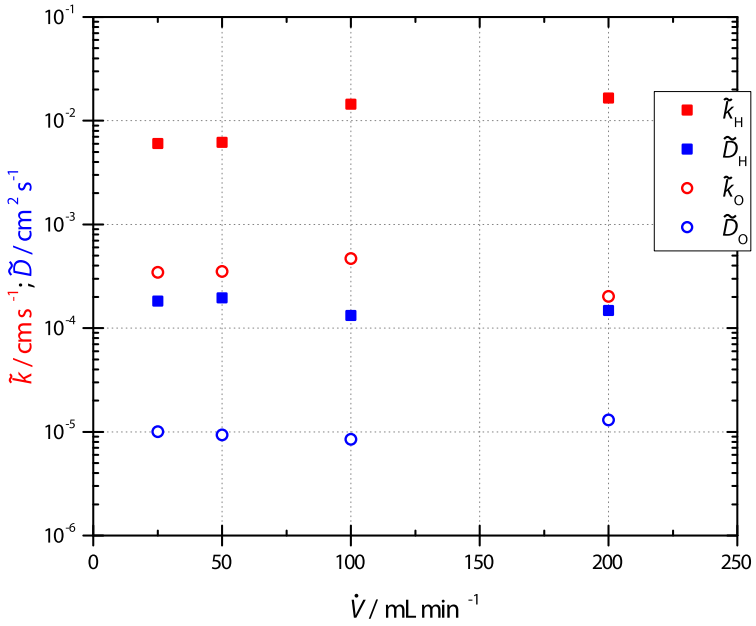

Figure 7.7: Transport parameters of LaWO54 in dependency of the flow rate for hydrating steps of sample F011. T = 950 °C; pO_2 = 100 mbar; pH_2O = 10 mbar → 30 mbar.

7.2.1 Variation of Temperature and Partial Pressure of Oxygen: Relaxation Curves

7.2.1.1 Decreasing the Partial Pressure of Oxygen

Starting at the conditions described above, the constant partial pressure of oxygen was first decreased by one order of magnitude to 10 mbar. From the shape of the relaxation curve, one can immediately see the lower contribution of the fast kinetic. The minimum of the relaxation is already reached after 18 s while it is reached after 36 s for a pO_2 of 100 mbar. The drop in conductivity up to the minimum (not to confuse with the power factor $\tilde{B}$, which is absolute larger and also negative) is much smaller than in the curve depicted in Fig. 7.1 (0.018 mS cm^{-1} versus 0.055 mS cm^{-1} for high pO_2 — the fact that the power factor $\tilde{B}$ for low pO_2 is also −0.055 mS cm^{-1} is a coincidence). The initial conductivity, σ^0, and the difference in conductivity, $\Delta\sigma$, are slightly lower than for high pO_2.

The resulting kinetic transport parameters obtained by fitting the diffusion model to the experimental data shown in Fig. 7.8 are summarized in Tab. 7.3. The kinetic transport parameters are almost independent of pO_2 but the power factors, $\tilde{A}$, $\tilde{B}$ and $\tilde{C}$, do differ significantly from the power factors for pO_2 = 100 mbar (see Tab. 7.1). They indicate that the two-fold behavior is less pronounced for lower pO_2. A detailed pO_2 dependence will be presented in Section 7.2.4.

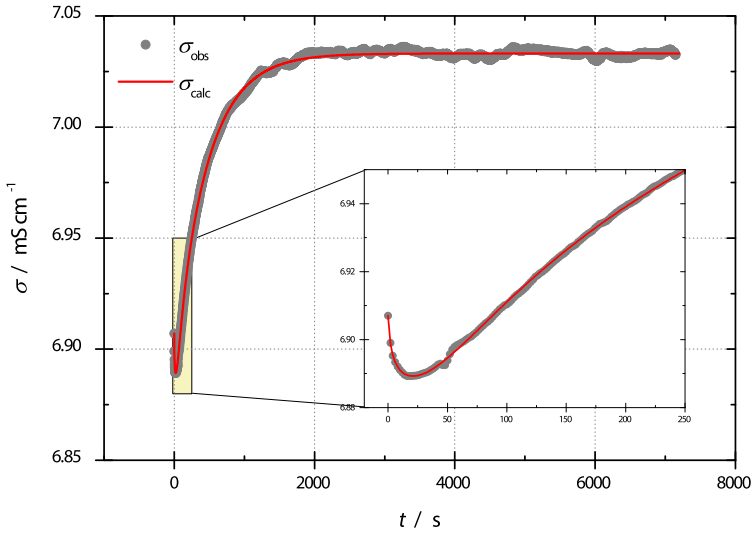

Figure 7.8: Relaxation curve of sample F002 after a hydrating step from pH_2O = 10 mbar to 30 mbar. T = 950 °C; pO_2 = 10 mbar. The red line is the fit to the experimental data (gray symbols). The inset is a magnification of the yellow rectangle.

Table 7.3: Transport parameters obtained by fitting the diffusion model to the relaxation curve shown in Fig. 7.8. T = 950 °C; pO_2 = 10 mbar; ΔpH_2O = 20 mbar (10 mbar → 30 mbar).

Parameter	Fitted Value
Surface reaction rate of hydrogen $\tilde{k}_H$	2.86×10^{-2} cm s^{-1}
Diffusion coefficient of hydrogen $\tilde{D}_H$	3.54×10^{-4} cm^2 s^{-1}
Surface reaction rate of oxygen $\tilde{k}_O$	9.01×10^{-4} cm s^{-1}
Diffusion coefficient of oxygen $\tilde{D}_O$	2.19×10^{-5} cm^2 s^{-1}
Power factor $\tilde{A}$	6.907 mS cm^{-1}
Power factor of hydrogen $\tilde{B}$	−0.055 mS cm^{-1}
Power factor of oxygen $\tilde{C}$	0.181 mS cm^{-1}

7.2.1.2 Decreasing the Temperature

In a second step, the temperature has been decreased to 700 °C compared to the conditions described in Section 7.1.1. This temperature has been chosen because it has been reported that the electronic conductivity emerges above ≈ 750 °C (to be precise: below 750 °C, LaWO54 shows predominantly protonic conductivity and ambipolar conductivity is achieved by 'suitable doping and/or increasing the temperature')[10] and hence, single fold relaxation behavior should be observed as reported by Solís *et al.*[38] The kinetic should follow the slow oxygen kinetic. The fast hydrogen kinetic is not present because charge neutrality is only maintained by proton interstitials and oxygen vacancies. A fast hydrogen diffusion would lead to a significant charge separation and a Nernst field created by these two charge carriers, which is analog to the common oxidative relaxation steps,

where the flux of fast electron holes is coupled to the oxygen flux by the Nernst field accelerating the oxygen species and slowing down the electron holes.

However, the sample did not follow single fold behavior but instead a two-fold behavior as shown in Fig. 7.9. The curve is not non-monotonic as described for hydration kinetics, e.g. in References [69, 102, 103]. A two-fold monotonic behavior was observed. The obtained transport parameters are summarized in Tab. 7.4. Both, the surface reaction rate and the diffusion coefficient of oxygen, are almost one order of magnitude lower for 700 °C. However, the parameters for hydrogen are even higher than the parameters obtained for 950 °C — not in accordance with Arrhenius-type behavior of $\tilde{k}$ and $\tilde{D}$. The contribution of the fast kinetics to the relaxation curve is very small ($\tilde{B}$) and the fit, shown in Fig. 7.9, does not show a good agreement with the very start of the relaxation (see inset in Fig. 7.9). This might be attributed to the weighting of the fit (even if the fit is weighted to further increase the influence of the start of the relaxation, the apparent fit does not improve) or to the fact that the switching process is influencing the first few seconds of the relaxation curve, which is extremely important for determination of the transport parameters of the fast kinetics.

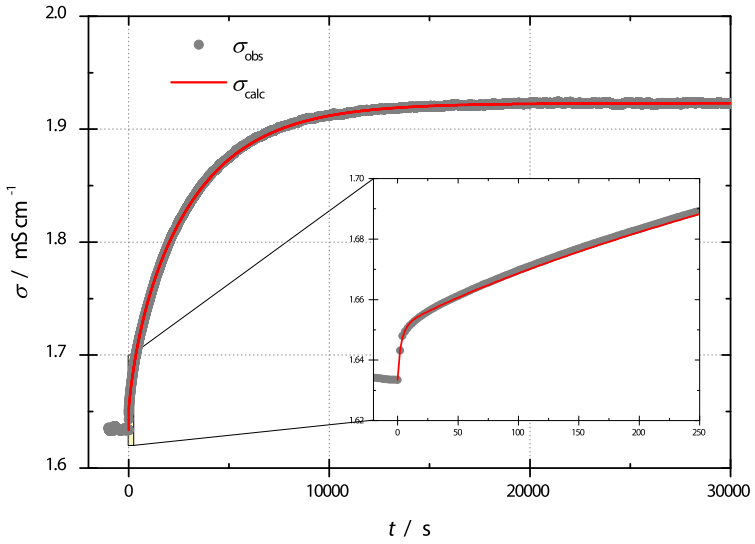

Figure 7.9: Relaxation curve of sample F002 after a hydrating step from pH_2O = 10 mbar to 30 mbar. T = 700 °C; pO_2 = 100 mbar. The red line is the fit to the experimental data (gray symbols). The inset is a magnification of the yellow rectangle.

Table 7.4: Transport parameters obtained by fitting the diffusion model to the relaxation curve shown in Fig. 7.9. T = 700 °C; pO_2 = 100 mbar; ΔpH_2O = 20 mbar (10 mbar → 30 mbar).

Parameter	Fitted Value
Surface reaction rate of hydrogen $\tilde{k}_H$	1.13×10^{-1} cm s^{-1}
Diffusion coefficient of hydrogen $\tilde{D}_H$	2.76×10^{-3} cm^2 s^{-1}
Surface reaction rate of oxygen $\tilde{k}_O$	9.24×10^{-5} cm s^{-1}
Diffusion coefficient of oxygen $\tilde{D}_O$	3.28×10^{-6} cm^2 s^{-1}
Power factor $\tilde{A}$	1.634 mS cm^{-1}
Power factor of hydrogen $\tilde{B}$	0.017 mS cm^{-1}
Power factor of oxygen $\tilde{C}$	0.272 mS cm^{-1}

7.2.1.3 Decreasing the Temperature and the Partial Pressure of Oxygen

Finally, the pO_2 and the temperature were decreased to pO_2 = 10 mbar and T = 700 °C. Both effects described above are reflected in the relaxation curve, shown in Fig. 7.5: the two-fold behavior is less pronounced than for the relaxation curve at high pO_2 (Fig. 7.9) indicated by a lower power factor $\tilde{B}$ and the shape of the relaxation curve is also two-fold monotonic in contrast to the shape of the relaxation curve at 950 °C. The transport parameters are similar to the parameters obtained at higher pO_2 except for the surface reaction rate of hydrogen. The fit is independent of the surface reaction rate of hydrogen because the relaxation is limited by the diffusion of hydrogen (see Section 7.1.3).

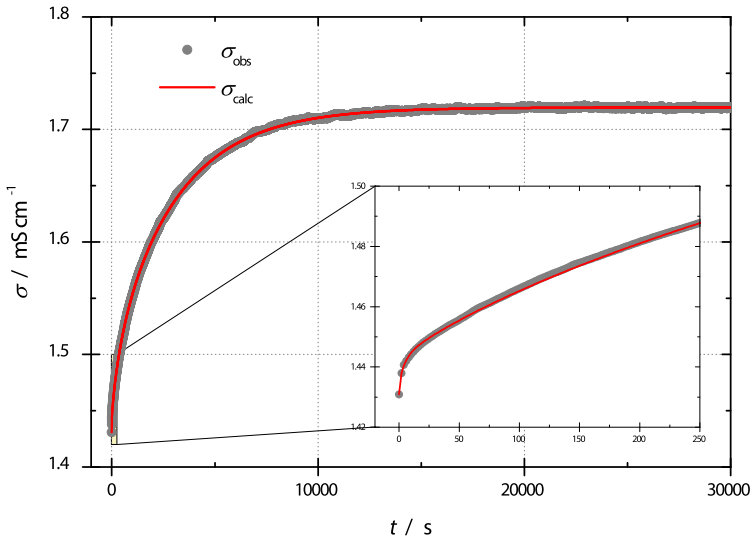

Figure 7.10: Relaxation curve of sample F002 after a hydrating step from pH_2O = 10 mbar to 30 mbar. T = 700 °C; pO_2 = 10 mbar. The red line is the fit to the experimental data (gray symbols). The inset is a magnification of the yellow rectangle.

Table 7.5: Transport parameters obtained by fitting the diffusion model to the relaxation curve shown in Fig. 7.10. T = 700 °C; $p\mathrm{O}_2$ = 10 mbar; $\Delta p\mathrm{H}_2\mathrm{O}$ = 20 mbar (10 mbar → 30 mbar).

Parameter	Fitted Value
Surface reaction rate of hydrogen $\tilde{k}_\mathrm{H}$	independent
Diffusion coefficient of hydrogen $\tilde{D}_\mathrm{H}$	1.62×10^{-3} cm^2 s^{-1}
Surface reaction rate of oxygen $\tilde{k}_\mathrm{O}$	1.30×10^{-4} cm s^{-1}
Diffusion coefficient of oxygen $\tilde{D}_\mathrm{O}$	3.12×10^{-6} cm^2 s^{-1}
Power factor $\tilde{A}$	1.431 mS cm^{-1}
Power factor of hydrogen $\tilde{B}$	0.012 mS cm^{-1}
Power factor of oxygen $\tilde{C}$	0.277 mS cm^{-1}

7.2.1.4 Conclusion of the Relaxation Curves

For high temperatures, LaWO54 shows a two-fold non-monotonic relaxation behavior upon hydration. This has been exemplary shown for 950 °C and $p\mathrm{O}_2$s of 10 mbar and 100 mbar in Sections 7.1.1 and 7.2.1.1, whereas LaWO54 shows two-fold monotonic relaxation behavior for low temperatures (700 °C). The power factor $\tilde{B}$ has the same sign (positive for hydration) as the power factor $\tilde{C}$ at low temperatures.

For both temperatures, the two-fold behavior is less pronounced for lower $p\mathrm{O}_2$, indicated by lower power factors for the fast kinetic, $\tilde{B}$.

A detailed analysis of the power factors is necessary to explain the two-fold monotonic behavior at low temperatures.

7.2.2 Definition of Power Factors

The power factors used in Eq. (7.6) are the contribution of each single fold relaxation curve to the resulting two-fold curve as a superposition. In literature, the power factors are *'constants each involving the mobilities and initial and final concentrations of the defects involved'*[70] (see Section 4.6). In this section, the power factors will be derived for the simple case of a surface reaction limited relaxation of lanthanum tungstate. The question, if the conductivity can be an observable of the concentrations of hydrogen and oxygen, will also be treated. For oxidation and reduction behavior without protonic contribution to the conductivity, the link between electrical conductivity and oxygen vacancy concentration has already been established in Section 4.1 and, in more detail, in Reference [82].

7.2.2.1 Relaxation without Diffusion Limitation

The power factors will be derived for the special case of a relaxation without diffusion limitation, simplifying the time-dependent function to a simple exponential function for a first order reaction (see Section 3.1.4). As soon as a proton or an oxygen ion is incorporated into the bulk phase, the concentrations of protons, oxygen ions and electron holes are equilibrated instantaneously ('$\tilde{D} = \infty$') so that the concentrations are not a function of space x. For the sake of simplicity, the geometry of the sample is a one-dimensional plane sheet. Some parts of this section are a repetition of the theory presented in Chapters 3 and 4 to establish a coherent derivation of the power factors.
The geometry of the sample is a plane sheet with distance $2a$ between the two planes at $x = -a$ and $x = a$ in the one-dimensional treatment. At the center of the sample, $x = 0$, the flux is zero due to symmetry (see Section 4.3.5). At the left surface, $x = -a$, an excerpt of the plane with infinite extent is chosen, area A (blue area in Fig. 7.11). Due to a step-like change in chemical potential of species i, a flux through area A, j_i, is effected by surface reaction. By this flux, the volume V (light blue cuboid) is filled with species i until the chemical potential between bulk and gas phase is equilibrated. The right volume is filled by a flux through the second surface area at $x = a$ (gray area).

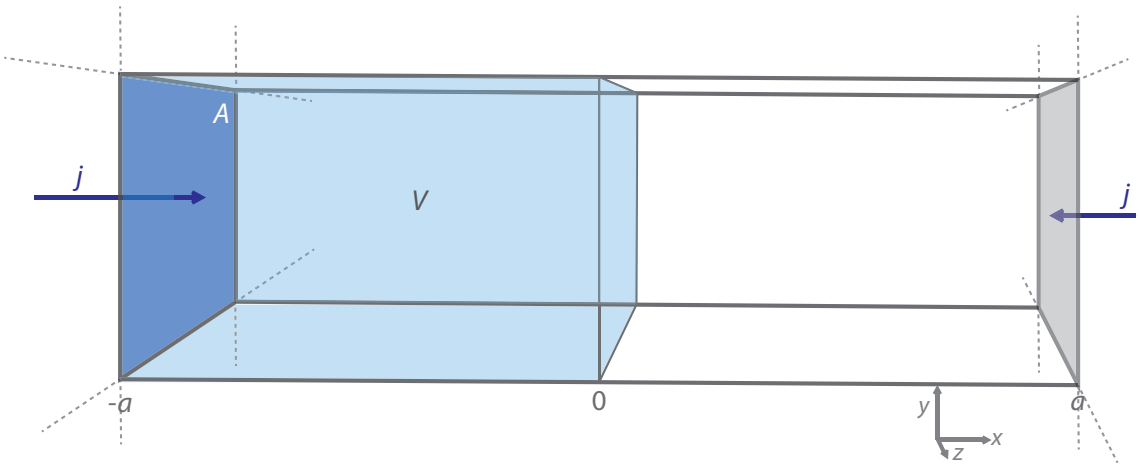

Figure 7.11: Parallel planes with a one-dimensional diffusion problem (compare to Fig. 4.2).

In general, the flux of species i, j_i, through surface area A without diffusion limitation is defined as

$$j_i = \frac{1}{A} \cdot \frac{dn_i}{dt} = \frac{V}{A} \cdot \frac{dc_i}{dt} = a \cdot \frac{dc_i}{dt} = \tilde{k}_i \left(c_i^{\infty} - c_i(t)\right) \Leftrightarrow \frac{dc_i}{dt} = \frac{\tilde{k}_i}{a} \cdot \left(c_i^{\infty} - c_i(t)\right) \tag{7.7}$$

with the bulk concentration of species i in equilibrium, c_i^{∞}, the time-dependent bulk concentration of species i, $c_i(t)$, and the ambipolar surface reaction rate of species i, $\tilde{k}_i$. N.B.: By the simplification of an infinite diffusion coefficient, the use of average concentrations is not necessary and the surface concentration used in Eq. (3.18) is equal to the concentration within the bulk phase.

Integration of Eq. (7.7) yields

$$\frac{c_i(t) - c_i^0}{c_i^\infty - c_i^0} = 1 - e^{-\frac{\tilde{k}_i}{a}t} \tag{7.8}$$

For a step-like change in $p\mathrm{H_2O}$ (hydration), the incorporation equation of water, Eq. (3.10), can be split into two reactions: the incorporation of oxygen and the incorporation of hydrogen. The reactions prior to the rate determining incorporation reactions into the bulk are in pre-equilibrium (see Section 3.1.4). The experimental relaxation curves show that two different kinetics are present, a fast kinetic assigned to the incorporation of hydrogen and a slow kinetic assigned to the incorporation of oxygen (see Section 7.1.2.1).

Flux and time-dependent concentration of oxygen in the bulk phase

The slow oxygen incorporation into the two virtual sublattices of lanthanum tungstate (see Section 2.2.1.2) follow the reactions

$$\frac{1}{2}\mathrm{O_2(g)} + \mathrm{v_O^{\bullet\bullet}} \rightleftharpoons \mathrm{O_O^\times} + 2\mathrm{h^\bullet} \qquad \text{and} \qquad \frac{1}{2}\mathrm{O_2(g)} + v_v^\times \rightleftharpoons \mathrm{O_v''} + 2\mathrm{h^\bullet} \tag{7.9}$$

The flux of oxygen — either by an incorporation onto a thermal vacancy ($\mathrm{v_O^{\bullet\bullet}}$) or onto a structural vacancy ($v_v^\times$) — is defined as

$$j_\mathrm{O} = \tilde{k}_\mathrm{O}(c_\mathrm{O}^\infty - c_\mathrm{O}(t)) \tag{7.10}$$

The concentration of oxygen that is in equilibrium with the surrounding gas phase, c_O^∞, is in fact a function of time as it is a function of the time-dependent concentration of proton interstitials. It can be linked by the laws of mass action for the incorporation of hydrogen and water, Eqs. (3.6) and (3.1), resulting in

$$[\mathrm{v_O^{\bullet\bullet}}] = \frac{55.5[\mathrm{H_i^\bullet}]^2}{K_{\mathrm{H_2}}^2 p\mathrm{H_2} \cdot K_{\mathrm{O_2}}\sqrt{p\mathrm{O_2}}} \tag{7.11}$$

For small step-sizes the change in oxygen vacancy concentration is small compared to the overall oxygen content, rendering c_O^∞ a constant. If this simplification is applied, the time-dependent oxygen concentration is yielded by integration of Eq. (7.10):

$$c_\mathrm{O}(t) = c_\mathrm{O}^0 + (c_\mathrm{O}^\infty - c_\mathrm{O}^0) \cdot \left(1 - e^{-\frac{\tilde{k}_\mathrm{O}}{a}t}\right) \tag{7.12}$$

Flux and time-dependent concentration of hydrogen in the bulk phase

The incorporation of hydrogen has been introduced in Section 3.1.2 and can be reduced to the incorporation equation

$$\frac{1}{2}\mathrm{H_2(g)} + \mathrm{h^\bullet} \rightleftharpoons \mathrm{H_i^\bullet} \tag{7.13}$$

It does not matter, if the proton is forming a hydroxy-anion on a regular oxygen site ($\mathrm{OH_O^\bullet}$) or on an occupied structural vacancy site ($\mathrm{OH_v'}$).

The bulk concentration of hydrogen, which is in equilibrium with the gas atmosphere, c_H^∞, is not a constant but a function of the oxygen vacancy concentration, analog to Eq. (7.11). The change in proton concentration caused by a change in oxygen vacancy concentration cannot be neglected. The change of the oxygen vacancy concentration is a function of time with a slow kinetic dependent on $\tilde{k}_\mathrm{O}$.

Hence, the concentration c_i^∞ in Eq. (7.7) must be replaced by the time-dependent equilibrium concentration, written

$$c_i^\infty \rightarrow c_\mathrm{H}^\infty([\mathrm{v_O^{\bullet\bullet}}]^0) + \left[c_\mathrm{H}^\infty([\mathrm{v_O^{\bullet\bullet}}]^\infty) - c_\mathrm{H}^\infty([\mathrm{v_O^{\bullet\bullet}}]^0)\right] \cdot \left(1 - e^{-\frac{\tilde{k}_\mathrm{O}}{a}t}\right) \tag{7.14}$$

New final and initial concentrations are used here:

$c_\mathrm{H}^\infty([\mathrm{v_O^{\bullet\bullet}}]^\infty) = c_\mathrm{H}^\infty$: bulk concentration of hydrogen ($\mathrm{H_i^\bullet}$) in the new equilibrium.

$c_\mathrm{H}^0([\mathrm{v_O^{\bullet\bullet}}]^0) = c_\mathrm{H}^0$: initial bulk concentration of hydrogen.

$c_\mathrm{H}^\infty([\mathrm{v_O^{\bullet\bullet}}]^0)$: equilibrium bulk concentration of hydrogen for the final $p\mathrm{H_2O}$ but for the initial oxygen vacancy concentration (in the general case; for lanthanum tungstate, the initial oxygen vacancy concentration must be replaced by $[\mathrm{v_O^{\bullet\bullet}}]^0 + [v_v^\times]^0$, which has been omitted for readability). This concentration is only achieved if the mobility of oxygen is zero (or approximately deep within the sample, e.g. in a semi-infinite medium, beyond the diffusion length of oxygen at a given time).

Inserting the time-dependent equilibrium concentration of hydrogen, defined in Eq. (7.14), into the flux equation, Eq. (7.7), the flux of hydrogen can be obtained:

$$j_\mathrm{H} = \tilde{k}_\mathrm{H}\left\{c_\mathrm{H}^\infty([\mathrm{v_O^{\bullet\bullet}}]^0) + \left[c_\mathrm{H}^\infty([\mathrm{v_O^{\bullet\bullet}}]^\infty) - c_\mathrm{H}^\infty([\mathrm{v_O^{\bullet\bullet}}]^0)\right] \cdot \left(1 - e^{-\frac{\tilde{k}_\mathrm{O}}{a}t}\right) - c_\mathrm{H}(t)\right\} \tag{7.15}$$

From Eq. (7.15) it can be assumed that the time-dependent concentration of hydrogen is a function of both kinetics. As an approach, the concentration of hydrogen is dependent on an initial concentration with parameter α, a part dependent on the fast kinetic with parameter β and a part dependent on the slow kinetic with parameter γ.

In this approach, the time-dependent hydrogen concentration can be written as

$$c_\mathrm{H}(t) = \alpha + \beta\left(1 - e^{-\frac{\tilde{k}_\mathrm{H}}{a}t}\right) + \gamma\left(1 - e^{-\frac{\tilde{k}_\mathrm{O}}{a}t}\right) \tag{7.16}$$

The parameters α, β and γ in this paragraph, which have no relation to other appearances of these characters within this work, can be obtained by inserting this approach into Eq. (7.15), i.e. deriving

Eq. (7.16) with respect to time (see Eq. (7.7)) and inserting the approach into $c_H(t)$ of the right part of Eq. (7.15):

$$\frac{a}{\tilde{k}_H}\frac{c_H(t)}{dt} = c_H^{\infty}([v_O^{\bullet\bullet}]^0) + \left[c_H^{\infty}([v_O^{\bullet\bullet}]^{\infty}) - c_H^{\infty}([v_O^{\bullet\bullet}]^0)\right]\cdot\left(1 - e^{-\frac{\tilde{k}_O}{a}t}\right) - c_H(t) \tag{7.17}$$

$$\Leftrightarrow 0 + \frac{\beta\tilde{k}_H}{\tilde{k}_H}\cdot e^{-\frac{\tilde{k}_H}{a}t} + \frac{\gamma\tilde{k}_O}{\tilde{k}_H}\cdot e^{-\frac{\tilde{k}_O}{a}t}$$
$$= c_H^{\infty}([v_O^{\bullet\bullet}]^0) + \left[c_H^{\infty}([v_O^{\bullet\bullet}]^{\infty}) - c_H^{\infty}([v_O^{\bullet\bullet}]^0)\right]\cdot\left(1 - e^{-\frac{\tilde{k}_O}{a}t}\right)$$
$$- \alpha - \beta\left(1 - e^{-\frac{\tilde{k}_H}{a}t}\right) - \gamma\left(1 - e^{-\frac{\tilde{k}_O}{a}t}\right)$$

The resulting parameters, i.e. the contributions of both kinetics to the time-dependent concentration of hydrogen, are

$$\alpha = c_H^0([v_O^{\bullet\bullet}]^0) \tag{7.18}$$

$$\beta = c_H^{\infty}([v_O^{\bullet\bullet}]^{\infty}) - c_H^0([v_O^{\bullet\bullet}]^0) - \frac{c_H^{\infty}([v_O^{\bullet\bullet}]^{\infty}) - c_H^{\infty}([v_O^{\bullet\bullet}]^0)}{1 - \frac{\tilde{k}_O}{\tilde{k}_H}} \tag{7.19}$$

$$\gamma = \frac{c_H^{\infty}([v_O^{\bullet\bullet}]^{\infty}) - c_H^{\infty}([v_O^{\bullet\bullet}]^0)}{1 - \frac{\tilde{k}_O}{\tilde{k}_H}} \tag{7.20}$$

If the hydrogen kinetic is much faster than the oxygen kinetic, $\tilde{k}_H \gg \tilde{k}_O$, Eq. (7.16) using the parameters from Eqs. (7.18) to (7.20) can be simplified to

$$c_H(t) = c_H^0([v_O^{\bullet\bullet}]^0) \tag{7.21}$$
$$+ \left[c_H^{\infty}([v_O^{\bullet\bullet}]^0) - c_H^0([v_O^{\bullet\bullet}]^0)\right]\left(1 - e^{-\frac{\tilde{k}_H}{a}t}\right)$$
$$+ \left[c_H^{\infty}([v_O^{\bullet\bullet}]^{\infty}) - c_H^{\infty}([v_O^{\bullet\bullet}]^0)\right]\left(1 - e^{-\frac{\tilde{k}_O}{a}t}\right)$$

Merkle *et al.*[115] have simulated depth profiles and concentration relaxation curves of charge carriers upon hydration in the *p*-type regime of perovskite type protonic conductors with diffusion limitation only. They have found two-fold concentration profiles of hydrogen for 700 K, where the transference number of protons is larger than the transference number of oxygen vacancies.

The chemical potentials of hydrogen and oxygen with the considerations discussed above are plotted as a sketch in Fig. 7.12. This sketch includes a depth-profile originating from a diffusion limitation, which will be discussed later. The profile of hydrogen using the simplifications for Eq. (7.21) can be divided into two parts: i) the fast kinetic, caused by the difference in pH_2O, but with the initial oxygen vacancy concentration (orange part in Fig. 7.12); ii) the increase of the chemical potential of hydrogen caused by the difference in $[v_O^{\bullet\bullet}]$ with the slow oxygen kinetic (light blue part in Fig. 7.12). The red curve is the resulting chemical potential of hydrogen as a superposition of the orange and light blue parts.

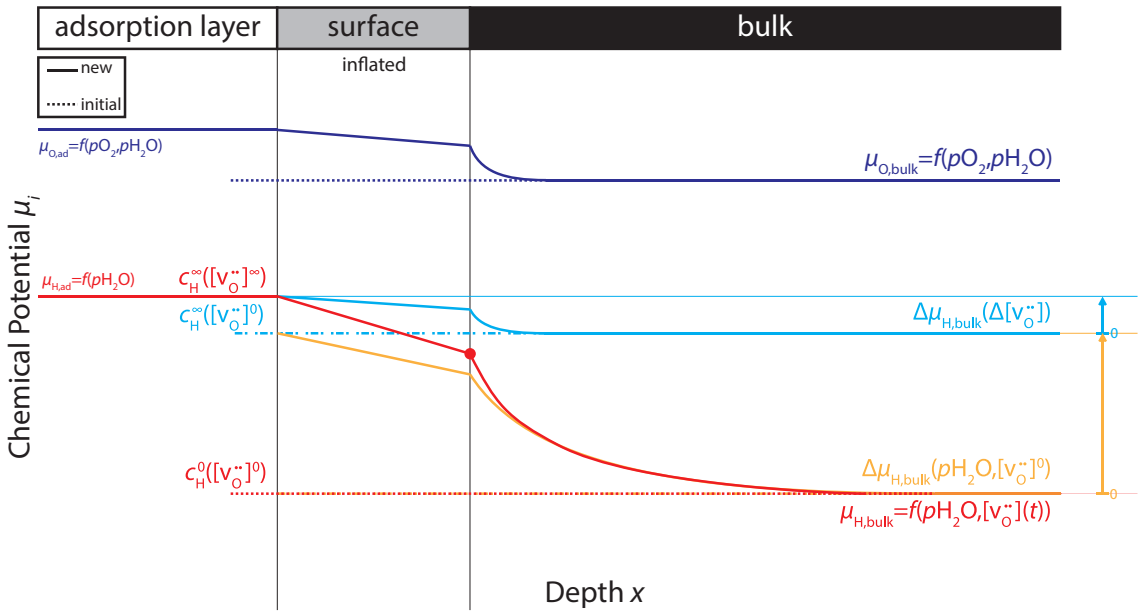

Figure 7.12: Sketch: chemical potential of hydrogen and oxygen on a hydrating step at time $0 < t < t_H^{\infty} < t_O^{\infty}$ with the relaxation times t_i^{∞} in which the equilibrium of species i is reached. The red (effective) line is two-fold. Light blue: contribution of the change in $[v_O^{\bullet\bullet}]$. Orange: contribution of ΔpH_2O at the initial oxygen vacancy concentration, $[v_O^{\bullet\bullet}]^0$.

7.2.2.2 Conductivity and Change in Conductivity

The electrical conductivity, the property that is measured in ECR experiments, is dependent on the charge, charge mobility and concentration of each charge carrier, recapitulating Eq. (4.1)

$$\sigma = \sum_i \sigma_i = F \sum_i (|z_i| u_i c_i) \tag{7.22}$$

Important for ECR experiments is the time-dependent change in concentration measured by the conductivity. For small steps in pH_2O, the charge mobility and charge of each species is assumed to be constant. According to the incorporation equations, the following species show a change in concentration over time: hydrogen ($H_i^{\bullet}$), oxygen ($v_O^{\bullet\bullet}$ and in LaWO54 also O_v'') and electrons (e' or $h^{\bullet}$). The time-dependent electrical conductivity, $\sigma(t)$, can be derived by inserting the concentration of oxygen, Eq. (7.12), and the simplified concentration of hydrogen, Eq. (7.21), into Eq. (7.22), with the time-dependent change in concentration of the charge carriers involved, $c_i \rightarrow c_i(t)$, yielding

$$\sigma(t) = A + B\left(1 - e^{-\frac{k_H}{a}t}\right) + C\left(1 - e^{-\frac{k_O}{a}t}\right) + Ec_{h^{\bullet}}(t) \tag{7.23}$$

with

$$A = F\left[|z_H| u_H c_H^0 + |z_O| u_O c_O^0 + \sum_{i,\mathrm{t-indep.}} |z_i| u_i c_i\right]$$

$$B = F|z_{\mathrm{H}}|u_{\mathrm{H}}\left[c_{\mathrm{H}}^{\infty}([\mathrm{v}_{\mathrm{O}}^{\bullet\bullet}]^{0}) - c_{\mathrm{H}}^{0}([\mathrm{v}_{\mathrm{O}}^{\bullet\bullet}]^{0})\right]$$

$$C = F|z_{\mathrm{O}}|u_{\mathrm{O}}(c_{\mathrm{O}}^{\infty} - c_{\mathrm{O}}^{0}) + F|z_{\mathrm{H}}|u_{\mathrm{H}}\left[c_{\mathrm{H}}^{\infty}([\mathrm{v}_{\mathrm{O}}^{\bullet\bullet}]^{\infty}) - c_{\mathrm{H}}^{\infty}([\mathrm{v}_{\mathrm{O}}^{\bullet\bullet}]^{0})\right]$$

$$E = F|z_{\mathrm{h}^{\bullet}}|u_{\mathrm{h}^{\bullet}}$$

With power factor A for the initial concentrations of hydrogen, oxygen and all time-independent charge carriers, B the power factor for the hydrogen concentration change with the fast kinetic and C the power factor for the change in oxygen concentration and the change in hydrogen concentration dependent on the change in oxygen vacancy concentration with the slow kinetic. The change in electron hole concentration is summarized as $E \cdot c_{\mathrm{h}^{\bullet}}(t)$ and will further be unraveled in the following section.

7.2.2.3 Electron Hole Concentration via Electroneutrality Condition

The simplified electroneutrality condition (see Section 2.2.2) for donor-doped LaWO54 in the *p*-type regime is

$$\begin{aligned} & 3[\mathrm{W}_{\mathrm{La}}^{\bullet\bullet\bullet}] + [\mathrm{h}^{\bullet}] + 2[\mathrm{v}_{\mathrm{O}}^{\bullet\bullet}] + [\mathrm{H}_{\mathrm{i}}^{\bullet}] = 2[\mathrm{O}_{v}''] \\ \Leftrightarrow\ & [\mathrm{h}^{\bullet}] = 2([\mathrm{O}_{v}''] - [\mathrm{v}_{\mathrm{O}}^{\bullet\bullet}]) - [\mathrm{H}_{\mathrm{i}}^{\bullet}] - 3[\mathrm{W}_{\mathrm{La}}^{\bullet\bullet\bullet}] \end{aligned} \tag{7.24}$$

The *change* in electron hole concentration is of interest in relaxation experiments, thus $[\mathrm{h}^{\bullet}] \longrightarrow [\mathrm{h}^{\bullet}](t) - [\mathrm{h}^{\bullet}]^{0}$. As the concentration of tungsten on lanthanum site does not change with time, it is canceled. The change in electron hole concentration can be written as

$$[\mathrm{h}^{\bullet}](t) - [\mathrm{h}^{\bullet}]^{0} = 2\left[\left([\mathrm{O}_{v}''](t) - [\mathrm{O}_{v}'']^{0}\right) - \left([\mathrm{v}_{\mathrm{O}}^{\bullet\bullet}](t) - [\mathrm{v}_{\mathrm{O}}^{\bullet\bullet}]^{0}\right)\right] - \left[[\mathrm{H}_{\mathrm{i}}^{\bullet}](t) - [\mathrm{H}_{\mathrm{i}}^{\bullet}]^{0}\right] \tag{7.25}$$

The oxygen defects in lanthanum tungstate have been discussed in Section 2.2.1.2. It is divided into two virtual sublattices — the regular oxygen sublattice and the two structural vacancies per unit cell. The defects in both virtual sublattices, $\mathrm{v}_{\mathrm{O}}^{\bullet\bullet}$ and O_{v}'', are of interest for the change in electron hole concentration. Together with their relative neutral counterpart, they are in the following relation:

$$[\mathrm{O}_{\mathrm{O}}^{\times}] + [\mathrm{v}_{\mathrm{O}}^{\bullet\bullet}] = 54 \qquad \text{and} \qquad [\mathrm{O}_{v}''] + [v_{v}^{\times}] = 2 \tag{7.26}$$

The total concentration of oxygen at time t is the sum of all occupied oxygen ions in the anion sublattice, converting from defect fraction to volume concentration according to Eq. (2.1),

$$c_{\mathrm{O}}(t) = \left([\mathrm{O}_{v}''](t) + [\mathrm{O}_{\mathrm{O}}^{\times}](t)\right) \cdot \frac{1}{N_{\mathrm{A}} \cdot V_{\mathrm{UC}}} \tag{7.27}$$

In Eq. (7.25), only charged defects occur. $[\mathrm{O}_{\mathrm{O}}^{\times}]$ must be replaced by the oxygen vacancy concentration by inserting Eq. (7.26) into Eq. (7.27), yielding

$$c_{\mathrm{O}}(t) = \left([\mathrm{O}_{v}''](t) + 54 - [\mathrm{v}_{\mathrm{O}}^{\bullet\bullet}](t)\right) \cdot \frac{1}{N_{\mathrm{A}} \cdot V_{\mathrm{UC}}} \tag{7.28}$$

In Eq. (7.25), the *change* in oxygen (vacancy) concentration with time is used, hence the summand 54 is removed:

$$c_{\mathrm{O}}(t) - c_{\mathrm{O}}^{0} = \left[\left([\mathrm{O}_v''](t) - [\mathrm{O}_v'']^0\right) - \left([\mathrm{v}_{\mathrm{O}}^{\bullet\bullet}](t) - [\mathrm{v}_{\mathrm{O}}^{\bullet\bullet}]^0\right)\right] \cdot \frac{1}{N_{\mathrm{A}} \cdot V_{\mathrm{UC}}} \tag{7.29}$$

The time-dependent volume concentration (converted with Eq. (2.1)) of electron holes can be written as

$$c_{\mathrm{h}\bullet}(t) = c_{\mathrm{h}\bullet}^{0} + 2\left[c_{\mathrm{O}}(t) - c_{\mathrm{O}}^{0}\right] - \left[c_{\mathrm{H}}(t) - c_{\mathrm{H}}^{0}\right] \tag{7.30}$$

by inserting Eq. (7.29) into Eq. (7.25) and converting the protonic defect fraction into a volume concentration.

The concentrations of oxygen and hydrogen at time t have been analyzed in Section 7.2.2.1. They are defined in Eq. (7.12) and the simplified hydrogen concentration in Eq. (7.21) and can be inserted into Eq. (7.30). The oxygen concentration and the change in hydrogen concentration, which is dependent on the change in oxygen concentration, is merged as a prefactor for the slow kinetic's function, yielding

$$\begin{aligned} c_{\mathrm{h}\bullet}(t) =& c_{\mathrm{h}\bullet}^{0} \\ &+ \left\{2\left[c_{\mathrm{O}}^{\infty} - c_{\mathrm{O}}^{0}\right] - \left[c_{\mathrm{H}}^{\infty}([\mathrm{v}_{\mathrm{O}}^{\bullet\bullet}]^{\infty}) - c_{\mathrm{H}}^{\infty}([\mathrm{v}_{\mathrm{O}}^{\bullet\bullet}]^0)\right]\right\} \cdot \left(1 - e^{-\frac{k_{\mathrm{O}}}{a}t}\right) \\ &- \left[c_{\mathrm{H}}^{\infty}([\mathrm{v}_{\mathrm{O}}^{\bullet\bullet}]^0) - c_{\mathrm{H}}^{0}([\mathrm{v}_{\mathrm{O}}^{\bullet\bullet}]^0)\right] \cdot \left(1 - e^{-\frac{k_{\mathrm{H}}}{a}t}\right) \end{aligned} \tag{7.31}$$

When Eqs. (7.23) and (7.31) are combined, $E \cdot c_{\mathrm{h}\bullet}(t)$ can be split and assigned to the three power factors A, B and C, which now become the ambipolar power factors $\tilde{A}$, $\tilde{B}$, and $\tilde{C}$:

$$\sigma(t) = \tilde{A} + \tilde{B}\left(1 - e^{-\frac{\tilde{k}_{\mathrm{H}}}{a}t}\right) + \tilde{C}\left(1 - e^{-\frac{\tilde{k}_{\mathrm{O}}}{a}t}\right) \tag{7.32}$$

with

$$\tilde{A} = F\left[|z_{\mathrm{H}}|u_{\mathrm{H}}c_{\mathrm{H}}^{0} + |z_{\mathrm{O}}|u_{\mathrm{O}}c_{\mathrm{O}}^{0} + |z_{\mathrm{h}\bullet}|u_{\mathrm{h}\bullet}c_{\mathrm{h}\bullet}^{0} + \sum_{i,\mathrm{t-indep.}} |z_i|u_i c_i\right] \tag{7.33}$$

$$\tilde{B} = F\left[c_{\mathrm{H}}^{\infty}([\mathrm{v}_{\mathrm{O}}^{\bullet\bullet}]^0) - c_{\mathrm{H}}^{0}([\mathrm{v}_{\mathrm{O}}^{\bullet\bullet}]^0)\right](|z_{\mathrm{H}}|u_{\mathrm{H}} - |z_{\mathrm{h}\bullet}|u_{\mathrm{h}\bullet}) \tag{7.34}$$

$$\begin{aligned} \tilde{C} =& F\left[c_{\mathrm{O}}^{\infty} - c_{\mathrm{O}}^{0}\right](|z_{\mathrm{O}}|u_{\mathrm{O}} + 2|z_{\mathrm{h}\bullet}|u_{\mathrm{h}\bullet}) \\ &+ F\left[c_{\mathrm{H}}^{\infty}([\mathrm{v}_{\mathrm{O}}^{\bullet\bullet}]^{\infty}) - c_{\mathrm{H}}^{\infty}([\mathrm{v}_{\mathrm{O}}^{\bullet\bullet}]^0)\right](|z_{\mathrm{H}}|u_{\mathrm{H}} - |z_{\mathrm{h}\bullet}|u_{\mathrm{h}\bullet}) \end{aligned} \tag{7.35}$$

For time-independent contributions, $c_i = c_i^0$ is valid. Thus, the initial contributions of all charge carriers to the conductivity can be added up in the power factor $\tilde{A}$:

$$\tilde{A} = F\sum_i |z_i|u_i c_i^0 \tag{7.36}$$

7.2.2.4 Extending to the Diffusion Model with Surface Reaction Limitation

In first publications using two-fold relaxation techniques, a diffusion model without surface limitation has been used.[69, 70] Lim *et al.*[103] replaced the diffusion limited function by the diffusion model's function that is also used in this work, including a surface reation limitation:

$$f_{\tilde{D}}(t) \rightsquigarrow f_{\tilde{k},\tilde{D}}(t) = 1 - \sum_{i=1}^{\infty} \frac{2L_a^2 \cdot e^{-\frac{\beta_i^2 \tilde{D} t}{a}}}{\beta_i^2(\beta_i^2 + L_a^2 + L_a)} \tag{7.37}$$

However, the use of these functions is not unproblematic: the diffusion of both species is dependent on four diffusivities (see Section 3.2.3) and the surface reaction cannot be described by simple exponential functions in a general treatment (see previous section). In this section, the diffusion of both species will be treated first, followed by simplifications that have to be made in order to use $f_{\tilde{k},\tilde{D}}(t)$ to describe the relaxation behavior.
Fick's second law can be written in vector notation from Eqs. (3.33) and (3.34):

$$\dot{\vec{c}} = \begin{pmatrix} \dot{c}_{\mathrm{v}_\mathrm{O}^{\bullet\bullet}} \\ \dot{c}_{\mathrm{H}_\mathrm{i}^{\bullet}} \end{pmatrix} = \begin{pmatrix} D_{\mathrm{VV}} & D_{\mathrm{VH}} \\ D_{\mathrm{HV}} & D_{\mathrm{HH}} \end{pmatrix} \begin{pmatrix} c''_{\mathrm{v}_\mathrm{O}^{\bullet\bullet}} \\ c''_{\mathrm{H}_\mathrm{i}^{\bullet}} \end{pmatrix} = \boldsymbol{D}\vec{c}'' \tag{7.38}$$

To describe the fluxes with a diffusion model dependent on two effective diffusion coefficients, the matrix must be diagonalized, rendering Fick's second law

$$\boldsymbol{S}^T\dot{\vec{c}} = \boldsymbol{S}^T\boldsymbol{D}\boldsymbol{S}(\boldsymbol{S}^T\vec{c}'') \tag{7.39}$$

The matrix $\boldsymbol{D}$ can be diagonalized by finding the eigenvalue(s) λ so that the determinant of the matrix becomes zero,

$$\left|\begin{pmatrix} D_{\mathrm{VV}} - \lambda & D_{\mathrm{VH}} \\ D_{\mathrm{HV}} & D_{\mathrm{HH}} - \lambda \end{pmatrix}\right| = 0 \tag{7.40}$$

The eigenvalues λ_1 and λ_2 are

$$\lambda_{1,2} = \frac{D_{\mathrm{VV}} + D_{\mathrm{HH}}}{2} \pm \sqrt{\left(\frac{D_{\mathrm{VV}} + D_{\mathrm{HH}}}{2}\right)^2 - (D_{\mathrm{VV}}D_{\mathrm{HH}} - D_{\mathrm{HV}}D_{\mathrm{VH}})} \tag{7.41}$$

The normalized eigenvectors of the matrix $\boldsymbol{D}$ with normalization factors m and n, $m\vec{x}_1$ and $n\vec{x}_2$, are accordingly

$$m\vec{x}_1 = \begin{pmatrix} -\frac{mD_{\mathrm{VH}}}{D_{\mathrm{VV}}-\lambda_1} \\ m \end{pmatrix} \quad \text{and} \quad n\vec{x}_2 = \begin{pmatrix} -\frac{nD_{\mathrm{VH}}}{D_{\mathrm{VV}}-\lambda_2} \\ n \end{pmatrix} \tag{7.42}$$

The matrices $\boldsymbol{S}$ and $\boldsymbol{S}^T$ used to diagonalize the matrix $\boldsymbol{D}$ can be derived from the eigenvectors

$$\boldsymbol{S} = \begin{pmatrix} -\frac{mD_{\mathrm{VH}}}{D_{\mathrm{VV}}-\lambda_1} & -\frac{nD_{\mathrm{VH}}}{D_{\mathrm{VV}}-\lambda_2} \\ m & n \end{pmatrix} \quad \text{and} \quad \boldsymbol{S}^T = \begin{pmatrix} -\frac{mD_{\mathrm{VH}}}{D_{\mathrm{VV}}-\lambda_1} & m \\ -\frac{nD_{\mathrm{VH}}}{D_{\mathrm{VV}}-\lambda_2} & n \end{pmatrix} \tag{7.43}$$

A new concentration vector, $\vec{\tilde{c}} = \boldsymbol{S}^T \vec{c}$, can be used to describe Fick's second law dependent on the eigenvalues and the derivation of only one (decoupled) concentration, $\tilde{c}_i$. The eigenvalues are the effective diffusion coefficients, $\lambda_1 = D_{\mathrm{V}}^{\mathrm{eff}}$ and $\lambda_2 = D_{\mathrm{H}}^{\mathrm{eff}}$.

$$\dot{\tilde{c}}_1 = \lambda_1 \tilde{c}_1'' \tag{7.44}$$

$$\dot{\tilde{c}}_2 = \lambda_2 \tilde{c}_2'' \tag{7.45}$$

The concentration profiles of the new concentrations $\tilde{c}_i$ can be described by the analytical solution of the diffusion model using diffusion limitation only[85]

$$\frac{\tilde{c}_i(x,t) - \tilde{c}_i^0}{\tilde{c}_i^\infty - \tilde{c}_i^0} = 1 - \frac{4}{\pi} \sum_{n=0}^{\infty} \frac{(-1)^n}{2n+1} \cdot \cos\left(\frac{(2n+1)\pi x}{2a}\right) \cdot \exp\left\{-\frac{(2n+1)^2 \pi^2 \lambda_i t}{4a^2}\right\} \tag{7.46}$$

In a final step, the decoupled concentrations $\vec{\tilde{c}}$ can be transformed to the concentrations of the species using the matrix $\boldsymbol{S}$ by

$$\begin{pmatrix} c_{\mathrm{V}_{\mathrm{O}}^{\bullet\bullet}} \\ c_{\mathrm{H}_{\mathrm{i}}^{\bullet}} \end{pmatrix} = \boldsymbol{S} \begin{pmatrix} \tilde{c}_1 \\ \tilde{c}_2 \end{pmatrix} \tag{7.47}$$

The resulting concentration profiles of each species can be described with pre-factors by

$$c_{\mathrm{V}_{\mathrm{O}}^{\bullet\bullet}}(x,t) = -\frac{m D_{\mathrm{VH}}}{D_{\mathrm{VV}} - \lambda_1} \cdot \tilde{c}_1(x,t,\lambda_1) - \frac{n D_{\mathrm{VH}}}{D_{\mathrm{VV}} - \lambda_2} \cdot \tilde{c}_2(x,t,\lambda_2) \tag{7.48}$$

$$c_{\mathrm{H}_{\mathrm{i}}^{\bullet}}(x,t) = m \cdot \tilde{c}_1(x,t,\lambda_1) + n \cdot \tilde{c}_2(x,t,\lambda_2) \tag{7.49}$$

The resulting total conductivity, $\sigma(t) = F \sum_i |z_i| u_i c_i(t)$, can be expressed by integration of the concentration profiles of each species over length a in the one-dimensional treatment. The electron hole concentration must be included, which is given by the electroneutrality condition and Eqs. (7.48) and (7.49).

If the surface reaction has to be added to the diffusion model an analytical solution is not possible as the equilibrium concentrations, c_i^∞, are functions of time. The problem must be solved numerically. However, there are cases that can be treated with the analytical function: i) the electron hole concentration or mobility is zero resulting in single fold relaxation; ii) all diffusivities are equal resulting also in a single fold relaxation and iii) one of the cross-coefficients is negligible. The latter case will be examined further as this simplification can be used for the material and experimental conditions that have been investigated in this work.

The transference number of oxygen vacancies, $t_{\mathrm{V}_{\mathrm{O}}^{\bullet\bullet}}$, is very small rendering D_{VH} small (see Eq. (3.36)). As a consequence the second pre-factor of Eq. (7.48) is approximately zero and $n \approx 1$. The concentration of oxygen vacancies is thus independent of the gradient in concentration $\tilde{c}_2$, which itself has a negligible contribution of oxygen vacancy concentration. With small D_{VH} the effective diffusion coefficient for oxygen vacancies becomes $\lambda_1 \approx D_{\mathrm{VV}}$. The transference number of oxygen

vacancies, however, cannot become exactly zero as this would mean that no oxygen diffusion is possible. With

$$\frac{D_{\mathrm{VH}}}{D_{\mathrm{VV}}-\lambda}=\frac{D_{\mathrm{HH}}-\lambda}{D_{\mathrm{HV}}} \tag{7.50}$$

the resulting division of two very small values (left side) can be replaced by the right side of Eq. (7.50). The time-dependent concentration profile of oxygen vacancies, Eq. (7.48), can thus be transformed into

$$c_{\mathrm{v_O^{\bullet\bullet}}}(x,t)=-\frac{m\,(D_{\mathrm{HH}}-\lambda_1)}{D_{\mathrm{HV}}}\cdot\tilde{c}_1(x,t,\lambda_1)-\frac{nD_{\mathrm{VH}}}{D_{\mathrm{VV}}-\lambda_2}\cdot\tilde{c}_2(x,t,\lambda_2) \tag{7.51}$$

The first pre-factor of Eq. (7.51) is usually not negligible and as a consequence, the normalization factor m is not near zero or unity, rendering both, the concentration of oxygen vacancies and of proton interstitials, a function of λ_1, which is the effective diffusion coefficient of oxygen vacancies. The concentration $\tilde{c}_1$ has contributions of the oxygen vacancy concentration and proton interstitial concentration. The cross-coefficients have a large impact on the pre-factors but with $\lambda_1 \approx D_{\mathrm{VV}}$ and $\lambda_2 \approx D_{\mathrm{HH}}$ they are negligible for describing the shape of the concentration profiles, $\tilde{c}_i(x,t,\lambda_i)$.
The oxygen concentration shows a single fold concentration profile and, by integration, a single fold relaxation curve. The boundary condition at the surface is fulfilled: the surface reaction has an equilibrium concentration of oxygen that is independent of time linked with Fick's first law dependent on the effective diffusion coefficient of oxygen (see Eq. (4.15)). For the hydrogen concentration, the boundary condition is, however, more complex:

$$\begin{aligned}\tilde{k}_{\mathrm{H}}\left\{c_{\mathrm{H}}^{\infty}([\mathrm{v_O^{\bullet\bullet}}]^0)+\left[c_{\mathrm{H}}^{\infty}([\mathrm{v_O^{\bullet\bullet}}]^{\infty})-c_{\mathrm{H}}^{\infty}([\mathrm{v_O^{\bullet\bullet}}]^0)\right]\cdot f_{\tilde{k}_{\mathrm{O}},\tilde{D}_{\mathrm{O}}}(x=-a,t)-c_{\mathrm{H}}^{\mathrm{surf}}(t)\right\}\\ =-\lambda_1\frac{\partial^2 m\tilde{c}_1}{\partial x^2}-\lambda_2\frac{\partial^2 n\tilde{c}_2}{\partial x^2}\end{aligned} \tag{7.52}$$

The contribution of proton interstitial concentration to the concentration $\tilde{c}_1$ is $m\tilde{c}_1$ and the part that changes with oxygen vacancy concentration. With $n \approx 1$ the concentration $\tilde{c}_2$ has a negligible contribution of the oxygen vacancy concentration and with $\lambda_2 \gg \lambda_1$ and $\tilde{k}_{\mathrm{H}} \gg \tilde{k}_{\mathrm{O}}$ the oxygen vacancy concentration of the initial state is used. The concentrations used on the left side of Eq. (7.52) and in the derivation of the power factors can be set into relation to the concentrations used on the right side: $c_{\mathrm{H}}^{\infty}([\mathrm{v_O^{\bullet\bullet}}]^{\infty})-c_{\mathrm{H}}^{\infty}([\mathrm{v_O^{\bullet\bullet}}]^0)=m(\tilde{c}_1^{\infty}-\tilde{c}_1^0)$ and $c_{\mathrm{H}}^{\infty}([\mathrm{v_O^{\bullet\bullet}}]^0)-c_{\mathrm{H}}^0([\mathrm{v_O^{\bullet\bullet}}]^0)=n(\tilde{c}_2^{\infty}-\tilde{c}_2^0)$. The power factors for surface reaction and diffusion limited relaxations with small $t_{\mathrm{v_O^{\bullet\bullet}}}$ and the power factors derived in Section 7.2.2 are similar. They cannot be used if the diffusion model is not described by an analytical but a numerical solution. The experimental curves can be fitted by the analytical solution and effective diffusion coefficients near the direct diffusion coefficients can be assumed for the relaxation experiments used in this work.

7.2.2.5 Detailed Analysis of Surface Reaction Kinetics

In Section 3.1.4, the kinetics of the surface reaction upon hydration have been discussed phenomenologically. In this section, a detailed analysis of the surface reaction kinetics with exemplary rate determining steps will be presented. The exact mechanism is, however, unknown.
In the first step, a water molecule from the gas phase is adsorbed at the surface. This reaction should be very fast and is thus in pre-equilibrium. The reaction and corresponding law of mass action is

$$H_2O(g) \rightleftharpoons H_2O_{ad} \qquad \text{with} \qquad K_1 = \frac{[H_2O_{ad}]}{pH_2O} \tag{7.53}$$

In the second step, the adsorbed water molecule dissociates into two adsorbed hydrogen atoms and an oxygen atom. This reaction is most likely not concerted but can be combined to a single reaction as it should also be very fast and in pre-equilibrium:

$$H_2O_{ad} \rightleftharpoons 2H_{ad} + O_{ad} \qquad \text{with} \qquad K_2 = \frac{[H_{ad}]^2[O_{ad}]}{[H_2O_{ad}]} \tag{7.54}$$

The adsorbed hydrogen atom can be incorporated into the bulk phase at the expense of an electron hole. This should be the rate determining step for the incorporation of hydrogen. It is a single electron transfer and a first order reaction is likely.

$$H_{ad} + h^\bullet \underset{\overleftarrow{k}_H}{\overset{\vec{k}_H}{\rightleftharpoons}} H_i^\bullet \qquad \text{with} \qquad K_3 = \frac{\vec{k}_H}{\overleftarrow{k}_H} = \frac{[H_i^\bullet]}{[H_{ad}][h^\bullet]} \tag{7.55}$$

Adsorbed oxygen requires a vacancy for the incorporation, creating two electron holes. The transfer of the second electron is assumed to be the rate determining step, here. Thus, the first electron transfer is also in pre-equilibrium. The law of mass action is shown for the second, rate determining reaction step.

$$O_{ad} + v_O^{\bullet\bullet} \rightleftharpoons O_{ad}^- + v_O^{\bullet\bullet} + h^\bullet \underset{\overleftarrow{k}_O}{\overset{\vec{k}_O}{\rightleftharpoons}} O_O^\times + 2h^\bullet \qquad \text{with} \qquad K_5 = \frac{\vec{k}_O}{\overleftarrow{k}_O} = \frac{[O_O^\times][h^\bullet]}{[O_{ad}^-][v_O^{\bullet\bullet}]} \tag{7.56}$$

For a small change in pH_2O the fractions of the species involved in the rate determining reaction are changed by a small amount (x for Eq. (7.55) and y for Eq. (7.56)). The defect fractions are dependent on the equilibrium defect fractions and the change x and/or y, respectively:

$$\begin{aligned} [H_{ad}] &= [H_{ad}]^{eq} - x & [H_i^\bullet] &= [H_i^\bullet]^{eq} + x \\ [h^\bullet] &= [h^\bullet]^{eq} - x + y & [O_{ad}^-] &= [O_{ad}^-]^{eq} - y \\ [v_O^{\bullet\bullet}] &= [v_O^{\bullet\bullet}]^{eq} - y & [O_O^\times] &= [O_O^\times]^{eq} + y \end{aligned} \tag{7.57}$$

The derivatives with respect to time of the variables x and y and thereby the change of the concentrations of hydrogen (proton interstitials) and oxygen are

$$\frac{dx}{dt} = \frac{dc_H}{dt} = \vec{k}_H([H_{ad}]^{eq} - x)([h^\bullet]^{eq} - x + y) - \overleftarrow{k}_H([H_i^\bullet]^{eq} + x) \tag{7.58}$$

$$\frac{dy}{dt} = \frac{dc_O}{dt} = \vec{k}_O([O_{ad}^-]^{eq} - y)([v_O^{\bullet\bullet}]^{eq} - y) - \overleftarrow{k}_O([O_O^\times]^{eq} + y)([h^\bullet]^{eq} - x + y) \tag{7.59}$$

Only the terms that are linearly dependent on x or y are considered, yielding a matrix for $\dot{x}$ and $\dot{y}$:

$$\begin{pmatrix} \dot{x} \\ \dot{y} \end{pmatrix} = \begin{pmatrix} \vec{k}_H([h^\bullet]^{eq} - [H_{ad}]^{eq}) - \overleftarrow{k}_H & \vec{k}_H[H_{ad}]^{eq} \\ \overleftarrow{k}_O[O_O^\times]^{eq} & -\vec{k}_O([O_{ad}^-]^{eq} + [v_O^{\bullet\bullet}]^{eq}) - \overleftarrow{k}_O([O_O^\times]^{eq} + [h^\bullet]^{eq}) \end{pmatrix} \begin{pmatrix} x \\ y \end{pmatrix} \tag{7.60}$$

This matrix can be diagonalized analogously to the matrix of the diffusion fluxes, Eq. (7.38). Two new variables, $\tilde{x}$ and $\tilde{y}$, are obtained, each consisting of the diagonalized parts of x and y, with the eigenvalues λ of the matrix as surface reaction constants:

$$\dot{\tilde{x}} = \lambda_1 \tilde{x} \tag{7.61}$$

$$\dot{\tilde{y}} = \lambda_2 \tilde{y} \tag{7.62}$$

By integration, two simple exponential functions are obtained, one with the fast effective hydrogen kinetic ($\lambda_1 \equiv \tilde{k}_H$) and one with the slow effective oxygen kinetic ($\lambda_2 \equiv \tilde{k}_O$). Analogously to the diffusion limited case, the concentration change of hydrogen and oxygen is dependent on both kinetics. However, the contribution of the oxygen content to the fast kinetic has been neglected in Section 7.2.2.1. The approach of using two simple exponential functions for the change in hydrogen concentration — one with a fast hydrogen kinetic and one with a slow oxygen kinetic — is consistent with the derivation in this section.

The precise boundary condition for the surface exchange, see Eq. (7.52) in the previous section, would require the surface reaction kinetics discussed here. However, the surface reaction and the diffusion flux cannot be linked directly as the diagonalized concentrations in both cases are different, $\tilde{x} \neq \tilde{c}_1$ and $\tilde{y} \neq \tilde{c}_2$. The eigenvalues, λ, used in Eqs. (7.61) and (7.62) are, of course, different from the eigenvalues used in Eqs. (7.44) and (7.45). If the contribution of oxygen to the fast kinetic is to be negected, D_{VH} (see previous section) and $\overleftarrow{k}_O[O_O^\times]^{eq}$ must be small.

7.2.2.6 Influence on Two-fold Relaxation Curves

The power factor $\tilde{A}$ describes the initial contribution of each charged species to the conductivity. Multiple concentrations, charges and charge mobilities are summarized here and cannot be further determined.

The power factor $\tilde{B}$ describes the contribution of the fast kinetic assigned to hydrogen but it does not contain the entire concentration change of hydrogen and its corresponding change in electron hole concentration. Only the concentration change for the initial oxygen vacancy concentration is reflected here. The power factor $\tilde{B}$ is connected to the time-dependent concentration change in hydrogen concentration of the bulk, which is always positive, if the pH_2O is increased (hydration). The value of $\tilde{B}$ is determined by a competition between electron hole and proton mobility. Electron holes are usually more mobile than protons, thus $\tilde{B}$ is negative for hydrating steps. The charge of both defects is +1. Consequently, the initial drop in conductivity upon hydration is compensated by

high proton mobility. The high proton mobility is also responsible for the increase of conductivity upon hydration though the concentration of electron holes is slightly decreased overall. At low temperatures like 700 °C, the power factor $\tilde{B}$ is positive upon hydration. In this case, protons show a higher mobility than electron holes, rendering the term $|z_H|u_H - |z_{h\bullet}|u_{h\bullet}$ positive, assuming an equal charge of both defects.

The power factor $\tilde{C}$ contains the total change in oxygen concentration. From the incorporation equation of water, Eq. (3.10), one oxygen ion is incorporated together with two protons. However, due to the decrease in oxygen vacancy concentration, the equilibrium in Eq. (3.1) is shifted to the left side. Hence, the change in oxygen concentration is less than twice the total change in hydrogen concentration. The change in hydrogen concentration, which is dependent on the change in oxygen vacancy concentration is also influencing the power factor $\tilde{C}$. If the proton mobility is lower than the mobility of electron holes, the power factor $\tilde{C}$ is decreased. At low temperatures, the mobility of electron holes is lower than the mobility of protons, hence the power factor $\tilde{C}$ is increased upon hydration.

7.2.2.7 Normalization of Two-fold Relaxation Curves

As the transport parameters are determined from the shape of the relaxation curve and the diffusion model is defined for a normalized time-dependent concentration curve, $M(t)/M^{\infty}$, single fold relaxation curves, e.g. upon oxidation or reduction, are often normalized with Eq. (4.6). The use of normalized curves for fitting to two-fold relaxation curves is also possible. Two new amplitude factors, A_H corresponding to $\tilde{B}$ and A_O corresponding to $\tilde{C}$, describe the contribution of each single fold curve.[70] The sum of both amplitude factors is unity, $A_H + A_O = 1$. The amplitude factors A_H and A_O can be set into relation with the power factors $\tilde{B}$ and $\tilde{C}$ by

$$A_H = \frac{\tilde{B}}{\tilde{B} + \tilde{C}} \qquad \text{and} \qquad A_O = \frac{\tilde{C}}{\tilde{B} + \tilde{C}} \tag{7.63}$$

The power factor $\tilde{A}$ is the offset of the relaxation curve, σ^0. The normalized curve however, starts at zero. The time-dependent normalized conductivity curve with surface reaction limitation can be described by

$$\sigma_{norm}(t) = 1 - \left(A_H \cdot e^{-\frac{\tilde{k}_H}{a} t} + A_O \cdot e^{-\frac{\tilde{k}_O}{a} t} \right) \tag{7.64}$$

For normalized curves, the change in normalized conductivity is always $\Delta\sigma_{norm} = +1$. Using the (not normalized) total conductivity, $\Delta\sigma$ can be negative. In a special case, if $\Delta\sigma = \tilde{B} + \tilde{C} = 0$, a normalization is not possible. The amplitude factors A_O and A_H in Eq. (7.63) are not defined and also the normalization function, Eq. (4.6), is not defined because of a division by zero.

7.2.3 Influence of Power Factors for Dehydrating Steps

The relaxation curve for a dehydrating step, $\Delta p\mathrm{H_2O} < 0$, has been discussed in Section 7.1.4. The two-fold non-monotonic behavior for high temperatures, 950 °C, has power factors with different signs than for hydration. Transport parameters, except for the surface reaction of hydrogen, are approximately equal to the transport parameters for hydrating steps. This behavior is expected as the transport parameters are determined for the final conditions.

The absolute values of the power factors, however, differ from the power factors of hydrating steps. This can be compared with the difference in $\Delta\delta$ for reductive and oxidative steps, described in Section 7.1.4. The difference in hydrogen concentration should not be equal for hydrating and dehydrating steps although the thermodynamic factor for water or hydrogen is not known.

The power factor $\tilde{B}$, however, states that the surface reaction constant and the diffusion coefficient for hydrogen are determined not for the final oxygen vacancy concentration but for the initial oxygen vacancy concentration (see Eq. (7.34)). The oxygen vacancy concentration is dependent on the $p\mathrm{O_2}$, which is equal for hydrating and dehydrating steps before and after switching to the second stream, but also on $p\mathrm{H_2O}$. The initial $p\mathrm{H_2O}$ differs for both steps by one order of magnitude. This cannot only explain the difference in the power factors but also the difference for the transport parameters of hydrogen for hydrating and dehydrating steps.

7.2.4 Dependence on the Partial Pressure of Oxygen

Two relaxation curves at 950 °C have already been presented in Sections 7.1 and 7.2.1.1. The result showed that the two-fold behavior is less pronounced for lower $p\mathrm{O_2}$. The $p\mathrm{O_2}$-dependence of hydrating steps from 10 mbar $p\mathrm{H_2O}$ to 30 mbar at 950 °C is shown in Figs. 7.13 and 7.14. The transport parameters in Fig. 7.13 do not indicate a clear dependence on $p\mathrm{O_2}$. The diffusion coefficients (blue symbols) increase slightly with decreasing $p\mathrm{O_2}$ and the surface reaction rates scatter. For a $p\mathrm{O_2}$ of 100 mbar, the surface reaction rate of hydrogen is near the limit of the determinability (see Section 7.1.3), indicated by large error bars.

In contrast, the power factors show a clear dependence on $p\mathrm{O_2}$, see Fig. 7.14. The total conductivity is decreasing significantly, caused by a decrease in electron hole concentration. However, the proton concentration is slightly increased with decreasing $p\mathrm{O_2}$. The $p\mathrm{O_2}$-dependence of defect fractions has been simulated with arbitrary equilibrium constants in Fig. 2.8. The mobility of the defects involved does not show a huge dependence on $p\mathrm{O_2}$ as the diffusion coefficients of hydrogen and oxygen are almost independent of $p\mathrm{O_2}$. The fact that the two-fold behavior is less pronounced is reflected in the $p\mathrm{O_2}$-dependence of the power factor $\tilde{B}$, which approaches zero, and the relation between $\tilde{B}$ and $\tilde{C}$: at low $p\mathrm{O_2}$, $\tilde{C}/\tilde{B}$ is much larger. The mobilities of the defects involved are also contributing to the power factors $\tilde{B}$ and $\tilde{C}$, but as discussed above, they do not change significantly with $p\mathrm{O_2}$. A definite statement on the change in proton concentration cannot be made as the change is split into both power factors. A lower $\tilde{B}$ is caused by a lower concentration change of protons for

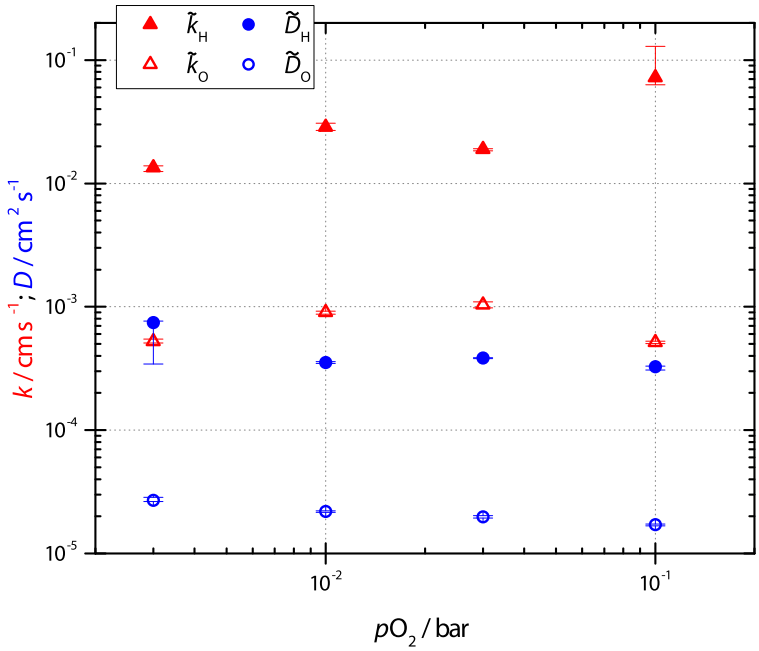

Figure 7.13: Transport parameters in dependency of the pO_2 at 950 °C for hydrating steps with ΔpH_2O = 20 mbar (10 mbar → 30 mbar). Closed symbols are the parameters for the fast kinetic, open symbols for the slow kinetic.

the initial oxygen vacancy concentration. However, a part of the change in proton concentration is lowering $\tilde{C}$ at high temperatures. $\tilde{C}$ is, in fact, lower for lower pO_2, but this can also be caused by a lower difference in oxygen concentration. Knowledge of the equilibrium constants K_{O_2} and K_{H_2O}, and corresponding reference points would give a deeper insight into this dependence.

7.2.5 Dependence on Temperature — Arrhenius Plots

With decreasing temperature, the relaxation curves switch from two-fold non-monotonic to two-fold monotonic behavior. The transport parameters are significantly lower. In Fig. 7.15, the transport parameters upon hydration at pO_2 = 100 mbar are plotted against the inverse temperature in a temperature range from 650 °C to 950 °C. The transport parameters for oxygen, $\tilde{k}_O$ and $\tilde{D}_O$, could be determined in the entire temperature regime and show a clear dependence on temperature. They increase with increasing temperature linearly in an Arrhenius plot. The corresponding dimensionless parameters L_a are plotted in Fig. 7.16 as black symbols. The transport parameters for oxygen can be determined simultaneously. However, the transport parameters of hydrogen (closed symbols in Fig. 7.15) show only a linear behavior for temperatures at or above 750 °C. The surface reaction rate of hydrogen at 950 °C is near the limit of the determinability (see Fig. 7.16), causing a large error bar. For 700 °C, both parameters could be determined ($L_{a,H}(700\,°C) \approx 0.9$), but they are not within the trend of higher temperatures. The influence of the fast kinetic on the relaxation

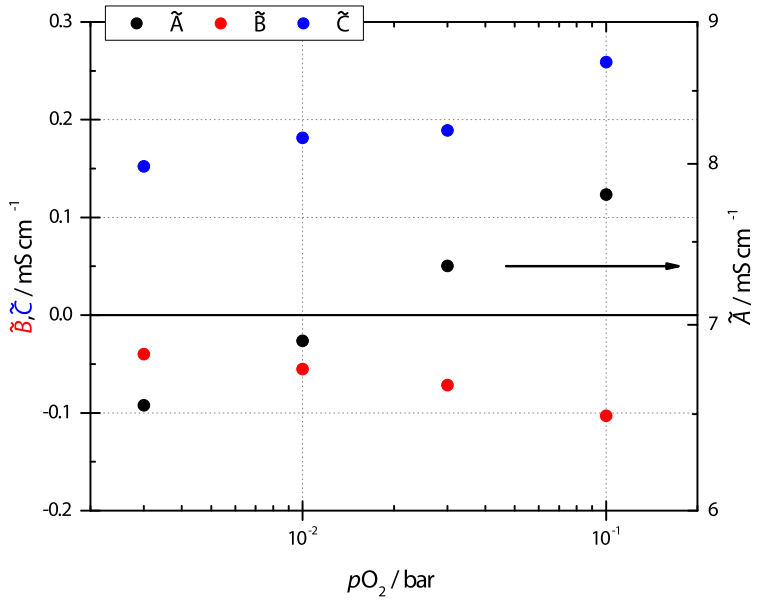

Figure 7.14: Power factors in dependency of pO_2 at 950 °C for hydrating steps with ΔpH_2O = 20 mbar (10 mbar → 30 mbar). The initial conductivity, σ^0 or $\tilde{A}$, is plotted at the right y-scale.

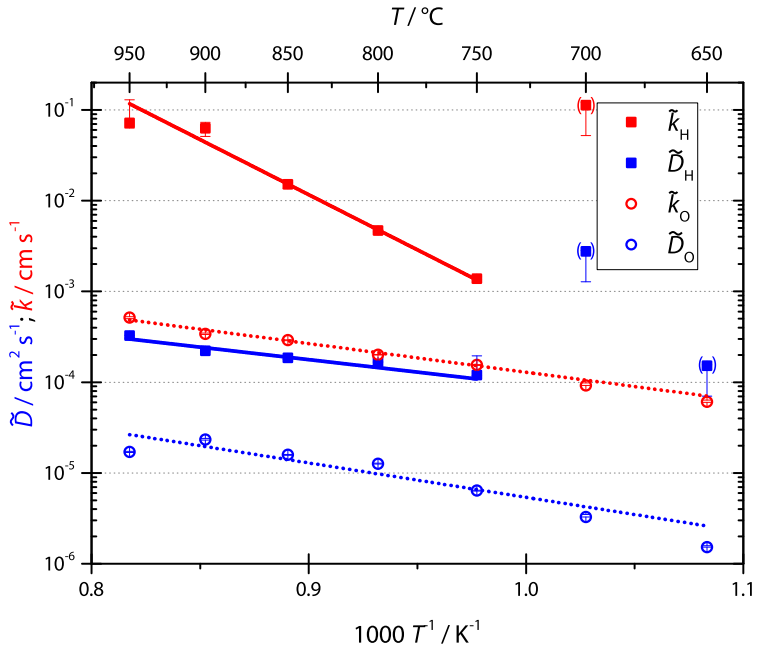

Figure 7.15: Transport parameters versus the inverse temperature for hydrating steps with ΔpH_2O = 20 mbar (10 mbar → 30 mbar) for a pO_2 of 100 mbar.

curve is very small at this temperature, hence the fit is not very sensitive to the parameters of the fast kinetic. This is also reflected in large error bars. For 650 °C, the fit is independent of the surface reaction rate of hydrogen. The diffusion coefficient is, however, approximately within the trend of

the diffusion coefficient of hydrogen at larger temperatures. The corresponding power factors are

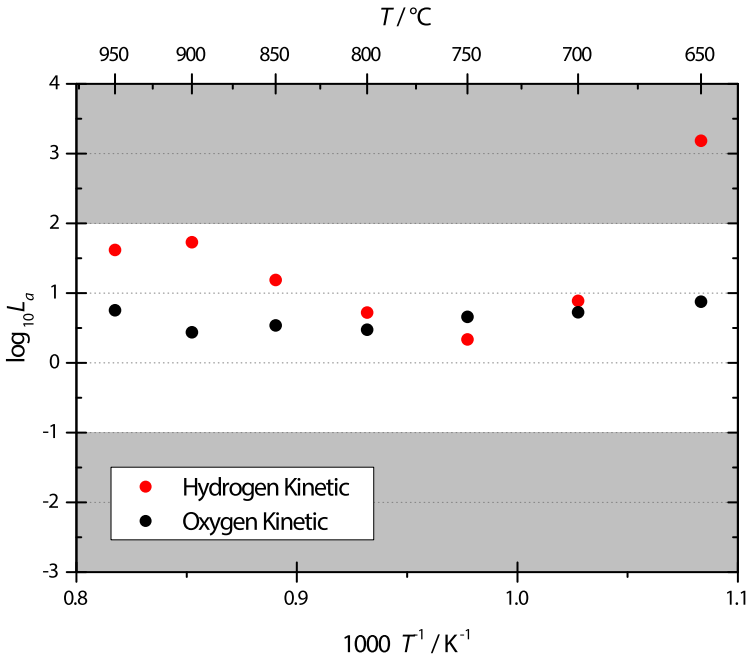

Figure 7.16: The dimensionless parameter $L_a = a\tilde{k}/\tilde{D}$ versus inverse temperature for the transport parameters plotted in Fig. 7.15. The gray area encloses the regime with simultaneous determinability of both parameters.

shown in Fig. 7.18. The initial conductivity, σ^0 or $\tilde{A}$, also shows linear behavior in an Arrhenius plot. However, a small curvature can be interpreted, which will correspond to the results of Haugsrud and Kjølseth[5] in Fig. 2.10. They have measured the total conductivity in a larger temperature range, with a curvature for high $p\mathrm{H_2O}$.

The power factors of the fast hydrogen kinetic, $\tilde{B}$, increase with decreasing temperature upon hydration. Between 700 °C and 750 °C, the power factor switches the sign. For higher temperatures, the charge mobility of electron holes is higher than the charge mobility of protons. At lower temperatures, it is vice versa. For $\tilde{B} = 0$, both mobilities are equal, assuming a charge of +1. The resulting relaxation curve would be single fold although three independent mobile charge carriers are present. A sketch of the charge mobilities of protons and electron holes is shown in Fig. 7.17. The activation energy for electron holes is much higher than for protons. However, exact values for the activation energies cannot be determined with the methods used in this work.

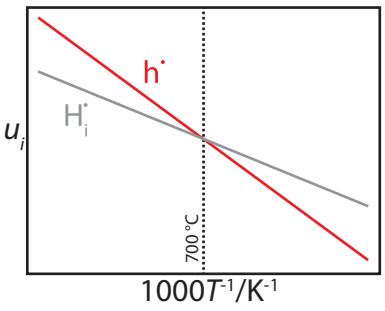

Figure 7.17: Sketch of the charge mobilities of hydrogen and electron holes versus inverse temperature.

The power factor $\tilde{C}$ does not show a clear dependence on temperature. The mobility of all charge carriers decreases with decreasing temperature according to the Nernst–Einstein equation, Eq. (3.30). The difference in oxygen non-stoichiometry also decreases. The dampening of the curve by the hydrogen concentration change with slow kinetic is turned into an amplification of the curve below approx. 700 °C. However, this might also just be scattering like for the pO_2-dependence in Fig. 7.14.

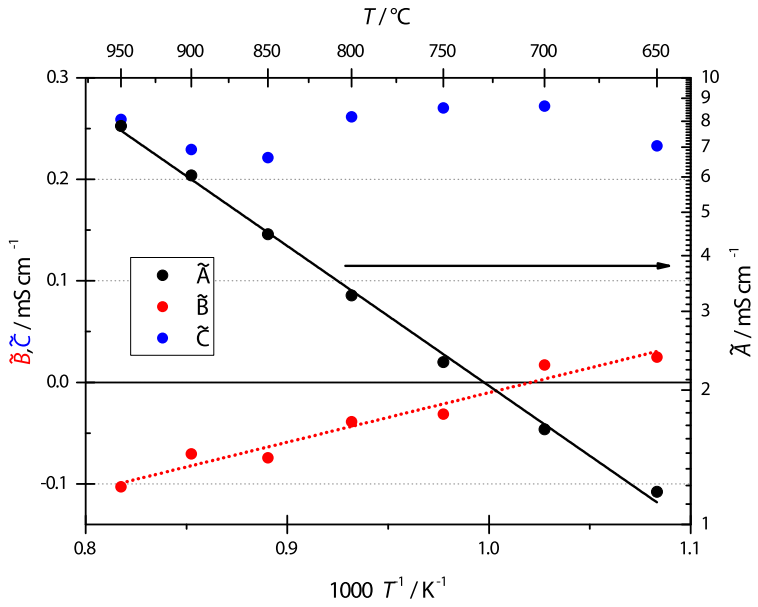

Figure 7.18: Power factors versus the inverse temperature for hydrating steps with ΔpH_2O = 20 mbar (10 mbar → 30 mbar) for a pO_2 of 100 mbar. The initial conductivity, σ^0 or $\tilde{A}$, are plotted on the right y-scale.

For the transport parameters and the total conductivity (for a different pH_2O as the transport parameters are determined for the final pH_2O), the activation energy can be calculated with

$$\tilde{k} = \tilde{k}^{\ominus} \cdot e^{-\frac{E_A}{RT}}, \qquad \tilde{D} = \tilde{D}^{\ominus} \cdot e^{-\frac{E_A}{RT}} \qquad \text{and} \qquad \sigma = \sigma^{\ominus} \cdot e^{-\frac{E_A}{RT}} \tag{7.65}$$

from the slope in the Arrhenius plots, Figs. 7.15 and 7.18. The resulting activation energies are summarized in Tab. 7.6 in kJ mol^{-1} and in eV.

The activation energies for $\tilde{D}_H$, $\tilde{k}_O$ and $\tilde{D}_O$ are rather low while the activation energy of the fast kinetic's surface reaction rate is very high compared to typical activation energies upon oxidation ($E_A(\tilde{k}_{ox})$ = 1.3(2) eV and $E_A(\tilde{D}_{ox})$ = 1.1(2) eV determined by Solís *et al.*[38] for LaWO54). The low activation energy for the surface reaction rate of oxygen, $\tilde{k}_O$, might be attributed to the fact that the source of oxygen is important for the incorporation kinetic. This has been shown for barium titanate by Kessel *et al.*[53] and for YSZ by Pietrowski *et al.*[54] as well. Hence, the oxidation behavior will be investigated in Section 7.3.

Table 7.6: Activation energies for hydrating steps with ΔpH_2O = 20 mbar (10 mbar → 30 mbar) and pO_2 = 100 mbar.

Parameter	E_A/kJ mol^{-1}	E_A/eV
$\tilde{k}_H$	220 ± 22	2.28 ± 0.22
$\tilde{D}_H$	47 ± 6	0.49 ± 0.07
$\tilde{k}_O$	65 ± 2	0.67 ± 0.02
$\tilde{D}_O$	83 ± 11	0.86 ± 0.12
σ^0	60 ± 1	0.62 ± 0.01

The results presented here are in agreement with the results presented by Solís *et al.* for hydration kinetics ($E_A(\tilde{k}_O) = 0.57(10)$ eV and $E_A(\tilde{D}_O) = 0.58(20)$ eV).[38] They have studied the relaxation behavior upon hydration near the regime where proton and electron hole mobilities are equal. Hence, the two-fold behavior cannot be identified because of low absolute $\tilde{B}$. Additionally, they switched from dry to wet O_2, resulting in a small ΔpO_2.
They are also in agreement with the statement of Magrasó and Haugsrud that LaWO54 has little electronic contribution to the total conductivity below 700 °C.[10] The concentration is yet high enough to ensure the change in electron hole concentration, which is necessary for the hydration with three independent mobile charge carriers.

7.3 Electrical Conductivity Relaxation upon Oxidation

The relaxation behavior upon oxidation has been investigated to show that the incorporation of oxygen originating from water is favored over that from oxygen molecules. For oxidation reactions, the pH_2O remains constant while changing the pO_2, $\Delta pH_2O = 0$ and $\Delta pO_2 > 0$. The first experiments were conducted under dry conditions with a step in pO_2 from 30 mbar to 100 mbar. The relaxation curve is shown in Fig. 7.19. The first peculiarity is the short relaxation time.
The transport parameters obtained by fitting the classical diffusion model to the single fold relaxation curves upon oxidation, $\tilde{k}_{ox}$ and $\tilde{D}_{ox}$, are plotted as closed symbols versus the inverse temperature in Fig. 7.20 in a temperature range from 700 °C to 950 °C. As a reference, the transport parameters of oxygen upon hydration are plotted with open symbols.
The experimental results of the oxidation kinetic are in agreement with Solís *et al.*[38] The transport parameters upon oxidation are approximately one order of magnitude larger than upon hydration for the oxygen kinetics. This applies also to the transport parameters at high temperatures, where the electronic contribution to the conductivity is high. The activation energies are $E_A(\tilde{k}_{ox}) = 117(10)$ kJ mol^{-1} = 1.22(10) eV and $E_A(\tilde{D}_{ox}) = 100(17)$ kJ mol^{-1} = 1.04(17) eV. Compared to the activation energies for hydrating steps they are larger as it would be expected if the incorporation of oxygen originating from water is favored. It has not been expected that the diffusivity and surface reaction for oxidation are faster than for hydration. Oxidation measurements in

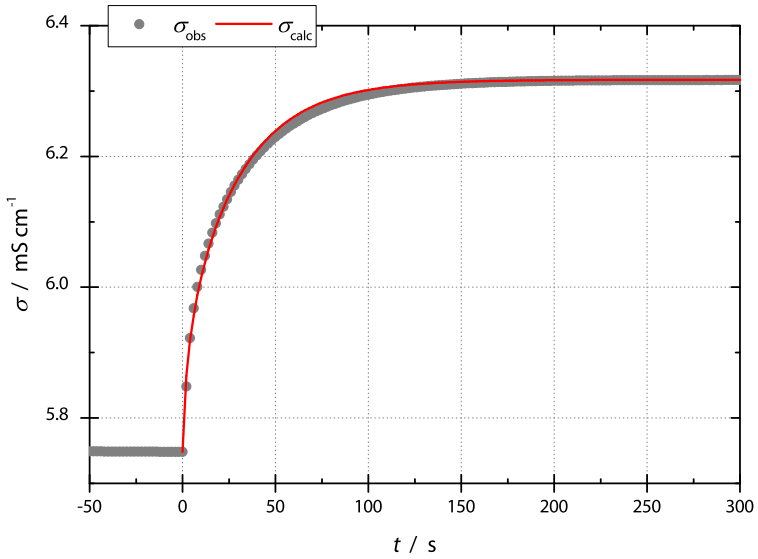

Figure 7.19: Relaxation curve upon oxidation with dry gas streams. ΔpO_2 = 70 mbar (30 mbar → 100 mbar) at 950 °C.

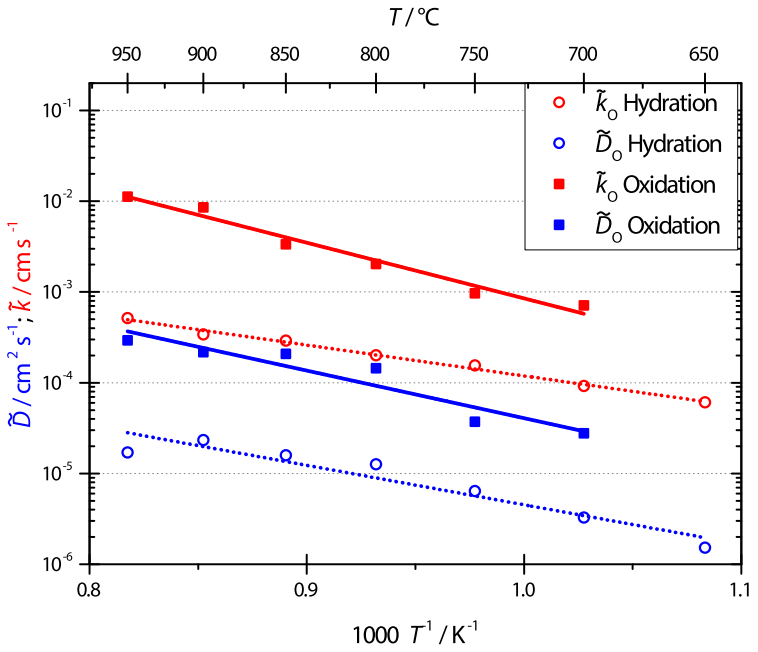

Figure 7.20: Transport parameters of oxygen versus the inverse temperature for hydrating steps (open symbols) with ΔpH_2O = 20 mbar (10 mbar → 30 mbar) for a pO_2 of 100 mbar and for dry oxidative steps with ΔpO_2 = 70 mbar (30 mbar → 100 mbar).

dependence of pH_2O have been carried out in order to investigate if this difference is caused by the hydrogen content and the lack of electron holes for the low transport parameters of oxygen upon hydration. The pH_2O was constant throughout the entire experiment, achieved by water vapor

saturators heated to the same temperature. The results are shown in Fig. 7.21.

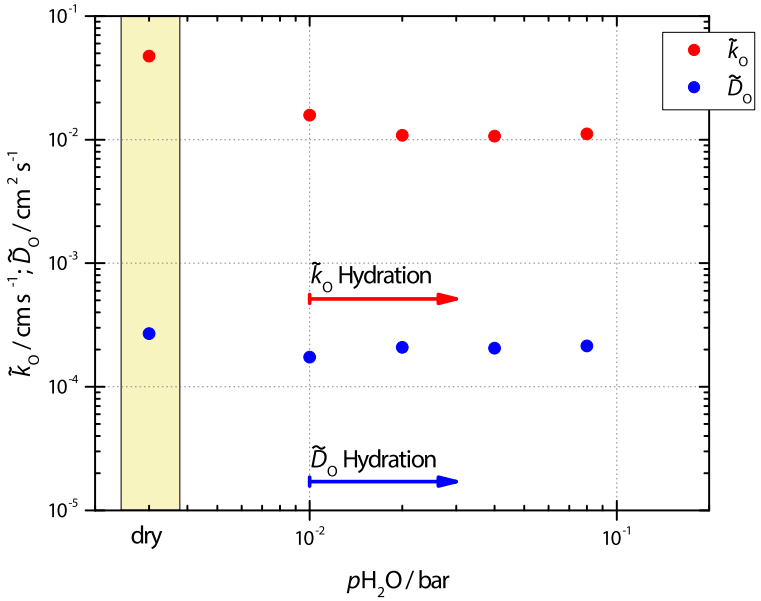

Figure 7.21: Transport parameters of oxygen versus pH_2O for oxidative steps with ΔpO_2 = 70 mbar (30 mbar → 100 mbar) at 950 °C. The transport parameters of the hydration is plotted as arrows from the initial to the final pH_2O. For the 'dry' conditions, the pH_2O is unknown but lower than 1×10^{-5} bar.

With increasing pH_2O, the transport parameters of oxidative steps decrease. This might be attributed to the fact that the oxygen flux is compensated by slow protons instead of fast electron holes. However, even at very high pH_2O, the transport parameters are not as low as the transport parameters obtained for hydrating steps, which are indicated by arrows in Fig. 7.21. The difference in the surface reaction rate might be caused by a different rate determining step during the incorporation process.

Simulations of Poetzsch *et al.*[71] for the surface flux at $t = 0$ for a change in pO_2 or pH_2O while keeping the other partial pressure constant have shown that the diffusivity of oxygen upon oxidation can in extreme cases even exceed the diffusivity of electron holes. The diffusivity of oxygen upon hydration can be much slower. The simulations are based on Eq. (3.31). A significant electronic contribution to the conductivity (rather large $t_{h\bullet}$) leads to a lower transference number of proton interstitials. Thus, the diffusivity of oxygen vacancies upon hydration is lowered by high contributions of proton interstitials and electron holes. In contrast, the diffusivity of oxygen upon oxidation is increased by a high electronic transference number.

8

FTIR Relaxation Experiments

For oxidation without protonic contribution to the electrical conductivity, the conductivity is a direct observable of the concentration of oxygen vacancies. For protonic conductors, mobilities of protons and electron holes contribute almost equally to the overall conductivity change upon concentration changes. For relaxation experiments, the use of other observables is possible, if they are dependent on the concentration that is of interest. The weight can be measured by thermogravimetry. However, the weight change caused by protons is hard to measure. An alternative is an optical measurement of the absorbance of hydroxy-groups by FTIR. The benefit of this method is that the absorbance is not influenced by electron hole conductivity or oxygen conductivity. With Lambert–Beer's law, the concentration of hydroxy-anions is directly accessible. Experiments presented in this chapter were performed by Tobias Romstadt B.Sc. during his research internship.

8.1 Thermal Radiation of Furnace

To obtain a significant mobility of protons and electron holes, the sample must be heated. However, the thermal radiation is also IR radiation. The reactor has been heated to temperatures between 20 °C and 500 °C and emission spectra were recorded in order to determine if the emission of the reactor is significant. They are depicted in Fig. 8.1. There is a small temperature dependence of the emission curves but the difference is small and no significant emission bands appear for higher temperatures.

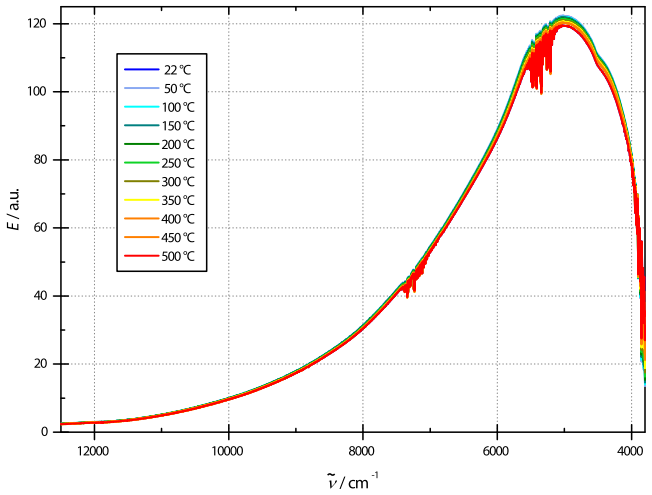

Figure 8.1: NIR emission spectra of the tungsten lamp transmitting through the tempered reactor and HOQ310 quartz glass.

8.2 Blank Reactor

Before and after the switch of the four-way valve, the gas concentrations of water are different and eventually also the adsorbed water species at the quartz glass. A time-dependent measurement of the reactor without sample during a switch in pH_2O has been performed in order to check whether the humidity of the gas phase has an effect on the measurement. The reference spectrum, I_0, is the measurement while the reactor is flushed with dry gas. The result is shown in Fig. 8.2.

The change in humidity of the gas phase has no effect on the emission spectrum. There are no additional bands evolving with time while the reactor is flushed with humid gas.

8.3 Absorption Spectrum of Lanthanum Tungstate

Using pellets with thicknesses below one millimeter, the absorption is too high so that nearly no transmission could be detected. Therefore, thin films of LaWO54 on NIR transmittable HOQ310 quartz glass substrates have been measured. For thicknesses of a couple of hundred nanometers, no absorption bands could be detected. A film with a much higher thickness of approx. 3 µm to 5 µm has been prepared (see Section 6.1.4). The emission spectrum for a humid atmosphere of the PLD film is shown in Fig. 8.3. The overall intensity of the emission spectrum is much lower. Additionally, absorption bands are present, e.g. at $\tilde{\nu}$ = 5010 cm^{-1} and $\tilde{\nu}$ = 4440 cm^{-1}. However, these absorption bands are almost equidistant, which might be caused by reflections at the material boundaries and constructive and destructive interference. Hence, these equidistant emission lines are dependent on the material thickness. Another explanation might be overtones. This behavior has not yet been

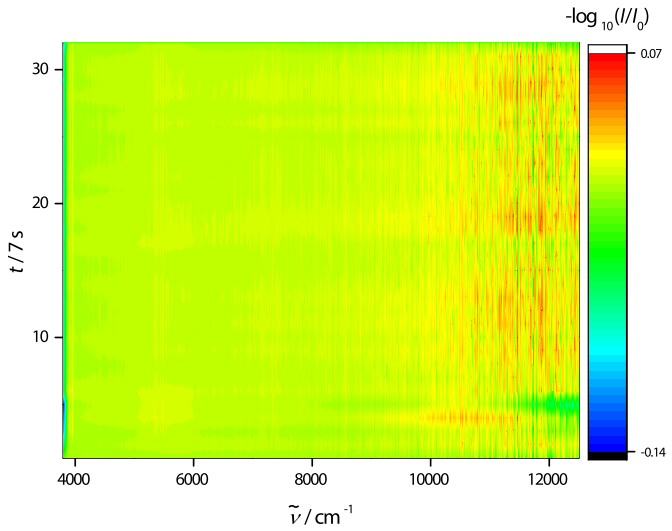

Figure 8.2: NIR emission spectra of the tungsten lamp transmitting through the tempered reactor and HOQ310 quartz glass in dependency of time after a switch from dry to humid atmosphere. pO_2 = 100 mbar and pH_2O_{humid} = 100 mbar at 400 °C. Time stepping of the consecutive measurements is approximately 7 s.

analyzed further.

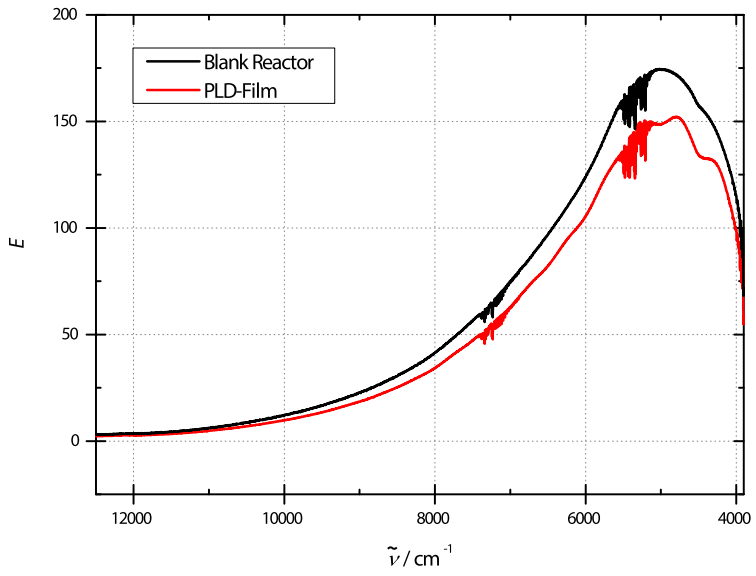

Figure 8.3: NIR emission spectrum of the fifth PLD film compared to the spectrum of the blank reactor. pO_2 = 100 mbar and pH_2O = 100 mbar at 400 °C.

Additional emission spectra were recorded in dependence on time before and after a switch from dry to humid conditions (see Fig. 8.4). The reference, I_0, is the equilibrium of the sample with dry gas short before the switch in pH_2O.

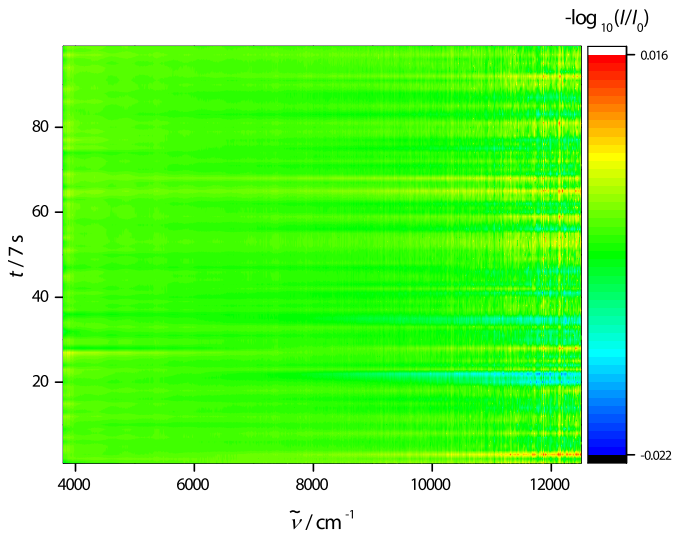

Figure 8.4: NIR emission spectrum of the fifth PLD film in dependency of time after a switch from dry to humid atmosphere. pO_2 = 100 mbar and pH_2O_{humid} = 100 mbar at 400 °C. Time stepping of the consecutive measurements is approximately 7 s.

Here, a time-dependent change in one of the absorption bands could not be detected upon hydration of the sample. Either the change in absorption of hydroxy-anions is too small compared to the noise or the absorption band of hydroxy-anions has not been identified yet. Further experiments with thicker samples and / or in the MIR regime are necessary to investigate the hydrogen relaxation behavior of LaWO54 thin films with FTIR.

8.4 Relaxation Behavior with Lambert–Beer's Law

A thin film is basically the same geometry like the parallel planes described in Section 4.3, only that there is a limit of the material at $x = 0$, an inert blocking material. For this material, the flux through the center is also zero. The sample's half-thickness in the model using two parallel planes is the thickness of the film when using PLD thin films.

With Lambert–Beer's law, Eq. (5.4), the concentration of hydrogen in the form of hydroxy-anions is proportional to the absorption band's intensity, $-\log(I/I_0) \propto c$. By a normalization function, the transport parameters can be determined. The absolute concentration is not necessary as it will need an (unknown) extinction coefficient ϵ_λ.

$$\frac{M_H^t}{M_H^\infty} = \frac{c_H^t - c_H^0}{c_H^\infty - c_H^0} = \frac{-\log\left(\frac{I}{I_0}\right)(t) + \log\left(\frac{I}{I_0}\right)(t=0)}{-\log\left(\frac{I}{I_0}\right)(t=\infty) + \log\left(\frac{I}{I_0}\right)(t=0)} \tag{8.1}$$

It is not important, which spectrum is used as a reference spectrum as long as it is the same spectrum for all concentrations. One can either use the spectrum of the blank reactor with or without an

undeposited quartz glass substrate to measure the reference spectrum like it would be done in classic IR spectroscopy. Another approach is using the dry sample as a reference spectrum and treating LaWO54 with a low protonic content as the solvent. The latter method has been used here.
As discussed in the previous chapter, the hydrogen concentration shows a two-fold relaxation behavior. A part of the hydrogen change follows the fast kinetic while the part dependent on the change in oxygen concentration changes with the slow kinetic. This should be reflected in the time-dependency of the IR spectrum. Here, the resulting curve is also a superposition of two single fold relaxation curves. The relation between both factors is

$$P_{\text{fast}} = \frac{c_{\text{H}}^{\infty}([\text{v}_{\text{O}}^{\bullet\bullet}]^0) - c_{\text{H}}^{0}([\text{v}_{\text{O}}^{\bullet\bullet}]^0)}{c_{\text{H}}^{\infty} - c_{\text{H}}^{0}} \qquad \text{and} \qquad P_{\text{slow}} = \frac{c_{\text{H}}^{\infty}([\text{v}_{\text{O}}^{\bullet\bullet}]^{\infty}) - c_{\text{H}}^{\infty}([\text{v}_{\text{O}}^{\bullet\bullet}]^0)}{c_{\text{H}}^{\infty} - c_{\text{H}}^{0}} \tag{8.2}$$

for the equation

$$\frac{-\log\left(\frac{I}{I_0}\right)(t) + \log\left(\frac{I}{I_0}\right)(t=0)}{-\log\left(\frac{I}{I_0}\right)(t=\infty) + \log\left(\frac{I}{I_0}\right)(t=0)} = P_{\text{fast}} \cdot f_{\tilde{k}_{\text{H}},\tilde{D}_{\text{H}}}(t) + P_{\text{slow}} \cdot f_{\tilde{k}_{\text{O}},\tilde{D}_{\text{O}}}(t) \tag{8.3}$$

The goal of this method was to support the result that electronic contribution below 750 °C is large enough to enable fast hydrogen diffusion. In an ideal case, the contribution of both kinetics is large enough to see two-fold concentration relaxation of hydrogen.

9

Conclusion

The electrical conductivity relaxation technique has been used to investigate the transport properties of lanthanum tungstate with respect to hydrogen and oxygen permeability. Lanthanum tungstate shows — depending on the conditions chosen in the experiment — two-fold monotonic, non-monotonic and single fold behavior in ECR experiments. This behavior has been explained by a derivation of the power factors for the contributions of each kinetic to the two-fold relaxation curve. For high temperatures, the charge mobility of electron holes is larger than the charge mobility of protons and consequently, non-monotonic behavior is observed upon hydration. For temperatures below 750 °C, the charge mobility of protons is larger than the charge mobility of electron holes and hence, two-fold monotonic behavior is observed. The power factor of the fast kinetic, $\tilde{B}$, switches the sign. At the temperature where $\tilde{B} = 0$, a single fold relaxation curve is observed because fast protons are introduced at the expense of electron holes with equal mobility and charge. The electrical conductivity relaxation technique is thus not suitable for the determination of transport parameters for the fast hydrogen kinetic. Other techniques such as weight or optical relaxation methods must be used instead. They give an insight on the concentration without an influence of the charge mobilities. FTIR measurements have been performed but a further investigation is necessary to support the ECR data.

In addition to the power factor $\tilde{B}$, making the determination of transport parameters impossible, the simultaneous determinability of all four transport parameters has been investigated. Depending on the sample size, at least three parameters can be determined in a single ECR experiment if the absolute value of $\tilde{B}$ is large enough.

In contrast to relaxation upon oxidation and reduction, the initial state is important for the fast kinetic. The fast hydrogen kinetic is dependent on the initial oxygen vacancy concentration, which

might differ significantly for hydrating and dehydrating steps.

The activation energies of the slow oxygen kinetic upon hydration are rather low with $E_A(\tilde{k}_O) = 65(2)\,\mathrm{kJ\,mol^{-1}}$ and $E_A(\tilde{D}_O) = 83(11)\,\mathrm{kJ\,mol^{-1}}$. Hence, oxidation experiments were performed. Higher activation energies were obtained with $E_A(\tilde{k}_{ox}) = 117(10)\,\mathrm{kJ\,mol^{-1}}$ and $E_A(\tilde{D}_{ox}) = 100(17)\,\mathrm{kJ\,mol^{-1}}$ but the transport parameters were more than one order of magnitude larger than the transport parameters upon hydration. This behavior cannot be explained yet.

In addition to the temperature-dependency of the transport parameters and power factors, the $p\mathrm{O_2}$-dependence has been investigated. For decreasing $p\mathrm{O_2}$, the two-fold behavior is less pronounced, indicated by decreasing absolute power factors. This, however, cannot be attributed to different mobilities as they should be almost constant because the diffusion coefficients are independent of $p\mathrm{O_2}$. The difference in hydrogen concentration must be smaller.

The conductivity relaxation method yields seven parameters: the transport parameters $\tilde{k}_H$, $\tilde{D}_H$, $\tilde{k}_O$ and $\tilde{D}_O$, and the power factors, $\tilde{A}$, $\tilde{B}$ and $\tilde{C}$. However, the number of unknown parameters is higher: The surface reaction rates $\tilde{k}_H$ and $\tilde{k}_O$, the charge mobilities, $u_{\mathrm{H_i^{\bullet}}}$, $u_{\mathrm{h^{\bullet}}}$ and $u_{\mathrm{v_O^{\bullet\bullet}}}$, and the concentrations in the form of the equilibrium constants $K_{\mathrm{O_2}}$ and $K_{\mathrm{H_2O}}$ with two reference points, $c_O(p\mathrm{O_2}, p\mathrm{H_2O}, T)$ and $c_H(p\mathrm{O_2}, p\mathrm{H_2O}, T)$ are unknown. Additional experiments yielding e.g. the reference points of the concentrations would be necessary to determine all unknown parameters.

A

Fitting Procedure

The analytical solution to the diffusion model, Eq. (7.6), has been fitted to the experimental data with a MATLAB script that will be discussed in this chapter. The script presented here is the function that simulates a curve and calculates the sum of the residuals, either with a weighting or unweighted. The function crank2D2f_function is called by an optimization routine, providing five independent variables, $\tilde{k}_{\mathrm{H}}$, $\tilde{D}_{\mathrm{H}}$, $\tilde{k}_{\mathrm{O}}$, $\tilde{D}_{\mathrm{O}}$ and $\tilde{B}$, with initial guesses for the variable (vector) k. Usually, an individual optimization routine was used but also MATLAB's internal functions fminsearch or the optimization toolbox's functions for simulated annealing or a genetic algorithm were used to find the global minimum of the fit.

Before fitting, the experimental data is read from a file into the variables time and sigma of the workspace and the sample's half-thicknesses into the variables a and b. For each relaxation, the number of constant time steps in the final equilibrium is determined from the relaxation curve. The number of roots, N, is 100 for all fits presented in this work.

Listing A.1: MATLAB script for fitting the two-dimensional model for two-fold relaxation profiles to the experimental data

```
1 function [ERR] = crank2D2f_function(k)
2 conststeps = 20;
3 N = 100;
4 t = evalin('base', 'time');
5 sigma = evalin('base', 'sigma');
6 a = evalin('base', 'a');
7 b = evalin('base', 'b');
```

In a first step, the dimensionless parameter L_a is calculated for hydrogen and oxygen and both also

for the second dimension (Lines 8, 9, 10 and 11). The final conductivity, sigmainf, is averaged over the amount of constant steps to flatten the noise (Line 14). The power factor $\tilde{A}$ is the conductivity of the first datapoint (Line 15). The power factor $\tilde{C}$ (gammaOxygen) can be calculated by the initial and final conductivity and the varied power factor $\tilde{B}$ (betaHydrogen) by $\tilde{C} = \sigma^{\infty} - \sigma^{0} - \tilde{B}$ (Line 17). The diffusion coefficients are copied to an internal variable as they are used in the iteration to increase performance (Lines 10 and 13), as well as $\tilde{B}$ for readability. The resulting power factors are copied into MATLAB's workspace as a return value for the optimization script (Lines 18–20).

```
8  LaO = a.*k(1)./k(2);
9  LbO = b.*k(1)./k(2);
10 DO = k(2);
11 LaH = a.*k(3)./k(4);
12 LbH = b.*k(3)./k(4);
13 DH = k(4);
14 sigmainf = mean(sigma(end-conststeps:end));
15 sigmanull = sigma(1);
16 betaHydrogen=k(5);
17 gammaOxygen = sigmainf - sigmanull - betaHydrogen;
18 assignin('base', 'Atilde', sigmanull);
19 assignin('base', 'Btilde', betaHydrogen);
20 assignin('base', 'Ctilde', gammaOxygen);
```

In the next step, the first N positive roots of the equation $La - \beta \tan \beta = 0$ have been determined. Likewise for hydrogen and oxygen and for both dimensions (Lines 26–33). The vectors for the roots and for the calculated relaxation curve have been preallocated to increase performance (Lines 21–25). The interval for the fit is not π but a shorter interval to avoid the discontinuity of the tangential function. The interval for the first root is chosen manually because only positive roots are used in the diffusion model.

```
21 Z1=zeros(1,N);
22 Z2=zeros(1,N);
23 Z3=zeros(1,N);
24 Z4=zeros(1,N);
25 Ytemp=zeros(1,numel(t));
26 betafn = @(beta) beta.*tan(beta)-LaO;DB = -pi/2:pi:(N+1)*pi;Z1(1) = fzero(betafn,[0 1.570796325]);
27 parfor x = 2:N;Z1(x) = fzero(betafn,[DB(x)+1e-10 DB(x+1)-1e-10]);end;
28 betafn = @(beta) beta.*tan(beta)-LbO;DB = -pi/2:pi:(N+1)*pi;Z2(1) = fzero(betafn,[0 1.570796325]);
29 parfor x = 2:N;Z2(x) = fzero(betafn,[DB(x)+1e-10 DB(x+1)-1e-10]);end;
30 betafn = @(beta) beta.*tan(beta)-LaH;DB = -pi/2:pi:(N+1)*pi;Z3(1) = fzero(betafn,[0 1.570796325]);
31 parfor x = 2:N;Z3(x) = fzero(betafn,[DB(x)+1e-10 DB(x+1)-1e-10]);end;
32 betafn = @(beta) beta.*tan(beta)-LbH;DB = -pi/2:pi:(N+1)*pi;Z4(1) = fzero(betafn,[0 1.570796325]);
33 parfor x = 2:N;Z4(x) = fzero(betafn,[DB(x)+1e-10 DB(x+1)-1e-10]);end;
```

In the next part of code, the relaxation curve is simulated with the analytical solution to the diffusion model, Eq. (7.6). For each time step, the absolute conductivity is calculated and stored in the vector Ytemp (Line 42). Each time step can be distributed to one of the cores in the parallel pool (Line 34). To decrease the number of iterations, the sum for each dimension and species is calculated (Lines 37–40) and afterwards the product of both dimensions per species is multiplied with the corresponding power factor.

```
34 parfor x = 1:numel(t);
35 sumaO=0;sumbO=0;sumaH=0;sumbH=0;
36 for y = 1:N;
37 sumaO=sumaO+(2.*LaO.^2*exp(-Z1(y).^2.*DO.*t(x)./a.^2))./(Z1(y).^2.*(Z1(y).^2+LaO.^2+LaO));
38 sumbO=sumbO+(2.*LbO.^2*exp(-Z2(y).^2.*DO.*t(x)./b.^2))./(Z2(y).^2.*(Z2(y).^2+LbO.^2+LbO));
39 sumaH=sumaH+(2.*LaH.^2*exp(-Z3(y).^2.*DH.*t(x)./a.^2))./(Z3(y).^2.*(Z3(y).^2+LaH.^2+LaH));
40 sumbH=sumbH+(2.*LbH.^2*exp(-Z4(y).^2.*DH.*t(x)./b.^2))./(Z4(y).^2.*(Z4(y).^2+LbH.^2+LbH));
41 end;
42 Ytemp(x) = sigmainf-betaHydrogen*sumaH*sumbH-gammaOxygen*sumaO*sumbO;
43 end;
```

In last part of the code, the residuals are summarized, here with the weighting that has been introduced in Eq. (7.5) (Line 47), and commented out without error weighting (Line45). Finally, the calculated and experimental curves are plotted with a semilogarithmic and linear x-axis (time-scale), Lines 48–58.

```
44 % Normal fit:
45 %ERR = sum((Ytemp' - sigma).^2);
46 % Weighted fit:
47 ERR = sum(rdivide(((Ytemp' - sigma).^2),(t+1)));
48 subplot(2,1,1);
49 semilogx(t,sigma,'bo',t,Ytemp','r-');
50 title('Semilogarithmisch')
51 xlabel('$t/\mathrm{s}$','interpreter','latex');
52 ylabel('$\sigma/\mathrm{mS\ cm^{-1}}$','interpreter','latex');
53 subplot(2,1,2);
54 plot(t,sigma,'bo',t,Ytemp','r-');
55 title('Linear');
56 xlabel('$t/\mathrm{s}$','interpreter','latex');
57 ylabel('$\sigma/\mathrm{mS\ cm^{-1}}$','interpreter','latex');
58 drawnow;
```

Each call of this function requires approximately one second of computation time. This time may vary with computer power, cores, number of time steps and roots etc.

B

Plant Construction

B.1 Software

The previous measurement software 'TestPoint' has been replaced by a new software, rewritten from scratch, using Microsoft Visual Studio 2010 and 2015 and the program language C# with .NET 4.5 and WPF for the graphical user interface. Third party .NET libraries that were included are OxyPlot and the libraries provided by the ADDIDATA relay card and Keithley's Digital MultiMeter 2701 and SourceMeter 2611B.

The software creates two output files, the file YYYYMMDD-##.dat contains the main data of the experiment including the data read from the first digital multimeter. The second data file YYYYMMDD-##_2.dat contains the data from the second digital multimeter. The first datafile has a header with information on the settings that are controlled by the software and data lines with date/time, the voltage of the four point DC conductivity measurement in V, the voltage of the oxygen sensor in V, the temperature at the oxygen sensor in °C, the voltage of Channel 111 in V, and the information, which gas stream is currently directed into the sample (1 or 2).

Listing B.1: Contents of the first data file created by the ECR measurement software.

```
1 //  ECR measurement
2 // Date : 20160111
3 // User : lfr
4 // T : 847 C
5 // I : 0.0001 A
6 // MFC 1 : 180 23.065 0 0.32 mL/min
7 // : 24.09 C
```

```
// MFC 2 : 180 23.065 0 0.112 mL/min
// : 6.98 C
// Interval: 2000 ms
// DD−MM−YYYY HH:MM:SS,U(sample),U(pO2sensor),T,U(CH111),MFC−Set
11.01.2016 08:56:54,−0.00281785941,0.0173051357,846.61969,−0.015606652,1
11.01.2016 08:56:56,−0.00232632295,0.0173041448,846.61377,0.00632960536,1
11.01.2016 08:56:58,−0.00199771323,0.017304318,846.631348,−0.0486616045,1
```

The second datafile has only data with date/time, milliseconds, the voltage at the sample in V and the active gas stream (1 or 2).

Listing B.2: Contents of the second data file created by the ECR measurement software.

```
11.01.2016 08:56:51,643,−0.00354520814,1
11.01.2016 08:56:51,751,−0.00348751293,1
11.01.2016 08:56:51,932,−0.00339422422,1
```

The datafiles are split into files for each step by a small program reading the active stream number. The main window of the software provides information about the last values that were read from the first multimeter. The data acquisition can be startet and stopped and the measurement interval for the first and the second multimeter can be set. Below are red and green lights to indicate if the data acquisition, the relaxation timer for the four way valve and the source meter are active. The green light beside 'MFC Sets' indicates which stream is currently directed into the reactor. At the bottom of the screen, the file name of the first output file of the current measurement is shown. The voltage of the sample (CH102) and the voltage of the oxygen sensor (CH103) are plotted in dependence of the last 500 time steps. A screenshot is shown in Fig. B.1.

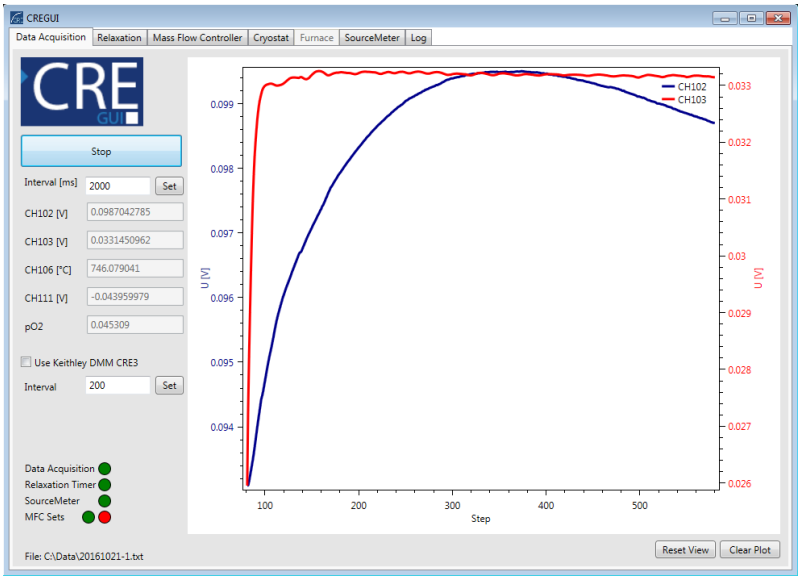

Figure B.1: Main window of the software controlling the experimental setup.

The relaxation timer, i.e. the four way valve, is controlled in the second tab. The four way valve can be switched manually by the button 'Switch MFC Set' or timed with the relaxation timer provided in seconds for an amount of cycles, i.e. two switches are one cycle. If the relaxation time is larger than four hours, the inactive stream is set to zero flux after 10 minutes and the flow rate that is set in the 'Mass Flow Controller' tab is reapplied two hours before the next switch to flush the tubes and assure a constant pO_2 and pH_2O. A screenshot is shown in Fig. B.2.

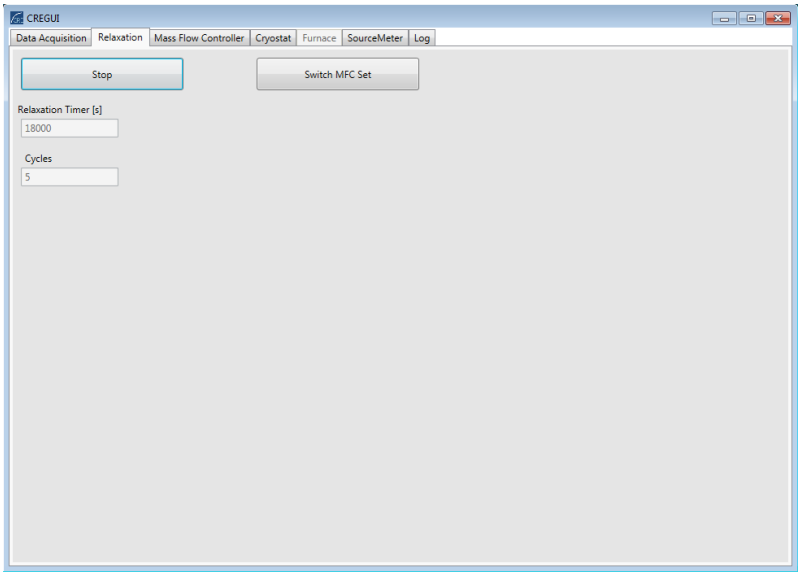

Figure B.2: Setting the relaxation timer and controlling the four way valve in the GUI.

In the next tab, the two streams are mixed by the MFCs. The desired flow rate can be set in the left field below the progress bars and the correction factor can be set in the right field, which is 1.0 for oxygen and nitrogen. The set flow rate as percentage of the maximum flow rate of the MFC is shown in the upper progress bar and the current flow rate measured internal by the MFC is shown in the lower progress bar. A screenshot is shown in Fig. B.3.

The water vapor pressure is set in the tab 'Cryostat'. The cryostats for the main saturators can only be set here. The temperature of the presaturation must be set at the cryostats manually. The pumps can be startet via the software and the current temperature at the cryostat can be read on demand. Pump speed and energy saving mode can be switched on and off. The cryostats communicate with the computer by simple SerialPort text commands. The readback of the thermocouples within the water vapor saturators is not yet implemented. A screenshot is shown in Fig. B.4.

The furnace control, planned for the next tab, is not yet implemented because temperature-dependent measurements are of no interest. In the following tab, the constant current source can be controlled. The constant current and the maximum voltage can be set. However, for the I–V curves, a separate program, which is a combination of the functions used here, in the 'Data Acquisition' tab, and additional functions was used. A screenshot is shown in Fig. B.5.

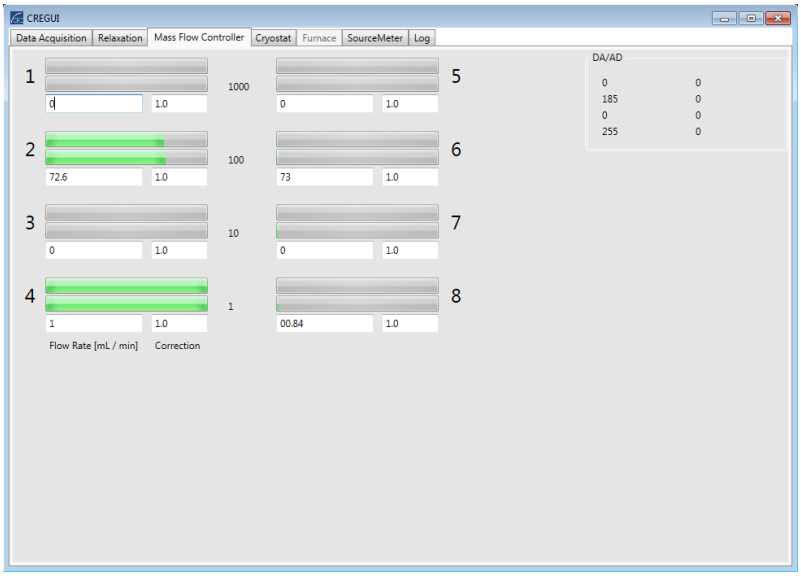

Figure B.3: Adjustment of the fluxes of the MFCs. The upper progress bar is the flow value set and the lower progress bar of each MFC is the readback. In the top right corner the byte that is sent so the digital-analog converter is shown.

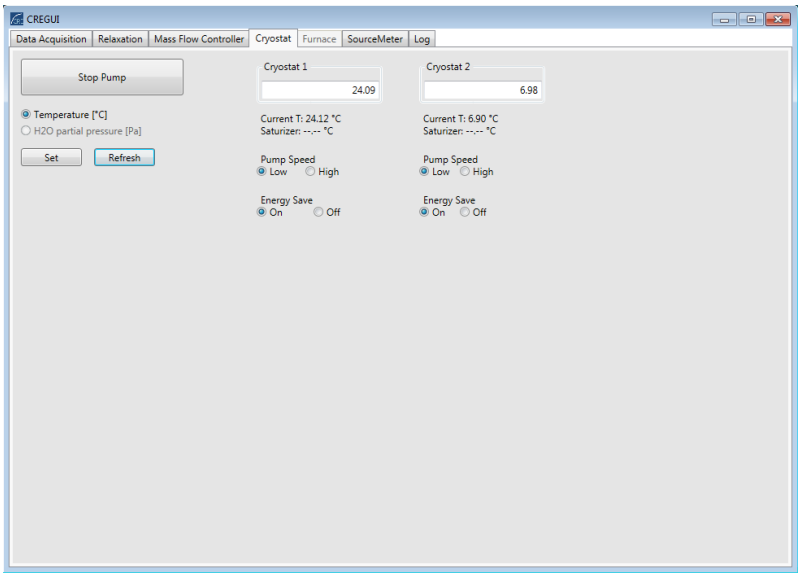

Figure B.4: The cryostats for the main water vapor saturators are controlled in this tab.

In the last tab (see Fig. B.6), events and errors are shown with a timestamp.

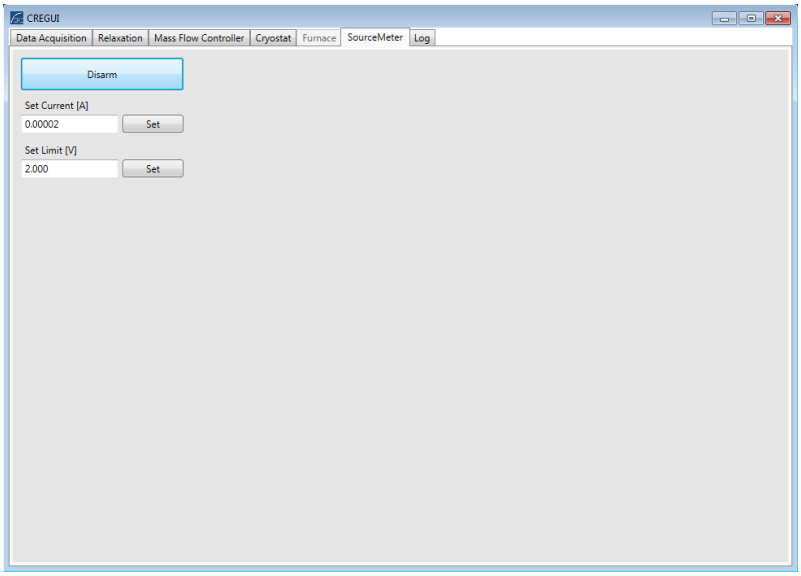

Figure B.5: This part of the software controls the constant current source.

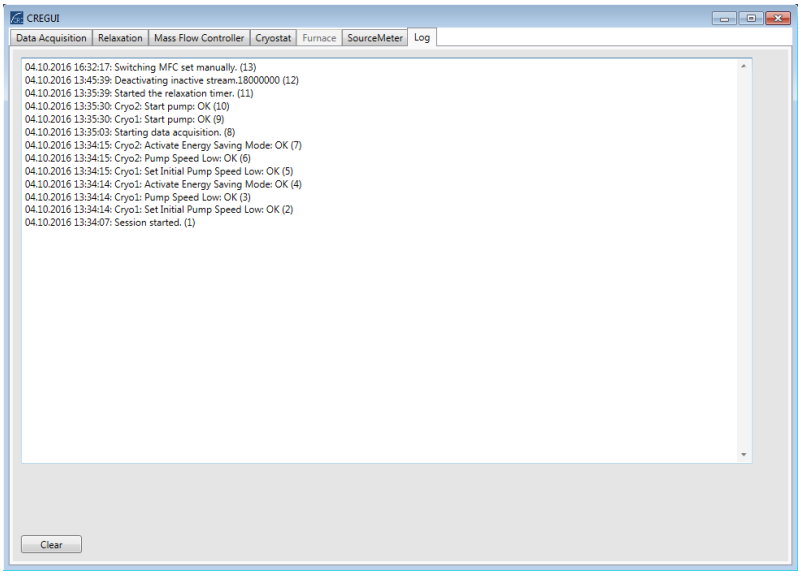

Figure B.6: Events and errors are shown in the log-window with a timestamp.

B.2 Mass flow controllers and DA/AD converter

The analog mass flow controllers are controlled by a voltage of up to 5 V. It is set by a digital-analog converter assembled by the electronic workshop.

The data type used to set the output voltage is one byte, leading to a sub-division into 256 steps ($0 = 0\,\mathrm{V} = 0\,\mathrm{mL\,min^{-1}}$, $255 = 5\,\mathrm{V} = \dot{V}_{\mathrm{max}}$). All MFCs are standardized on nitrogen and the correc-

tion factor for oxygen is one, leading to a resolution limitation by the DA converter of

$$\Delta \dot{V} = \frac{\dot{V}_{\max}}{255} \tag{B.1}$$

The deviation of the MFC itself is 0.5% according to the manufacturer MKS. The precision of the DA converter is thus sufficient. The monitoring of the flow rate works vice versa: a voltage between 0 V and 5 V is applied at one pin and is digitalized to twelve bit, resulting in a higher resolution of the measurement than of the controlling process.

The software addresses two sets of Digital–Analog converters (TLC5602C, Texas Instruments Inc., USA) and Analog–Digital converters (ADS7841, Texas Instruments Inc., USA) via a Universal Asynchronous Receiver/Transmitter (CDP6402, Harris Corporation, USA). The latter is connected by SerialPort.

B.3 Water Vapor Saturator

For the water vapor saturators, yellow cooling fluid consisting of water, ethylene glycol and so called 'inhibitors' was used (Cryo 30, Lauda Dr. R. Wobser GmbH & Co. KG, Germany). The temperature was set so that the desired temperature was measured at the thermocouple within the colling fluid right beside the water reservoir. The fluctuation of the temperature within the water vapor saturator is approximately ±0.05 °C. The temperatures and corresponding water vapor pressures used in the experiment are summarized in Tab. B.1.

Table B.1: Water vapor pressures for different temperatures.

Temperature T/°C	Water vapor pressure $p\mathrm{H_2O}$/mbar
6.98	10
24.09	30
45.84	100

B.4 Four way valve

The four way valve (Valco Instruments Co. Inc., VICI A 90) is controlled by a magnetic valve (Bürkert 5420) with pressured air. The magnetic valve changes the active stream if the voltage is switched between high and low. The switching process is controlled by a galvanic isolated relay card (ADDIDATA APCI-2200) in the computer. While the voltage is set to high, the active stream is provided by MFCs 1 to 4 and saturators 1 and 3, while it is set to low, the active stream is provided by MFCs 5 to 8 and saturators 2 and 4. The opening contact ÖK is not used. If the voltage of relay number 0 is set to high by setting b_Set1DigitalOutputOn(0), the voltage applied to pin 1 is directed to pin 18.

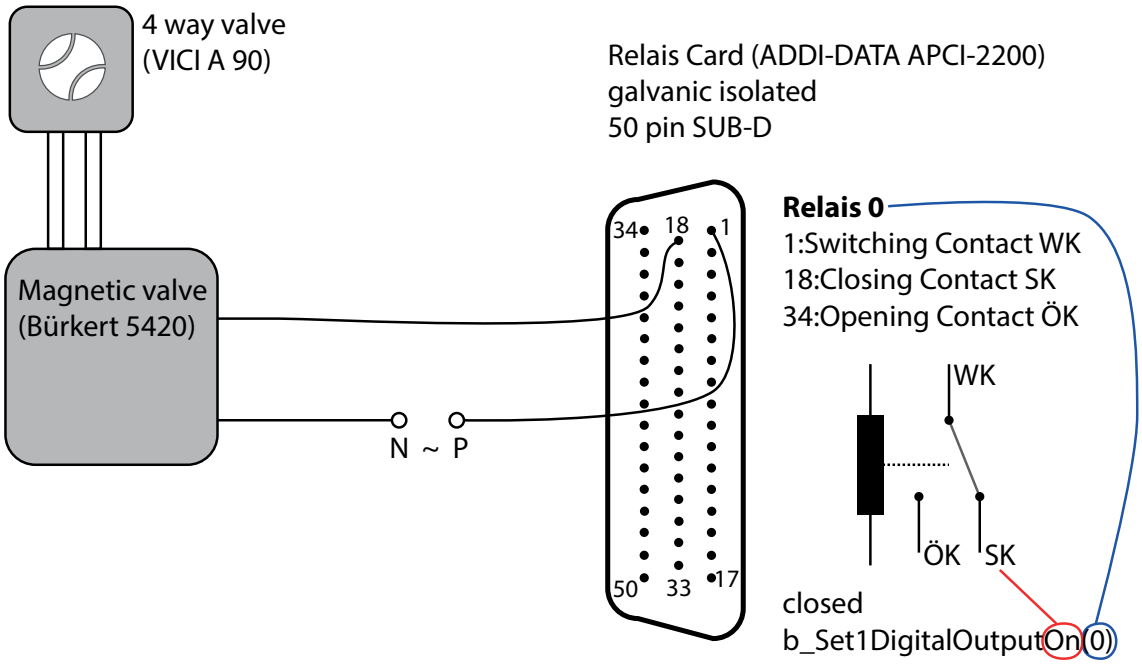

Figure B.7: Control scheme of the four way valve.

References

[1] T. Shimura, S. Fujimoto, H. Iwahara, *Solid State Ionics* **2001**, *143*, 117–123.

[2] R. Haugsrud, *Solid State Ionics* **2007**, *178*, 555–560.

[3] A. Magrasó, C. Frontera, D. Marrero-López, P. Núñez, *Dalton Transactions* **2009**, 10273.

[4] R. Haugsrud, T. Norby, *Nature Materials* **2006**, *5*, 193–196.

[5] R. Haugsrud, C. Kjølseth, *Journal of Physics and Chemistry of Solids* **2008**, *69*, 1758–1765.

[6] M. J. Zayas-Rey, L. dos Santos-Gómez, J. M. Porras-Vázquez, E. R. Losilla, D. Marrero-López, *Journal of Power Sources* **2015**, *294*, 483–493.

[7] S. Escolástico, M. Schroeder, J. M. Serra, *Journal of Materials Chemistry A* **2014**, *2*, 6616.

[8] M. Balaguer, C. Solís, F. Bozza, N. Bonanos, J. M. Serra, *Journal of Materials Chemistry A* **2013**, *1*, 3004.

[9] M. Yoshimura, A. Rouanet, *Materials Research Bulletin* **1976**, *11*, 151–158.

[10] A. Magrasó, R. Haugsrud, *J. Mater. Chem. A* **2014**, *2*, 12630–12641.

[11] A. Magrasó, C. H. Hervoches, I. Ahmed, S. Hull, J. Nordström, A. W. B. Skilbred, R. Haugsrud, *J. Mater. Chem. A* **2013**, *1*, 3774–3782.

[12] T. Scherb, *Strukturelle Charakterisierung von Wasserstoff trennenden Gasseparationsmembranen auf Lantanoid-Wolframat-Basis*, Helmholtz-Zentrum Berlin für Materialien und Energie, Berlin, **2011**.

[13] T. Scherb, S. A. Kimber, C. Stephan, P. F. Henry, G. Schumacher, J. Just, S. Escolástico, J. M. Serra, J. Seeger, A. H. Hill, *ArXiv e-prints* **2013**, arXiv:1305.3385v1 [cond–mat.mtrl–sci].

[14] L.-E. Kalland, A. Magrasó, A. Mancini, C. Tealdi, L. Malavasi, *Chemistry of Materials* **2013**, *25*, 2378–2384.

[15] J. Seeger, M. E. Ivanova, W. A. Meulenberg, D. Sebold, D. Stöver, T. Scherb, G. Schumacher, S. Escolástico, C. Solís, J. M. Serra, *Inorganic Chemistry* **2013**, *52*, 10375–10386.

[16] N. Diot, O. Larcher, R. Marchand, J. Kempf, P. Macaudière, *Journal of Alloys and Compounds* **2001**, *323-324*, 45–48.

[17] J. Seeger, *Entwicklung protonenleitender Werkstoffe und Membranen auf Basis von Lanthan-Wolframat für die Wasserstoffabtrennung aus Gasgemischen*, Forschungszentrum Jülich, Jülich, **2013**.

[18] S. Erdal, L.-E. Kalland, R. Hancke, J. M. Polfus, R. Haugsrud, T. Norby, A. Magrasó, *International Journal of Hydrogen Energy* **2012**, *37*, 8051–8055.

[19] R. D. Shannon, *Acta Crystallographica Section A* **1976**, *32*, 751–767.

[20] A. Magrasó, J. M. Polfus, C. Frontera, J. Canales-Vázquez, L.-E. Kalland, C. H. Hervoches, S. Erdal, R. Hancke, M. S. Islam, T. Norby, R. Haugsrud, *Journal of Materials Chemistry* **2012**, *22*, 1762.

[21] L. G. Harrison, *Transactions of the Faraday Society* **1961**, *57*, 1191.

[22] A. Atkinson, *Solid State Ionics* **1984**, *12*, 309–320.

[23] F. A. Kröger, H. J. Vink, *Solid State Physics* **1956**, *3*, 307–435.

[24] M. Martin in *Diffusion in condensed matter*, (Eds.: P. Heitjans, J. Kärger), Springer, Berlin, New York, **2005**, pp. 211–248.

[25] M. Kilo, G. Borchardt, B. Lesage, S. Weber, S. Scherrer, M. Schroeder, M. Martin, *Key Engineering Materials* **2002**, *206-213*, 601–604.

[26] S. Beschnitt, T. Zacherle, R. A. de Souza, *The Journal of Physical Chemistry C* **2015**, *119*, 27307–27315.

[27] C. Wagner, W. Schottky, *Z. Phys. Chem. B* **1930**, *11*, 163–210.

[28] J. Frenkel, *Z. Physik* **1926**, *35*, 652–669.

[29] R. K. Datta, R. Roy, *Journal of the American Ceramic Society* **1967**, *50*, 578–583.

[30] T. Norby, *Journal of the Korean Ceramic Society* **2010**, *47*, 19–25.

[31] K.-D. Kreuer, *Chemistry of Materials* **1996**, *8*, 610–641.

[32] K. Kreuer, *Annual Review of Materials Research* **2003**, *33*, 333–359.

[33] M. E. Björketun, P. Sundell, G. Wahnström, D. Engberg, *Solid State Ionics* **2005**, *176*, 3035–3040.

[34] R. Hoffmann, *Angewandte Chemie* **1987**, *99*, 871–906.

[35] D. M. Smyth, *The defect chemistry of metal oxides*, Oxford University Press, New York and Oxford, **2000**.

[36] H.-I. Yoo, M. Martin, *Physical Chemistry Chemical Physics* **2010**, *12*, 14699.

[37] M. Amsif, A. Magrasó, D. Marrero-López, J. C. Ruiz-Morales, J. Canales-Vázquez, P. Núñez, *Chemistry of Materials* **2012**, *24*, 3868–3877.

[38] C. Solís, S. Escolástico, R. Haugsrud, J. M. Serra, *The Journal of Physical Chemistry C* **2011**, *115*, 11124–11131.

[39] R. Hancke, S. Fearn, J. A. Kilner, R. Haugsrud, *Physical Chemistry Chemical Physics* **2012**, *14*, 13971–13978.

[40] R. Hancke, Z. Li, R. Haugsrud, *International Journal of Hydrogen Energy* **2012**, *37*, 8043–8050.

[41] R. Hancke, A. Magrasó, T. Norby, R. Haugsrud, *Solid State Ionics* **2013**, *231*, 25–29.

[42] O. F. Lohne, M. Sogaard, K. Wiik, *Journal of The Electrochemical Society* **2013**, *160*, F1282–F1292.

[43] A. Falkenstein, D. N. Mueller, R. A. De Souza, M. Martin, *Solid State Ionics* **2015**, *280*, 66–73.

[44] S. Escolástico, C. Solís, J. M. Serra, *Solid State Ionics* **2012**, *216*, 31–35.

[45] V. Gil, J. Gurauskis, C. Kjølseth, K. Wiik, M.-A. Einarsrud, *International Journal of Hydrogen Energy* **2013**, *38*, 3087–3091.

[46] H. Yoon, T. Oh, J. Li, K. L. Duncan, E. D. Wachsman, *Journal of The Electrochemical Society* **2009**, *156*, B791.

[47] Y. Guo, Y. Lin, R. Ran, Z. Shao, *Journal of Power Sources* **2009**, *193*, 400–407.

[48] L. Yang, S. Wang, K. Blinn, M. Liu, Z. Liu, Z. Cheng, *Science (New York N.Y.)* **2009**, *326*, 126–129.

[49] R. Merkle, J. Maier, *Physical Chemistry Chemical Physics* **2002**, *4*, 4140–4148.

[50] D. Poetzsch, R. Merkle, J. Maier, *Journal of the Electrochemical Society* **2015**, *162*, F939–F950.

[51] C. Wagner, *Ber. Bunsenges. Phys. Chem.* **1968**, *70*.

[52] J. Maier, *Solid State Ionics* **1998**, *112*, 197–228.

[53] M. Kessel, De Souza, R. A., H.-I. Yoo, M. Martin, *Applied Physics Letters* **2010**, *97*, 21910.

[54] M. J. Pietrowski, De Souza, R. A., M. Fartmann, R. ter Veen, M. Martin, *Fuel Cells* **2013**, n/a.

[55] L. W. Barr, *Defect and Diffusion Forum* **1997**, *143-147*, 3–10.

[56] R. A. De Souza, J. A. Kilner, *Solid State Ionics* **1998**, *106*, 175–187.

[57] R. A. De Souza, J. Zehnpfenning, M. Martin, J. Maier, *Solid State Ionics* **2005**, *176*, 1465–1471.

[58] R. A. De Souza, M. Martin, *MRS Bulletin* **2009**, *34*, 907–914.

[59] E. O. Kirkendall, *Trans. AIME* **1942**, *147*, 104–109.

[60] H. Mehrer, *Diffusion in solids: Fundamentals, methods, materials, diffusion-controlled processes*, Springer, Berlin, New York, **2007**.

[61] K. Kreuer, *Solid State Ionics* **1999**, *125*, 285–302.

[62] C. de Grotthuss, *Ann. Chim.* **1806**, *58*, 54–74.

[63] N. Agmon, *Chemical Physics Letters* **1995**, *244*, 456–462.

[64] De Souza, R. A., *Advanced Functional Materials* **2015**, *25*, 6326–6342.

[65] R. Haase, *Thermodynamics of irreversible processes*, Dover, New York, **1990**.

[66] H. Schmalzried, *Chemical kinetics of solids*, VCH, Weinheim and Cambridge, **1995**.

[67] S. R. d. Groot, P. Mazur, *Non-equilibrium thermodynamics*, Dover Publications, New York, **1984**.

[68] H.-I. Yoo, C.-E. Lee, *Journal of the American Ceramic Society* **2005**, *88*, 617–623.

[69] H.-I. Yoo, J.-Y. Yoon, J.-S. Ha, C.-E. Lee, *Physical Chemistry Chemical Physics* **2008**, *10*, 974.

[70] H.-I. Yoo, C.-E. Lee, *Solid State Ionics* **2009**, *180*, 326–337.

[71] D. Poetzsch, R. Merkle, J. Maier, *Advanced Functional Materials* **2015**, *25*, 1542–1557.

[72] D. R. Lide, *CRC handbook of chemistry and physics: A ready-reference book of chemical and physical data*, 88th ed. / editor-in-chief, David R. Lide, CRC, Boca Raton, Fla. and London, **2008**.

[73] H. Duenwald, C. Wagner, *Z. Phys. Chem.* **1934**, *22*, 198–207.

[74] F. Viani, *Oxidation of Metals* **1984**, *21*, 309–327.

[75] I. Yasuda, *Journal of The Electrochemical Society* **1994**, *141*, 1268.

[76] I. Yasuda, M. Hishinuma, *Journal of Solid State Chemistry* **1996**, *123*, 382–390.

[77] T. Bieger, J. Maier, R. Waser, *Solid State Ionics* **1992**, *53-56*, 578–582.

[78] I. Denk, F. Noll, J. Maier, *Journal of the American Ceramic Society* **1997**, *80*, 279–285.

[79] J. J. Kim, S. R. Bishop, N. Thompson, Y. Kuru, H. L. Tuller, *Solid State Ionics* **2012**, *225*, 198–200.

[80] K. Kishio, K. Suzuki, T. Hasegawa, T. Yamamoto, K. Kitazawa, K. Fueki, *Journal of Solid State Chemistry* **1989**, *82*, 192–202.

[81] B. Ma, *Solid State Ionics* **1996**, *83*, 65–71.

[82] C.-R. Song, H.-I. Yoo, *Solid State Ionics* **1999**, *120*, 141–153.

[83] L. J. van der Pauw, *Philips Research Reports* **1958**, *13*, 1–9.

[84] G. Rietveld, C. Koijmans, L. Henderson, M. J. Hall, S. Harmon, P. Warnecke, B. Schumacher, *IEEE Transactions on Instrumentation and Measurement* **2003**, *52*, 449–453.

[85] J. Crank, *The Mathematics of Diffusion*, second ed., Oxford University Press, Oxford (UK), **1975**.

[86] H. S. Carslaw, J. C. Jaeger, *Conduction of heat in solids*, 2nd ed., Clarendon, Oxford, **1959**.

[87] D. N. Mueller, R. A. De Souza, J. Brendt, D. Samuelis, M. Martin, *Journal of Materials Chemistry* **2009**, *19*, 1960.

[88] M. Leonhardt, R. A. De Souza, J. Claus, J. Maier, *Journal of The Electrochemical Society* **2002**, *149*, J19.

[89] J. Maier, *Journal of the American Ceramic Society* **1993**, *76*, 1212–1217.

[90] S. Wang, A. Verma, Y. Yang, A. Jacobson, B. Abeles, *Solid State Ionics* **2001**, *140*, 125–133.

[91] M. W. den Otter, H. J. M. Bouwmeester, B. A. Boukamp, H. Verweij, *Journal of The Electrochemical Society* **2001**, *148*, J1–J6.

[92] W. Preis, E. Bucher, W. Sitte, *Journal of Power Sources* **2002**, *106*, 116–121.

[93] S. Wang, P. van der Heide, C. Chavez, A. Jacobson, S. Adler, *Solid State Ionics* **2003**, *156*, 201–208.

[94] R. A. Cox-Galhotra, S. McIntosh, *Solid State Ionics* **2010**, *181*, 1429–1436.

[95] A. Falkenstein, Diplomarbeit, RWTH Aachen, Aachen, **2012**.

[96] P. Fielitz, G. Borchardt, *Solid State Ionics* **2001**, *144*, 71–80.

[97] Y. Li, K. Gerdes, H. Diamond, X. Liu, *Solid State Ionics* **2011**, *204-205*, 104–110.

[98] F. Ciucci, *Solid State Ionics* **2013**, *239*, 28–40.

[99] J. Blair, D. S. Mebane, *Solid State Ionics* **2015**, *270*, 47–53.

[100] M. Katsuki, S. Wang, M. Dokiya, T. Hashimoto, *Solid State Ionics* **2003**, *156*, 453–461.

[101] F. He, X. Jin, T. Tian, H. Ding, R. D. Green, X. Xue, *Journal of the Electrochemical Society* **2015**, *162*, F951–F958.

[102] H.-I. Yoo, J.-K. Kim, C.-E. Lee, *Journal of The Electrochemical Society* **2009**, *156*, B66–B73.

[103] D.-K. Lim, T.-R. Lee, B. Singh, J.-Y. Park, S.-J. Song, *Journal of the Electrochemical Society* **2014**, *161*, F710–F716.

[104] Shimadzu Corporation, FTIR Talk Letter Vol. 15: Fourier Transform and Apodization.

[105] H. Günzler, H.-U. Gremlich, *IR-Spektroskopie: Eine Einführung*, 4., vollst. überarb. und aktualisierte Aufl., Wiley-VCH, Weinheim, **2003**.

[106] M. P. Pechini, *pat.*, 3,330,697.

[107] M. Yoshimura, J. Ma, M. Kakihana, *Journal of the American Ceramic Society* **1998**, *81*, 2721–2724.

[108] S. Escolástico, V. B. Vert, J. M. Serra, *Chemistry of Materials* **2009**, *21*, 3079–3089.

[109] J. Schumacher, Bachelor thesis, RWTH Aachen, Aachen, **2014**.

[110] H. Krischner, B. Koppelhuber-Bitschnau, *Roentgenstrukturanalyse und Rietveldmethode*, **1994**.

[111] R. A. Young, *The Rietveld method*, International Union of Crystallograhy and Oxford University Press, [Chester, England], Oxford, and New York, **1993**.

[112] Y. Tsur, C. A. Randall, *Journal of the American Ceramic Society* **2000**, *83*, 2062–2066.

[113] J. Rodríguez-Carvajal, An Introduction to the Program FullProf, **1997**.

[114] E. Vøllestad, A. Gorzkowska-Sobas, R. Haugsrud, *Thin Solid Films* **2012**, *520*, 6531–6534.

[115] R. Merkle, R. Zohourian, J. Maier, *Solid State Ionics* **2016**, *288*, 291–297.

[116] J. E. ten Elshof, M. Lankhorst, H. J. M. Bouwmeester, *Journal of The Electrochemical Society* **1997**, *144*, 1060.

[117] E. Bucher, A. Egger, P. Ried, W. Sitte, P. Holtappels, *Solid State Ionics* **2008**, *179*, 1032–1035.

[118] D. N. Mueller, R. A. De Souza, H.-I. Yoo, M. Martin, *Chemistry of Materials* **2012**, *24*, 269–274.

[119] M. Lankhorst, J. E. ten Elshof, *Journal of Solid State Chemistry* **1997**, *130*, 302–310.

Acronyms

CAS Chemical Abstracts Service.

ECR electrical conductivity relaxation.

EDX energy dispersive X-ray spectroscopy.

FEM finite element method.

FTIR Fourier-transform infrared.

HTM hydrogen transport membrane.

IEDP isotope exchange depth profile.

IR infrared.

LaWO54 $La_{5.4}WO_{11.1-0.2\delta}$.

MFC mass flow controller.

MIEC mixed ionic–electronic conductor.

MIR mid infrared.

NIR near infrared.

OTM oxygen transport membrane.

PC-SOFC proton conducting solid oxide fuel cell.

PLD pulsed laser deposition.

SEM scanning electron microscopy.

s.g. space group.

SOEC solid oxide electrolyzer cell.

sof site occupancy factor.

SOFC solid oxide fuel cell.

ToF-SIMS time-of-flight secondary ion mass spectrometry.

XRD X-ray diffraction.

YSZ yttria stabilized zirconia, $Y_xZr_{1-x}O_2$.

List of Symbols

e' free electron.

$\tilde{D}_H$ ambipolar diffusion coefficient of hydrogen.

$\tilde{D}_O$ ambipolar diffusion coefficient of oxygen.

$h^{\bullet}$ electron hole.

$H_i^{\bullet}$ protonic interstitial.

k_B Boltzmann's constant.

$\tilde{k}_H$ ambipolar surface reaction rate of hydrogen.

$\tilde{k}_O$ ambipolar surface reaction rate of oxygen.

$O_O^{\times}$ relative neutral oxygen on oxygen site.

$OH_O^{\bullet}$ hydroxy-anion on oxygen site.

$O_{\frac{54}{56}O}^{\frac{4}{56}\prime}$ oxygen on anion sublattice site (fractional notation for lanthanum tungstate).

O_v'' occupied structural oxygen vacancy.

N_A Avogadro number.

pO_2 partial pressure of oxygen.

pH_2 partial pressure of hydrogen.

pH_2O partial pressure of water vapor.

$v_O^{\bullet\bullet}$ oxygen vacancy.

$v_{\frac{54}{56}O}^{\frac{108}{56}\bullet}$ oxygen vacancy (fractional notation for lanthanum tungstate).

V_{UC} volume of the unit cell.

$v_v^{\times}$ structural vacancy.

List of Figures

List of Tables